Dapeng Chen Chengtian Lin Andrey Maljuk Fang Zhou

# Growth and Characterization of Bulk Superconductor Material



# **Springer Series in Materials Science**

# Volume 243

# Series editors

Robert Hull, Charlottesville, USA Chennupati Jagadish, Canberra, Australia Yoshiyuki Kawazoe, Sendai, Japan Richard M. Osgood, New York, USA Jürgen Parisi, Oldenburg, Germany Tae-Yeon Seong, Seoul, Republic of Korea (South Korea) Shin-ichi Uchida, Tokyo, Japan Zhiming M. Wang, Chengdu, China The Springer Series in Materials Science covers the complete spectrum of materials physics, including fundamental principles, physical properties, materials theory and design. Recognizing the increasing importance of materials science in future device technologies, the book titles in this series reflect the state-of-the-art in understanding and controlling the structure and properties of all important classes of materials.

More information about this series at http://www.springer.com/series/856

Dapeng Chen · Chengtian Lin Andrey Maljuk · Fang Zhou

# Growth and Characterization of Bulk Superconductor Material



Dapeng Chen Max Planck Institute for Solid State Research Stuttgart Germany

Chengtian Lin
Max Planck Institute for Solid State
Research
Stuttgart
Germany

Andrey Maljuk Leibniz Institute for Solid State and Materials Research Dresden Germany

Fang Zhou Institute of Physics Chinese Academy of Sciences University of Chinese Academy of Sciences Beijing China

ISSN 0933-033X ISSN 2196-2812 (electronic) Springer Series in Materials Science ISBN 978-3-319-31546-1 ISBN 978-3-319-31548-5 (eBook) DOI 10.1007/978-3-319-31548-5

Library of Congress Control Number: 2016937938

### © Springer International Publishing Switzerland 2016

This work is subject to copyright. All rights are reserved by the Publisher, whether the whole or part of the material is concerned, specifically the rights of translation, reprinting, reuse of illustrations, recitation, broadcasting, reproduction on microfilms or in any other physical way, and transmission or information storage and retrieval, electronic adaptation, computer software, or by similar or dissimilar methodology now known or hereafter developed.

The use of general descriptive names, registered names, trademarks, service marks, etc. in this publication does not imply, even in the absence of a specific statement, that such names are exempt from the relevant protective laws and regulations and therefore free for general use.

The publisher, the authors and the editors are safe to assume that the advice and information in this book are believed to be true and accurate at the date of publication. Neither the publisher nor the authors or the editors give a warranty, express or implied, with respect to the material contained herein or for any errors or omissions that may have been made.

Printed on acid-free paper

This Springer imprint is published by Springer Nature The registered company is Springer International Publishing AG Switzerland

# **Preface**

The key point in condense matter science is the discovery of new class of compounds with interesting features in physics and chemistry, such as structure, electronic properties, magnetization and superconductivity. The first superconductor of mercury was discovered dropping to zero resistance at liquid helium temperature of 4.2 K by Heike Kammerlingh Onnes, a Dutch physicist from Leiden University in 1908. After half a century, Bernd Matthias et al. found superconductivity at 23.3 K in Nb<sub>3</sub>Ge with the cubic A15 structure in 1967. Almost no one, least of all Bernd Matthias who discovered more than a thousand superconductors, imagined superconductivity in such materials at that time.

About 80 years passed, superconductivity remained a property of metals at very low temperatures. A breakthrough in the history of materials science came in the 1980s, the  $T_{\rm c} \sim 30~{\rm K}$  in La<sub>1-x</sub>Sr<sub>x</sub>CuO<sub>4</sub> ceramics was discovered by Bednorz and Muller. Sleight and co-workers found Ba<sub>1-x</sub>K<sub>x</sub>BiO<sub>3</sub> (1989) at 34 K. This remarkable discovery has renewed the interest in superconductive research. One major point to superconductivity in these materials is the mixed valence of Bi and Cu. These compounds are structurally derived from the perovskite type, and only shortly later materials with so far unimaginable critical temperatures were discovered. The most prominent is YBa<sub>2</sub>Cu<sub>3</sub>O<sub>7-\delta</sub> (YBCO) with a critical temperature of 92 K, well above the boiling point of liquid nitrogen. The up-to-date highest transition temperature close to 135 K was observed in HgBa<sub>2</sub>Ca<sub>2</sub>Cu<sub>3</sub>O<sub>8+\delta</sub> ceramics in 1990s.

In spite of the immense scientific efforts on the cuprate-based materials with more than one hundred thousand publications till now, the detailed physical mechanism still remains uncertain. Hence, the late discovery of superconductivity in non-cuprate compounds is paid a great attention: The rare earth transition metal borocarbides (1994), the unusual features in conventional superconductors; high transition temperature  $T_c \sim 40$  K in MgB<sub>2</sub> (2001), an ordinary s-p metal; sodium cobaltate Na<sub>x</sub>CoO<sub>2</sub> (2003), a strongly correlated electron system. Apart from the high transition temperature of 40 K, two-band superconductivity was the other

vi Preface

unexpected phenomenon in MgB<sub>2</sub> which is the only superconductor with substantiated theoretical and experimental evidence for two-band superconductivity.

An "iron age" came in 2008. The discovery of a new family of high critical temperature iron and arsenic superconductors (FeAs) marked a new major revolution in the world of superconductivity. The new compounds, which do not contain copper (Cu) but have iron (Fe), arsenic (As), oxygen (O), and fluorine (F) will help scientists to solve some of the mysteries in the area of solid-state physics. These compounds reveal many properties similar to high- $T_c$  cuprates, and at the same time superconducting state has multiband character. The experimental investigations revealed a great variety of "exotic" physical properties in the above-presented compounds such as multiband and anistropic effects in the superconducting state. Detailed comparison of the available data for new class of superconductors, especially with the high- $T_c$  cuprates, might be helpful to improve our present incompetent understanding of challenging novel members of the rich and rapidly growing family of superconductors.

This book deals with the new class of materials of unconventional superconductors—cuprate compounds, sodium cobaltates and iron pnictides. It gives a major review of preparation, synthesis and growth of high-quality single crystals, as well as their characterization to achieve the new perspective of high- $T_c$  superconductors and deeper theoretical understanding of superconducting mechanisms. There is an increasing number of fundamental properties of these compounds which are relevant to future applications, opening new possibilities. The layout of this book consists of five chapters. Chapter 1 is devoted to the description of  $La_{2-x}M_xCuO_4$  (M = Ba, Sr, Ca) cuprate superconductors. In this chapter, the growth technique including its up-to-date improvements with respect to the detailed growth method is discussed. Large and high-quality  $La_{2-x}M_xCuO_4$  single crystals were produced by traveling solvent floating zone (TSFZ) technique. The compounds show a simple layered structure of  $CuO_2$  planes featured with hole-doping dependent anomalies. The doping effects of M = Ba and Sr on the superconductivity in the compounds, especially at certain specific *magic* hole concentrations, are given.

Chapter 2 gives a generalization of the growth of high-quality and centimeter-sized YBCO and REBCO (RE = rare earth) single crystals using either flux or top seeded solution growth (TSSG) method. The superconducting behavior of YBCO shows a "dome" shape when under-, optimal-, and over-doped respective to deficient, optimum, and over-doped oxygen contents in the compound. The oxygen content of the crystal can be tuned by post-growth treatment of oxygenation/deoxygenation. The as-grown single crystals exhibit twin domains and can be detwinned by ferroelastic polling and enabled to probe the charge reservoir in the CuO<sub>2</sub> planes. YBa<sub>2</sub>Cu<sub>4</sub>O<sub>8</sub> is another important single crystal for the study of its chemical and physical properties, since it is twin-free and shows higher thermal stability with oxygen stoichiometry. The KOH flux growth of YBa<sub>2</sub>Cu<sub>4</sub>O<sub>8</sub> single crystal provided a simple way to access the reasonable size of samples. In this chapter, we present detailed procedures for the best quality crystal growth. Various attempts to improve the crystal quality are described. Large single crystal growth of some other rare earth cuprates is also presented in this chapter.

Preface vii

In Chap. 3, we have summarized the growth of  $Bi_{2+x}Sr_{2-x}Ca_{n-1}Cu_nO_{2n+4+\delta}$  (denoted as 2201 for n=1, 2212 for n=2 and 2223 for n=3) single crystals, which has been hampered by the complexities of the materials and the lack of their phase diagrams. The most common crystal growth technique adopted for these oxides is the "flux" method, where the starting materials are dissolved in a melt, which is usually formed by excess of CuO,  $Bi_2O_3$ , or KCl/NaCl mixture. The crystals are produced by slow cooling of the melt. This method, however, suffers from several drawbacks: (1) crystals are contaminated with a crucible material, (2) crystals are difficult to detach from a crucible, (3) crystals contain flux inclusions. In most cases these drawbacks can be overcome by the traveling solvent floating zone method. Moreover, this method is suitable for growing crystals of incongruently melting compounds and has been thus successfully used to grow large crystals of the high- $T_c$  La<sub>2</sub>Sr<sub>x</sub>CuO<sub>4</sub> and  $Bi_{2+x}Sr_{2-x}Ca_{n-1}Cu_nO_{2n+4+\delta}$  (n=1, 2, and 3) superconductors. In this chapter, we describe the growth of large, undoped and doped, high-quality Bi-2201, Bi-2212, and Bi-2223 crystals as well as their characterization.

Chapter 4 presents a systematic study on growing single crystals of  $Na_xCoO_2$  (x=0.32-1.00) and hydrated  $Na_xCoO_2 \cdot yH_2O$  (x=0.22-0.47, y=1.3). The experiments demonstrate that nearly pure  $\alpha$ - (x=0.90-1.00) and  $\alpha$ - (x=0.75) phases of  $Na_xCoO_2$  large crystals could be obtained using the optical floating zone method. The detailed processes of Na-extraction and hydration in the crystals to expand the c-lattice parameters are presented. A review on the single crystal growth of  $Na_xCoO_2$  family and the hydrated cobaltates becoming superconductors is described in this chapter. The property of the parent crystal and the superconductor derived from them is also reported.

The last chapter of the book, Chap. 5, is devoted to the "iron age", i.e., superconducting pnictides and chalcogenides. This chapter focuses on the various single crystal growth techniques applied to the new class of high-temperature superconductors, iron-based layered pnictides, such as the parent compounds  $AFe_2As_2$  (A = Ba, Sr, Ca) (122), hole-doped  $A_{1-x}K_xFe_2As_2$ , electron/hole-doped  $AFe_{2-x}M_xAs_2$  (M = Co, Ni, Mn, Cr), isovalently doped  $AFe_2As_{2-x}P_x$ ,  $A_xFe_{2-y}Se_2(A = K, Rb, Cs)$  (122), the chalcogenides  $Fe_{1-\delta}Te_{1-x}Se_x$  (11), AFePn (A = Li and Na; Pn = P and As) (111), Ln(O/F)FePn (1111) and type ( $Li_{1-x}Fe_x$ ) OHFe<sub>1-y</sub>Se (FeSe11111). Detailed single crystal growth methods (fluxes, Bridgman, floating zone), the associated procedures, and their impact on crystal size, quality, and physical properties are demonstrated. A number of detailed growth parameters on FeSe11111 layered superconductors using hydrothermal growth for ion-exchange method are also included.

This book has been written aiming to provide materials scientists with an in-depth overview of the past, present, and future of high-temperature superconductors. Specialist readers will be given updated information on the research forefront of the study of various high- $T_{\rm c}$  families and some hints on the possibility of enhancing  $T_{\rm c}$  and on finding new high- $T_{\rm c}$  compounds. The high- $T_{\rm c}$  superconductivity is real and there is no reason that  $T_{\rm c}$  does not increase beyond 135 K. So, it is a realistic challenge in materials sciences to search for new superconducting

viii Preface

materials with higher  $T_{\rm c}$  and/or to enhance  $T_{\rm c}$  of the known superconducting materials. A message that the author would like to pass to researchers, especially young researchers and graduate students, is not to give up the challenges to the problems of high-temperature superconductivity.

Stuttgart, Germany Stuttgart, Germany Dresden, Germany Beijing, China Dapeng Chen Chengtian Lin Andrey Maljuk Fang Zhou

# **Contents**

1	1 ne	The $K_2NiF_4$ -Type Cuprate Superconductors $La_{2-x}Ni_xCuO_4$					
	(M=Ba, Sr, Ca)						
	Fang	Zhou					
	1.1	Introduction	1				
	1.2	Phase Diagram and Distribution Coefficient of Dopants					
		in La <sub>2</sub> CuO <sub>4</sub>	4				
	1.3	Travelling-Solvent Floating-Zone (TSFZ) Technique	6				
	1.4	TSFZ Growth and Characterization of La <sub>2-x</sub> M <sub>x</sub> CuO <sub>4</sub>	8				
	1.5	Doping Effect on Superconductivity: 1/8 Anomaly					
		in La <sub>2-x</sub> Ba <sub>x</sub> CuO <sub>4</sub> and Magic Doping Concentrations					
		in $La_{2-x}Sr_xCuO_4$	12				
	1.6	Concluding Remarks	18				
	Refe	rences	19				
2	YBCO and Some Other Rare Earth Cuprates						
	Dapeng Chen and Chengtian Lin						
	2.1	Introduction	23				
	2.2	Phase Diagram	24				
	2.3	Centimeter-Sized Single Crystal Growth of Y-123					
		and RE-123	27				
	2.4	Ferroelastic Detwinning	33				
	2.5	Defects and Etch Pits in Y-123	35				
	2.6	Flux Growth of Pure and Doped Y-124	39				
	References						
3	Bi-B	ased High-T <sub>c</sub> Superconductors	47				
	Andr	ey Maljuk and Chengtian Lin					
	3.1	Introduction					
	3.2						
		3.2.1 Material Chemistry	49				
		3.2.2 Phase Diagram	50				

x Contents

		3.2.3	Flux Growth	53						
		3.2.4	Floating Zone (FZ) Growth of Large Crystals	54						
	3.3	La-Do	pped Bi-2201	59						
		3.3.1	Flux Growth	60						
		3.3.2	FZ Growth	61						
		3.3.3	Superconductivity	67						
	3.4	Pb-Do	pped Bi-2201	68						
		3.4.1	FZ Growth	69						
		3.4.2	Post Growth Annealing and Superconductivity	71						
	3.5	Bi-221	12 Compound	72						
		3.5.1	Flux Growth	72						
		3.5.2	Bridgman Growth	78						
		3.5.3	FZ Growth of Large-Size Crystals	82						
	3.6	Bi-222	23 Compound	94						
		3.6.1	Main Growth Difficulties	94						
		3.6.2	Flux Growth	96						
		3.6.3	FZ Growth	98						
	Refer	ences.		110						
4	Crystal Growth and Characterization of Na <sub>x</sub> CoO <sub>2</sub>									
7	and Na <sub>x</sub> CoO <sub>2</sub> ,yH <sub>2</sub> O									
	Dapeng Chen and Chengtian Lin									
	4.1									
	4.2		Layer Na <sub>x</sub> CoO <sub>2</sub>	117						
		4.2.1	Single Crystal Growth	118						
		4.2.2	Melting Behavior of Two-Layer Na <sub>x</sub> CoO <sub>2</sub>	120						
		4.2.3	Sodium Extraction and Hydration	125						
		4.2.4	Hydration Dynamics	126						
		4.2.5	Deintercalation Process	129						
	4.3	Three-	-Layer Na <sub>x</sub> CoO <sub>2</sub>	131						
		4.3.1	Crystal Structure	131						
		4.3.2	Single Crystal Growth	131						
	4.4	Sodiu	m Cobalt Oxyhydrates Superconductor	134						
		4.4.1	Crystal Structure	135						
		4.4.2	Superconductivity and Phase Diagram	137						
	4.5	Conclu	usion	140						
	References									
5	Crystal Growth and Characterization of Iron-Based									
_			ctor	143						
	Dapeng Chen, Chengtian Lin, Andrey Maljuk and Fang Zhou									
	5.1	-	uction	143						
	5.2		vpe AFe <sub>2</sub> As <sub>2</sub> (A=Ba, Sr)							

Contents xi

	5.2.1	Single Crystal Growth by the Flux Method	146
	5.2.2	Features of K Doped Crystals Grown from	
		Sn Flux and Self-flux	148
5.3	Electro	on/Hole-Doped BaFe <sub>2-x</sub> M <sub>x</sub> As <sub>2</sub> (M=Mn, Cr,	
	Co, an	nd Ni)	153
	5.3.1	Crystal Structure and Segregation Coefficient	154
	5.3.2	Annealing Effect on the Superconductivity	155
5.4	Isoval	ently Doped BaFe <sub>2</sub> (As <sub>1-X</sub> P <sub>x</sub> ) <sub>2</sub> Single Crystals	
	Grown	by the Bridgman Method	156
5.5	122 T	ype Iron Chalcogenides A <sub>x</sub> Fe <sub>2-y</sub> Se <sub>2</sub>	
	(A=K,	Rb and Cs)	158
	5.5.1	Single Crystal Growth	159
	5.5.2	Microstructure and Phase Separation	162
5.6	11 Ty	pe Iron Chalcogenides	164
	5.6.1	Binary FeSe Crystal Growth by Flux and TSFZ	
		Methods	165
	5.6.2	$Fe_{1-\delta}Te_{1-x}Se_x$ Crystals Grown by the Bridgman	
		and Self-flux Method	169
5.7	111 T	ype of AFePn (A=Li and Na; Pn=P and As)	171
5.8	1111	Type of Ln(O/F)FePn (Ln=Rare Earth Elements;	
	Pn=P	and As)	174
5.9		-Type $(Li_{1-x}Fe_x)OHFe_{1-y}Se$ and Its Implication	
	for Iron-Based Family		
	5.9.1	Electronic Phase Diagram	177
	5.9.2	Crystal Synthesis via Ion/Cluster Exchange	
		and Strong Two Dimensionality	179
	5.9.3	Recent Results by ARPES and STS	184
5.10	Conclu	usion	185
Refer	ences.		185
_			405
iex			193

# Chapter 1 The K<sub>2</sub>NiF<sub>4</sub>-Type Cuprate Superconductors La<sub>2-x</sub>M<sub>x</sub>CuO<sub>4</sub> (M=Ba, Sr, Ca)

Fang Zhou

**Abstract** The  $K_2NiF_4$ -type compounds  $La_{2-x}M_xCuO_4$  (M=Ba, Sr, Ca) are the cuprate superconductors which play an important role to the study of the intrinsic electronic properties and the influence of doping on superconductivity. Large and high-quality  $La_{2-x}M_xCuO_4$  single crystals can be grown by TSFZ technique. The compounds are of a layered structure containing single  $CuO_2$  planes and show remarkable and informative hole-doping dependent anomalies. In this chapter, the growth technique, including its up-to-date developments, and the detailed growth procedures are introduced. The doping effects on the superconductivity in  $La_{2-x}Ba_xCuO_4$  and  $La_{2-x}Sr_xCuO_4$ , especially at certain specific magic hole concentrations, are presented.

## 1.1 Introduction

The discovery of superconductivity at  $\sim 30~\rm K$  in La–Ba–Cu–O system by Bednorz and Müller in 1986 [1] marks the beginning of the era of high-temperature cuprate superconductors. This superconducting system is derived from the parent compound La<sub>2</sub>CuO<sub>4</sub>, which, however, is an antiferromagnetic Mott insulator. La<sub>2</sub>CuO<sub>4</sub> has a K<sub>2</sub>NiF<sub>4</sub>-type structure consisting of a stacking of single CuO<sub>2</sub> planes alternating with two LaO layers along c axis (Fig. 1.1a). The CuO<sub>2</sub> planes extending in a- and b-direction are the key structural unit common to all the cuprate superconductors discovered to date, which becomes superconducting as charge carriers of certain concentrations are doped into. The layer-structured cuprates are quasi-two-dimensional and the interplanar couplings of CuO<sub>2</sub> planes in the transverse c-direction are weak. Charge carriers of holes can be induced in the CuO<sub>2</sub> planes of La<sub>2</sub>CuO<sub>4</sub> by partially substituting the trivalent rare-earth cations La<sup>3+</sup> with, for instance, divalent alkaline-earth ones  $M^{2+}$  (La<sub>2-x</sub>M<sub>x</sub>CuO<sub>4</sub>, M=Ba, Sr, Ca), or by intercalating oxygen anions to the interstitial sites in lanthanum tetrahedrons

1

Institute of Physics, Chinese Academy of Sciences, University of Chinese Academy of Sciences, 100190 & 100049 Beijing, China e-mail: fzhou@iphy.ac.cn

F. Zhou (\subseteq)

<sup>©</sup> Springer International Publishing Switzerland 2016

D. Chen et al., Growth and Characterization of Bulk Supercond

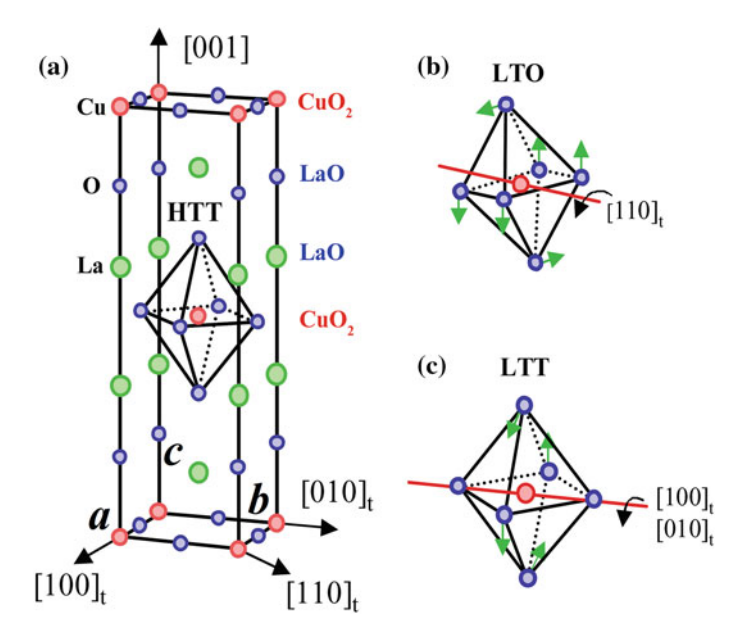
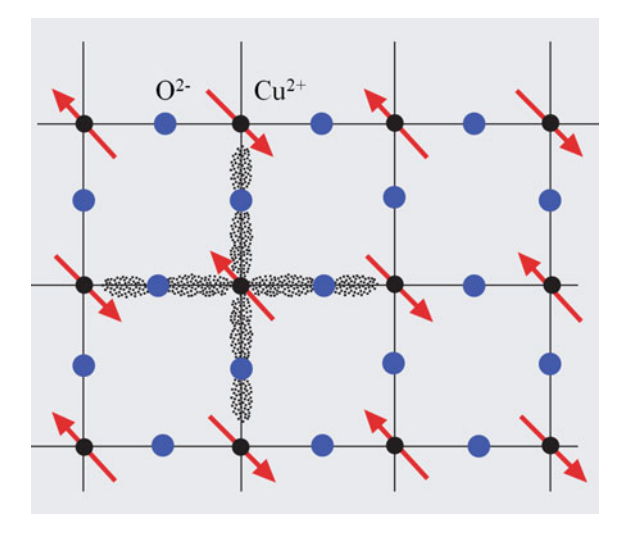


**Fig. 1.1 a** Unit cell of La<sub>2</sub>CuO<sub>4</sub> in the HTT phase (I4/mmm). **b** Tilt direction of the CuO<sub>6</sub> octahedra in the LTO phase (Bmab). **c** The CuO<sub>6</sub> octahedra in the LTT phase ( $P4_2/ncm$ ) tilt alternatively about [100], and [010], in adjacent layers. From [2]

via electrochemical oxidation [3, 4] and/or under high oxygen pressures (La<sub>2</sub>CuO<sub>4</sub>  $_{+\delta}$ ) [5, 6]. In this chapter, the cations doped La<sub>2-x</sub>M<sub>x</sub>CuO<sub>4</sub> are concerned, where the insulating (La<sup>3+</sup>, M<sup>2+</sup>)O layers serve as the charge "reservoir".

The parent state of CuO<sub>2</sub> planes in undoped La<sub>2</sub>CuO<sub>4</sub> is schematically represented in Fig. 1.2 [7]. The Cu/O atoms form an approximately square lattice, with a

**Fig. 1.2** The undoped state of CuO<sub>2</sub> plane formed by Cu–O–Cu square lattice. From [7]

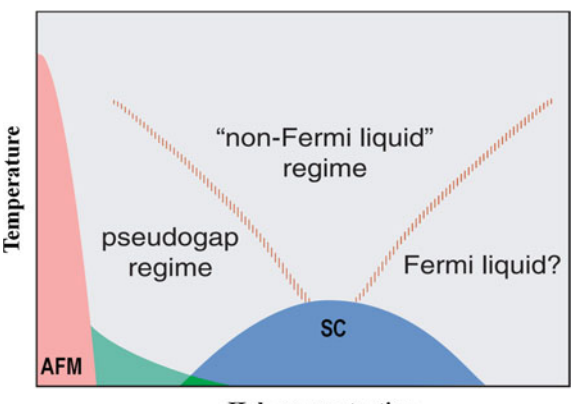


1.1 Introduction 3

Cu-O-Cu spacing  $\sim 3.8$  Å for the nearest-neighboring Cu's bonded to "p<sub>\sigma</sub> orbitals" (the shaded area) of the O atoms in between them. The highest occupied band contains one electron per unit cell, which cannot move owing to strong electron-electron repulsion at a doubly occupied site supposed to be created by its jumping. The Mott insulator differs fundamentally from a conventional band insulator, where electron motion is blocked by the Pauli exclusion principle when the highest occupied band contains two electrons. The superexchange interaction mediated by the oxygen " $p_{\sigma}$  orbitals" favors anti-parallel spin alignment on the nearest-neighboring Cu sites as indicated by the red arrows, leading to the long-range antiferromagnetic order. Upon the electron occupancy per unit cell is reduced from 1 to 1-x by doped holes of a concentration x, the antiferromagnetic ordering temperature decreases rapidly (schematic red region in Fig. 1.3), and charge conduction is restored as the hole doping creates sites to which electrons can jump without suffering the Coulomb repulsion. When doped with sufficient amount of holes, the superconducting long-range order occurs in a dome-like blue region in Fig. 1.3. The doping level at which the superconducting transition temperature  $(T_c)$ is maximal is referred to as "optimal", while those lower and higher than the optimal one as "under-doping" and "over-doping", respectively.

The high-temperature tetragonal (HTT) structure of La<sub>2</sub>CuO<sub>4</sub> with the *14/mmm* symmetry is characteristic of untilted CuO<sub>6</sub> octahedra thus ideally flat CuO<sub>2</sub> planes (Fig. 1.1a). With decreasing temperature, La<sub>2</sub>CuO<sub>4</sub> undergoes a second-order transition at 525 K [8] from the HTT phase to a low-temperature orthorhombic (LTO) phase of the space group *Bmab*. The CuO<sub>6</sub> octahedra of LTO structure are tilted by a small angle about the tetragonal [110]<sub>t</sub> axis (Fig. 1.1b), so that the CuO<sub>2</sub> planes become to be buckled to certain extent rather than flat. The LTO unit cell is doubled, with its orthorhombic [100]<sub>o</sub> axis along the tilt axis diagonal to the Cu–O–Cu square lattice shown in Fig. 1.2. In Ba doped La<sub>2-x</sub>Ba<sub>x</sub>CuO<sub>4</sub> (LBCO) system, in addition, occurs at lower temperatures a first-order transition from LTO to another

Fig. 1.3 Schematic of electronic phase diagram for hole-doped cuprate superconductors. From [7]



Hole concentration

low-temperature phase of either a low-temperature tetragonal (LTT;  $S.G.\ P42/ncm$ ) or a low-temperature less-orthorhombic (LTLO;  $S.G.\ Pccn$ ) structure [2]. In LTT phase, the  $CuO_6$  octahedra tilt about the axis parallel to the square lattice, but alternatively along [100], and [010], directions in adjacent octahedron layers (Fig. 1.1c) [9–11]. In LTLO the tilt axis runs along an intermediate in-plane direction [12]. In LBCO, doping dependent static stripe order correlated with the LTO-LTT structure transition strongly suppresses the superconductivity; while in Sr doped  $La_{2-x}Sr_xCuO_4$  (LSCO) where the LTT phase is absent, instead robust intrinsic superconducting states emerge in the vicinity of some specific *magic* hole concentrations.

High-quality single crystals are requisite to the study on intrinsic physical properties of high- $T_c$  cuprate superconductors. Anisotropic electronic properties of the cuprates, quasi-two-dimensional in crystal and electronic structures, can be measured reliably only on single crystal samples, and the samples of large size are demanded by important measurements such as, especially, neutron scattering. Compared to crystal growth from a flux solution by slow cooling or top-seeding, the travelling-solvent floating-zone (TSFZ) technique has proven to be the only one capable of fabricating ten-centimeter long high-quality  $K_2NiF_4$ -type and other cuprate single crystals of pure phases with uniform and controllable doping levels. It is also very successful in growing large binary FeSe superconductor [13] and many other functional materials [14].

In Sects. 1.2, 1.3 and 1.4, we will focus on concept, technique and experiment aspects with regard to TSFZ procedures. The doping effect on the superconductivity of LBCO and LSCO, especially at certain particular magic hole-doping fractions, will be presented in Sect. 1.5. We will conclude in Sect. 1.6 with general remarks.

# 1.2 Phase Diagram and Distribution Coefficient of Dopants in La<sub>2</sub>CuO<sub>4</sub>

The stoichiometric compound La<sub>2</sub>CuO<sub>4</sub>, formed in pseudo-binary La<sub>2</sub>O<sub>3</sub>–CuO system, melts incongruently at a peritectic temperature  $\sim 1327$  °C (Fig. 1.4) [15]. Below this temperature, the composition of liquid in equilibrium with La<sub>2</sub>CuO<sub>4</sub> of 50 mol% CuO ranges approximately from 75 to 90 mol% CuO in the temperature range from  $\sim 1327$  to  $\sim 1075$  °C, following the liquidus line. These are the composition and temperature conditions feasible to grow incongruent La<sub>2</sub>CuO<sub>4</sub> from the liquid. In a corresponding solid-liquid equilibrium available for a solid-solution system, the solubility of a dopant in the solid-solution phase ( $x_S$ ) differs from its solubility in the liquid phase ( $x_L$ ). The ratio of the two given concentrations, dependent on each other, is defined as the distribution coefficient  $k = x_S/x_L$ . For non-stoichiometric La<sub>2-x</sub>M<sub>x</sub>CuO<sub>4</sub> as an M doped solid-solution, the effective distribution coefficients  $k_{eff}$  for Ba, Sr and Ca dopants in a slow-cooling

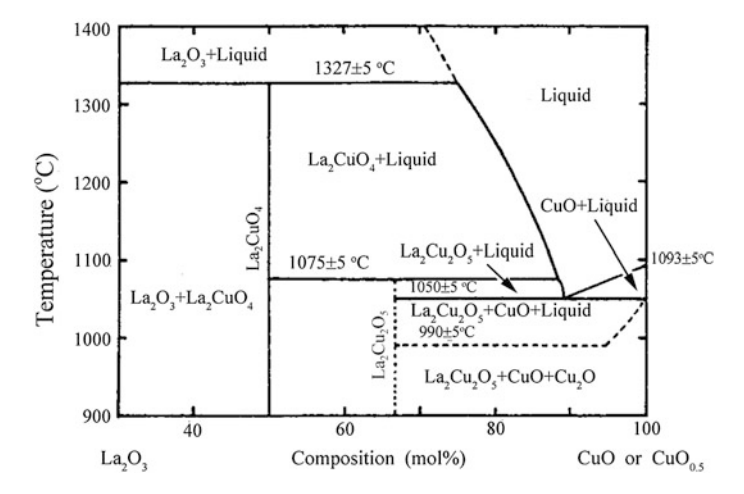
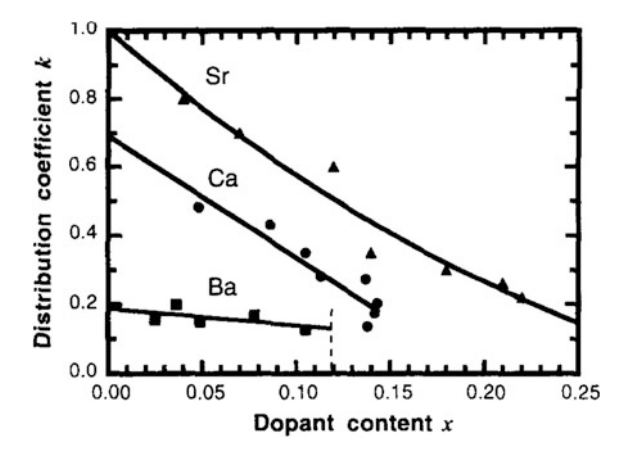


Fig. 1.4 Phase diagram of La<sub>2</sub>O<sub>3</sub>-CuO system in oxygen. From [15]

floating-zone (SCFZ) process [16] were determined earlier [17, 18]. The results at different doping levels are shown in Fig. 1.5. That can be taken as a starting point for one to estimate the optimal dopant contents in the solvents from which  $La_2_{-x}M_xCuO_4$  can be crystallized in a travelling-solvent floating-zone process.

Figure 1.6a is a schematic phase diagram for a hypothetical binary A–B system with solid-solution regions including  $\beta$ . The  $\beta$  phase exists below a peritectic temperature  $T_p$  within a certain range of composition, no longer forming a "line phase", like La<sub>2</sub>CuO<sub>4</sub>, at a specific peritectic composition P. The solid-solution  $\beta$  at S of a composition  $x_S$  is in equilibrium with the liquid at L (the solvent) of a composition  $x_L$  different from  $x_S$ . The distribution coefficient is less than unity as  $x_S < x_L$ , the same as those for La<sub>2-x</sub>M<sub>x</sub>CuO<sub>4</sub>. In a thermodynamic equilibrium process, any shift of solvent L on the liquidus line (as indicated by the red arrows) resulting from a

Fig. 1.5 Effective distribution coefficients of the dopants Sr, Ca and Ba into La<sub>2</sub>CuO<sub>4</sub>. From [18]



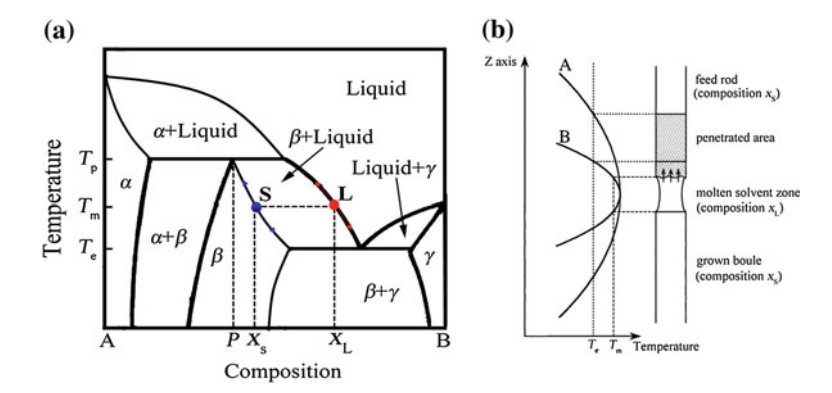


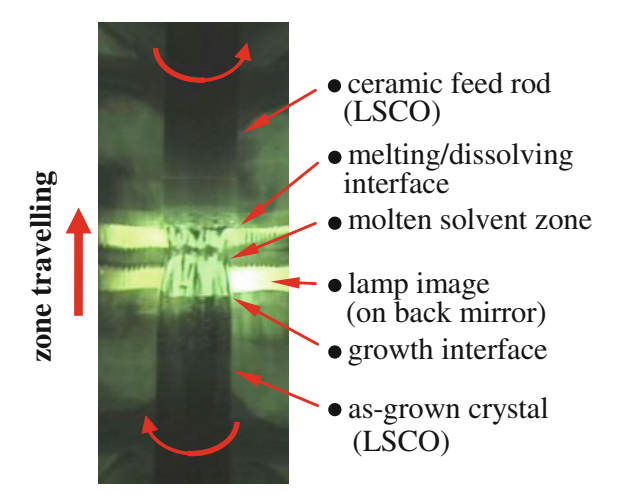
Fig. 1.6 a. Phase diagram for a hypothetical binary A–B system with solid-solution regions including  $\beta$ . b (Adapted based on Fig. 10 of [19]). Schematic illustrations of a TSFZ configuration for the solid-solution  $\beta$  at S of the composition  $x_S$  in equilibrium with the solvent L of the composition  $x_L$ , as the case shown in (a), and of the solvent penetration reduced by a sharper vertical temperature profile B. Here  $T_m$  and  $T_e$  are the melting (or dissolving) and eutectic temperatures, respectively, as indicated in (a)

variation in composition and/or temperature will lead to a corresponding shift of solid S on the solidus line (indicated by the blue arrows), i.e., the composition of solid-solution S will change concomitantly. That is what should be prevented if one wants to grow a doped incongruent compound with a fixed composition  $x_{\rm S}$  throughout the sample. Experimentally, it depends on how to control a constant composition and temperature of the solvent from which the crystal is being grown.

# 1.3 Travelling-Solvent Floating-Zone (TSFZ) Technique

The TSFZ technique was first reported in the crystal growth of incongruent compounds of yttrium iron garnet (YIG,  $Y_3Fe_5O_{12}$ ) with the pure [20] or substituted [21] compositions, after a successful attempt to grow incongruent YFe<sub>2</sub>O<sub>4</sub> [22]. Thanks to its unique vertical configuration (Figs. 1.6b and 1.7), this technique is specially suited for growing doped incongruent materials from melts. The vertical design makes it possible for a molten solvent zone of an average composition  $x_L$  to form in between an as-grown crystal of a composition  $x_S$  and a feed rod of almost the same composition as the crystal (Fig. 1.6a, b). In a stable TSFZ process, at both the growth and melting (or dissolving) interfaces, the solid phase S, with the composition  $x_S$  and at the temperature  $T_m$ , is in a quasi-thermodynamic equilibrium with the molten solvent phase L, composition  $x_L$  and temperature  $T_m$ , corresponding to the solid-liquid equilibrium between S and L shown in Fig. 1.6a. This is the basic thermodynamic condition required for a smooth and successful TSFZ growth process. The molten solvent is held in position by its surface tension when travelling upwards. A usual focused infrared-heating establishes at the growth and melting

Fig. 1.7 A snapshot in a smooth and successful TSFZ growth process of a  $La_2$   $_{-x}Sr_xCuO_4$  single crystal



interfaces a high vertical temperature gradient, like the case of temperature profile B in Fig. 1.6b, which is the driving force for crystal growth. The crucible- and flux-free growth, void of contamination from container materials and other impurities, is carried out in a space enclosed by a quartz tube. In the following we will take actual cases as example to discuss the essentials involved in TSFZ procedures.

A typical smooth and successful growth process of a  $La_{2-x}Sr_xCuO_4$  single crystal [23, 24] is shown in Fig. 1.7. It is characteristic of a very stable molten zone with well-defined solid-liquid borders. The molten zone was heated at a constant power by four halogen lamp-images focused with a horizontal quartet ellipsoidal mirror (not shown). The almost isodiametric cylindrical feed rod was made of well-prepared polycrystalline  $La_{2-x}Sr_xCuO_4$ , with a small CuO excess to compensate for its evaporation during the growth. A ceramic solvent pellet was prepared separately, with an initial composition rich in CuO (78–84 mol% CuO) based on the phase diagram (Fig. 1.4) and an appropriate content of Sr estimated by taking into account its effective distribution coefficients  $k_{eff}$  (Fig. 1.5). The solvent pellet was heated to melt between the feed rod and a seed crystal in the very beginning. The feed rod and grown crystal were rotated in opposite directions to improve liquid homogeneity and to achieve uniform horizontal temperature profiles encircling the molten zone.

As the molten zone slowly travels upwards at a constant rate with a mechanical motion of the heating parts, at the lower growth interface,  $La_{2-x}Sr_xCuO_4$  crystal is continuously precipitated from the molten solvent in equilibrium with it, while simultaneously at the upper melting interface, an equal amount of polycrystalline  $La_{2-x}Sr_xCuO_4$  is dissolved from the feed rod into the molten solvent to compensate for the mass consumption including the evaporation loss of CuO. Therefore a slow growth (travelling) rate and a well-stirring by the rotation are required to allow for a sufficient mass transportation in the molten zone. A dense, isodiametric and straight

feed rod is important for keeping a stable shape and volume of the molten zone, in which case a constant temperature distribution in the molten zone is expected at a fixed heating power, provided a small variation in the ambient temperature. With proper manipulations, such a self-stabilizing growth process, like that shown in Fig. 1.7, can be maintained, usually starting from a growth length about one centimeter, more or less. As a consequence, both the composition and temperature distributions of the molten solvent zone will be kept constant. From this point onward until the end of growth, the duration about one week, uniformly doped high-quality large single crystal of the exact chemical formula  $La_{2-x}Sr_xCuO_4$  can be continuously grown from the solvent.

However, an unstable molten zone does happen in some cases, sometimes depending on materials. If the feed rod is less dense and uniform, the solvent may severely penetrate into the feed rod through capillary intertices until reaching a eutectic point at  $T_e$  (shaded area in Fig. 1.6b). In a worse case, that may lead to a harmful jagged melting interface with varying shapes, causing fluctuations in the volume (shape), composition and temperature of the molten zone. Experimentally, that may be avoided or reduced to a great extent with a well-prepared highly dense feed rod [23–25], or by improving the vertical temperature gradient (Fig. 1.6b) [19, 26], or by adding a certain amount of B<sub>2</sub>O<sub>3</sub> into the solvent in its preparation process [27]. Moreover, a steep temperature gradient will also prevent some possible unstable growth interface from happening. For instance, an unstable growth interface would otherwise develop in presence of a constitutional supercooling related to a rejection of excess CuO and Sr into liquid during crystallization, because of the distribution coefficients <1. Besides, while an approximately flat growth interface is ideal for crystal growth, the real growth, and melting as well, interfaces become convex into molten zone and more as closer to the centers. Occasionally the two interfaces even touch one another. A fast rotation is usually needed to reduce the interface convexity.

# 1.4 TSFZ Growth and Characterization of La<sub>2-x</sub>M<sub>x</sub>CuO<sub>4</sub>

The earliest attempts to grow the  $K_2NiF_4$ -type cuprate crystals by slow cooling or top-seeding flux methods date back to the year of 1987, soon after the Bednorz and Müller's paper. Among them, superconducting LSCO crystals up to 8 mm in lateral dimension was grown from CuO flux solution [28]. The TSFZ technique was first applied in growing larger LSCO single crystals in 1989, and an as-grown crystal  $\sim 6$  mm in diameter and 40 mm in length was obtained [29, 30]. Since then, much work has been done in the TSFZ growth and characterization of  $La_{2-x}M_xCuO_4$  crystals, especially the  $La_{2-x}Sr_xCuO_4$  system exhibiting a wide doping range for Sr atoms. This section will not aim to be systematically documented, but will rather pay attention to subsequent improvements and developments in this field.

Precursor powders for La<sub>2-x</sub>M<sub>x</sub>CuO<sub>4</sub> feed rods were commonly prepared by solid-state reactions using as raw materials relevant high-purity oxides and

alkaline-earth carbonates or nitrates [25]. A small amount of CuO (1–4 mol%) in excess was added in order to compensate for its evaporation loss. The precursor powders were hydrostatically pressed under a high pressure of hundreds MPa to form a compact cylindrical rod, before it was well-sintered and post-processed into a ceramic feed rod good for TSFZ growth.

As emphasized earlier, fabrication of a dense and uniform, in both composition and heating history, feed rod is an important step in TSFZ procedures. The precursor powders very fine in particle size and homogeneous in composition would have a high sintering activity. Highly fine and micro-homogeneous precursor powders were produced via sol-gel approaches [24, 25], and, combined with a hydrostatic pressing under a high pressure over 600 MPa, very dense and uniform LSCO feed rods were obtain after *well-sintered* at elevated temperatures of 1240–1280 °C, depending on compositions, for a short duration of 2 h [24]. That contributed much to a smooth and stable TSFZ growth. Special attention should be paid to make a uniformly sintered feed rod usually over dozen-centimeter long. It proves that a kind of vertical furnace is effective for the purpose, where, during sintering, the feed rod can be kept rotating and moving up and down to attain an identical heating history throughout the whole rod.

The solvent pellets were prepared by the solid-state reaction in a simpler way. The composition was rich in CuO (77–85 mol% CuO), based on the phase diagram of La<sub>2</sub>O<sub>3</sub>–CuO (Fig. 1.4). The concentration of dopant M in solvent was appropriately chosen considering the distribution coefficients (Fig. 1.5), so that the proper solid-liquid equilibrium could be established through self-adjusting of the TSFZ process soon after the start of crystal growth. In order to reduce bubbles possibly emerging in molten solvent at the very start, it was suggested to heat the pellets at a high enough temperature just below the melting temperature [24].

The use of seed crystals along tetragonal [100], or [110], directions is effective to achieve a well oriented TSFZ growth, though the growth can also be started on a polycrystalline rod as a "pseudo-seeding" [25]. The crystal growth was usually carried out under 0.2–0.4 MPa oxygen pressure. A common growth rate was 1 mm/h, while slower rates of 0.4–0.8 mm/h were also used in some experiments. Some experimental details involved in TSFZ procedures were also discussed in the literature [14, 31–36].

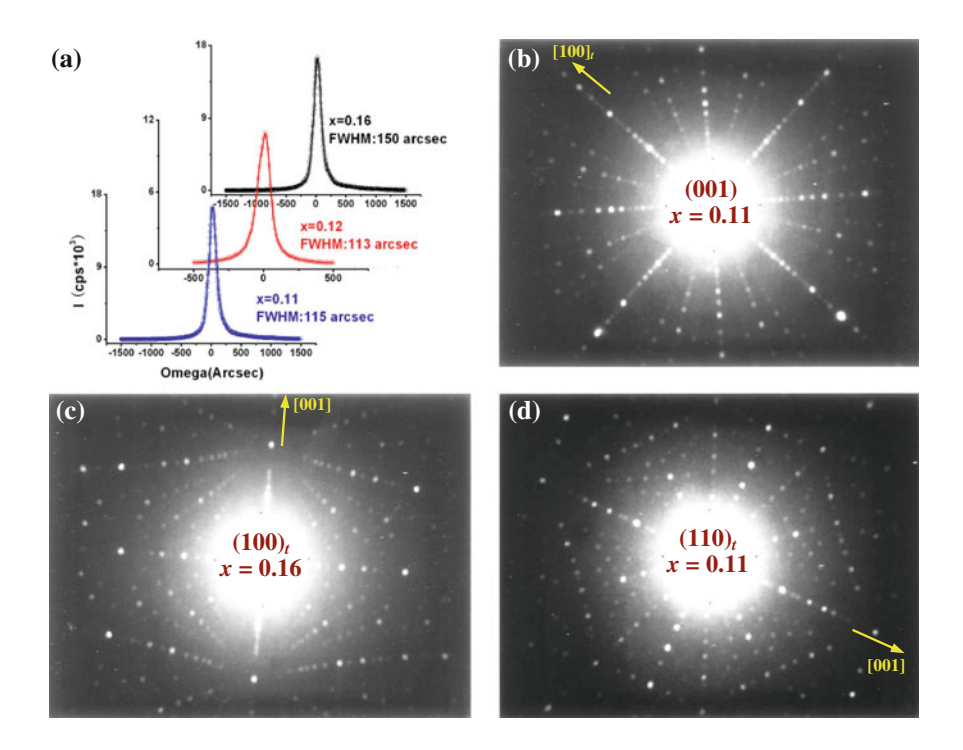
A series of under- and over-doped LSCO single crystals of high quality were grown by TSFZ [18, 23, 36], showing a crystal mosaicity of  $0.10^{\circ}$  in terms of the full-width-at-half-maximum (FWHM) of x-ray rocking curves for (006) [36] or (008) [23] Bragg reflections. A typical large-sized as-grown  $La_{2-x}Sr_xCuO_4$  (x = 0.11) crystal,  $\sim 6.6$  mm in diameter and 100 mm in length, is shown in Fig. 1.8, which has been carefully checked to be subgrain-free after a distance of growth (usually 2–3 cm) starting on a seed crystal [23, 24]. Thanks to the use of highly dense and uniform feed rods and a slow growth rate of 0.6 mm/h, large  $La_{2-x}Sr_xCuO_4$  single crystals of higher quality were produced [24]. Double-crystal x-ray rocking curves of (008) reflection show the much smaller crystal mosaic of only 113-150 arcsec. ( $0.03-0.04^{\circ}$ ) in terms of FWHM (Fig. 1.9a); and the x-ray Laüe spots from different crystal orientations are all well defined and can be well



Fig. 1.8 Photograph of an as-grown  $La_{2-x}Sr_xCuO_4$  (x = 0.11) crystal  $\sim 6.6$  mm in diameter and 100 mm in length. From [24]

indexed, as evident in the Laüe patterns for (001) (Fig. 1.9b),  $(100)_t$  (Fig. 1.9c) and  $(110)_t$  (Fig. 1.9d) crystal planes in tetragonal notation.

In the over-doping regime of  $\text{La}_{2-x}\text{Sr}_x\text{CuO}_4$ , however, subgrains were present for x = 0.25 and 0.30 crystals grown at a rate of 1.0 mm/h, as well as inclusions of  $\text{La}_{2-x}\text{Sr}_{1+x}\text{Cu}_2\text{O}_{6+\delta}$  for x = 0.30 besides the subgrains [18]. Formation of the



**Fig. 1.9 a** Double-crystal x-ray rocking curves of (008) Bragg reflection for  $\text{La}_{2-x}\text{Sr}_x\text{CuO}_4$  (x = 0.11, 0.12, 0.16) single crystals grown by TSFZ. **b**-**d** are the x-ray back-reflection Laüe patterns with different crystal orientations along (001) (for x = 0.11), (100), (for x = 0.16) and (110), (for x = 0.11) planes in tetragonal notation, respectively. **a** and **b** are from [24]; **c** and **d** are reported for the first time here

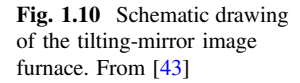
subgrains could be avoided at a slower rate of 0.8 mm/h. The precipitation of  $La_{2-x}Sr_{1+x}Cu_2O_{6+\delta}$  was attributed to a constitutional supercooling related to a high Sr content in the solvent.

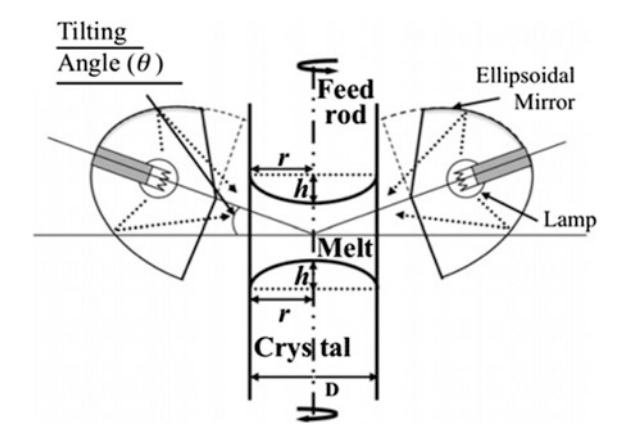
An under-doped  $\text{La}_{2-x}\text{Sr}_x\text{CuO}_4$  (x=0.08) crystal was specially grown using a double lamp-image furnace, as this doping level is close to 0.09 at which HTT-LTO transition occurs at room temperature [25]. The sample of  $T_c \sim 20$  K displayed, as expected, a weak orthorhombicity compared to parent  $\text{La}_2\text{CuO}_4$ . The rocking curve of neutron diffraction gave a FWHM  $\sim 0.2^\circ$  for (006) reflection.

A series of highly under-doped La<sub>2-x</sub>Sr<sub>x</sub>CuO<sub>4</sub> single crystals, spanning the insulating-superconducting phase boundary, were grown by TSFZ method [37]. The onset superconducting transition temperatures were observed to be 6.3, 11.6, and 17.0 K for the samples with x = 0.056, 0.06, and 0.07, respectively. No superconductivity was detected for x = 0.053 down to 2 K. The lower critical concentration  $x_c$  for superconductivity was thus estimated to lie between x = 0.053 and 0.056.

 $La_{2-x}Ba_xCuO_4$  crystals of x < 0.15 were grown by TSFZ using crystallized feed rods under low oxygen partial pressures  $(10^{-2}-10^{-3})$  atm), in order to reduce an otherwise deep penetration of solvent into feed rod and a formation of Ba-enriched compounds resulting in molten zone instability [33]. The growth rate was slow (0.5 mm/h) to avoid impurity phases in the crystals and a La<sub>2</sub>CuO<sub>4</sub> crystal was used as the seed. The typical size of grown boules was 4 mm in diameter and 100 mm in length, but a mosaic structure was present in the crystals by Laüe experiment. The crystals doped at  $x \sim 0.10$  and 0.14 showed onset superconducting transitions at 23 and 25 K, respectively. However, higher O<sub>2</sub> pressures (0.2–0.4 MPa) were also used to grow La<sub>2-x</sub>Ba<sub>x</sub>CuO<sub>4</sub> crystals by TSFZ [38, 39]. Under 0.4 MPa pressure of flowing  $O_2$ ,  $La_{2-x}Ba_xCuO_4$  (x = 0.11) single crystal of good quality was grown at a rate of 1.0 mm/h [39]. The feed rod was in 1 mol% excess of CuO; the solvent composition was of a molar ratio (La<sub>1.875</sub>Ba<sub>0.125</sub>):Cu = 3:7, corresponding to 82 mol% CuO in La<sub>2</sub>O<sub>3</sub>-CuO phase relation. La<sub>2</sub>O<sub>3</sub> inclusions were observed in initially grown part of the as-grown ingot, which broke into pieces a few days in air. A single crystal 5 mm diametral and 20 mm long was obtained from the rest part, showing a depressed  $T_{\rm c} \sim 10~{\rm K}$  as expected because of this doping level (0.11) close to that of "1/8 anomaly". Two kinks at  $\sim$ 256 and  $\sim$ 53 K evident in the temperature dependences of electrical resistivity were attributed to HTT-LTO and LTO-LTT structural transitions, respectively. Strongly suppressed T<sub>c</sub>'s of 4 K or  $\sim 2.4$  K were reported for exact x = 1/8 LBCO single crystals grown by TSFZ [40, 41].

The solubility limit of Ca in  $\text{La}_2\text{CuO}_4$  was determined to be about 0.14 in a SCFZ process [17]. However, the doping level of Ca in  $\text{La}_{2-x}\text{Ca}_x\text{CuO}_4$  crystals grown by TSFZ seemed to be saturated at  $x \sim 0.10$ , despite its further increased concentrations in feeds and solvents [18, 42]. The as-grown ingot was of a 5 mm diameter and a 30 mm length. The grown crystals of x = 0.05 did not superconduct down to 5 K. The superconductivity in the crystals of x = 0.075 and 0.09 was observed to occur at  $T_c \sim 15$  K, independent on the Ca concentration, and to show a broadened and unsaturated diamagnetic transition.





By the horizontally designed common lamp-image heating, the diameter of grown crystal is limited owing to the interface convexity. It was reported that, using a quartet ellipsoidal mirror tilted up by an angle  $\theta$  (Fig. 1.10), LSCO crystals of a larger diameter could be grown [43]. At a tilting-angle  $\theta$  = 20°, this kind of TSFZ experiment yielded LSCO crystals with a maximum diameter of 10 mm. The experimental results suggested that the evaporation of CuO was reduced with increasing tilting-angle. At the same time, however, the vertical temperature gradient at the melting interface was also reduced.

Recently, an important development in TSFZ technique is the use of laser diodes as the heating source: five or seven laser diodes assembled surrounding the molten zone produce parallel and homogeneous well-concentrated laser beams of a wavelength 975 nm and a rectangular cross section [44]. By this laser-heating, the average vertical temperature gradient can be substantially increased,  $\sim 5$  times higher than the lamp-image heating, and a more uniform horizontal temperature distribution encircling the molten zone be attained as well. The laser-heating enables stable and reproducible crystal growth of some incongruently melting materials difficult to be grown by conventional techniques, for example the materials of LBCO and BiFeO<sub>3</sub> [45].

# 1.5 Doping Effect on Superconductivity: 1/8 Anomaly in La<sub>2-x</sub>Ba<sub>x</sub>CuO<sub>4</sub> and Magic Doping Concentrations in La<sub>2-x</sub>Sr<sub>x</sub>CuO<sub>4</sub>

Intensive studies have been made on the preparation of both the poly- and single-crystal samples of  $La_{2-x}M_xCuO_4$ , and their physical properties characterized by various probes including, for instance, transport and magnetic measurements, neutron scattering and ARPES. Among the hole-doped cuprates,  $La_{2-x}Sr_xCuO_4$  (LSCO) tolerates the dopant (Sr) in a wide range of concentration, leading to a more complete electronic phase diagram. At a very low doping (x < 0.02), LSCO is an

antiferromagnetic Mott insulator. After crossing a spin-glass state (0.02 < x < 0.05), the schematic green region in Fig. 1.3) [46, 47], it becomes a superconductor (0.05 < x < 0.26) and then behaves as a normal metal (0.26 < x < 0.6) [48] before finally turns out to be a semiconductor (x > 0.6) [49]. In the superconducting regime, the critical temperature of LSCO reaches its maximum (38 K) at the hole density x = 0.16.

The investigation on the doping and temperature dependences of physical properties is important for acquiring a better understanding of high- $T_c$  superconductivity and strong electron correlation in cuprates. For example, although the superconducting critical temperature  $T_c$  of LSCO shows in general a dome-shaped doping dependence, a "plateau" at 30 K, like that shown in Fig. 1.11, always appears around the doping level x = 1/9 ( $\sim 0.111$ ) in the underdoping regime [50–53]. This is in contrast to the observation on La<sub>2-x</sub>Ba<sub>x</sub>CuO<sub>4</sub> (LBCO) where the superconductivity almost disappears at x = 1/8 (0.125), leading to a double  $T_c$  maximum ( $\sim 30$  K) at  $x \sim 0.095$  and  $\sim 0.155$  (Fig. 1.12). The "1/8 anomaly" in LBCO arousing much interest in the field of high- $T_c$  cuprates has been clarified to correlate with one-dimensional static charge and spin stripe order, which coincide with and develop below, respectively, the structure transition from LTO to LTT phase [2]. The stripe order pinned by the electron-lattice coupling [54] is most pronounced at x = 1/8, where both diffraction peak intensities for charge and spin stripe order show a maximum while fall off for  $x \neq 1/8$  (Fig. 1.13).

In La<sub>2-x</sub>Sr<sub>x</sub>CuO<sub>4</sub>, however, the LTT phase is absent. Instead, two distinct intrinsic superconducting phases noticeably develop in the vicinity of specific

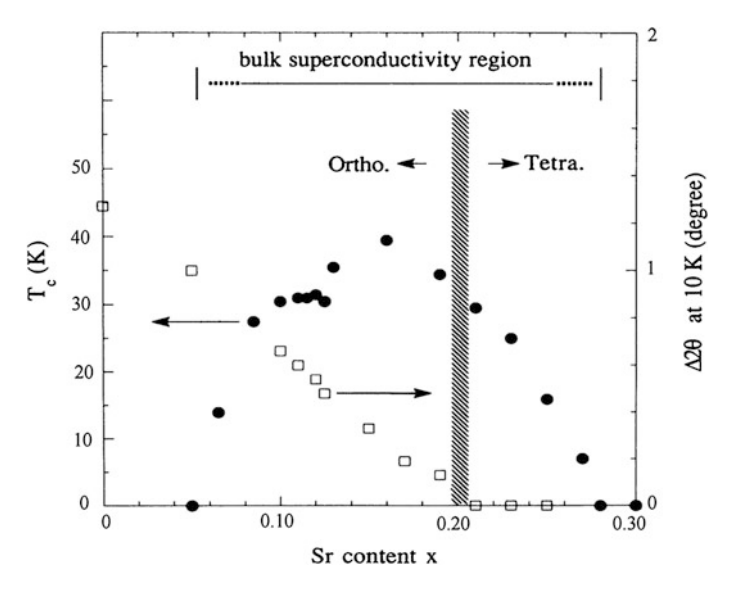


**Fig. 1.11** Doping dependence of  $T_c$  (solid circles), the bulk superconductivity region and orthorhombic splitting (400)-(040) at 10 K (squares) in La<sub>2-y</sub>Sr<sub>y</sub>CuO<sub>4</sub>. From [50]

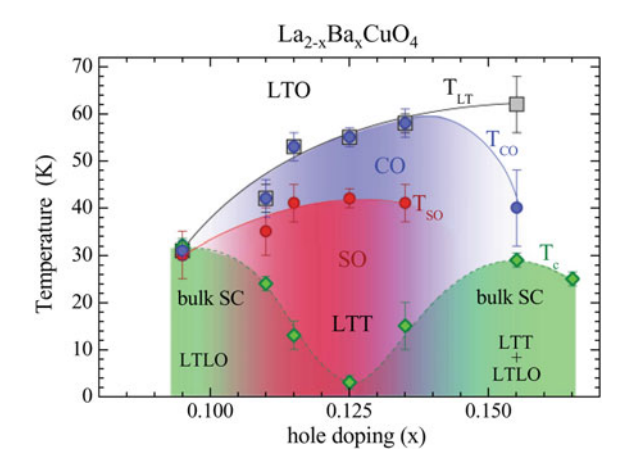


Fig. 1.12 Temperature vs hole-doping phase diagram of  $\text{La}_{2-x}\text{Ba}_x\text{CuO}_4$  single crystals. Onset temperatures:  $T_c$  of bulk superconductivity (SC),  $T_{\text{CO}}$  of charge stripe order (CO),  $T_{\text{SO}}$  of spin stripe order (SO), and  $T_{\text{LT}}$  of the low-temperature structural phases LTT and LTLO. At base temperature CO, SO, and SC coexist at least in the crystals with  $0.095 \le x \le 0.135$ . Solid and dashed lines are guides to the eye. From [2]

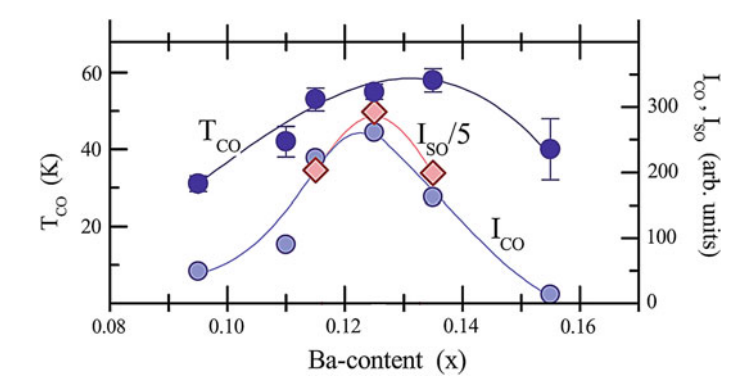


Fig. 1.13 Diffraction peak intensities  $I_{CO}$  and  $I_{SO}$  for charge and spin stripe order, respectively, and the charge stripe order temperature  $T_{CO}$  as functions of doping in  $La_{2-x}Ba_xCuO_4$ . From [2]

magic hole concentrations of  $x = 1/4^2$  (0.0625) and  $1/3^2$  ( $\sim$  0.111), respectively, in the under-doping regime. This has been evidenced by the studies of magnetism, far-infrared charge dynamics and electron transport on a series of high quality La<sub>2-x</sub>Sr<sub>x</sub>CuO<sub>4</sub> single crystal samples (x = 0.063, 0.070, 0.090, 0.100, 0.111, 0.125) [23, 52, 53, 55–57].

The so-called magic doping concentrations are two-dimensional hole densities  $P_{MD} = m/n^2$  where m and n are positive integers with, for the two most prominent series, n = 3 or 4 and  $m \le n$  [58]. The intrinsic superconducting phases at the magic

dopings are characteristic of a single narrow diamagnetic transition with an onset  $T_c$  of either 15 K ( $x = 1/4^2$ ) or 30 K ( $x = 1/3^2$ ) which remains robust under fields up to 5 T, and of a local minimum ( $x = 1/4^2$ ) or an unusual drop ( $x = 1/3^2$ ) in the Meissner fraction (Fig. 1.14) [52, 57]. This is in sharp contrast to the apparent non-intrinsic superconducting phases at some other doping levels showing a much broader diamagnetic transition and a field-sensitive onset  $T_c$  which settles from a higher value into either 30 K or 15 K, depending on dopings, as the field increases above 1 T (see Fig. 3 of [57]). Such field dependences of  $T_c$  are characteristically different from that of conventional type II superconductors or granular superconductors where there is only one non-robust superconducting state showing a monotonic decrease in  $T_c$  under field.

Nevertheless, those apparently puzzling phenomena are explicable from the dynamic nano-scale domains of charge phases with a *universal* length scale (300–1100 Å) [59]. By systematically examining the field-dependent Meissner signal sizes in various crystal samples, in terms of the comparability of inter-vortex spacing to the universal length scale of underlying dynamic electronic textures, it has been argued that there is a distinct superconducting condensate state for each intrinsic superconducting phase, suggesting that the intrinsic superconducting phases at magic doping concentrations are the pristine electronic phases for high- $T_c$  superconductivity [57]. The formation of the intrinsic superconducting states is

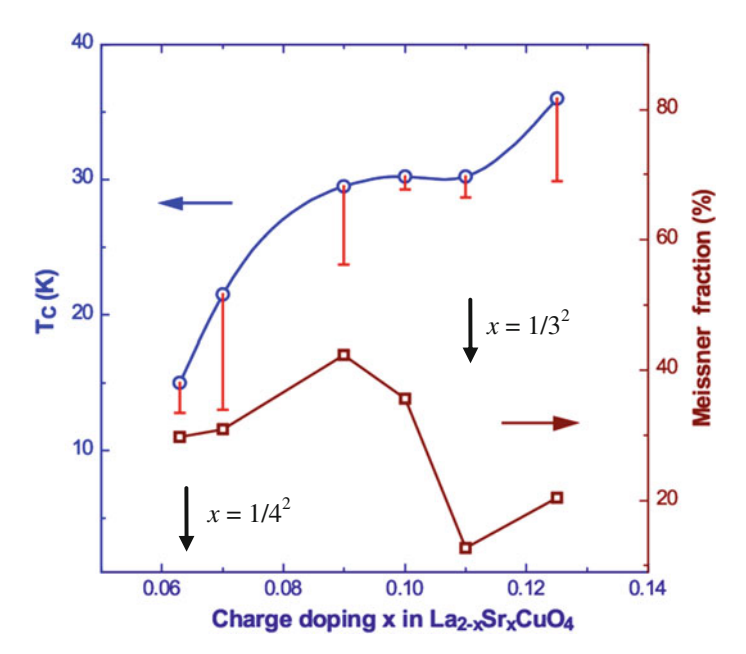


**Fig. 1.14** Onset superconducting transition temperature  $T_c$ , transition width (indicated by the length of the *vertical bars*) and Meissner fraction as functions of hole concentration for  $La_{2-x}Sr_xCuO_4$  single crystals (x = 0.063, 0.070, 0.090, 0.100, 0.111, 0.125). The data were obtained from dc magnetic measurements. Lines are guides to the eye. From [52]

compatible with a *composite* charge model [55]. This charge model stresses that only a very small fraction of the total holes, coupled to underlying *two-dimensional charge lattices* formed by the rest of the holes, is responsible for the superconductivity and the normal state free charge transport, including intrinsically coherent *c*-axis charge transport [56].

Moreover, at the magic hole density x = 1/9 (n = 3), a new phase boundary  $T_{m2}(H)$  has recently been discovered below the first order vortex melting line in the vortex solid phase, by field-cooled magnetization measurements on La<sub>1.89</sub>Sr<sub>0.11</sub>CuO<sub>4</sub> single crystal and critical scaling analysis (Fig. 1.15) [58]. The coupling between superconductivity and antiferromagnetism has been found to be attractive below  $T_{m2}(H)$  with a negative coupling constant v < 0, evidencing that the antiferromagnetism microscopically coexists and collaborates with the high- $T_c$  superconductivity in cuprates.

At another magic doping x = 1/16 (n = 4), despite the extremely under-doping level in the vicinity of an insulator-superconductor transition, a remarkably sharp quasiparticle peak in the nodal region was observed in La<sub>1.937</sub>Sr<sub>0.063</sub>CuO<sub>4</sub> single crystal by high-resolution ARPES (Fig. 1.16a) [60]. The sharp peak abruptly turns into a broad edge upon energy dispersing above  $\sim 70$  meV (indicated by a red arrow). Meanwhile, an enhanced upturn in the MDC (momentum distribution curve) width, proportionally related to the scattering rate of electrons, was evident at the same energy scale (Fig. 1.16b) [61], suggestive of a stronger scattering mechanism above  $\sim 70$  meV.

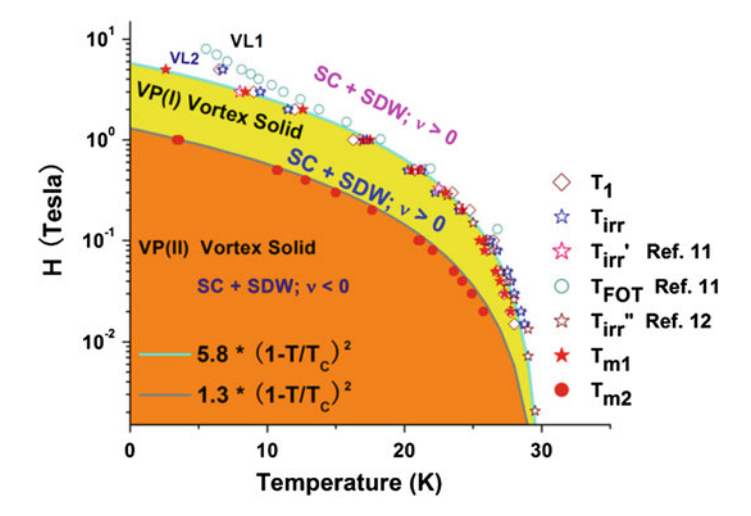


**Fig. 1.15** Magnetic phase diagram of  $\text{La}_{2-x}\text{Sr}_x\text{CuO}_4$  crystals around x=1/9. Various characteristic temperatures identified by magnetic measurements ( $T_I$  &  $T_{irr}$ ), reported in the literatures ( $T_{irr}$ ,  $T^n_{irr}$  &  $T_{FOT}$ ) and extracted by the critical fittings ( $T_{m1}$  &  $T_{m2}$ ) are plotted together for comparison.  $T_{m1}(H)$  &  $T_{m2}(H)$  are the boundaries separating vortex liquid (VL) phase from vortex phase I (VP(I)) and VP(I) from vortex phase II (VP(II)), respectively. From [58]

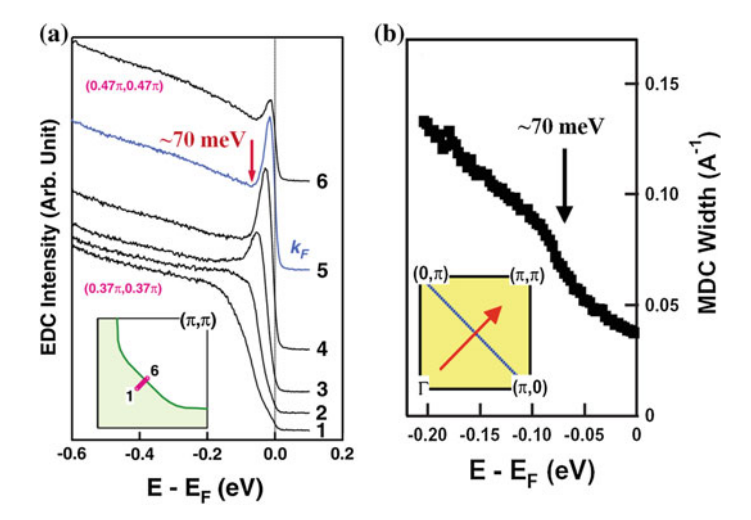


**Fig. 1.16** Some ARPES data on La<sub>1.937</sub>Sr<sub>0.063</sub>CuO<sub>4</sub> ( $x \sim 1/16$ ) single crystal at 20 K. **a** Energy distribution curves (EDCs) along the nodal direction in a second Brillouin zone. The *red arrow* indicates the energy of  $\sim 70$  meV below which the quasiparticle survives and above which it turns into a broad edge. From [60]. **b** The MDC width (electron-scattering rate) shows an enhanced upturn at the same energy scale  $\sim 70$  meV, as indicated by an arrow. From [61]

Recently, it has been shown that, in the under-doping regime, a maximum stabilization energy is gained at the magic number concentrations of n = 4(x = 1/16) and 3 (x = 1/9) for two-dimensional lattices formed by holes of oxygen-character and b<sub>2g</sub> symmetry [62]. Interestingly, a maximum energy gain arises as well at the hole density x = 0.100, which bears the same feature of a single narrow diamagnetic transition with an onset  $T_c = 30$  K (i.e. on the  $T_c$  plateau) as confirmed in LSCO crystal samples (Fig. 1.14). The relevant results are detailed by developing the idea of a stabilized exciton phase formed during a Mott-Hubbard transition. An earlier theoretical calculation did yield a crystalline arrangement of the doped holes at x = 1/16 for a reasonable choice of parameters [63]. The energy gain for charge ordered d-wave resonating valence bond (RVB) states in doped cuprates was estimated within a generalized t-J model [64]. While the kinetic energy favors a uniform charge distribution, the long-range Coulomb repulsion tends to spatially modulate the charge density in favor of charge ordered RVB states. On the other hand, hole-doping dependence of in-plane resistivity was carefully examined on a series of high-quality La<sub>2-x</sub>Sr<sub>x</sub>CuO<sub>4</sub> single crystals [65]. A tendency towards charge ordering at particular doping fractions of 1/16, 3/32, 1/8 and 3/16 was reported (Fig. 1.17), consistent with the SO(5) theory prediction of two-dimensional checkerboard ordering of the Cooper pairs at magic rational doping fractions  $(2 m + 1)/2^n$  (m and n are integers) [66–68].

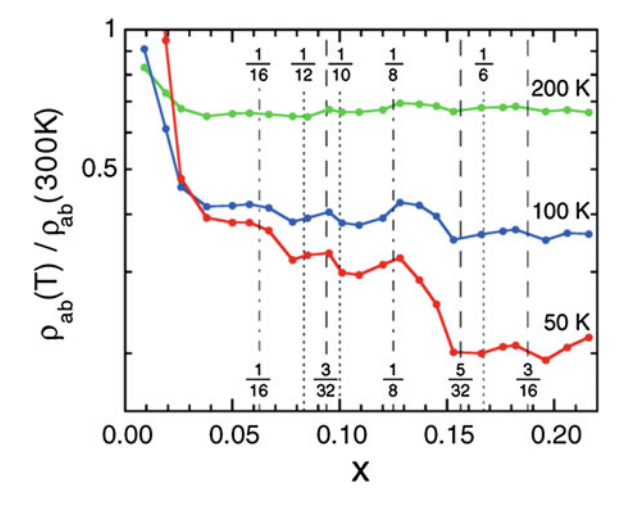


Fig. 1.17 x dependence of  $\rho_{ab}(T)/\rho_{ab}$  (300 K) at T=200, 100 and 50 K for La<sub>2-x</sub>Sr<sub>x</sub>CuO<sub>4</sub> single crystals. The hole motion tends to be hindered at low temperature at  $x\approx0.06$ , 0.09, 0.13 and 0.18. The magic doping fractions expected for the checkerboard order and the 1D stripes are shown by dashed and dotted lines, respectively; dash-dotted lines show the fractions both models predict. From [65]

# 1.6 Concluding Remarks

Among the cuprate superconductors, the  $K_2NiF_4$ -type  $La_{2-x}M_xCuO_4$  is important for the study on cuprate physics in many respects. It exhibits a wide charge doping range showing remarkable and informative doping dependent anomalies, while having fewer components and a simple layered structure containing single  $CuO_2$  planes. Moreover, the TSFZ crystal growth of the substituted  $La_{2-x}M_xCuO_4$  has turned out to be very successful and fruitful. Large and high-quality single crystal samples with desired and uniform substitutions have been produced to meet the demand in various specific experimental measurements on intrinsic, anisotropic electronic properties. That has greatly promoted the investigation and understanding of the underlying physics of cuprates. In the aspect of the growth technique, the application of semiconductor laser as the heating source is a new and important development in TSFZ technique, which is promising to make it more powerful to prepare incongruent single crystals difficult for conventional growth methods.

It should be noted that, on one hand, the substitution of dopant M<sup>2+</sup> for host La<sup>3+</sup> in La<sub>2</sub>CuO<sub>4</sub> induces hole carriers in the CuO<sub>2</sub> planes eventually leading to the superconductivity; on the other hand, it also modifies more or less the crystal lattice of La<sub>2</sub>CuO<sub>4</sub>, because the dopant, as an introduced "impurity", has a different atomic size and chemical valence compared to that of La<sup>3+</sup>. Both have significant influences on the electronic properties. In La<sub>2</sub>CuO<sub>4</sub> structure, the La<sup>3+</sup> sites with nine coordinated oxygen anions easily accommodate Sr<sup>2+</sup> cations having an ionic radius (1.45 Å, by Shannon and Prewitt [69, 70, 71]) properly bigger than La<sup>3+</sup> (1.356 Å) [72].

The tilt axis of the  $CuO_6$  octahedra is kept diagonal (LTO) to the Cu-O-Cu square lattice and the buckling of  $CuO_2$  planes is reduced with strontium substitution in the under-doping regime, where the robust intrinsic superconducting phases noticeably develop in the vicinity of the magic hole fractions ( $La_{2-x}Sr_xCuO_4$ ). But it is neither the case for the replacement of  $La^{3+}$  by  $Ca^{2+}$  (1.32 Å) which is too smaller in size, resulting in its low solubility in  $La_2CuO_4$ , nor for  $Ba^{2+}$  (1.61 Å) which is too bigger, leading to the alternating tilt axes parallel (LTT) to the Cu-O bonds, which pins the charge and spin stripe order thus strongly suppresses the superconductivity (the 1/8 anomaly in  $La_{2-x}Ba_xCuO_4$ ). These have made the cuprate physics more complicated.

Soon after the discovery of high- $T_c$  superconductivity derived from La<sub>2</sub>CuO<sub>4</sub> through hole doping, Anderson [73] pointed out that a common, unique feature of the doped cuprates is the proximity to a peculiar insulating magnetic phase with low dimensionality and the underlying physics is hence predominantly electronic and magnetic. This is particularly true in view of anomalous phenomena in cuprates fundamentally different from conventional metal physics, especially the one- or two-dimensional charge and spin physics correlated to the crystal chemistry predominating in La<sub>2-x</sub>Ba<sub>x</sub>CuO<sub>4</sub> and La<sub>2-x</sub>Sr<sub>x</sub>CuO<sub>4</sub>, respectively. With the advances in crystal growth and probing techniques, fruitful results with important implications for the high- $T_c$  superconductivity have been obtained and concepts proposed for attempts to understand them in the past three decades. However, to fully characterize the anomalous phenomena present in the high- $T_c$  superconductors has been a challenging task. A systematic understanding of the microscopic high- $T_c$  mechanism is still lacking up to date.

# References

- 1. J.G. Bednorz, K.A. Muller, Z. Phys. B Condens. Matter 64, 189 (1986)
- M. Hucker, M. von Zimmermann, G.D. Gu, Z.J. Xu, J.S. Wen, G.Y. Xu, H.J. Kang, A. Zheludev, J.M. Tranquada, Phys. Rev. B 83, 104506 (2011)
- 3. A. Wattiaux, J.C. Park, J.C. Grenier, M. Pouchard, C. R. Acad. Sci. Ser II 310, 1047 (1990)
- J.C. Grenier, A. Wattiaux, N. Lagueyte, J.C. Park, E. Marquestaut, J. Etourneau, M. Pouchard, Physica C 173, 139 (1991)
- J.E. Schirber, B. Morosin, R.M. Merrill, P.F. Hlava, E.L. Venturini, J.F. Kwak, P.J. Nigrey, R.J. Baughman, D.S. Ginley, Phys. C 152, 121 (1988)
- J.D. Jorgensen, B. Dabrowski, S.Y. Pei, D.G. Hinks, L. Soderholm, B. Morosin, J.E. Schirber, E.L. Venturini, D.S. Ginley, Phys. Rev. B 38, 11337 (1988)
- 7. J. Orenstein, A.J. Millis, Science 288, 468 (2000)
- 8. R.J. Birgeneau, C. Stock, J.M. Tranquada, K. Yamada, J. Phys. Soc. Jpn. 75, 111003 (2006)
- 9. J.D. Axe, A.H. Moudden, D. Hohlwein, D.E. Cox, K.M. Mohanty, A.R. Moodenbaugh, Y. Xu, Phys. Rev. Lett. 62, 2751 (1989)
- 10. Y. Maeno, A. Odagawa, N. Kakehi, T. Suzuki, T. Fujita, Phys. C 173, 322 (1991)
- 11. J.M. Tranquada, B.J. Sternlieb, J.D. Axe, Y. Nakamura, S. Uchida, Nature 375, 561 (1995)
- M.K. Crawford, R.L. Harlow, E.M. McCarron, W.E. Farneth, J.D. Axe, H. Chou, Q. Huang, Phys. Rev. B 44, 7749 (1991)
- M. Ma, D. Yuan, Y. Wu, H. Zhou, X. Dong, F. Zhou, Supercond. Sci. Technol. 27, 122001 (2014)

- 14. S.M. Koohpayeh, D. Fort, J.S. Abell, Prog. Cryst. Growth Charact. 54, 121 (2008)
- 15. H. Kojima, I. Tanaka, Jpn. J. Appl. Phys. Ser. 7, 76 (1992)
- 16. I. Shindo, J. Cryst. Growth **50**, 839 (1980)
- I. Tanaka, J. Yamamoto, Y. Mori, H. Tanabe, M.K.R. Khan, H. Kojima, Phys. C 225, 185 (1994)
- H. Kojima, J. Yamamoto, Y. Mori, M.K.R. Khan, H. Tanabe, I. Tanaka, Phys. C 293, 14 (1997)
- C.-H. Lee, N. Kaneko, S. Hosoya, K. Kurahashi, S. Wakimoto, K. Yamada, Y. Endoh, Supercond. Sci. Technol. 11, 891 (1998)
- 20. S. Kimura, I. Shindo, J. Cryst. Growth 41, 192 (1977)
- 21. I. Shindo, N. Li, K. Kitamura, S. Kimura, J. Cryst. Growth 46, 307 (1979)
- 22. I. Shindo, N. Kimizuka, S. Kimura, Mater. Res. Bull. 11, 637 (1976)
- F. Zhou, W.X. Ti, J.W. Xiong, Z.X. Zhao, X.L. Dong, P.H. Hor, Z.H. Zhang, W.K. Chu, Supercond. Sci. Tech. 16, L7 (2003)
- X.L. Shen, Z.C. Li, C.X. Shen, W. Lu, X.L. Dong, F. Zhou, Z.X. Zhao, Chin. Phys. B 18, 2893 (2009)
- 25. C. Marin, T. Charvolin, D. Braithwaite, R. Calemczuk, Phys. C 320, 197 (1999)
- S. Hosoya, C.H. Lee, S. Wakimoto, K. Yamada, Y. Endoh, Phys. C 235–240(Part 1), 547 (1994)
- 27. A. Maljuk, S. Watauchi, I. Tanaka, H. Kojima, J. Cryst. Growth 212, 138 (2000)
- 28. Y. Hidaka, Y. Enomoto, M. Suzuki, M. Oda, T. Murakami, J. Cryst. Growth 85, 581 (1987)
- 29. I. Tanaka, H. Kojima, Nature 337, 21 (1989)
- 30. I. Tanaka, K. Yamane, H. Kojima, J. Cryst. Growth 96, 711 (1989)
- 31. T.F.S. Hosoya, T. Kajitani, K. Hiraga, K. Oh-Ishi, Y. Syono, K. Yamada, Y. Endoh, T. Takahashi, H. Katayama-Yoshida, Jpn. J. Appl. Phys. Ser. 7, 81 (1992)
- 32. K. Oka, M.J.V. Menken, Z. Tarnawski, A.A. Menovsky, A.M. Moe, T.S. Han, H. Unoki, T. Ito, Y. Ohashi, J. Cryst. Growth 137, 479 (1994)
- 33. T. Ito, K. Oka, Phys. C 231, 305 (1994)
- A.M. Balbashev, D.A. Shulyatev, G.K. Panova, M.N. Khlopkin, N.A. Chernoplekov, A.A. Shikov, A.V. Suetin, Phys. C 256, 371 (1996)
- 35. A.K.M.A. Islam (Ed.), in *High-Tc Superconductors: Proceedings of the 12th Anniversary HTS Workshop*. Rajshahi (1998)
- 36. S. Komiya, Y. Ando, X.F. Sun, A.N. Lavrov, Phys. Rev. B 65, 214535 (2002)
- M. Fujita, K. Yamada, H. Hiraka, P. Gehring, S. Lee, S. Wakimoto, G. Shirane, Phys. Rev. B 65, 064505 (2002)
- J. Yu, Y. Yanagida, H. Takashima, Y. Inaguma, M. Itoh, T. Nakamura, Phys. C 209, 442 (1993)
- 39. T. Adachi, T. Noji, Y. Koike, Phys. Rev. B 64, 144524 (2001)
- M. Fujita, H. Goka, K. Yamada, J.M. Tranquada, L.P. Regnault, Phys. Rev. B 70, 104517 (2004)
- 41. T. Valla, A.V. Fedorov, J. Lee, J.C. Davis, G.D. Gu, Science 314, 1914 (2006)
- 42. M.K.R. Khan, Y. Mori, I. Tanaka, H. Kojima, Phys. C 262, 202 (1996)
- M.A.R. Sarker, S. Watauchi, M. Nagao, T. Watanabe, I. Shindo, I. Tanaka, Phys. C 472, 87 (2012)
- 44. T. Ito, T. Ushiyama, Y. Yanagisawa, Y. Tomioka, I. Shindo, A. Yanase, J. Cryst. Growth 363, 264 (2013)
- 45. T. Ito, T. Ushiyama, Y. Yanagisawa, R. Kumai, Y. Tomioka, Cryst. Growth Des. 11, 5139 (2011)
- F.C. Chou, N.R. Belk, M.A. Kastner, R.J. Birgeneau, A. Aharony, Phys. Rev. Lett. 75, 2204 (1995)
- 47. S. Wakimoto, G. Shirane, Y. Endoh, K. Hirota, S. Ueki, K. Yamada, R.J. Birgeneau, M.A. Kastner, Y.S. Lee, P.M. Gehring, S.H. Lee, Phys. Rev. B **60**, R769 (1999)
- 48. J.B. Torrance, Y. Tokura, A.I. Nazzal, A. Bezinge, T.C. Huang, S.S.P. Parkin, Phys. Rev. Lett. 61, 1127 (1988)

References 21

- 49. K. Sreedhar, P. Ganguly, Phys. Rev. B 41, 371 (1990)
- 50. T. Nagano, Y. Tomioka, Y. Nakayama, K. Kishio, K. Kitazawa, Phys. Rev. B 48, 9689 (1993)
- 51. P.G. Radaelli, D.G. Hinks, A.W. Mitchell, B.A. Hunter, J.L. Wagner, B. Dabrowski, K.G. Vandervoort, H.K. Viswanathan, J.D. Jorgensen, Phys. Rev. B 49, 4163 (1994)
- 52. F. Zhou, P.H. Hor, X.L. Dong, W.X. Ti, J.W. Xiong, Z.X. Zhao, Phys. C 408-410, 430 (2004)
- 53. F. Zhou, P.H. Hor, X.L. Dong, Z.X. Zhao, Sci. Technol. Adv. Mater. 6, 873 (2005)
- J.M. Tranquada, J.D. Axe, N. Ichikawa, Y. Nakamura, S. Uchida, B. Nachumi, Phys. Rev. B 54, 7489 (1996)
- Y.H. Kim, P.H. Hor, X.L. Dong, F. Zhou, Z.X. Zhao, Y.S. Song, W.X. Ti, J. Phys.: Condens. Matter 15, 8485 (2003)
- Y.H. Kim, P.H. Hor, X.L. Dong, F. Zhou, Z.X. Zhao, Z. Wu, J.W. Xiong, Phys. Rev. B 71, 092508 (2005)
- 57. X.L. Dong, P.H. Hor, F. Zhou, Z.X. Zhao, Solid State Commun. 145, 173 (2008)
- 58. X.L. Dong, P.H. Hor, F. Zhou, Z.X. Zhao, Solid State Commun. 152, 1513 (2012)
- 59. D. Mihailovic, Phys. Rev. Lett. **94**, 207001 (2005)
- X.J. Zhou, T. Yoshida, D.H. Lee, W.L. Yang, V. Brouet, F. Zhou, W.X. Ti, J.W. Xiong, Z.X. Zhao, T. Sasagawa, T. Kakeshita, H. Eisaki, S. Uchida, A. Fujimori, Z. Hussain, Z.X. Shen, Phys. Rev. Lett. 92, 187001 (2004)
- X.J. Zhou, T. Yoshida, A. Lanzara, P.V. Bogdanov, S.A. Kellar, K.M. Shen, W.L. Yang, F. Ronning, T. Sasagawa, T. Kakeshita, T. Noda, H. Eisaki, S. Uchida, C.T. Lin, F. Zhou, J. W. Xiong, W.X. Ti, Z.X. Zhao, A. Fujimori, Z. Hussain, Z.X. Shen, Nature 423, 398 (2003)
- 62. M. Pouchard, J.P. Doumerc, A. Villesuzanne, New J. Chem. 36, 796 (2012)
- 63. H.C. Fu, J.C. Davis, D.-H. Lee, arXiv:cond-mat/0403001v2 (2004)
- 64. H.X. Huang, Y.Q. Li, F.C. Zhang, Phys. Rev. B 71, 184514 (2005). See also P.W. Anderson, arXiv:cond-mat/0406038v1 (2004), where a two-dimensional crystal of hole pairs embedded in a sea of a d-wave RVB states was proposed, and the energy gain furnished by the long-range Coulomb interaction, something like the Madelung energy of the charge distribution of the "liquid crystal", was suggested
- 65. S. Komiya, H.-D. Chen, S.-C. Zhang, Y. Ando, Phys. Rev. Lett. 94, 207004 (2005)
- H.-D. Chen, J.-P. Hu, S. Capponi, E. Arrigoni, S.-C. Zhang, Phys. Rev. Lett. 89, 137004 (2002)
- 67. H.-D. Chen, O. Vafek, A. Yazdani, S.-C. Zhang, Phys. Rev. Lett. 93, 187002 (2004)
- 68. H.-D. Chen, S. Capponi, F. Alet, S.-C. Zhang, Phys. Rev. B 70, 024516 (2004)
- 69. R.D. Shannon, C.T. Prewitt, Acta Cryst. B 25, 925 (1969)
- 70. R.D. Shannon, C.T. Prewitt, Acta Cryst. B 26, 1046 (1970)
- 71. R.D. Shannon, Acta Cryst. A 32, 751 (1976)
- 72. M.J. Rosseinsky, K. Prassides, P. Day, J. Mater. Chem. **1**, 597 (1991)
- 73. P.W. Anderson, Science 235, 1196 (1987)

# Chapter 2 YBCO and Some Other Rare Earth Cuprates

Dapeng Chen and Chengtian Lin

**Abstract** The growth of high quality and centimeter-sized  $YBa_2Cu_3O_{7-\delta}$  and RE–Ba–Cu–O (RE = rare earth) single crystals can be achieved using either flux or traveling solvent floating zone (TSSG) method. The oxygen content of crystals can be tuned through the oxygenation/deoxygenation of the same sample by post growth annealing. The as-grown twinned single crystals are detwinned and enabled to probe the charge reservoir in  $CuO_2$  planes, which induced no carrier contributions from the other layers, such as CuO chains.  $YBa_2Cu_4O_8$  is another important compound for the study of its chemical and physical properties since it is twin-free and shows higher thermal stability with oxygen stoichiometry. The KOH flux growth of  $YBa_2Cu_4O_8$  single crystal provided a simple way to access the reasonable size of the samples. In this chapter, we present detailed procedures for the best quality crystal growth. Various attempts to improve the crystal quality are described. Large single crystal growth of some other rare earth cuprates is also presented.

### 2.1 Introduction

Superconductivity is one of the most exotic phenomena in condensed matter physics. The copper-oxide-based superconductors with high superconducting transition temperature,  $T_c$  (that is, larger than anticipated limit of about 25–30 K) were discovered in 1986 [1]. This year marks the beginning of worldwide efforts to investigate the high  $T_c$  superconductors. In the ensuing years, the transition temperature climbed to the record high of 138 K at ambient pressure [2]. Although the following years did not bring any progress towards a further increase in  $T_c$ , and the underlying mechanism remains unknown, the intensive investigation of high  $T_c$ 

D. Chen (⋈) · C. Lin

materials has played an important role in the advance of science and technology, and led to the development of theoretical models, as well as innovations in experimental techniques, including synthesis of high quality samples.

The discovery of Y-Ba-Cu-O (YBCO) superconductor [3] has stimulated a great deal of scientific and technological research into this family of materials. Over the past twenty eight years, three superconducting phases, YBa<sub>2</sub>Cu<sub>3</sub>O<sub>7-δ</sub> (Y-123),  $Y_2Ba_4Cu_7O_{15-\delta}$  (Y-247) and  $YBa_2Cu_4O_8$  (Y-124), were found in this family of materials. Among them, Y-123 has been chosen as the model system to investigate the superconducting mechanism of the copper-based superconductors because their advantages, such as the availability of high quality single crystals [4], the convenience of accessing different hole doping regimes through oxygenation/deoxygenation of the same sample, and by using detwinned single crystals one can probe the response of the CuO<sub>2</sub> planes without having to consider the contributions from other charge reservoir layers. Other rare earth (RE) cuprates such as ReBa<sub>2</sub>Cu<sub>3</sub>O<sub>7-8</sub> (RE-123) have also attracted physicists because some RE elements with large magnetic moments show superconductivity which is in conflict with conventional Bardeen-Cooper-Schrieffer theory [5].

Y-124 is a very important compound for study of its physical properties since it is twin-free and shows higher thermal stability than the well-known Y-123. However fewer studies on this compound, comparing to Y-123, were carried out since it was first synthesized twenty seven years ago [6–8]. The investigation of this phase was hampered by the convenience of accessing the reasonable size of single crystals, since the millimetres-sized Y-124 single crystals need to be grown in a specially designed apparatus under a high  $O_2$  pressure [9]. A new method using KOH as flux for obtaining high quality Y-124 single crystals with a size up to  $1.2 \times 0.5 \times 0.3$  mm<sup>3</sup> were reported recently [10, 11].

Although high quality and large size single crystals of Y-123, RE-123 and Y-124 can now been grown, there are still some unknowns and controversies awaiting further research on cleaner crystals. In this chapter, we present detailed single crystal growth procedures and their impact on crystal size and quality, as well as on their defects and growth mechanism. Various attempts to improve the superconducting quality will be described. Some other rare earth cuprates large single crystal growth and characterization will also be presented.

# 2.2 Phase Diagram

The phase diagrams of YBCO superconductor are very important for the synthesis, crystal growth and post-treatment. Many phase diagrams have been proposed for this family of material [9, 12–14]; however, there are several discrepancies among them caused by using different methods or various flux compositions. Therefore, the phase diagrams for crystal growth of 123 and 124, and the stability regions of

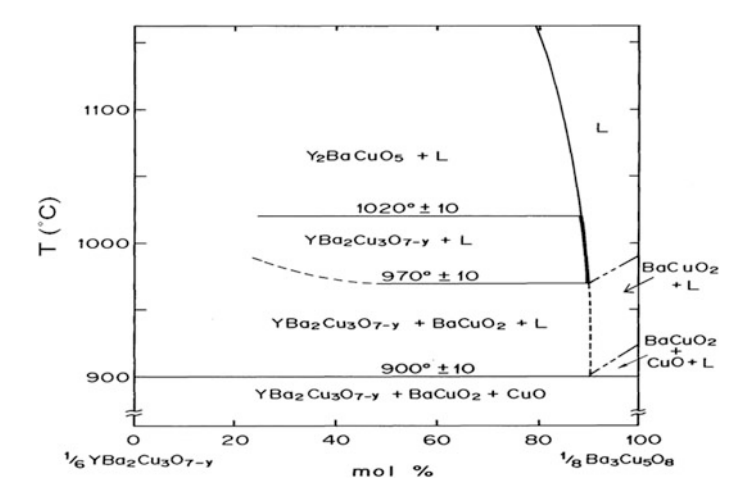


**Fig. 2.1** The temperature versus composition phase diagram of the  $YBa_2Cu_3O_{7-y}$ – $Ba_3Cu_5O_8$  system in air. The liquidus lines required for the solution growth of Y-123 single crystal are drawn by bold lines [12]

123, 124 and 247 phases are appreciably different. It have been revealed that YBCO and other compounds substituted with rare-earth ions are incongruent-melt substances, solution growth methods are usually employed to grow the single crystal. Here we will introduce the most technologically useful phase diagrams for solution growth of large and high quality crystals, as well as the stability conditions of the superconducting phases. Figure 2.1 shows the binary phase diagram on Y-123 to Ba<sub>3</sub>Cu<sub>5</sub>O<sub>8</sub> mixture proposed by Oka et al. [12]; it shows that the liquidus line required for the growth of Y-123 single crystal form solution was extremely narrow in concentration range. Though the attempts to grow Y-123 crystals based on this phase diagram did not quickly yield large single crystals, but the phase diagram researches have put a solid foundation for the understanding of the chemical circumstances around the YBCO, and finally resulted in large and high quality Y-123 crystals owing to the dedications of crystal growth scientists [4, 5, 15].

The stability regions of Y-123, Y-247 and Y-124 phases were studied as a function of temperature and partial pressure of oxygen by many groups [9, 14]. It revealed that the stability regions of these phases are appreciably different. Figure 2.2 shows the typical temperature-composition (T-C) diagram determined from XRD measurements at 1 atm [14], it shows that the phase boundary temperatures of 123/247 and 247/124 were about 870 and 817 °C, respectively, and 123/124 was 760 °C.

The P-T (pressure–temperature) diagram revealed that the 123 phase is stable only at high temperature and low  $P(O_2)$ , while 124 is stable at high  $P(O_2)$  and low temperature, The 247 phase is stable at intermediate temperatures and oxygen

Fig. 2.2 Temperature ranges for stability of 123, 247 and 124 phases at  $P(O_2) = 1$  atm [14]

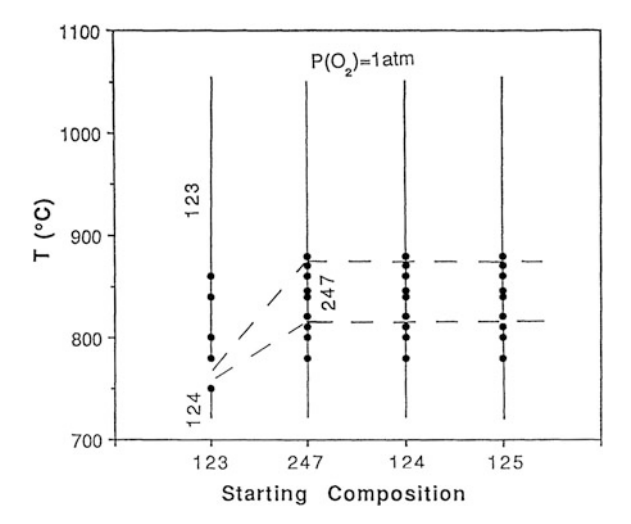
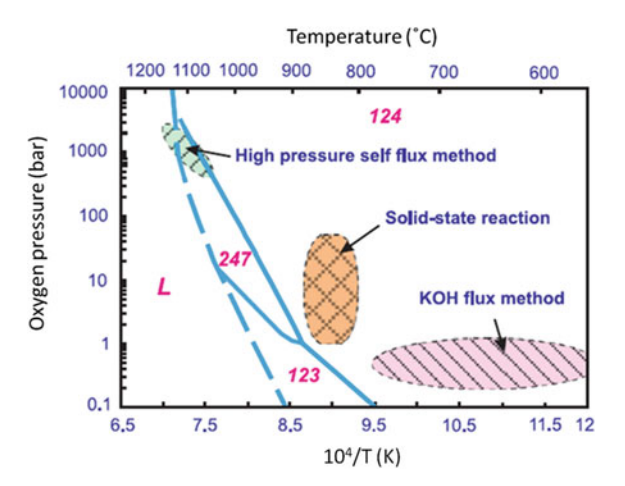


Fig. 2.3 P-T phase diagrams of Y-123, Y-247 and Y-124, modified by Sun et al. [11]



pressures between the 123 and 134 stability regions [14]. Figure 2.3 shows a P-T phase diagram, indicating three phases, Y-123, Y-124 and Y-247, formed in each specified region with different temperature and/or pressure. The three phase boundaries were determined by the study of a reversible reaction: Y-123 + CuO  $\leftrightarrow$  Y-124 or Y-247. The Y-124 phase can be stabilized at 890 °C under P(O<sub>2</sub>) = 1 bar, but it decomposes to Y-247 + CuO under P(O<sub>2</sub>)  $\geq$  1 bar or Y-123 + CuO under P(O<sub>2</sub>)  $\leq$  1 at above 890 °C. Therefore, bulk synthesis of Y-124 under ambient pressure should be carried out below the decomposition temperature of 890 °C. Three methods, high pressure self-flux, solid-state reaction, and KOH flux, have been reported for the synthesis of Y-124; the growth conditions are shown in Fig. 2.3. These phase diagrams have provided usefully guilds for YBCO single crystal growth and post-treatment.

# 2.3 Centimeter-Sized Single Crystal Growth of Y-123 and RE-123

Large, high-quality pure and doped  $YBa_2Cu_3O_{7-\delta}$  (Y-123) single crystals are important for the measurement of physical properties, particularly for the neutron-scattering experiment and electronic device application of the superconducting properties. However, the growth of large Y-123 single crystals in centimeters is always a challenge due to the fact that the Y-123 is an incongruent melt with thermal and chemical instability, high kinetic viscosity ( $v = 1 \times 10^{-2} \text{ cm}^2/\text{s}$ ) and low coefficient of diffusion ( $D = 1 \times 10^{-5} \text{ cm}^2/\text{s}$ ). Moreover, the corrosion of crucible materials is another serious problem in growing high-quality crystals. The flux method and top seeded solution growth (TSSG) method were proven to be the suitable techniques for obtaining the crystals sized 100 mm<sup>3</sup> [5, 16–19].

Figure 2.4 illustrated the flux method for Y-123 single crystal growth. Large crystals were grown from a highly concentrated flux containing 15 %  $YBa_2Cu_3O_{7-\delta}$  and 85 %  $Ba_3Cu_7O_{10}$ . The starting mixtures (usually 200 g, 3 N) of  $Y_2O_3$ ,  $BaCO_3$  and CuO were loaded in a zirconia crucible. The growth apparatus and procedures are illustrated in Fig. 2.4a. A Ni rod cold finger was mounted above the melt to create a sharp temperature gradient (Fig. 2.4b), which is the main driving force for

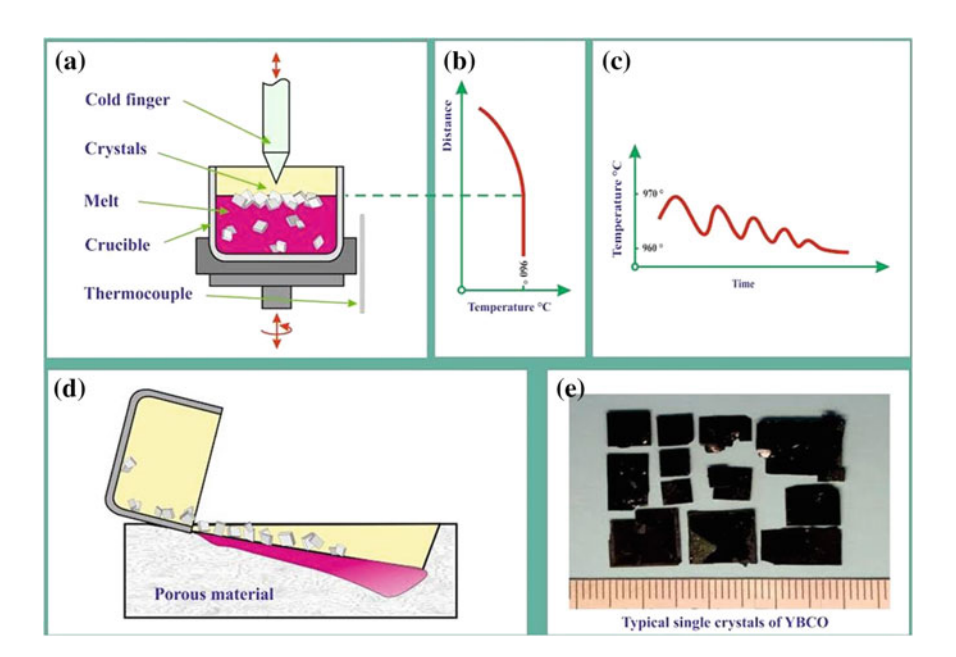


**Fig. 2.4** Schematic illustration for the Y-123 single crystal growth by flux method. **a** Growth apparatus. **b** Sharp temperature gradient created in the growth interface by cold finger. **c** Temperature oscillation method applied to reduce the number of nuclei. **d** Free-standing crystals obtained by separating residual melt, which is sucked by porous brick. **e** Typical single crystals of Y-123

growing crystals in the solid melt interface. During growth the crucible was rotated at 20 rpm to obtain a uniform temperature distribution and melt mixing. Because incongruent and incomplete melts contain various dispersed droplets, inclusions and impurities together with the Y-123 phase, a large number of nucleation centers are always present during the cooling procedure of crystal growth.

By the use of a temperature oscillation method, the number of nucleation centers can be reduced considerably. The temperature oscillations as shown in Fig. 2.4c, it allows small crystallites to remelt and gives the large crystals more space and nutrient supply for their own growth. This has resulted in large crystals being successfully obtained from the melt surface. The most suitable temperature for crystal growth was found to be in the range between 972 and 960 °C. When cooling terminated at this temperature range, the residual flux was poured into a porous brick by tipping the crucible over. This separation technique showed that the flux was absorbed by the brick and left crystals free standing and without contamination on the crystal surface, as shown in Fig. 2.4d. The crystals so obtained are as large as several square centimeters and over 2 mm thick. Some typical crystals are shown in Fig. 2.4e.

Centimeter sized pure and Ca doped Y-123 crystals can be grown by the TSSG method in air and oxygen environments [5, 19]. For the Ca doped Y-123 crystals growth, the initial composition with a molar ratio of Y:Ba:Cu = 1.0:7.2-24.0:11.8-54.0 plus additional Ca were used in the melt to maintain the growth in a constant supersaturating. This allows crystals to grow at a constant rate of up to 2 mm/d for 100 h. The apparatus for the crystal growth is schematically shown in Fig. 2.5. The starting mixtures (usually 350–370 g, 3 N) of Y<sub>2</sub>O<sub>3</sub>, BaCO<sub>3</sub>, CaCO<sub>3</sub>, and CuO were ground in a ball mill for over 4 h. The ground mixtures were then filled in an alumina crucible and heated in air at 880 °C in a chamber furnace for two days in order to decompose carbonates. The calcined mixtures were then transferred into Y-stabilized ZrO<sub>2</sub> crucible for the growth. MgO was used as a seed. During growth, the seed and the crucible were rotated at 40 rpm in opposite directions. A soaking temperature of about 1050  $^{\circ}\text{C}$  was used. The temperature of 1020  $^{\circ}\text{C}$  measured at the bottom of the crucible was higher than 1007 °C on the melt surface, which was cooled by the water flowing in the inside of the pull shaft. This large temperature difference sufficiently produced a heat convection transport from the bottom of the crucible to the surface of the melt and made the possible transportation of the mass Y+Ca easily.

The composition distribution in the crucible was studied by quench the melt to room temperature. The results of the major phases are shown in Fig. 2.6. The main composition of surface melt was the solvent of Ba–Cu–O mixed with Y-123 phase. The Y-123 phase was scattered on the melt surface and gradually concentrated in the middle crucible, corresponding to the peritectic point, P. During the growth, it was observed that several square millimeters floating thin particles shifted on the melt surface. These particles consisted of Y-123 phase, which were supersaturated by Y and Ca atoms transported from the bottom of the crucible to the surface of the melt by thermal convection. This allowed the growth of Y-123 crystal to take place on the surface by seeding. The surface melt was easily supersaturated by Y and Ca although the solubility of Y and Ca was low in the melt. Thus, Y-123 single crystal could be grown from the melt surface with a relatively high growth rate compared

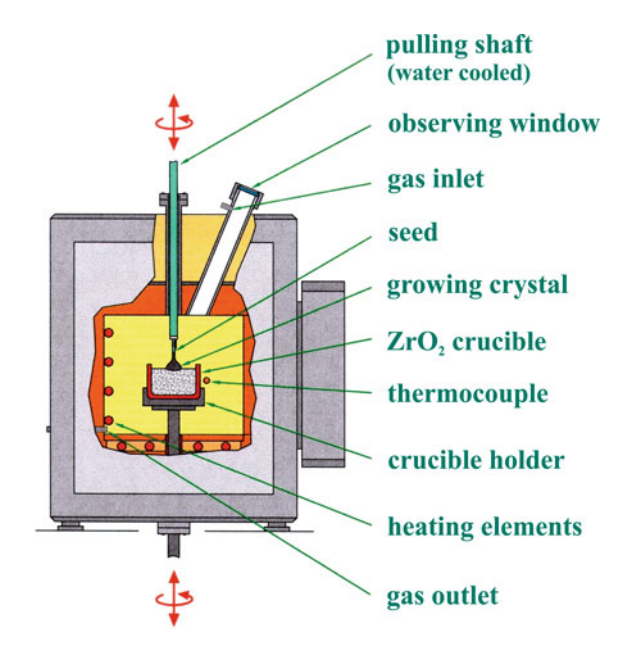


Fig. 2.5 Schematic illustration of the apparatus used to grow Ca-doped Y-123 single crystals [19]

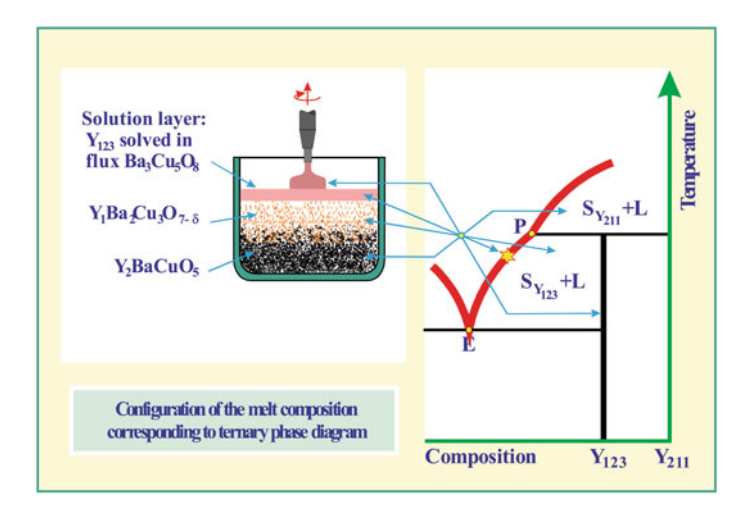
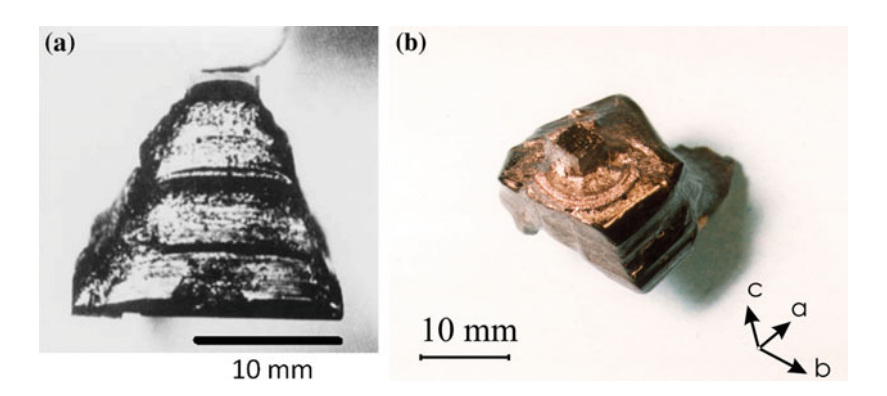


Fig. 2.6 Schematic drawing of the configuration of the melt composition corresponding to ternary phase diagram, where P is a peritectic point and E eutectic point [19]

with that of the flux method. The Y-211 majority phase or green phase was observed to deposit at the bottom of the crucible. The melt composition agrees very well with the ternary phase diagram of YBCO [15].

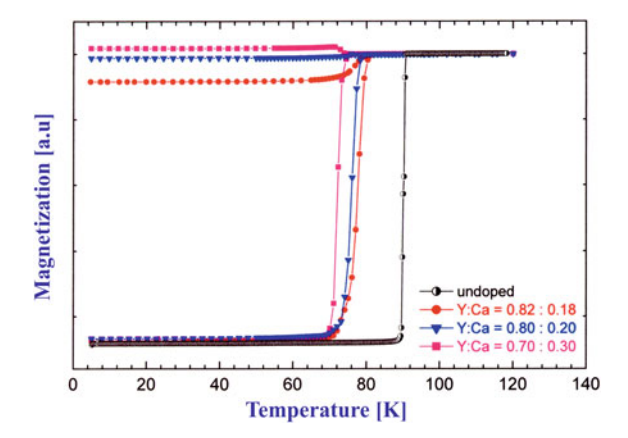
During seeding, the floating particles could impact onto seed or growing crystal, as a result, multi-nuclei occurred and poly-crystals with several large grains formed. Sometimes small crystalline could parasitize on a large growing crystal and were also caused by extra nuclei from the particles. The number of nuclei could be significantly reduced by a nucleation-controlled method, i.e., applying the temperature oscillation method [16]. Figure 2.7b shows a typical crystal obtained by the method and separated from the MgO seed under oxygen atmosphere. For obtaining large-sized crystal in an incongruent melt by the TSSG technique, it is important to maintain the growth processing in a constantly supersaturated melt and apply an extremely slow growth rate. Growth usually carried out at a constant rate of 1–2 mm/d. The running period of a growth was completed within 100 h due to the corrosion of crucible material. The growth could ease by a high viscosity of the melt containing BaZrO<sub>x</sub>; produced by a reaction of crucible material and melt when growing time was longer than 100 h.

It is known that the ionic radii of  $Ca^{2+}$  and  $Y^{3+}$  is  $R_{Ca}^{2+} = 0.99 \text{Å}$  and  $R_Y^{3+} = 0.93 \text{Å}$ , respectively. Therefore, the divalent ion  $Ca^{2+}$  can substitute preferentially for  $Y^{3+}$  due to the slight difference between the ionic radii. The substitution of Ca for Y generates holes to influence superconducting transition temperature  $T_c$  while not changing the crystal structure. The research revealed that the concentration of Ca increases continuously in proportion to the relative amount of Ca in the melt, and the segregation coefficient of Ca for the compound was estimated to be  $\sim 0.7$ . The segregation coefficient smaller than unity suggests a very low solubility of Ca as a substituent for Y in Y-123. Therefore, the Ca is hard to incorporate into the crystal. This may be partly due to the fact that the ionic radii of  $Ca^{2+}$  are slightly larger than that of  $Y^{3+}$ . However, complex thermodynamical argument is that it must be the dominant factor as this low Ca doping >0.55 in the melt.



**Fig. 2.7** Y-123 single crystals obtained by the TSSG method: **a** As-grown pure Y-123 single crystal produced under 1 atm oxygen pressure [5]; **b** by nucleation-controlled method. The as-grown crystal faces were identified by Laue X-ray [19]

Fig. 2.8 Temperature dependence of magnetization for the Ca-doped and undoped Y-123 single crystals grown by the TSSG method [19]



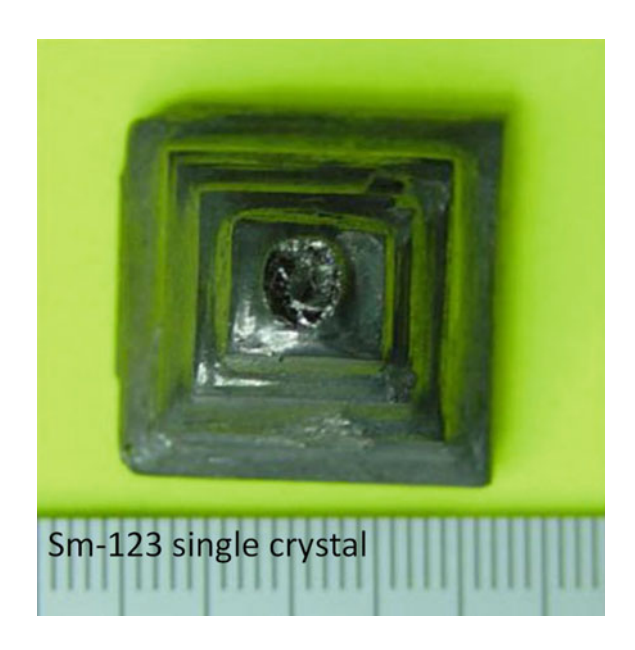
The result of magnetic susceptibility measurement showed a broad superconducting transition due to the oxygen insufficiency in the as-grown crystals. By post-annealing as-grown crystals in flowing oxygen at 535 °C for 48 h, oxygen was taken over by the compounds, resulting in a sharp transition width of 4 K. As show in Fig. 2.8, the superconducting transition temperature  $T_c$  reduces with increasing Ca content, 75 K at  $\chi = 0.30$ , 78 K at  $\chi = 0.20$ , 79 K at  $\chi = 0.18$  and 90 K at  $\chi = 0$ .

Rare earths (RE) can be substituted for yttrium without any destructive effects on the superconducting characteristics of Y-123 with the exception of RE = Ce and Pm [20–24]. In general,  $T_c$  and peritectic temperatures ( $T_p$ ) increase with increasing ionic radius of RE. However, at a certain point, a further increase in the ionic radius decreases or varies  $T_c$ . This is because RE ions easily substitute into the Ba site [25–27].

TSSG method and modified TSSG method also has been applied to RE-123 materials (RE = Pr, Sm, Nd) from the Ba–Cu–O solvent. It has been found that bulk single crystals of several cubic millimeters in size can be repeatedly produced after optimizing the growth conditions, such as the growth temperature, composition of the flux melt, crucible materials, etc. [28–30]. The typical growth procedure can be demonstrated through the Sm-123 crystals growth. Sm<sub>2</sub>O<sub>3</sub> crucibles were used so that the contamination from the crucible could be reduced to a minimum. High-quality Ba<sub>x</sub>Cu<sub>y</sub>O (the ratio of x to y ranged from 3:4 to 3:7) powders were used as raw materials for the solvent. Sm was not included in the precursor mixture. Instead, the Sm solute was supplied through the interaction between the molten solvent and the Sm<sub>2</sub>O<sub>3</sub> crucible. YBCO thin films were prepared by the thermal co-evaporation technique on the MgO single crystal. As hetero-seeds, these YBCO-deposited MgO crystals were used for the SmBCO crystal growth. These YBCO thin films are highly c-axis oriented. The rotation speed and the pulling rate were in the range 70–120 rpm and 0.10–0.20 mm h<sup>-1</sup>, respectively.

Figure 2.9 shows a photograph of a large-sized Sm-123 single crystal grown in  $Ba_3Cu_5O_z$  solvent at approximately 1056 °C in air. The crystal has a pyramid

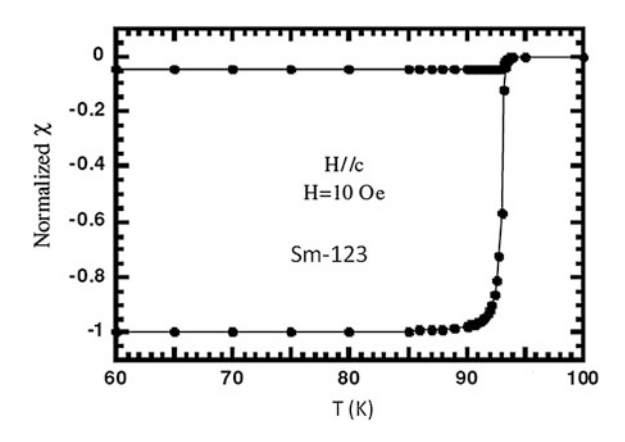
Fig. 2.9 The Sm-123 single crystal grown in air in the solution with the Ba/Cu ratio = 0.6. The size is  $23 \times 22 \text{ mm}^2$  in the a-b plane and 19 mm in the c-axis direction [31]



shape, with the bottom a–b plane of 23 × 22 mm<sup>2</sup>. The total growth time is 147 h. The average growth rate is approximately 0.13 mm h<sup>-1</sup> in the c-axis direction, which is higher than that in the YBCO system (nearly 0.05 mm h<sup>-1</sup> in the c-axis direction in ambient atmosphere by the modified TSSG method [32].

Figure 2.10 shows the temperature dependence of normalized magnetization for an oxygenated SmBCO crystal grown under the same conditions as mentioned above. The field of 10 Oe was applied parallel to the c-axis (H//c) from 60 to 100 K. The high  $T_c$  of 93 K with a sharp transition width  $\Delta T$  of less than 1 K (the difference between 10 and 90 % transition to the zero-field cooled (ZFC) value at 60 K) is clearly displayed, indicating the high quality of the crystal.

Fig. 2.10 Temperature dependence of magnetization for the SmBCO single crystals grown in air in the solution with the Ba/Cu ratio = 0.6 [31]



# 2.4 Ferroelastic Detwinning

The ferroelastic transition of the tetragonal to the orthorhombic (denoted as T–O henceforth) phase in the high-T<sub>c</sub> superconductor Y-123 on cooling is normally accompanied by the spontaneous occurrence of twin domains which appear to compensate the internal strains. These twin domains are visible as giving rise to sharp and contrasted images in polarizing microscopes as well as electron microscopes. Their presence in the superconducting, orthorhombic Y-123 phase still poses a problem in obtaining a clear resolution of the a–b anisotropy of physical properties. There have extensive investigations to characterize the microstructures and understand their possible influence on the superconducting properties [33, 34]. In situ observation of the motion of ferroelastic domain switching during the T–O phase transformation in Y-123 has been achieved by using high temperature optical microscope [35].

Single crystals were grown from high concentration flux containing 15 %  $YBa_2Cu_3O_{7-\delta}$  and 85 %  $Ba_3Cu_7O_{10}$  in a zirconia crucible. The growth details are described in Sect. 2.3. The structure of crystals is tetragonal as they are grown at above 960 °C. When they were cooled slowly through the T–O transition temperature in the presence of oxygen, these crystals would undergo a structural transformation to the orthorhombic phase.

A detwinning apparatus which can directly in situ observe the twin motion procedure is schematically illustrated in Fig. 2.11. A square-shaped crystal was placed between two quartz plates with the stress being applied along the [1 0 0] direction. The temperature of the crystal was raised at a constant stress of about  $2.5 \times 10^7$  N/m<sup>2</sup> and the domain pattern controlled visually by using a high temperature optical microscope. Polarized optical images of an as-grown Y-123 single crystal before and after successive heat treatments are shown in Fig. 2.12a-d, respectively. At 250 °C the crystal started to homogenize by means of lateral wall movements. The image of the twin domains show a decreasing colour contrast following successive heat treatments to higher temperatures at 350 and 450 °C, respectively, suggesting that the twin density is decreasing and the crystal remains orthorhombic with a large, single domain after detwinning. A few small cracks seen on the bottom indicate that non-uniform stress occurred due to an irregular shape of the specimen. Therefore a sample with perfect rectangle or square shape is always necessary for the thermomechanical detwinning. When releasing the stress totally at the detwinning temperature, no elastic back switching was observed.

The detwinned crystal was characterized by the temperature dependence of susceptibility and shows a sharp transition  $T_c$  at 91 K with  $\Delta T \sim 1$  K. If the transition temperatures are representative of the crystal phase, then one might expect more than one phase to be observed due to the simultaneous presence of both orthorhombic and tetragonal phases that sample underwent its T–O transition temperature during cooling after growth, as result in double or broad transition. Therefore, it indicates that the detwinned crystal contains only one orthorhombic phase in an optimally doped state.

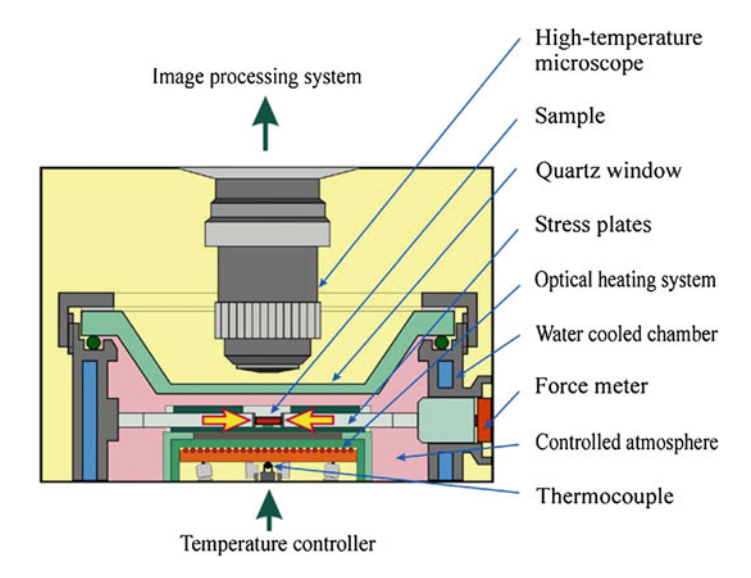
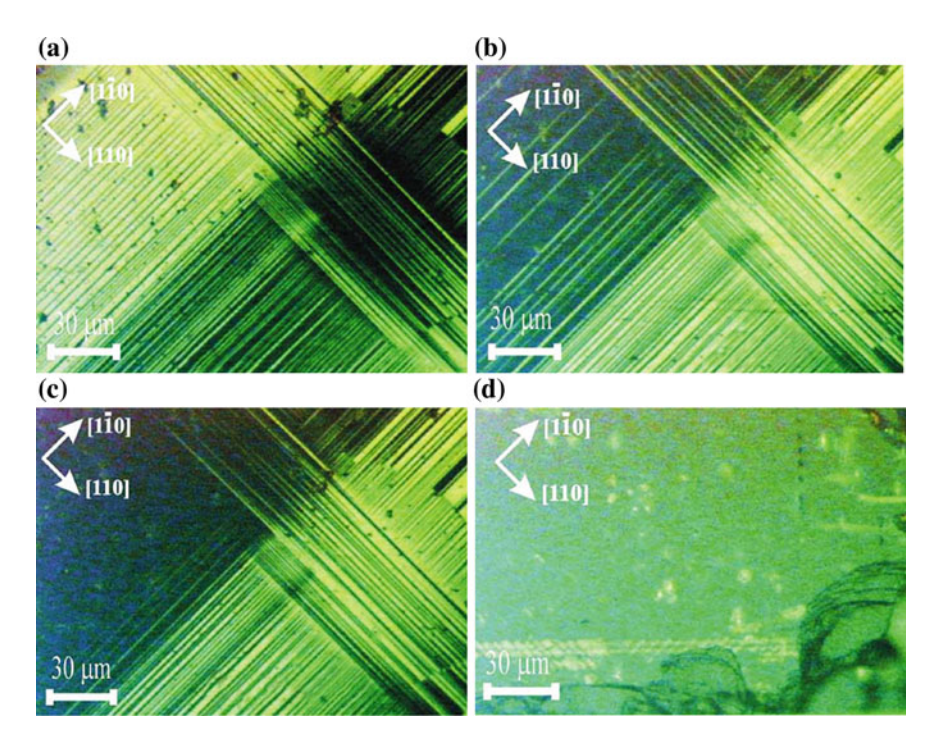


Fig. 2.11 Schematic diagram of the in situ observation technique for the detwinning of Y-123 single crystals

Instead of applying a uniaxial pressure, removal of twins was carried out by quenching specimens above the T-O transition temperature. The technique provided a means of maintaining an oxygen partial pressure, which was advantageous in retaining the oxygen content of the crystal despite the high temperature treatment. The as grown sample was fully oxygenated and then heated up to 400, 650, 800 and 930 °C for 5 min, respectively, and followed by rapid quenching in Ar. The polarized optical images of the quenched specimen show similar decreasing colour contrast with heating temperatures, referred to Fig. 2.12a-d. The twin density is decreasing but the crystal remains orthorhombic or there is an increasing volume of the crystal becoming tetragonal phase present in the twin boundary regions. At the final two states of 800 and 930 °C a uniform colour is over the whole crystal and this indicates a nearly full conversion to the tetragonal phase. The tetragonal phase in this case is always accompanied by the presence of a tweed structure [34], which was needed to relieve the internal strain. The superconducting transition T<sub>c</sub> drops to 40 K even in the tetragonal phase, by quenching at 800 °C. The T<sub>c</sub> completely suppressed by quenching at 930 °C, which is a tetragonal phase. The availability of twin-free YBCO should be promotional to a further quantifiable study of a = b anisotropy of physical properties [36].



**Fig. 2.12** Polarizing optical micrographs showing gradual changes in the twin domain structure of YBCO single crystal by the applied stress of  $2.5 \times 10^7$  N/m<sup>2</sup> parallel [1 0 0] and heating at **a** as-grown state, **b** 250 °C for 30 min, **c** 350 °C for 30 min and **d** 450 °C for overnight, respectively [35]

#### 2.5 Defects and Etch Pits in Y-123

In order to study the surface and bulk defects of Y-123 single crystal, chemical etching has been applied on the as grown crystals for direct observation the defects [37, 38]. The crystals were grown in a melt containing a flux of excess BaO–CuO [16]. Free- standing crystals show large shiny surfaces of (100)/(010) and (001). The samples used in the following study are over  $2 \times 1 \times 0.5$  mm<sup>3</sup> and aluminum contamination was in the range 0.1–0.2 %. The  $T_c$  of the as-grown crystals was below 80 K, but after annealing in flowing oxygen,  $T_c$  rose to 90 K. The shiny surfaces obtained from as-grown crystals are suitable etching experiment. Three suitable etching solutions have been found, i.e., A (Acetic acid), B (1HNO<sub>3</sub> (or 1HCl) : 4 acetic acid : 4 methanol) and C (1HNO<sub>3</sub> (or 1HCl) : 4 acetic acid (or  $4H_2O$ )).

The formation of etch pits at dislocation sites on a (001) surface depends upon the etching rates. Figure 2.13 shows a schematic representation of the atomic arrangement in Y-123. Early studies [39] have shown that Y-123 terminates with a CuO plane in the (001) direction and this may be related with the observation that the (001) surface is chemically highly active. The lattice strain associated with a

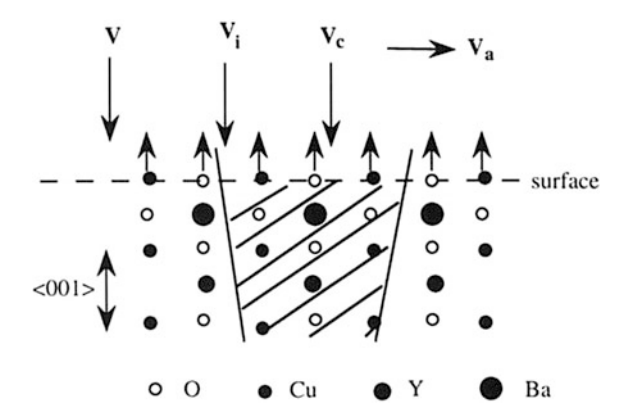
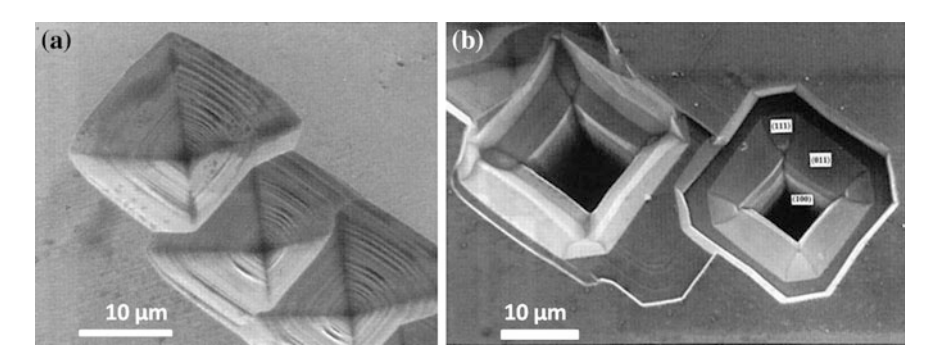


Fig. 2.13 Schematic drawing of the etching process of Y-123 single crystal. V: etch rate normal to surface;  $V_c$  etch rate along dislocation;  $V_a$ : etch rate along surface;  $V_i$ : etch inclined between  $V_c$  and  $V_a$ , *arrows* emanating outwards from atoms indicate the missing bonds of chemically active surface and *shaded area* indicates the surrounding strain field [37]

screw dislocation greatly enhances the rate of etching, so the etching rate  $V_c$  on the strained area is much higher than the etching rate V normal to the unstrained area (as seen in Fig. 2.14b).

Figure 2.14a shows square pyramids of an etch pattern having four-sided walls with steps bounded by  $\{100\}/\{010\}$  and a sharp base. The depth of the pit is 5 µm, approximately measured by optical microscope. The pit of Fig. 2.14b contains several structural features: the triangular regions are assumed to be  $\{111\}$  planes and adjacent  $\{011\}$  with connecting region to be  $\{100\}/\{010\}$ . The centre is a deep square hole whose depth could not be measured by secondary electron microscope. Therefore the shape of base is undetectable, but the hole does not run through to the opposite surface of the crystal. The pits often appear in isolated clumps, shoulder to shoulder and heavily dislocated as tangles and clusters. These square pits are



**Fig. 2.14** Secondary electron micrograph taken at zero tilt, showing the tetragonal structure of the etch pits on the (001) surface produced by solution A after 4 h: **a** square steps bounded by <100>/<010> and **b** octagonal pattern of squares truncated by the <110> edges [37]

truncated by [110] edges in the (001) face. The geometric figure is octagonal, consisting of two intersecting squares at  $45^{\circ}$  rotation. The ratio of the lengths <100>/<110> is  $\sim0.88$ .

After etching, the topography of the originally smooth and shiny surface of an as-grown crystal became rough and consisted entirely of hillocks and etch pits. Figure 2.15a, b show the general features of the (001) surface of the crystal, with square and octagonal patterns originating from neighboring dislocations. Poly-spiral growth hillocks with etch pits at their centre suggest dislocation lines running up and passing through the centre of the growth spiral. As the hillocks grow, their bases spread outward, creating a continuous new layer of the crystal. There are also vicinal-hill type spirals showing square or octagonal-like morphology. The octagonal shape of growth hillock is indicative of the anisotropy in the step advancement velocity along <100>/<010> and <110> directions. The hillocks give evidence for a screw dislocation and suggest that the crystal grows according to the spiral growth mechanism under low supersaturation. These observations are consistent with classical crystal growth theory. Screw dislocations may provide flux pinning centers and determine the limits of the critical current density in single crystals [40].

The density of the spiral hillocks present in the (001) surface is estimated to be  $\sim 5 \times 10^5$  cm<sup>-2</sup>. The growth steps on the (001) surface are more or less parallel to each other, and defined by crystallographic planes. The square steps are bound by the <100>/<010> directions. The truncated squares have octagonal-like steps defined by the <110> direction; <100> and <010> are the strongest and the next-strongest PBC (periodic bond chain) directions. The relatively longer steps, which run along the <110> direction, correspond to the fast growing direction. Large flat terraces can be seen lying adjacent to the steps. This shows that the surface is reasonably clean. Due to the irregularities on the surface, the growth rate of one step can be slowed down and another step can catch up, resulting in a macro-step. Figure 2.15a, b also show the phenomenon of step bunching, and the retardation of the surface of the Y-123 single crystals indicates that two growth mechanisms, i.e. spiral growth and layer-by-layer growth, may both take place, which might be related to the growth conditions and the existence of screw dislocations in the crystals.

An asymmetry of the face on (001) is indicated by the typical etch patterns on the top and bottom surfaces of the same crystal. The top surface (Fig. 2.15a) consisted of screw dislocations and hillocks and the bottom one (Fig. 2.15b) exhibited only hillocks. The most likely candidates for the two surfaces are the Cu–O chain plane and the Ba–O plane along the <001> direction. All the etched samples revealed that the terminating surface on the (001) face of the crystal has polar characteristics and therefore is not symmetrical at the tip and bottom faces.

Characteristically different etch pit morphologies were observed on the (001) face (Fig. 2.15c, d). They are assigned to screw dislocation etch pits, because of the corresponding observation of spiral growth hillocks. Figure 2.15c shows a square pyramid of etch pattern having four-sided walls with different sized steps and square base bounded by <100>/<010>. The steps are believed to by the inner layer of crystal exposed by etching due to the spiral step growth mechanism. The

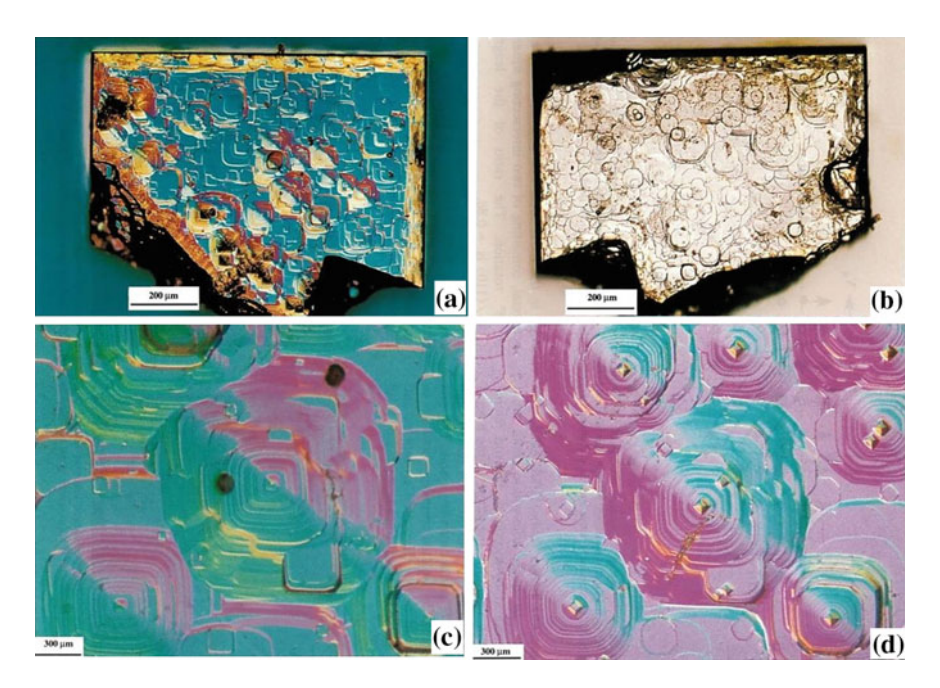


**Fig. 2.15** Screw dislocation etch pits produced by etching solution C for 3 min, by optical microscopy: **a** spiral growth hillocks accompanied by dislocations on the top surface (100); **b** hillocks on the bottom surface (001); **c** screw dislocation from a selected area of **a**; **d** the same area of **c** further etched by solution A for 5 min [37]

width of the step is approximately 3  $\mu m$  on average, as measured by optical microscope. The ratio of the lengths <100>/<010> is ~0.88. It is interesting to observe, as shown in Fig. 2.15d, that the base of the square of all etch patterns spreads outward and is truncated by <110> edges, after a further etching by solution A for 5 min. Comparing with Fig. 2.15c, the square base of Fig. 2.15d is rotated by 45° and bounded by <110>. The reason for this evolution is unknown but may be related to a change of the etching rate along different directions.

Figure 2.16a, b show pits with elliptical shapes and varying sizes, with long and short axes long <100>/<010> and <001> on the (100)/(010) face. As a result the density of the pits is of the order of 10<sup>4</sup> cm<sup>-2</sup> which is lower than that in (001). The etch pits in the as-grown (011) face are similar to those in (100)/(010), demonstrating that etching rates along <100>, <010> and <001> are anisotropic. Unlike screw dislocation etch pits, there are on steps along the wall, since (100)/(010) is of Hopper-like morphology [41] related to a two-dimensional nucleation growth mechanism, different from screw dislocation growth. Figure 2.16b show that two symmetrically smooth faces are divided by a groove lying along <100>/<010> and one sharp end was weakly etched. This is a distorted etch pit, probably caused by the dislocation core inclined to the surface.

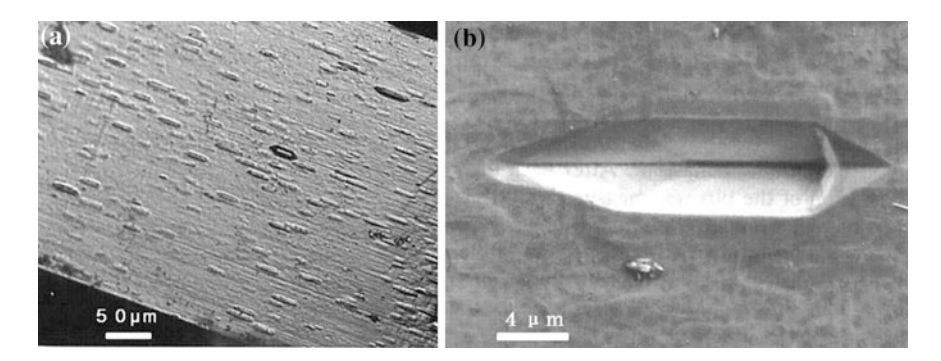


**Fig. 2.16** Typical etch pits in (100)/(010) produced by preferential etching using solution A for 4 h: **a** elliptical etch pit with long and short axes, by optical microscopy and **b** secondary electron micrograph of a distorted etch pit

The size and shape of the pits depend strongly upon the etching behavior. After each etch the dimension of the pits was measured and thus the etch rate determined. Solution A has a very low etch rate and produces a highly selective etching to reveal dislocations with clean and clear patterns. This slow etch rate allows for the formation of small protrusions and reveals the defects with minimum material removal. Solution B and C show a rapid attack and simply dissolve away any surface atoms, revealing both screw dislocations and spiral hillocks. The etch rates suggest that the velocity is anisotropic, with  $V_{a<1.10>} \sim 3.2 \, \mu m/h$  $V_{a<100>}\sim 2.8$  µm/h,  $V_{c<001>}\sim 1.3$  µm/h and  $V_{i<111>}\sim 1.0$  µm/h. These rates did not include the experiment with solutions B and C, whose rates are two orders of magnitude higher. The dimensions of the etch pits can be changed due to the etch rates V<sub>c</sub>, V<sub>a</sub> and V<sub>i</sub>, although the preferential etching at dislocation sites is a very complex phenomenon which dominates the whole etching procedure.

By chemical etching, dislocation etch pits have become visible on the surface of (001), (100)/(010) and (011). In general, pit morphology reflects the major symmetry of the crystal, and pit edges are found to be parallel to the <100>/<010> or <110> crystallographic axes. An understanding of dislocation formation and preferential etching requires detailed knowledge of surface chemical reactivity and surface reconstruction in Y-123.

# 2.6 Flux Growth of Pure and Doped Y-124

Y-124 single crystals with dimensions up to 4 mm were first prepared by a self-flux method under a high oxygen pressure up to 3000 bar at over 1100 °C [9]. This requires special apparatus and safety considerations. Recently, high quality Y-124 single crystals have been grown by using KOH as flux under ambient pressure, after optimized the growth conditions such as applying a stepwise-cooling method, crystals with sizes up to  $1.2 \times 0.5 \times 0.3$  mm<sup>3</sup> were achieved [10, 11].

The growth of Y-124 crystals is complex in the systems Y-123–CuO–KOH or Y-124–KOH, it involve several chemical reactions and processes like synthesis, dissolution and crystallization, as well as evaporation and creeping of molten KOH. Nevertheless, using KOH as solvent, it was found that Y-124 can be synthesized in air/oxygen via the reaction

$$YBa_2Cu_3O_{7-\delta} + CuO + \delta/2O_2 \rightarrow YBa_2Cu_4O_8$$

at a temperature as low as 550 °C. A high fraction (>95 %) of the Y-124 phase was obtained in less than 4 h. The fact is that the high oxidation state,  $Cu^{3+}$  can be stabilized in molten KOH [42, 43] and this favors the formation of Y-124. These results suggest that molten KOH is very effective in accelerating and enhancing the chemical reactions during the formation of Y-124.

The source material used was either a mixture of Y-123 and CuO powders in a molar ratio of 1:1 or Y-124 powders synthesized by a solid-state reaction. Y-124 powder samples were synthesized using high purity Y(NO<sub>3</sub>)<sub>3</sub>·6H<sub>2</sub>O, Ba(NO<sub>3</sub>)<sub>2</sub>, Cu (NO<sub>3</sub>)<sub>2</sub>·2.5H<sub>2</sub>O in a molar ratio of 1:2:4. The mixtures were ground and loaded in an Al<sub>2</sub>O<sub>3</sub> crucible, sintered at 800 °C for 100 h with several intermediate grindings. Y-123 polycrystalline powders were prepared by calcining the mixtures of 1YO<sub>1.5</sub>:2BaCO<sub>3</sub>:3CuO at 880 °C for 2 days for the decomposition of CO<sub>2</sub>. The calcined mixtures were then sintered at 920 °C in flowing oxygen for 2 days with several intermediate grindings.

The crystal growth was carried out in a vertical two heating zone tube furnace which provided a sharp temperature gradient. A schematic drawing of the setup is shown in Fig. 2.17. A total charge of 15–30 g of source materials and KOH with

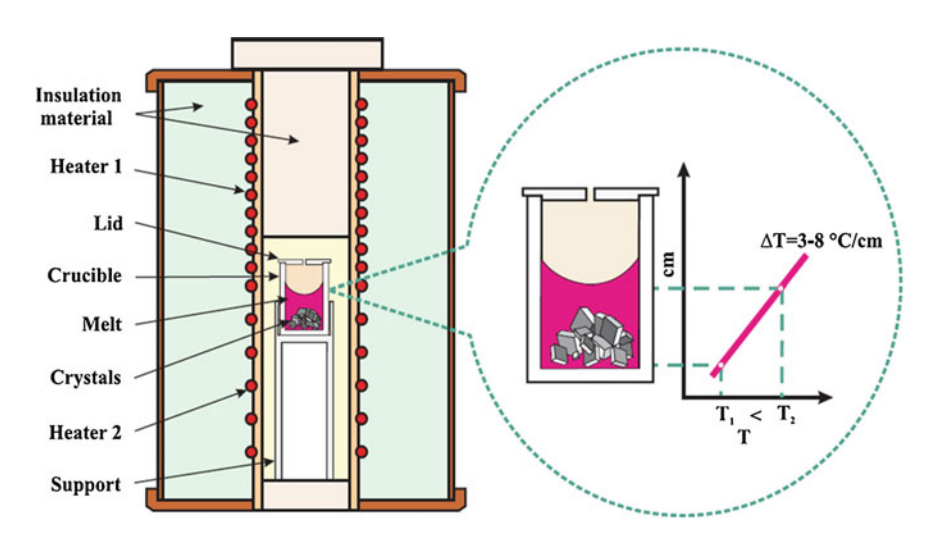


Fig. 2.17 The schematic of the two heating zone apparatus designed with a sharp temperature gradient  $\Delta T$ , ranging from 3–8 °C/cm between 550 and 750 °C for the crystallization temperature [11]

10–95 wt% was loaded in a crucible. The crucible was located at the middle position of the furnace.  $T_1$  and  $T_2$  denote the temperatures at the bottom and middle sites of the crucible, respectively. During growth the heating temperatures increased to about 720 °C for  $T_1$  and 760 °C for  $T_2$ , respectively, and were then maintained for 4 h. Subsequently, the temperatures were slowly decreased to  $T_1$  = 500 and  $T_2$  = 540 °C at a cooling rate of 0.5–5 °C h $^{-1}$ . A sharp temperature gradient  $\Delta T \sim 8$  down to 3 °C cm $^{-1}$  was created during the cooling procedure.

Molten KOH is very corrosive, and many metal oxides are soluble in the wet KOH melt. The ideal crucible material should have no reaction with the source materials. Wetting and creeping phenomena of the solution should be also taken into account in the choice of crucible materials. Five sorts of crucible material (Pt, SnO<sub>2</sub>, MgO, Al<sub>2</sub>O<sub>3</sub> and ZrO<sub>2</sub>) were investigated, as well as the creeping phenomenon. The crucibles containing source materials or/and KOH were heated at temperatures between 550 and 790 °C, and subsequently quenched for the investigation of the creeping behavior of the samples and the reactivity of the crucible materials. The results revealed that ZrO<sub>2</sub> is the optimal crucible material for the growth of Y-124 single crystals in KOH flux, since no corrosion or creeping observed. Al<sub>2</sub>O<sub>3</sub> is another candidate; however, the creeping should be suppressed by a sharp temperature gradient in the growing system.

The melting behavior of the mixtures of Y-124 and KOH was investigated by TG-DTA measurements and observed in a ventilated system [10]. It revealed that Y-124 starting melt in KOH at 494 °C and the Y-124 crystals formed between 550 and 800 °C. Further study [11] indicated that large crystals formed, accompanied by flux evaporation starting from 650 °C. The best solubility and crystal growth conditions are found in the temperature range 640–700 °C, which is the optimal crystallization temperature. At 850 °C, Y-124 entirely decomposed in KOH.

It also found that by the application of a sharp temperature gradient, the number of crystals is remarkably reduced. In addition, a method of stepwise cooling rate was applied to increase the size of crystals, i.e., a low cooling rate of 1 °C h<sup>-1</sup> was applied in the optimal temperature range between 640 and 700 °C. The schematic thermal profile is drawn in Fig. 2.18. As-grown crystals were preferentially found to grow at the bottom of crucible. After cooling, the crucible containing crystals and residual flux was removed from the furnace and quickly dipped into the methanol solvents, followed by rinsing for 0.5–2 h. The crystals were separated and then dried at 80 °C. A typical free crystal is shown in the inset of Fig. 2.19. The crystals exhibit rectangular or square platelet habits with the c-axis normal to the largest plane. Separated crystals were characterized by XRD and Raman spectroscopy, no impurity phases are observed.

Figure 2.19 shows the temperature dependence of the magnetization for a single crystal of Y-124, characterized by ac susceptibility in field-cooling and zero-field-cooling measurements in 10 Oe. A sharp transition temperature  $T_c$  occurs at 82.9 K.

The study of the influence of substitution on superconductivity in Y-124 is of great interest, since the compound is stoichiometric with fixed oxygen content in

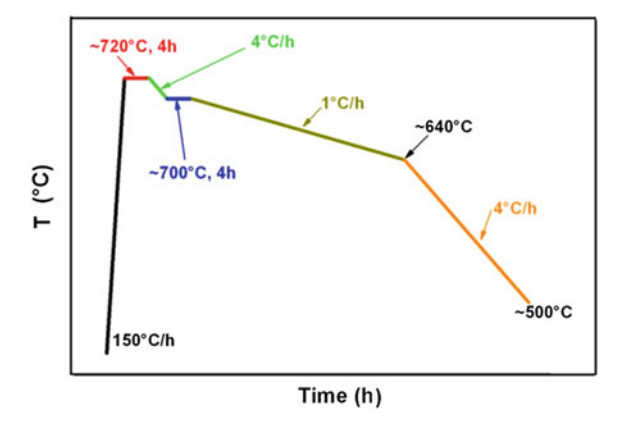
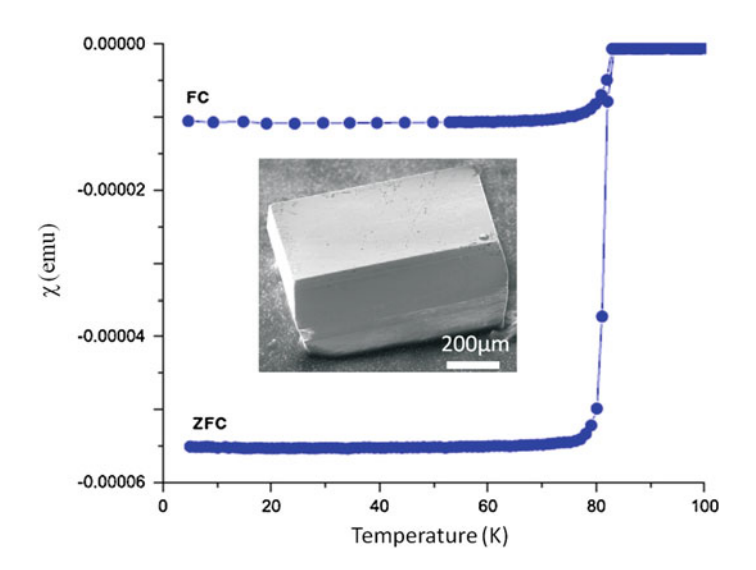


Fig. 2.18 Schematic of the thermal profile used to reduce multi-nuclei and improve the size of crystals [11]



**Fig. 2.19** Field-cooled and zero-field-cooled magnetization as a function of temperature for a Y-124 single crystal. Inset is a typical Y-124 single crystal [11]

the double Cu–O chain. This is unlike Y-123 with a single Cu–O chain, where a small variation of oxygen  $(\delta)$  can strongly influence on its superconductivity.

The crystals doped with Ca, Zn and Ni have been also successfully grown by this method, where various doping concentrations of Ca, Zn and Ni were applied during the growth. It revealed that the value of  $T_c$  increases with increasing Ca content, and reaches a maximum of 91 K at x = 0.12.  $T_c$  slightly decreases with a further increase of the substitution level to x = 0.16. The results are plotted in

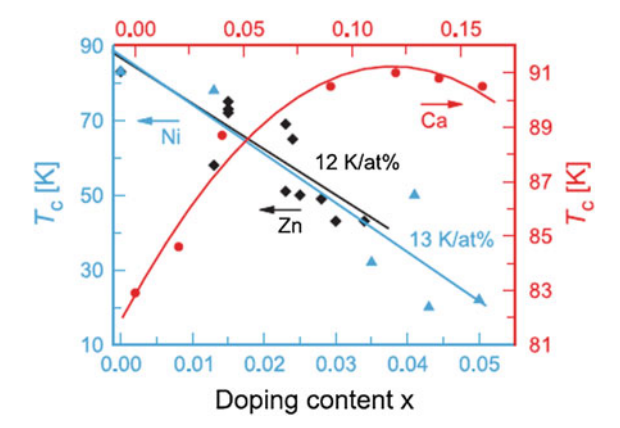


**Fig. 2.20** The plot of Tc values versus with dopant concentration for  $Y_{1-x}Ca_xBa_2Cu_4O_8$  with  $x=0,\ 0.02,\ 0.04,\ 0.09,\ 0.12,\ 0.14$  and 0.16, for  $YBa_2(Cu_{1-x}Zn_x)_4O_8$  with  $x=0,\ 0.015,\ 0.013,\ 0.023,\ 0.024,\ 0.025,\ 0.028$  and 0.034, and for  $YBa_2(Cu_{1-x}Ni_x)_4O_8$  with  $x=0,\ 0.013,\ 0.035,\ 0.041,\ 0.043$  and 0.050, respectively

Fig. 2.20, showing a dome shape of under-, optimal- and over-doped regimes. The doping content of Zn with  $0 \le x \le 0.034$  and Ni with  $0 \le x \le 0.05$  was determined in the final crystal form. Figure 2.20 is the plot of the  $T_c$  values with suppressed rates at 12 K/at % for the Zn and 13 K/at % for the Ni-doped Y-124, respectively. Both dopings show nearly the same suppression rates, but the  $T_c$  is lowered from 83 K for the pure compound to  $\approx 40$  and  $\approx 20$  K for the Zn-and Ni-doped Y-124 single crystals, respectively. Compared to the very broad transition  $T_c$  reported for both pure and doped ceramic samples [44–46], KOH flux growth crystals show a sharper transition with a width  $\Delta$   $T_c < 2$  K. All these properties indicate the high quality of the single crystals.

To summarize, using KOH as flux, the growth of Y-124 single crystals can be easily carried out under ambient pressure at low temperature.

### References

- 1. J.G. Bednorz, K.A. Müller, Z. Phys. B 64, 189–193 (1986)
- P. Dai, B.C. Chakoumakos, G.F. Sun, K.W. Wong, Y. Xin, D.F. Lu, Physica C 243, 201–206 (1995)
- M.K. Wu, J.R. Ashburn, C.J. Tong, P.H. Hor, R.L. Meng, L. Gao, Z.J. Huang, Y.Q. Wang, C. W. Chu, Phys. Rev. Lett. 58, 908 (1987)
- C.T. Lin, S.X. Li, W. Zhou, A.P. Mackenzie, W.Y. Liang, Physica (Amsterdam) 176C, 285 (1991)

- 5. Yuh Shiohara, Akihiko Endo, Mater. Sci. Eng.: R: Rep. 19(1), 1-86 (1997)
- 6. H.W. Zandbergen, R. Gronsky, K. Wang, G. Thomas, Nature 331, 596-599 (1988)
- 7. J. Karpinski et al., Nature 336(6200), 660-662 (1988)
- 8. P. Marsh et al., Nature **334**(6178), 141–143 (1988)
- 9. J. Karpinski, H. Schwer, K. Conder, E. Jilek, E. Kaldis, C. Rossel, H.P. Lang, T. Baumann, Appl. Supercond. 1, 333 (1993)
- 10. Y.T. Song, J.B. Peng, X. Wang, G.L. Sun, C.T. Lin, J. Cryst. Growth 300, 263 (2007)
- 11. G.L. Sun, Y.T. Song, C.T. Lin, Supercond. Sci. Technol. 21(12), 125001 (2008)
- 12. Kunihiko Oka et al., Jpn. J. Appl. Phys. 27, L1065 (1988)
- 13. K. Oka, H. Unoki, J. Cryst. Growth. 99(1), 922-924 (1990)
- 14. H. Murakami et al., Jpn. J. Appl. Phy. **29**(12R), 2720 (1990)
- 15. R.A. Laudise, L.F. Schneemeyer, R.L. Barns, J. Cryst. Growth 85(4), 569-575 (1987)
- 16. C.T. Lin, W. Zhou, W.Y. Liang, Physica C 195, 291 (1992)
- 17. H. Takei, H. Asaoka, Y. Iye, H. Takeya, Jpn. J. Appl. Phys. 30, L1102-1105 (1991)
- 18. M. Nakamura, Y. Yamada, Y. Shiohara, J. Mater. Res. 9, 1946 (1994)
- 19. C.T. Lin, B. Liang, H.C. Chen, J. Cryst. Growth 237-239, 778-782 (2002)
- 20. S. Hosoya, S. Shamoto, M. Onoda, M. Sato, Jpn. J. Appl. Phys. 26, L325 (1987)
- S. Kanbe, T. Hasegawa, M. Aoki, T. Nakamura, H. Koinuma, K. Kishio, K. Kitazawa, H. Takagi, S. Uchida, S. Tanaka, K. Fueki, Jpn. J. Appl. Phys. 26, L613 (1987)
- S. Hikami, S. Kagoshima, S. Kamiyama, T. Hirai, H. Minami, T. Masumi, Jpn. J. Appl. Phys. 26, L347 (1987)
- 23. T. Tamegai, A. Watanabe, I. Oguro, Y. Iye, Jpn. J. Appl. Phys. 26, 1987 (1987)
- J.M. Tarascon, W.R. McKinnon, L.H. Greene, G.W. Hull, E.M. Vogel, Phys. Rev. B 36, 326 (1987)
- 25. S.I. Yoo, R.W. McCallum, Physica C 210, 147 (1993)
- T. Wada, N. Suzuki, T. Maeda, A. Maeda, S. Uchida, K. Uchinokura, S. Tanaka, Appl. Phys. Lett. 52, 1989 (1988)
- 27. M. Daeumling, J.M. Seuntjens, D.C. Larbalestier, Nature 346, 332 (1990)
- M. Tagami, M. Sumida, Ch. Krauns, Y. Yamada, T. Umeda, Y. Shiohara, Physica C 235–240, 361 (1994)
- Ch. Krauns, M. Tagami, M. Nakamura, Y. Yamada, Y. Shiohara, Adv. Supercond. 7, 641 (1995)
- 30. M. Nakamura, H. Kutami, Y. Shiohara, Physica C 260, 297 (1996)
- 31. Xin Yao, Teruo Izumi, Yuh Shiohara, Supercond. Sci. Technol. 16(4), L13 (2003)
- 32. Y. Yamada, Y. Shiohara, Physica C 217, 182 (1993)
- 33. U. Welp, M. Grimsditch, H. You, W.K. Kwork, M.M. Fang, G.W. Grabtree, J.Z. Liu, Physica C 11, 1 (1989)
- 34. C.T. Lin, J. Chrosch, Y. Yan, W.Y. Liang, E.K.H. Salje, Physica C 242, 105 (1995)
- 35. C.T. Lin, A. Kulakov, In situ observation of ferroelastic detwinning of YBCO single crystals by high temperature optical microscopy. Physica C **408**, 27–29 (2004)
- V. Hinkov, S. Pailhès, P. Bourges, Y. Sisid, A. Ivanov, A. Kulakov, C.T. Lin, D.P. Chen, C. Bernhard, B. Keimer, Nature 430, 650 (2004)
- 37. C.T. Lin, J. Cryst. Growth 143(1), 110-114 (1994)
- 38. D. Prabhakaran et al., Physica C 319(1), 99-103 (1999)
- 39. P. Bordet et al., Crystal structure of Y<sub>0</sub>. 9Ba<sub>2</sub>. 1Cu<sub>3</sub>O<sub>6</sub>, a compound related to the high-T<sub>c</sub> superconductor YBa<sub>2</sub>Cu<sub>3</sub>O<sub>7</sub>. 687–689 (1987)
- 40. V.M. Pan, J. Alloy. Compd. 195, 387-394 (1993)
- 41. B.N. Sun, H. Schmid, J. Cryst. Growth 100(1), 297-302 (1990)
- 42. P. Claes, J. Glibert *Molten Salt Techniques*, vol 1, ed. by D.G. Lovering, R.J. Gale (Plenum, New York, 1983), pp 79–108

References 45

- 43. S.L. Stoll, A.M. Stacy, C.C. Torardi, Inorg. Chem. 33, 2761 (1994)
- 44. S. Ohara, M. Matsuda, Y. Watanabe, M. Takata, Appl. Phys. Lett. 59, 603 (1991)
- 45. T. Miyatake, T. Takata, K. Yamaguchi, K. Takamuku, N. Koshizuka, S. Tanaka, K. Shibutani, S. Hayashi, R. Ogawa, Y. Kawate, J. Mater. Res. 7, 5 (1992)
- M. Kawachi, N. Sato, E. Suzuki, S. Ogawa, K. Noto, M. Yoshizawa, Physica C 357–360, 1023 (2001)

# **Chapter 3 Bi-Based High-T<sub>c</sub> Superconductors**

Andrey Maljuk and Chengtian Lin

**Abstract** The growth of crystals of the high- $T_c$  oxide superconductors has been hampered by the complexities of the materials and the lack of their phase diagrams. The most common crystal growth technique adopted for these oxides is the "flux" method, where the starting materials are dissolved in a melt, which is usually formed by excess of CuO,  $Bi_2O_3$  or KCl/NaCl mixture. The crystals are produced by slow cooling of the melt. This method, however, suffers from several drawbacks: (1) crystals are contaminated with a crucible material, (2) crystals are difficult to detach from a solidified melt, (3) crystals contain flux inclusions. In most cases these drawbacks can be overcome by the traveling solvent floating zone (TSFZ) method. Moreover, this method is suitable for growing crystals of incongruently melting compounds and has been thus successfully used to grow large crystals of the high- $T_c$  La<sub>2</sub>Sr<sub>x</sub>CuO<sub>4</sub> and  $Bi_{2+x}$ Sr<sub>2-x</sub>Ca<sub>n-1</sub>Cu<sub>n</sub>O<sub>2n+4+ $\delta$ </sub> (denoted as 2201 for n = 1, 2212 for n = 2 and 2223 for n = 3) superconductors. In this work we report the growth of large and high quality 2201, 2212 and 2223 crystals as well as their characterization.

#### 3.1 Introduction

Since the discovery of high-temperature (high- $T_c$ ) superconductivity (SC) in cuprates by Nobel Prize winners J.G. Bednorz and K.A. Müller in 1986 a tremendous work has been done in synthesis of these materials. Here a crystal growth of high- $T_c$  superconductors plays an extremely important role for the fundamental research because physicists strongly need large size and high quality single crystals to study anisotropic physical properties of these materials. For the Bi-based superconductors, a homologous family with a general formula  $Bi_2Sr_2Ca_{n-1}Cu_nO_v$  where n=1,

A. Maljuk (⊠)

Leibniz Institute for Solid State and Materials Research, Dresden, Germany e-mail: a.malyuk@ifw-dresden.de

C. Lin

Max Planck Institute for Solid State Research, Stuttgart, Germany

<sup>©</sup> Springer International Publishing Switzerland 2016

D. Chen et al., *Growth and Characterization of Bulk Superconductor Material*, Springer Series in Materials Science 243, DOI 10.1007/978-3-319-31548-5\_3

2 and 3 is known, and superconducting temperature, T<sub>c</sub>, strongly varies with the number of CuO<sub>2</sub> layers, n:  $T_c \sim 10$  K (n = 1),  $T_c \approx 80$ –90 K (n = 2) and  $T_c \sim$ 110 K (n = 3). Much attention has been paid to the oxides with n = 2 and 3, namely Bi<sub>2</sub>Sr<sub>2</sub>CaCu<sub>2</sub>O<sub>v</sub> and Bi<sub>2</sub>Sr<sub>2</sub>Ca<sub>2</sub>Cu<sub>3</sub>O<sub>v</sub>, which get the superconducting transition temperatures over the temperature of liquid nitrogen (77 K). At the same time it is worth to mention that the real materials are always nonstoichiometric with respect to both the metallic and oxygen elements. Also, the atomic positions in real crystals structures are well shifted from the "ideal" ones that lead to incommensurate, quasi one-dimensional structural modulations in all Bi-based compounds. All together it makes superconducting properties of single crystals being highly sensitive to the history of samples preparation. From this point a detailed and accurate characterization of as-grown samples becomes very important. In addition our knowledge of the corresponding quaternary Bi<sub>2</sub>O<sub>3</sub>-SrO-CaO-CuO phase diagram is quite insufficient that complicated even more a growth of high quality superconducting single crystals in this system. For example, up to now the details of melting behaviour of Bi<sub>2</sub>Sr<sub>2</sub>CuO<sub>v</sub> and Bi<sub>2</sub>Sr<sub>2</sub>Ca<sub>2</sub>Cu<sub>3</sub>O<sub>v</sub> phases are not well understandable. Also, the quasi two-dimensional crystal structures of all Bi-base oxides make a growth rate highly anisotropic and this tendency dramatically increased from n = 1 to n = 3. Therefore, even nowadays it is very hard to prepare bulk and single-phase crystals of Bi<sub>2</sub>Sr<sub>2</sub>Ca<sub>2</sub>Cu<sub>3</sub>O<sub>v</sub> material. In general, the results of crystal growth of Bi-based superconductors have been published in many papers and even books. Unfortunately, they are well scattered and do not give readers a clear answer on what are the main difficulties in the crystal preparation and characterization of these materials. For example, in many cases Bi-based crystals possess a number of growth imperfections like non-superconducting impurities and intergrowth defects that strongly affect the superconducting properties of these samples. In this Chapter the authors try to collect all known data and acquaint a reader with the main growth approaches in the crystal preparation of Bi-based materials. A special attention was paid on accurate characterization of as-grown single crystals by different chemical and physical methods.

# 3.2 Undoped Bi-2201 Compound

Bi-based superconductors create homologous family of compounds with a different number of CuO planes per unit cell: Bi<sub>2</sub>Sr<sub>2</sub>CuO<sub>y</sub> (n = 1), Bi<sub>2</sub>Sr<sub>2</sub>CaCu<sub>2</sub>O<sub>y</sub> (n = 2) and Bi<sub>2</sub>Sr<sub>2</sub>Ca<sub>2</sub>Cu<sub>3</sub>O<sub>y</sub> (n = 3). Within this family the Fermi energy, resistivity, anisotropy and dimensionality are similar [1], although superconducting temperature,  $T_c$ , varies in a wide range 4 K <  $T_c$  < 110 K. Still the origin of large variation of  $T_c$  remains a major challenge in the modern solid state physics. Also, the interplay between the normal state pseudogap and unconventional superconductivity remains a highly debated issue. Since thermal fluctuations vanish at  $T \rightarrow 0$ , they should be less significant at  $T \sim T_c$  in low- $T_c$  cuprates. Therefore, it is instructive to study superconductivity and pseudogap in cuprates with very low  $T_c$  because it allows the

correct disentanglement of superconducting and pseudgap characteristics. From this point the undoped  $\mathrm{Bi_2Sr_2CuO_y}$  (hereafter Bi-2201) compound becomes the best model system and attracts a lot of interest in the past several years. For example, the low temperature study of high quality Bi-2201 single crystals with  $T_c \sim 4$  K reveals the large disparity of superconducting and pseudogap scales in this material [1] and allows simple and accurate estimation of  $H_{c2}$  without complications typical for other cuprates with higher  $T_c$  [2]. The above mentioned studies give a strong evidence for a paramagnetically limited superconductivity in Bi-2201.

Also, its relatively simple crystallographic structure compared with Bi-2212 and Bi-2223 phases and absence of intergrowth defects offer the unique possibility to study the intrinsic properties of the single CuO<sub>2</sub> plane. The last one is rather important because the single CuO<sub>2</sub> plane gives a single band and a single Fermi surface sheet, avoiding band structure complications originated from two-layered (Bi-2212) or multi-layered (Bi-2223) compounds where there is a pronounced band structure splitting [3]. Thus, it makes much easier to interpret ARPES and STM/STS results for Bi-2201 compound.

# 3.2.1 Material Chemistry

The first member (n = 1) of the homologous family of superconducting compounds Bi<sub>2</sub>Sr<sub>2</sub>Ca<sub>n-1</sub>Cu<sub>n</sub>O<sub>v</sub> is usually named by the nominal stoichiometric composition Bi<sub>2</sub>Sr<sub>2</sub>CuO<sub>v</sub> (Bi-2201 or Raveau phase). The actual composition of the orthorhombic Raveau phase is off-stoichiometric with the partial substitution of Bi for Sr. It forms  $Bi_{2+x}Sr_{2-x}CuO_v$  solid solution with  $0.15 \le x \le 0.4$  in air [4]. At the same time the fully stoichiometric Bi-2201 compound is an insulating phase with a monoclinic cell: a = 24.473 Å, b = 5.4223 Å, c = 21.959 Å and  $\beta = 105.40^{0} \text{ [5]}$ . The structure of this compound contains stepped (CuO<sub>2</sub>) layers, while the SC Raveau phase consists of infinite (CuO<sub>2</sub>) planes. In the literature the superconducting off-stoichiometric Raveau phase is often referred to as the Bi-2201 phase and this has given rise to a certain amount of confusion. So, it is necessary to separate SC (T<sub>c</sub> < 10 K) Bi-2201 phase which is always non-stoichiometric from the fully stoichiometric insulating Bi-2201 compound. The last one is often named as the "collapsed" phase because it has a c-axis which is 1 Å shorter than that of superconducting Bi-2201 material. The phase stability of Bi<sub>2+x</sub>Sr<sub>2-x</sub>CuO<sub>v</sub> solid solution was studied at 850 °C in air and at 740 °C in oxygen [4]. It was found that the Bi<sub>2</sub>  $_{+x}$ Sr<sub>2-x</sub>CuO<sub>v</sub> region of existence is limited to the range 0.15  $\leq x \leq$  0.4 in air (850 ° C). For  $0.0 \le x \le 0.15$  all the samples were multi-phases containing the Raveau phase, the "collapsed" phase and undefined impurity phase in a small amount. Superconductivity with T<sub>c</sub> about 6-8 K was observed for multi-phases samples only with nominal compositions x = 0.05 and 0.10. In oxygen (740 °C) the stability region of the Rayeau phase was extended to  $0.0 \le x \le 0.4$  although no SC transition was detected. In the range  $0.0 \le x \le 0.15$  all the samples showed the metallic-like type of conductivity, while in the range  $0.2 \le x \le 0.4$  they exhibited

semiconducting behaviour. At the same time the synthesis of nominally stoichiometric composition at 800 °C in nitrogen resulted in nearly pure "collapsed" phase. Moreover, the annealing of Raveau phase at 600 °C in nitrogen led to the phase decomposition. Thus, the stability of Raveau phase enhanced with oxygen pressure increasing while the stability of "collapsed" phase reduced. It shows the role of oxygen pressure on thermal stability of superconducting Bi-2201 material which is important for the practical crystal growth.

It is worth to mention that orthorhombic Bi-2201 phase has a well defined structural modulation which is caused by the incommensurability between the (BiO) layer and the perovskite block. This mismatch is reduced by cooperative atom displacements from the average positions and by incorporation of extra oxygen in the (BiO) layer. The modulated structure is then formed. Therefore, one could say that the modulated structure originates from the presence of extra oxygen in BiO planes. The modulation vector of the Bi-2201 phase has two components along b and c directions:  $q = b_s b + c_s c$ , where  $b_s$  and  $c_s$  parameters varies with x in Bi<sub>2+x</sub>Sr<sub>2-x</sub>CuO<sub>y</sub>. For x = 0.20 typical values of  $b_s$  and  $c_s$  are 0.21 and 0.61, respectively [6]. Incommensurate modulation causes satellites in the diffraction patterns. In the case of X-ray diffraction these satellites often overlap with the main reflections [4] that complicated peaks indexing.

# 3.2.2 Phase Diagram

All known compounds existing in the Bi<sub>2</sub>O<sub>3</sub>–SrO–CaO–CuO quaternary system at 850 °C in air are shown on Fig. 3.1. Numerous articles have been published on phase equilibria of Bi-based superconducting compounds in the sub-solidus region, but there are only a few papers describing the solid-liquid equilibria in this system.

**Fig. 3.1** Compounds in the Bi<sub>2</sub>O<sub>3</sub>–SrO–CaO–CuO system at 850 °C in air

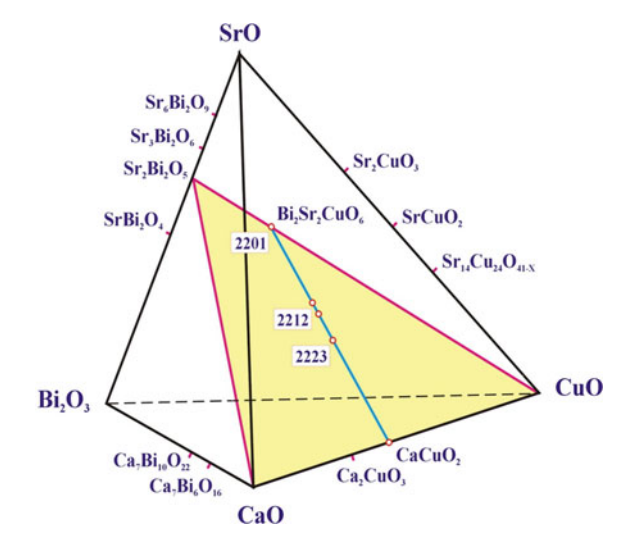
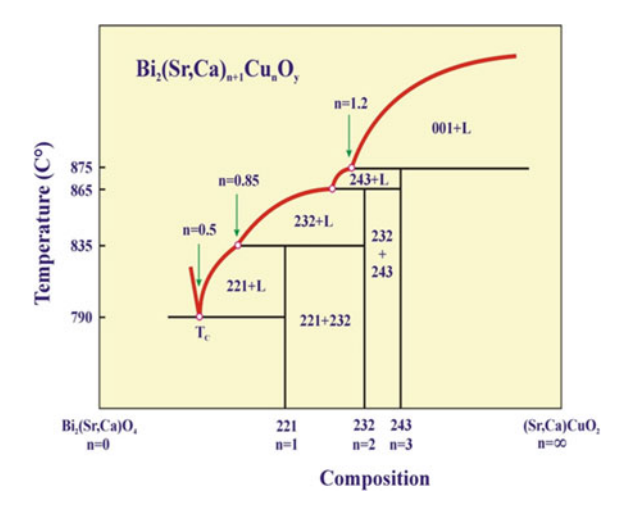


**Fig. 3.2** The pseudo-binary Bi<sub>2</sub>(Sr, Ca)O<sub>4</sub>–(Sr, Ca)CuO<sub>2</sub> phase diagram in air [7]. Reprinted with permission from Elsevier. All rights reserved



The most early publication studied melting behaviour of Bi-2201 phase was done in 1991 [7].

In-situ observations of samples melting and solidification were carried out by high-temperature optical microscope using the MgO plate. Utilizing of MgO container avoids the melt creeping out effect which is the serious problem for  $Al_2O_3$  and Pt crucibles. The authors [7] in-situ observed the incongruently melting of Ca-doped Bi-2201 phase at 865 °C in air according to the reaction  $Bi_2(Sr, Ca)_2CuO_y$  (solid)  $\rightarrow Bi_2(Sr, Ca)_3Cu_2O_y$  (solid) + Liquid. Based on these results the pseudo-binary phase diagram of  $Bi_2(Sr, Ca)O_4$ –(Sr, Ca)CuO<sub>2</sub> system was proposed as shown on Fig. 3.2.

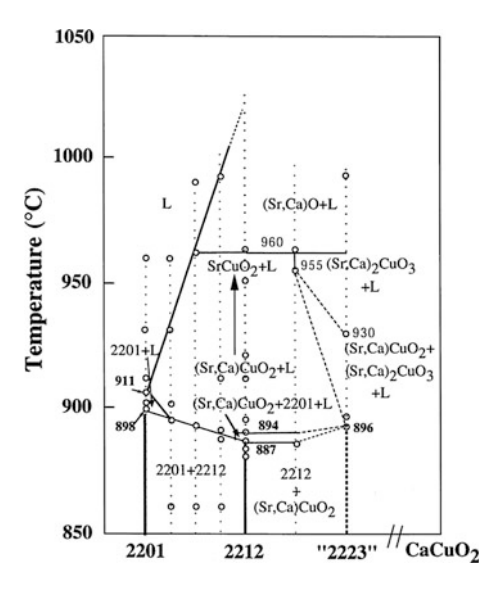
Unfortunately, this phase diagram gives no information of melting behaviour of the pure (Ca-free) Bi-2201 material. Much more detailed investigation was done in 1998 by another Japanese group [8]. The authors applied the unique in-situ facility which combined both high-temperature optical microscope and high-temperature X-ray diffraction units for the Bi<sub>2</sub>Sr<sub>2</sub>CuO<sub>y</sub>–CaCuO<sub>2</sub> system investigation. They directly observed melting and solidification processes of samples with the nominal Bi<sub>2</sub>Sr<sub>2</sub>CuO<sub>y</sub> composition synthesized at 840 °C in air. In parallel they monitored the sample composition by in-situ high-temperature X-ray diffraction although its resolution at temperatures above 600 °C was much worse compared with a standard resolution at room temperature. The results are shown on Fig. 3.3.

According to their data the partial melting of Bi-2201 sample starts at 898 °C, while the remaining solid was still Bi-2201. This mixed state was found to be stable at this temperature at least for 24 h but has a tendency to transform very slowly into SrCuO<sub>2</sub> and liquid after keeping for several days according to the reaction:

$$\text{Bi-2201} \overset{898 \, ^{\circ}\text{C}}{\longrightarrow} \text{Bi-2201} + L \, \left( \rightarrow \text{very slowly SrCuO}_2 + L \right) \overset{911 \, ^{\circ}\text{C}}{\longrightarrow} L$$

Nevertheless, only Bi-2201 phase was found in the quenched samples. Thus, it is not well understandable whether the  $SrCuO_2 + L$  state is the truth equilibrium or

Fig. 3.3 Pseudo-binary phase diagram of the Bi<sub>2</sub>Sr<sub>2</sub>CuO<sub>y</sub>–CaCuO<sub>2</sub> system in air [8]. Reprinted with permission from Elsevier. All rights reserved



not, because this transformation is too sluggish. A complete sample melting was observed above 911 °C based on the results of in-situ optical microscope and X-ray diffraction sample monitoring. From the thermodynamic point it is rather hard to interpret the above mentioned results because Bi-2201 phase can co-exist with itself and liquid under non-equilibrium conditions only (if initial composition was pure Bi-2201 phase). So, the following peritectic reaction seems to be truly equilibrium:

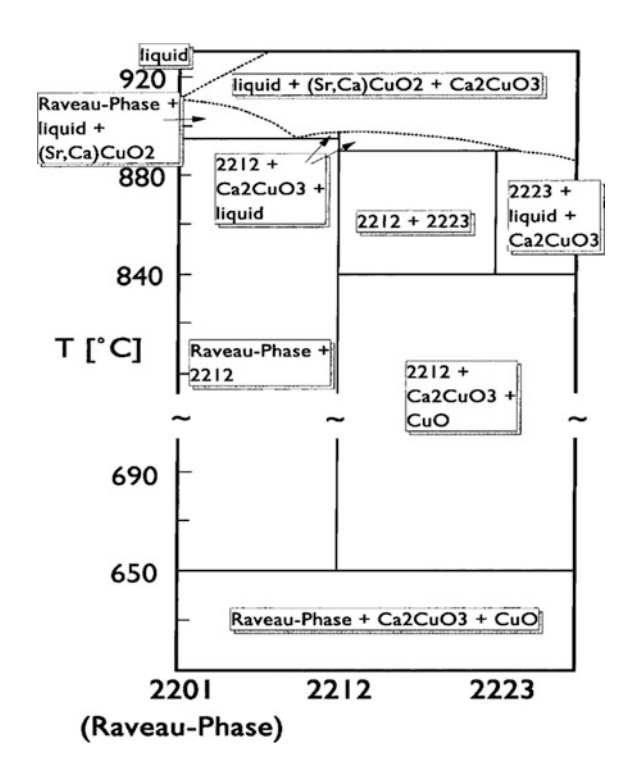
$$Bi-2201 (solid) \xrightarrow{898 {}^{\circ}C} SrCuO_2 (solid) + Liquid$$

However, it is difficult to explain why only Bi-2201 phase was detected in quenched samples because the reversed peritectic reaction is always not completed for any fast cooling process. Also, the nominally stoichiometric Bi-2201 sample synthesized in air has to contain at least three different phases: Raveau phase, "collapsed" phase and a very small quantity of impurity phase as it has been already discussed in Sect. 3.2.1. Thus, actually multi-phases samples were studied in [8] that complicated drastically the interpretation of these experiments. It means that a single phase Bi-2201 material (Raveau phase) has to be re-investigated in future because the nature of melting behavior plays the key role in growth of large-size and high-quality Bi-2201 single crystals.

Another Bi<sub>2</sub>O<sub>3</sub>–SrO–CaO–CuO phase diagram depicted on Fig. 3.4 was proposed in 2000 [9].

There are several obvious and serious contradictions between all published phase diagrams. One possible reason of the observed discrepancy may be caused by a difference in the inspection methods. Authors of [7, 9] determined phase compositions of quenched samples by X-ray diffraction at room temperature assuming that room temperature composition corresponded more or less to phase composition at

Fig. 3.4 Schematic presentation of phase diagram [9] within the range between Bi-2201 and Bi-2223 phases. Reprinted with permission from Cambridge University Press. All rights reserved



high temperatures. At the same it was demonstrated in [8] that a precipitated phase stable at high temperatures often rapidly transformed into another one during even very fast cooling. In any case this discrepancy is a good motivation for the research society for further detailed re-examination of Bi<sub>2</sub>O<sub>3</sub>–SrO–(CaO)–CuO system.

#### 3.2.3 Flux Growth

There are only a few reports on Bi-2201 crystal growth using either self-flux (CuO-based flux) [10] or KCl-flux [11] methods. Growth of thin plate-like crystals of Bi-2201 has been succeeded, although no reproducible superconductivity was observed. The typical self-flux growth experiment is the following [12]: the mixture of the starting materials of Bi<sub>2</sub>O<sub>3</sub>, SrCO<sub>3</sub> and CuO with typical purity of 4 N was ground and fired at 790–820 °C for 12 h several times. The powder products were melted in Al<sub>2</sub>O<sub>3</sub> crucible at 950–1000 °C for 3–5 h, then cooled slowly to 850–880 °C at a rate of  $\sim 1–2$  °C/h, followed by a furnace cooling to room temperature. The crystal platelets were removed mechanically after breaking the crucibles.

Usually flux-grown crystals always show several serious drawbacks [13]: (1) contamination due to the chemical reaction between melt and crucible materials,

such as  $Al_2O_3$  and Au at high temperatures above 900 °C; (2) flux inclusions (mainly CuO) in as-grown crystals; (3) small crystal size (<2 mm) with typical thickness along c-axis less than 0.1 mm; (4) difficulties in mechanical removing crystals from the remaining flux without damage for self-flux technique and (5) a small yield of the growth. Also, for the KCl-flux the possibility of  $K^+$  and  $Cl^-$  ions incorporation has to be taken into account. Another significant problem is that flux-grown samples demonstrate often poor reproducibility of superconducting properties [13].

For example, Bi-2201 crystals were grown by CuO flux method in Zr(Y)O<sub>2</sub> (YSZ), Al<sub>2</sub>O<sub>3</sub> and gold crucibles in [14]. The superconducting properties of as-grown crystals prepared in Al<sub>2</sub>O<sub>3</sub> crucibles were not reproducible. A few of crystals showed a resistive SC transition, but none showed significant evidence of magnetic shielding in ac susceptibility measurements. In contrast, the superconducting properties of crystals grown in either YSZ crucibles or gold crucibles were reproducible and both resistivity and ac susceptibility measurements indicated bulk superconductivity. The authors performed very accurate chemical analysis of crystal compositions using spark-source mass spectroscopy. The Al was found in crystals grown in alumina crucibles but at very low levels of 10–50 ppm. At the same time crystals prepared in YSZ containers had larger concentrations of both Zr (20–70 ppm) and Y (50–120 ppm). All crystals grown in gold crucibles showed no Au contamination (<5 ppm). At present it is not well understood why such small quantity of Al has such a dramatic effect on T<sub>c</sub>. Again, as-grown crystals were quite small and typically  $5 \times 5 \times 0.02$  mm<sup>3</sup> in size.

An interesting result was obtained in [15]. The authors applied micro-pulling down technique to grow free-standing Bi-2201 fibers. Nearly pure-phase (more than 90 %) Bi-2201 fibers could be obtained at pulling rate 0.08 mm/min in air. The grown fibers had a regular shape with uniform diameter around 1 mm and different lengths up to 8 cm which was limited only by the Pt crucible size and quantities of starting materials. The fibers were composed of plate-like crystals with thickness up to 10  $\mu m$  oriented along the pulling direction which was parallel to c-axis. Small and thin crystals could be cleaved from these fibers demonstrating the record value of  $T_{\rm c} \sim 20~{\rm K}$  for single crystalline and powder samples.

# 3.2.4 Floating Zone (FZ) Growth of Large Crystals

Most of disadvantages associated with the flux-method could be overcome by using the crucible-free Floating Zone (FZ) technique which has been successfully employed for the crystal growth of other high-T<sub>c</sub> superconductors like, for example, (La, Sr)<sub>2</sub>CuO<sub>4</sub> [16] and Bi<sub>2</sub>Sr<sub>2</sub>CaCu<sub>2</sub>O<sub>y</sub> [17]. The first Bi-2201 crystals prepared by FZ method were either non-superconducting [18] or needle-like [19]. All attempts to introduce the superconductivity by oxygen/argon annealing were failed. Also, the size of superconducting but needle-like samples gives no chance to perform most of physical measurements. The first superconducting and large size Bi-2201 samples suitable even for neutron inelastic experiments have been grown in 2001 [13].

#### 3.2.4.1 Crystal Growth and Characterization

The high-quality and bulk Bi-2201 samples have been prepared as follows in [13]. Feed rods for the growth experiments were made by the conventional solid state synthesis. Starting compositions of  $Bi_{2+x}Sr_{2-y}CuO_z$  were varied in the range of  $0 \le x \le 0.35$  and  $0 \le y \le 0.30$  to study the effect of composition on crystal size and superconductivity. Powder materials of 99.99 % purity  $Bi_2O_3$ ,  $SrCO_3$  and CuO were mixed with ethanol in agate mortar, dried and then pre-heated at 750 °C for 48 h in high-density  $Al_2O_3$  crucibles. The pre-heated mixture was pulverized carefully into fine powder and put into a thin rubber tuber with a diameter of 7–8 mm and a length of about 10 cm, then pressed hydrostatically into a straight feed rod under pressure of ~70 MPa. Finally, the rods were sintered at 840 °C for 48 h in flowing oxygen. Single crystals growth was carried out in a 4-mirror type image furnace with infra-red (IR) radiation equipped with four 300 W halogen lamps. The sketch of the image oven is shown on Fig. 3.5. The high temperature gradients (~150–300 °C/cm) required for the stable molten zone (MZ) maintaining can be ensured by proper focusing of all lamps at the common focus point.

The crystal growth was done in the enclosed quartz tube where the controlled oxygen pressures can be applied. As-sintered rod was divided into two pieces, and the shorter one ( $\sim$ 2 cm in length) was used as a seed and the longer as the feed rod. Both feed and seed rods were placed coaxially in the center of a silica tube. Prior to the crystal growth the high density feed rod ( $\sim$ 90 % of the crystal density) was obtained by pre-melting of as-sintered rod at a rapid rate of 27 mm/h. The authors [13] found that the quality of pre-melted feed rods play the key role in a successful growth run. Because using of high dense rods stabilized the molten zone and

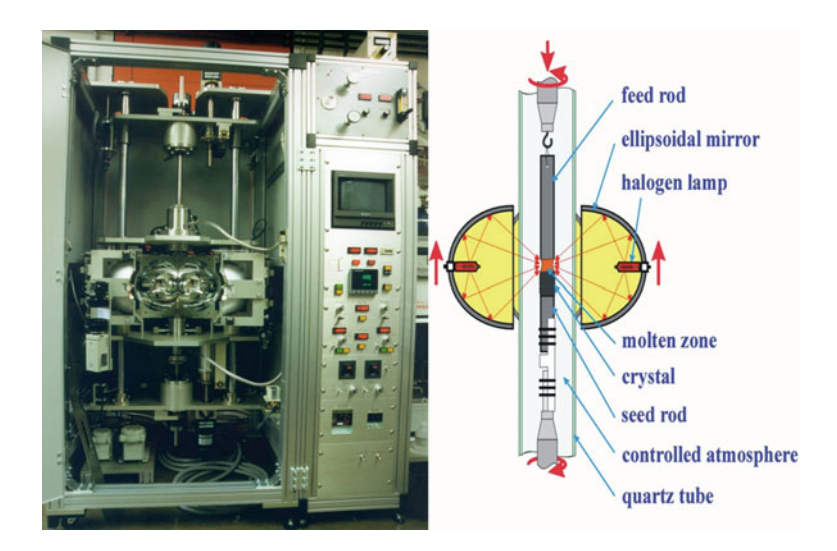


Fig. 3.5 Sketch of the four-mirror type image furnace with IR heating produced by CSI (Japan)

suppressed the liquid penetration onto the feed rod. The last effect usually terminated a TSFZ growth experiment in case of using low dense rods with density less than 75–80 %. Thus, a straight, high dense, long and equal-diameter feed rod is highly required to stabilize the molten zone over long growth periods (more than 24 h). Slow growth rates of 0.5-1.0 mm/ were applied during the growth to achieve faster grain selection. Both feed and seed rods were counter rotated (15–30 rpm) to ensure effective mixing and uniform temperature distribution in the molten zone. The oxygen pressure, ranging from 1 to 10 bars, was applied throughout pre-melting and crystal growth procedures. Typical as-grown Bi-2201 ingot is shown on Fig. 3.6a where a large facet parallel to the growth direction can be clearly seen. The facet was identified to be (001) by Laue back scattering experiment. The Bi-2201 crystals (Fig. 3.6b) cleaved from this ingot demonstrate large a-b planes and thickness up to 3 mm in the c-axis direction.

It was revealed that the crystal habit and size are strongly affected by the starting composition and much less than by oxygen pressure during pre-melting and growth processes (see Table 3.1). Also, the increasing of oxygen pressure leads to the less stable molten zone. No significant evaporation of Bi or Cu was observed independent from applied  $\rm O_2$  pressure. Only needle-like samples were prepared from Bi stoichiometric and nearly-stoichiometric starting compositions (ingot nos. 1–3). On the contrary, from Bi-rich compositions the large plate-like crystals were obtained (ingots nos. 4–10).

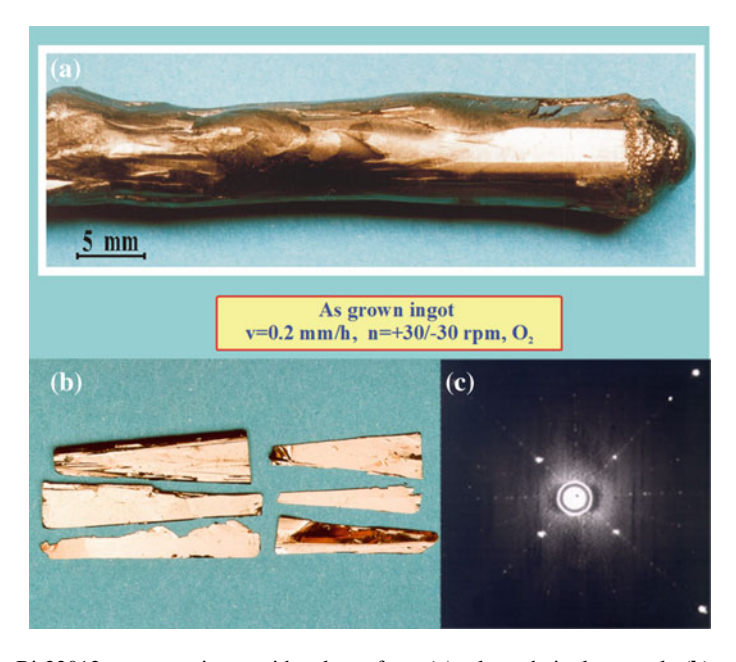


Fig. 3.6 Bi-22012 as-grown ingot with a large facet (a), cleaved single crystals (b) and X-ray Laue picture (c) taken from this facet [13]

Ingot number	Starting composition	Crystal composition	Growth rate, mm/h	Oxygen pressure, bar	Crystal habit	T <sub>c</sub> , (K)
1	Bi <sub>2.0</sub> Sr <sub>2.0</sub> Cu <sub>1.0</sub> O <sub>y</sub>	Bi <sub>2.11</sub> Sr <sub>2.16</sub> CuO <sub>y</sub>	0.5-1.0	2.0	Needle-like	ns
2	Bi <sub>2.1</sub> Sr <sub>1.9</sub> Cu <sub>1.0</sub> O <sub>y</sub>	Bi <sub>2.19</sub> Sr <sub>1.95</sub> CuO <sub>y</sub>	0.8	2.0	Needle-like	6.2
3	Bi <sub>2.1</sub> Sr <sub>1.9</sub> Cu <sub>1.0</sub> O <sub>y</sub>	Bi <sub>2.21</sub> Sr <sub>1.89</sub> CuO <sub>y</sub>	0.5-0.6	6.0	Needle-like	5.5
4	Bi <sub>2.2</sub> Sr <sub>1.8</sub> Cu <sub>1.0</sub> O <sub>y</sub>	Bi <sub>2.37</sub> Sr <sub>1.95</sub> CuO <sub>y</sub>	0.6	1.0	Plate-like	ns
5	Bi <sub>2.2</sub> Sr <sub>1.9</sub> Cu <sub>1.2</sub> O <sub>y</sub>	Bi <sub>2.20</sub> Sr <sub>2.01</sub> CuO <sub>y</sub>	0.3	3.0	Plate-like	5.0
6	Bi <sub>2.2</sub> Sr <sub>1.9</sub> Cu <sub>1.0</sub> O <sub>y</sub>	Bi <sub>1.93</sub> Sr <sub>1.66</sub> CuO <sub>y</sub>	0.5	10.0	Plate-like	3.5
7	Bi <sub>2.3</sub> Sr <sub>1.7</sub> Cu <sub>1.0</sub> O <sub>y</sub>	Bi <sub>2.35</sub> Sr <sub>1.81</sub> CuO <sub>y</sub>	0.8-1.0	2.5	Plate-like	ns
8	Bi <sub>2.3</sub> Sr <sub>1.7</sub> Cu <sub>1.0</sub> O <sub>y</sub>	Bi <sub>2.32</sub> Sr <sub>1.86</sub> CuO <sub>y</sub>	0.5	1.5	Plate-like	ns
9	Bi <sub>2.35</sub> Sr <sub>1.98</sub> Cu <sub>1.0</sub> O <sub>y</sub>	Bi <sub>2.32</sub> Sr <sub>2.17</sub> CuO <sub>y</sub>	0.6	3.0	Plate-like	8.5
10	$Bi_{2.35}Sr_{1.98}Cu_{1.0}O_{y}$	Bi <sub>2.38</sub> Sr <sub>2.15</sub> CuO <sub>y</sub>	0.5	8.0	Plate-like	7.1

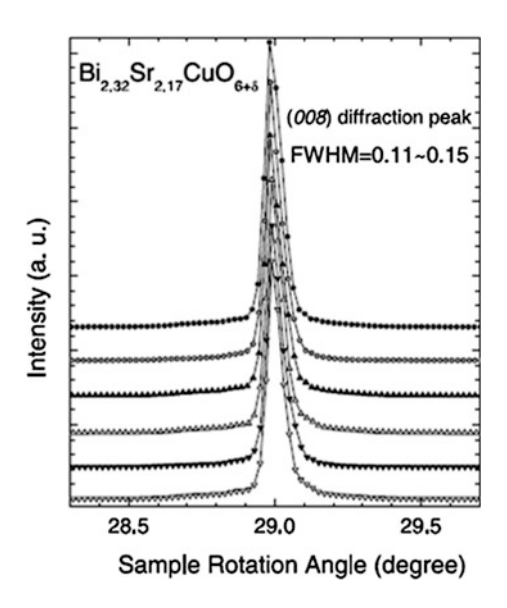
Table 3.1 Growth conditions, compositions and superconductivity of Bi-2201 crystals

ns Non-superconducting down to 2.0 K

The molten zone became unstable for the growth rates less than 0.5 mm/h. When the rate was less than 0.3 mm/h, the growth was frequently terminated by the MZ collapse. Growth rates of 0.5–1.0 mm/h were found to be suitable to maintain a relatively stable MZ and meanwhile to develop a planar growth interface throughout the entire growth.

X-ray rocking curves were measured in order to identify the crystal mosaicity in the (a, b) plane. Figure 3.7 demonstrates the results of these measurements done on three pieces cleaved from one thick  $\mathrm{Bi}_{2.32}\mathrm{Sr}_{2.17}\mathrm{CuO}_{\mathrm{y}}$  crystal (  $\sim$  1.5 mm thickness).

Fig. 3.7 X-ray rocking curves around the (008) Bragg peak measured on three pieces cleaved from one crystal. Both sides of these three samples were measured [13]



Crystal	Bi/Sr	Oxygen	a, (Å)	b, (Å)	c, (Å)	c, (Å),
composition	ratio	pressure, bar				sc
Bi <sub>1.93</sub> Sr <sub>1.66</sub> CuO <sub>y</sub>	1.16	10.0	5.414	5.319	24.248	24.250
			(1)	(8)	(5)	(8)
Bi <sub>2.21</sub> Sr <sub>1.89</sub> CuO <sub>y</sub>	1.17	6.0	5.314	5.399	24.363	24.3663
			(8)	(7)	(7)	(2)
Bi <sub>2.32</sub> Sr <sub>2.17</sub> CuO <sub>y</sub>	1.07	3.0	5.337	5.378	24.433	24.436
			(6)	(1)	(8)	(1)

Table 3.2 Crystal compositions and lattice parameters from powder XRD data

sc Single crystal XRD results

All peaks are quite narrow with FWHM =  $0.12^{\circ}$ – $0.15^{\circ}$ , indicating the perfect crystal quality in the *c*-direction. Also neutron diffraction experiments demonstrated high quality of thick Bi-2201 crystals ( $\sim 3$  mm thickness) with mosaicity less than  $3^{\circ}$ , and crystals with  $\sim 1$  mm thickness possess a mosaicity of  $1^{\circ}$ .

In order to check the phase purity of as-grown samples, a number of crystals from each ingot were ground into powders for XRD measurements. All reflections can be indexed to the pseudo- tetragonal structure and lattice parameters are listed in Table 3.2. No trace of impurity phases was found in these samples. At the same time ingot nos. 1, 2 and 7 contain a small quantity of a secondary phase identified as a  $Sr_{14}Cu_{24}O_{41}$ .

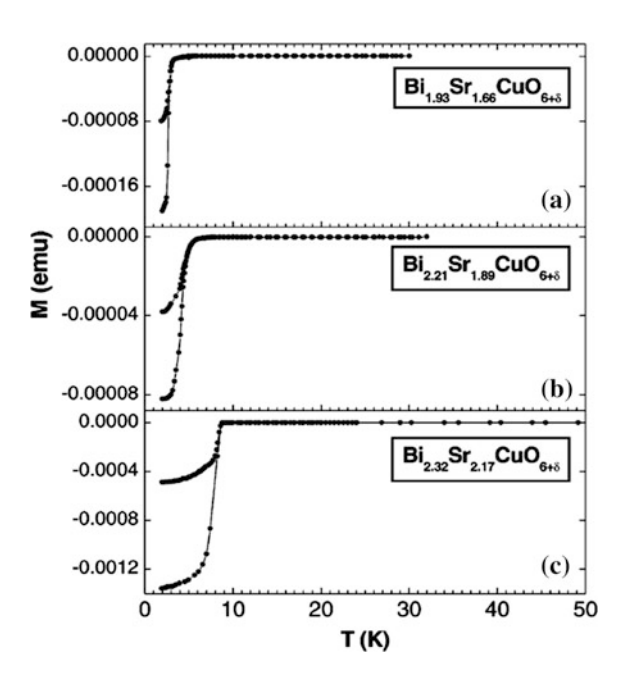
The formation of impurity phases strongly depends on (i) history of the sample preparation; (ii) degree of Sr-deficiency and (iii) applied oxygen partial pressure.

#### 3.2.4.2 Superconductivity

The results of magnetic susceptibility measurements exhibit superconductivity in six of 10 as-grown ingots. All superconducting crystals were prepared under oxygen pressure (2–10 bars). Usually 3–5 pieces of crystals cleaved from different portions of each ingot were measured. The results show that all samples cleaved from the one ingot demonstrate nearly the same  $T_c$ . Depending from starting composition and oxygen pressure  $T_c$  varies from 3.8 to 8.5 K. Figure 3.8 presents the superconducting transitions for the different samples  $Bi_{1.93}Sr_{1.66}CuO_y$ ,  $Bi_{2.21}Sr_{1.89}CuO_y$  and  $Bi_{2.32}Sr_{2.17}CuO_y$ , respectively. All transitions are quite sharp with  $\Delta T_c < 1.0$ –1.5 K. For the crystals grown from the same composition,  $T_c$  decreases with increasing oxygen pressure, suggesting that as-grown samples are in the overdoped region.

Nevertheless, the oxygen pressure of 2 bar and over was necessary to suppress the formation of "collapsed" phase which usually crystallized in form of needle-like crystals. Also, this non-superconducting "collapsed" phase was always precipitated from the stoichiometric starting composition even under elevated oxygen pressures. Based on these results the superconducting Bi-2201 crystals can be only grown from non-stoichiometric starting compositions under oxygen pressure of 2–10 bars.

Fig. 3.8 Magnetic susceptibility as a function of temperature for as-grown crystals: **a** Bi<sub>1.93</sub>Sr<sub>1.66</sub>CuO<sub>y</sub>, **b** Bi<sub>2.21</sub>Sr<sub>1.89</sub>CuO<sub>y</sub> and **c** Bi<sub>2.32</sub>Sr<sub>2.17</sub>CuO<sub>y</sub>, respectively [13]



It is worth to mention that superconducting Bi-2201 crystals are very stable in air without any sign of sample decomposition and degradation of superconducting properties even stored over years on a desk. The superconducting temperature slightly varies ( $\pm 1~\rm K$ ) with annealing either in oxygen or in argon.

# 3.3 La-Doped Bi-2201

The partial replacement of  $Sr^{2+}$  by large rare-earth elements ( $La^{3+}$ ,  $Nd^{3+}$ ) results in the dramatical increase of  $T_c$  up to 33–36 K for La content x=0.4 in  $Bi_2Sr_{2-x}$   $La_xCuO_y$  compound. The heterovalent substitution of  $La^{3+}$  for  $Sr^{2+}$  in the  $Bi_2Sr_{2-x}$   $La_xCuO_y$  system reduces holes number and thus pushes the system to the hole-underdoped regime. All reports on polycrystalline samples are in a good agreement with each other and reveal a parabolic-like dependence between  $T_c$  and La-content [20, 21]. It is quite interesting that although  $Tl_2Ba_2CuO_y$  and  $Bi_2Sr_2CuO_y$  materials possess very similar crystal structures, they exhibit surprisingly different superconducting transition temperatures (90 K for Tl-2201 and only 4–8 K for Tl-2201. The origin of this dramatic discrepancy was ascribed to the fact that Tl-2201 phase has a complicated incommensurate modulation structure while Tl-2201 phase does not show any modulation feature [22]. Nevertheless, powder Tl-2201 amounts as Tl-2201 with Tl-2201 w

compared with Tl-2201. Thus, the effect of structural modulation in Bi-2201 on superconductivity in this compound is still unclear. And this study requires the availability of high quality single crystals as well as the systematic investigation of La doping on superconducting properties. There are several reports on Flux and FZ growth of Bi<sub>2</sub>Sr<sub>2-x</sub>La<sub>x</sub>CuO<sub>y</sub> material discussed below.

#### 3.3.1 Flux Growth

A few groups have obtained La-doped Bi-2201 crystals using the CuO self-flux method [12, 23] in Pt or Al<sub>2</sub>O<sub>3</sub> crucibles. The typical growth route [12] is as follows: starting materials were weighed in the proportion Bi:Sr:La:Cu = 1.95:2.05-x: x:1.5 with nominal x = 0.05-1.0. The mixture was ground and fired for 1 or 2 times at 810-820 °C for about 20 h. After these pre-reactions, the mixture was well reground and finally put into a cylindrical Pt crucible. The crucible was mounted in a vertical tube furnace, and the powder was melted at 1050-1150 °C for 2-3 h and then cooled quickly to 970-980 °C. After that, the temperature was controlled to decrease very slowly at a rate of 0.8-2.0 °C/h to 850-870 °C. It was found that the crystal growth was performed in this slow cooling process. This was followed by a furnace cooling to room temperature by turning off the power. The crystal platelets were removed mechanically from a solidified melt. The sizes of crystals become generally smaller with the increase of La concentration in the initial mixture. Nevertheless, black and shiny crystals with surface dimensions of  $2 \times 2 \text{ mm}^2$  were obtained. The typical thickness along c-axis was less than 10-20 um. It was found that the actual La content in the crystal was always much higher than the nominal composition when the nominal one was lower than x = 0.6. Also, different crystals picked up from random places in the same crucible showed various La contents. The c-axis decreases with increasing of the actual La concentration demonstrated the perfect linear tendency in the good consistency with the reports on powder samples [20, 24]. The c-axis diminishing with La doping is well understandable because the ionic radius of La<sup>3+</sup> is 1.06 Å while the ionic radius of Sr<sup>2+</sup> is 1.16 Å. It is quite interesting that the Bi<sub>2</sub>Sr<sub>2-x</sub>La<sub>x</sub>CuO<sub>y</sub> crystal with the actual La composition x = 0.8 exhibited an incommensurate modulation in **b**direction while the modulation vector in undoped Bi-2201 crystals had both components along b and c directions (see Sect. 3.2.1). The resistivity measurements found the metallic conductivity in (a, b) plane while it was semiconducting along caxis. At the same time the magnetization measurements never gave 100 % diamagnetic signal suggesting any kind of chemical inhomogeneity in as-grown crystals. No data regarding the possible Pt or Al contamination was given.

An interesting growth approach was realized in [22] for the growth of double-doped  $Bi_{2-x}Pb_xSr_{2-y}La_yCuO_z$  crystals by  $Bi_2O_3$  self-flux method in high density  $Al_2O_3$  crucibles. The starting composition was of the nominal  $Bi_{1.8} + Pb_{0.2}Sr_{1.65}La_{0.35}CuO_z$  with x = 0.1, 0.2, 0.3, 0.4, 0.5. The excess of  $Bi_2O_3$  powder acts as a flux for the growth. Most of the experiments were carried out with 60 g

batches in 50 ml crucibles which were then placed in a vertical furnace with a strong temperature gradient 5-10 °C/cm. Optimum Bi<sub>2</sub>O<sub>3</sub> concentration for the growth was found to be x = 0.4. For sample x = 0.4, the mixture was first heated to 860 °C, where it was stayed for 5 h. Then it was rapidly heated to a maximum soaking temperature 1020 °C, soaked for 5 h so that the mixture could be melted perfectly. The melts were then cooled rapidly to 930 °C, and more slowly to 850 °C at 1 °C/h. When this final temperature was reached, the furnace was turned off and allowed to reach room temperature. With increasing of Bi<sub>2</sub>O<sub>3</sub> flux the soaking temperature is decreased from 1100 °C (x = 0.1) to 990 °C (x = 0.5). The crystals were separated from the solidified flux by cleavage. The largest crystals grown from the melts with x = 0.4 have dimensions up to  $8 \times 4 \times 0.05$  mm<sup>3</sup>. After mechanical cleavage melt-free crystals show smaller dimensions up to  $4 \times 2 \times 0.03$  mm<sup>3</sup>. A number of decahedron-like crystals, pale in colour and transparent comprised of Pb-Sr-Al-O were obtained from the walls of Al<sub>2</sub>O<sub>3</sub> crucible indicating a strong chemical reaction between the melt and the crucible. However, no traces of Al were detected in any of Bi-2201 crystals by XPS analysis. Unfortunately, more precise chemical analysis was not done. Authors believed that although Al can enter the outer of the melts at temperatures above 1000 °C still perfect crystals without Al contamination could be obtained from the center of melts. Nevertheless, no superconductivity was detected in Bi<sub>1,92</sub>Pb<sub>0,08</sub>Sr<sub>1,28</sub>La<sub>0,72</sub>CuO<sub>z</sub> crystal even after annealing at 450–500 °C either in oxygen (up to 10 bars) or under vacuum.

The X-ray rocking curves indicate high crystal quality of as-grown samples with FWHM about 0.5°. The electron diffraction patterns found incommensurate modulation in *a*-direction for Bi<sub>1.92</sub>Pb<sub>0.08</sub>Sr<sub>1.28</sub>La<sub>0.72</sub>CuO<sub>z</sub> crystal.

The  $Bi_2Sr_{2-x}R_xCuO_y$  (R = Nd, Sm) crystals were grown by  $Bi_2CuO_4$  flux in [25]. The gold crucibles were used for two reasons: (i) in contrast to  $Al_2O_3$  container, it does not react with a melt; (ii) its malleability makes crystal recovery easier from solidified melt. The cooling rate was 1 °C/h during the growth in  $\sim 910-970$  °C temperature range. Although large Sm-doped crystals  $9\times3\times0.03$  mm³ in size have been obtained none of them showed superconductivity. Only small  $1.0\times0.4\times0.03$  mm³ in size Nd and Sm doped samples with x=0.4 demonstrate superconductivity at  $T_c=21$  K and 14 K, respectively.

#### 3.3.2 FZ Growth

Thus, flux growth of La-doped Bi-2201 crystals shows several serious drawbacks: (i) La content in crystals is difficult to control; (ii) the size of crystals is very small, particularly along c-axis that restricted many physical measurements; (iii) poor superconducting properties. The first sizable Bi<sub>2</sub>Sr<sub>2-x</sub>La<sub>x</sub>CuO<sub>y</sub> single crystals were grown in a wide range of La doping by FZ technique in [26], but no detailed growth parameters have been given. The most systematic investigation of the FZ growth of La-doped Bi-2201 crystals was done in [27, 28]. According to these publications the growth route is as follows.

The source materials of Bi<sub>2</sub>O<sub>3</sub>, SrCO<sub>3</sub>, La<sub>2</sub>O<sub>3</sub> and CuO of 99.99 % purity were used to prepare feeds and seeds for the floating zone growth. The powders with mole ratios of 2Bi:(2-x)Sr:xLa:Cu, where x = 0.03, 0.06, 0.15, 0.20, 0.25, 0.38, 0.40, 0.60, 0.80 and 0.86, were well mixed by grinding in a ball mill and then loaded into alumina crucibles, respectively. Each mixture was calcined at the temperature of  $\sim$  790 °C for 12–24 h and ground with intermediate grindings. The calcined mixtures were then shaped into cylindrical bars of  $\sim 66 \times 120$  mm by pressing at an isostatic pressure of 200 MPa and sintered at 860 °C for 48 h. For a high-density rod used to growth, the sintered rod was pre-melted at the scanning velocity of  $\sim 27$  mm/h in oxygen flow. The crystal growth was carried out in the optical floating zone furnace (CSI, Japan), and heating power of 4 × 1.5 kW halogen lamps was used. The growth rates of 0.3–1.5 mm/h and oxygen pressures of 1.0-3.0 bars were applied throughout entire growth period. The rotations of 30 rpm for seed and feed were used to the upper (clockwise) and lower (anticlockwise) shafts, respectively. To obtain homogeneous composition distribution along crystal ingot, a pre-melted rod was hanged upside down on the upper shaft holder, which method is helpful to minimize a supersaturation melt occurred and obtain a homogeneous molten zone during growth.

It was found that the growth rate less than 0.5 mm/h leads to the frequent collapse of the molten zone. A higher growth rate ( $\geq 1.0$  mm/h) could significantly increase the stability of the molten zone; however, the size of obtained crystals is reduced as the growth rate is increased. The quenched solid—liquid interfaces of two ingots (grown at rates of 1.5 and 0.5 mm/h) were studied using optical polarized microscope. The crystal grown at the rate of 1.5 mm/h shows more inclusions than that grown at the rate of 0.5 mm/h. EDX analysis indicates that the inclusions are mainly  $Sr_{14}Cu_{24}O_{41}$  phase. Such inclusions resulted in a cellular solid—liquid interface leading to small grains. Therefore, a growth rate of 0.5–0.6 mm/h was chosen because it could both maintain a relatively stable MZ and produce larger crystals.

The low viscosity of undoped Bi-2201 melt makes the molten zone unstable during the growth. Adding La into Bi-2201 compound seems to slightly increase the viscosity of the MZ and, therefore, enhances the stability of the growth. As a result, the obtained La-doped Bi-2201 crystals are larger and thicker, and also exhibit a better morphology compared to the La-free Bi-2201 crystals. In order to study the growth mechanism the authors [27] quenched the molten zone during the growth of x = 0 and 0.43 crystals (x is actual La content), and observed the longitudinal section of the quenched solid—liquid interface under optical polarized microscope.

Several big inclusions were observed on the crystalline side of the solid – liquid interface for x = 0 crystal. However, x = 0.43 crystal exhibited clear planar solid – liquid interface; only a few small inclusions were found on the crystalline side. This result suggests that big inclusions interfere with the growth of larger grains. Adding La into Bi-2201 compounds hinders inclusion formation that leads to the growth of larger crystals. As a result large, black and shiny single crystals platelets sized up to

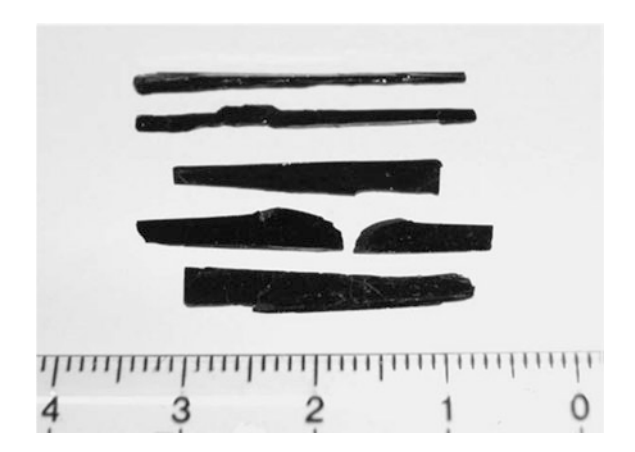


Fig. 3.9 Bi<sub>2.13</sub>Sr<sub>1.55</sub>La<sub>0.43</sub>CuO<sub>y</sub> single crystals cleaved from as-grown ingot [27]

 $\sim 20 \times 5 \times 1 \text{ mm}^3$  were cleaved from ingots prepared under optimal growth conditions (Fig. 3.9).

Also, the melting behaviour of  $Bi_{2.06}Sr_{1.92}La_{0.05}CuO_y$  crystal was investigated by the TG-DTA technique [28] showing the complicated two-step meting process. The melting starts at  $\sim 900$  °C associated with the sharp weigh loss on TG curve. Based on DTA and TG data it was stated that melting ends at  $\sim 940$  °C although the origin of very broad exothermal hump occurred between 940 and 1100 °C is still unclear.

A special attention was paid on La distribution [28] in as-grown ingots. For this purpose the crystal ingots were cut into several parts at an interval of 1 cm along the growth direction. The cut-parts were then cleaved to platelets for the EDX measurement. Six or nine measurements were made on each cleaved platelet and three in the radius direction. The results are shown in Fig. 3.10a–d. At the initial growth part in Fig. 3.10a, the crystal containing tiny grains and/or impurities appears to be a rough surface and seen by naked eye. The grain sizes gradually improved and shiny surface were observed at 6 cm measured from the initial growth position, as shown in Fig. 3.10c, d, respectively. A very large grain was obtained at 6 cm of the ingot. It is indicative of both size and quality of the crystal improved with increasing the ingot length.

The contents of Bi, Sr, La and Cu were determined by averaging EDX data and normalizing them to Cu = 1.00. The results are confirmed by ICP and in agreement with EDX. The compositions of Bi, Sr and La along growth direction are plotted in Fig. 3.11a–c, respectively. The variation of the composition is observed to be significantly higher at the initial parts and tends to be flat starting from 6 cm to the end of the ingot, which composition values are 2.03, 1.52 and 0.44 for Bi, Sr and La, respectively. It indicates that a homogeneous composition could be obtained after growth length reached at approximately 6 cm. This habit is observed to be similar for all crystals grown by FZ method.

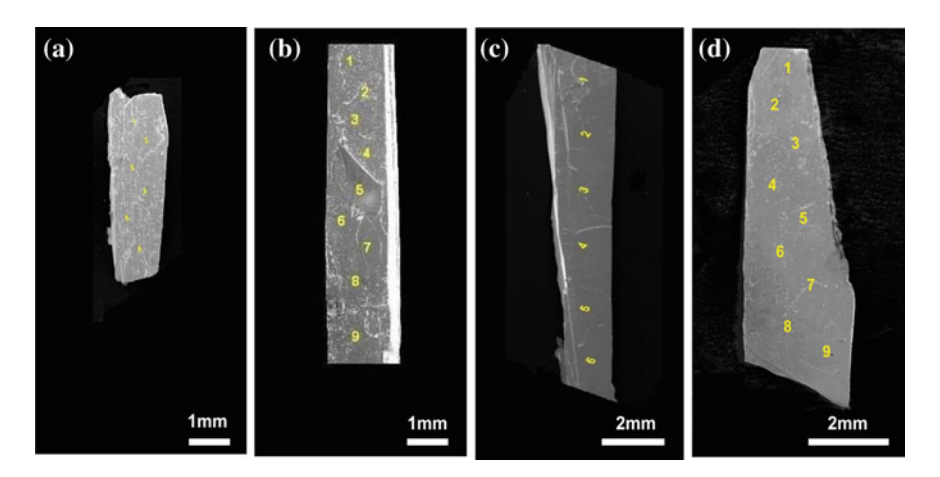


Fig. 3.10 SEM photos of  $Bi_2Sr_{2-x}La_xCuO_{6+\delta}$  (x = 0.44) crystal platelets obtained from the beginning to the end parts along the crystal growth direction. The numbers denote the EDX measurement spots. a Massive impurities and multi-nuclei visible at the beginning of 2 cm grown part, **b** The quality improved starting at 4 cm, **c** Shiny surface with homogeneous composition obtained at 6 and **d** 8 cm grown part of the crystal ingot [28]

The structure of cleaved crystals was identified by XRD. The XRD diffraction patterns were obtained using ground powders of as-grown single crystals. The lattice parameters derived from the powders XRD data are given in Table 3.3.

The crystals belong to the tetragonal structure with space group I4/mmm at room temperature. The results are in agreement with the previously reported data [23, 24]. The lattice parameter c shrinks slightly with increasing of La doping.

The effect of La doping on the lattice parameter c is also demonstrated by the (001) XRD patterns taken on the crystal plane, as shown in Fig. 3.12. The (001) peaks shift to the higher 20 angles with increasing of the La content. The XRD patterns in Fig. 3.12 exhibit only the (001) peaks for all doped compounds indicating pure phase and high quality of the samples. The X-ray rocking curve measured on the x=0.43 crystal (Fig. 3.13a) indicates that FWHM, which is correlated with the crystal mosaicity spread, is only about 0.11°. Neutron diffraction measurements were performed on selected crystals at the reactor *Orphee* (*Laboratorie Leon Brillouin*) on the cold triple-axis spectrometer. Figure 3.13b shows a typical neutron rocking curve measured on the x=0.43 crystal with dimensions of  $\sim 15 \times 3 \times 0.2$  mm<sup>3</sup>. The FWHM of 0.48° demonstrates the excellent crystal quality of this sample.

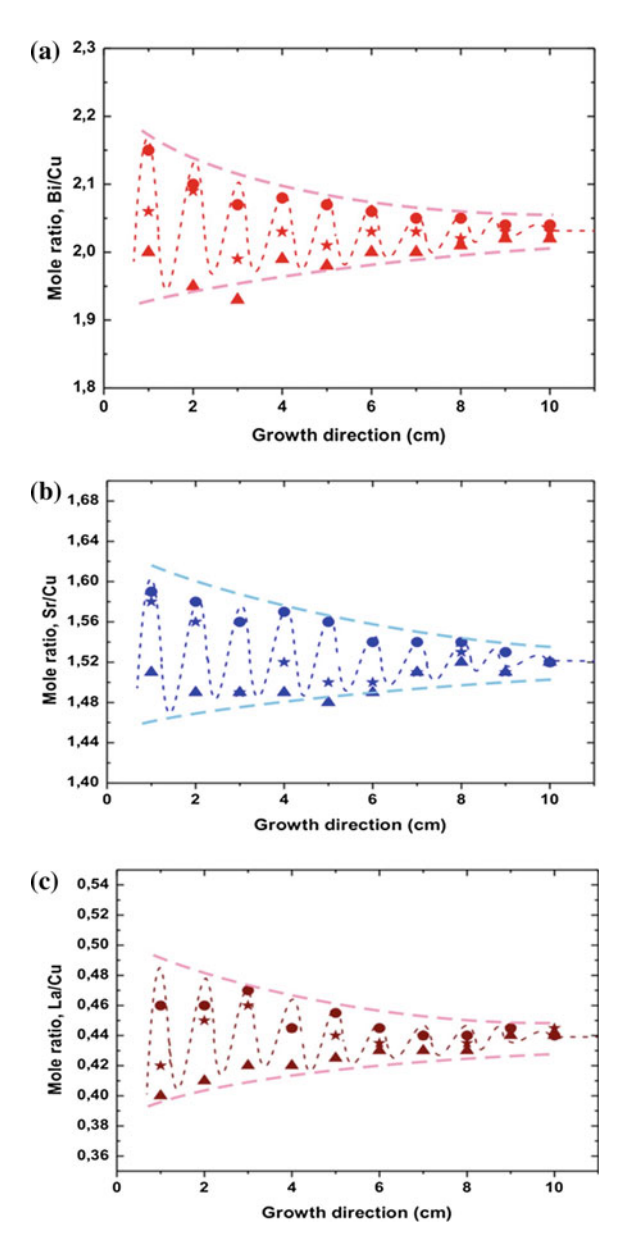
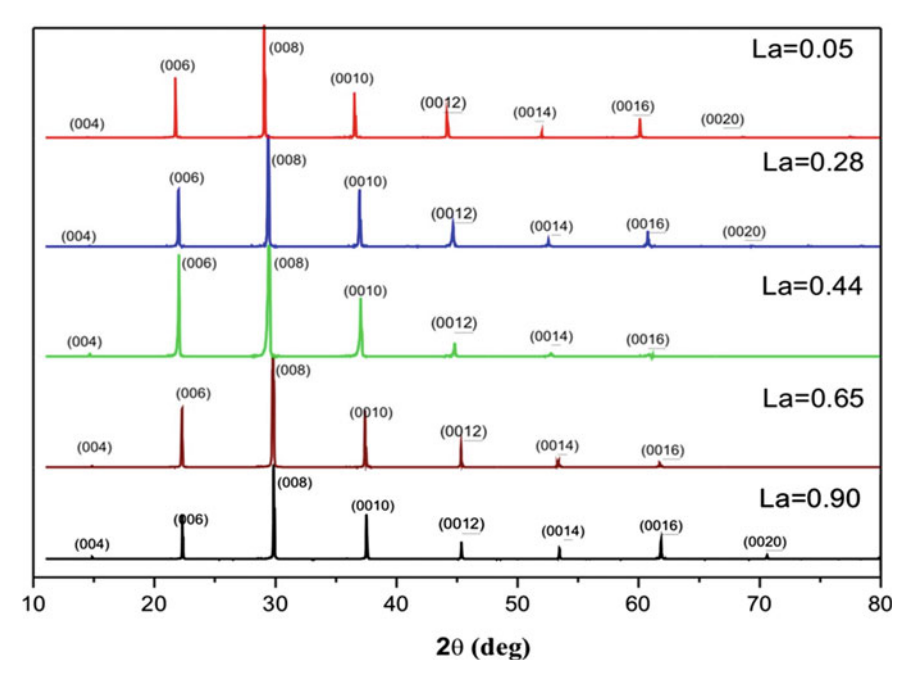


Fig. 3.11 a-c Variation of the compositions along the growth direction of the as-grown ingot for its initial doping x=0.40 (see in Table 3.1). The symbols of solid circles, stars and triangles are representative for highest, mid and lowest value measured at an interval of 1 mm along radius direction, respectively. The dashed lines are guided for eye, showing the high amplitude of compositional variation at beginning of the growth and tending to be flat (homogeneous composition) when the crystal rod approached at  $\sim 6$  cm [28]

Initial $x$ content in $Bi_2Sr_{2-x}La_xCuO_{6+\delta}$	Crystal composition	Pulling rate, mm/h	c (Å)	T <sub>c</sub>
0.03	Bi <sub>2.06</sub> Sr <sub>1.92</sub> La <sub>0.05</sub> CuO <sub>6+δ</sub>	0.5	24.586	10
0.06	Bi <sub>2.05</sub> Sr <sub>1.90</sub> La <sub>0.09</sub> CuO <sub>6+δ</sub>	0.5	24.515	14
0.15	Bi <sub>1.93</sub> Sr <sub>1.75</sub> La <sub>0.21</sub> CuO <sub>6+δ</sub>	0.5	24.453	24
0.20	Bi <sub>1.91</sub> Sr <sub>1.70</sub> La <sub>0.26</sub> CuO <sub>6+δ</sub>	0.5	24.431	26
0.25	Bi <sub>2.01</sub> Sr <sub>1.67</sub> La <sub>0.28</sub> CuO <sub>6+δ</sub>	0.5	24.376	30
0.38	Bi <sub>1.92</sub> Sr <sub>1.51</sub> La <sub>0.41</sub> CuO <sub>6+δ</sub>	0.5	24.343	33
0.40	Bi <sub>2.03</sub> Sr <sub>1.52</sub> La <sub>0.44</sub> CuO <sub>6+δ</sub>	0.5	24.336	32
0.60	Bi <sub>2.00</sub> Sr <sub>1.33</sub> La <sub>0.65</sub> CuO <sub>6+δ</sub>	0.5	24.124	20
0.80	Bi <sub>1.90</sub> Sr <sub>1.14</sub> La <sub>0.86</sub> CuO <sub>6+δ</sub>	0.5	24.021	-
0.86	$Bi_{1.86}Sr_{1.09}La_{0.90}CuO_{6+\delta}$	0.5	23.946	13

**Table 3.3** Lattice parameters and superconductivity of  $Bi_2Sr_{2-x}La_xCuO_{6+\delta}$  single crystals

The errors of all compositions are within 3 at. % by EDX



**Fig. 3.12** XRD patterns showing only the (00l) peaks for Bi<sub>2</sub>Sr<sub>2-x</sub>La<sub>x</sub>CuO<sub>y</sub> samples with x = 0.05, 0.28, 0.44, 0.65 and 0.90, respectively [28]

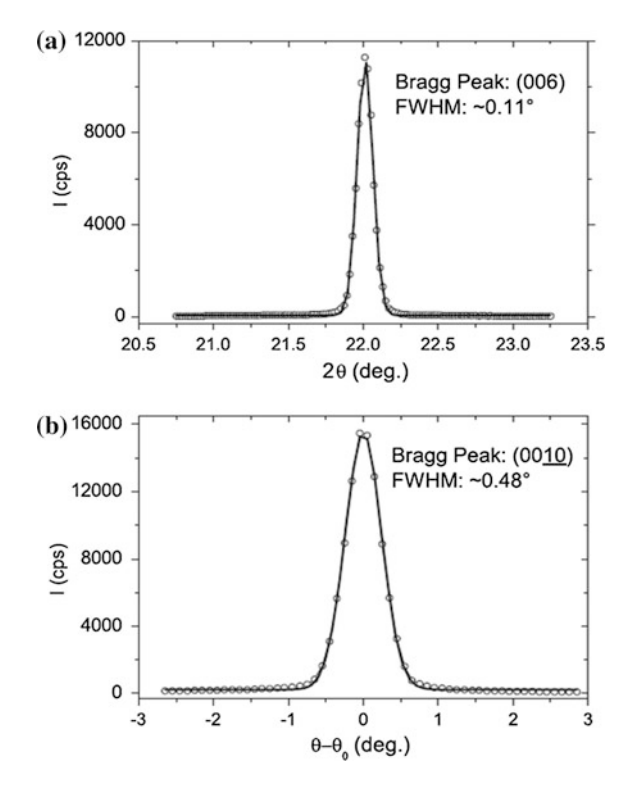
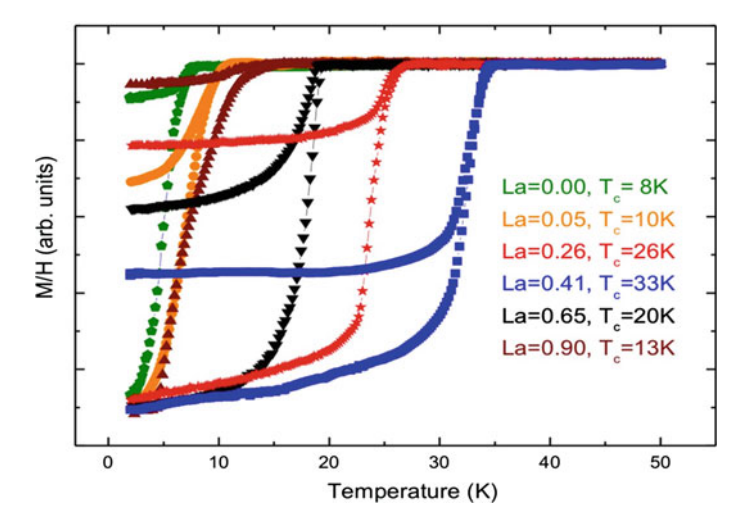


Fig. 3.13 a XRD rocking curve of (006) Bragg peak measured on the x = 0.43 crystal [27]; b neutron diffraction rocking curve of (00 10) Bragg peak measured on the x = 0.43 sample (crystal mass is  $\sim 100$  mg). Open circles are measured data; solid lines are Gaussian fits to the data

# 3.3.3 Superconductivity

The superconductivity of La-doped single crystals of  $Bi_2Sr_{2-x}La_xCuO_{6+\delta}$  was probed by ac susceptibility measurements. The results are given in Table 3.3. Some typical magnetic susceptibility curves are presented on Fig. 3.14.

It was found that  $T_c$  increases from 10 to 26 K with La doping content of the x=0.05 and 0.26, respectively. The maximum  $T_c=33$  K was found for x=0.41, indicating an optimal doping in agreement with a previous reports. The  $T_c$  drops to 20 and 13 K for the higher La doping level of x=0.65 and 0.90, suggesting that the samples are in an over doped regime. Figure 3.15 shows a dome shape of the  $T_c$  values against to the doping level for the under, optimum and over doped crystals, according to the data given in Table 3.3.



**Fig. 3.14** Temperature dependence of magnetic susceptibility of  $Bi_2Sr_{2-x}La_xCuO_{6+\delta}$  crystals. The 10 Oe FC and ZFC of magnetic fields were applied [28]

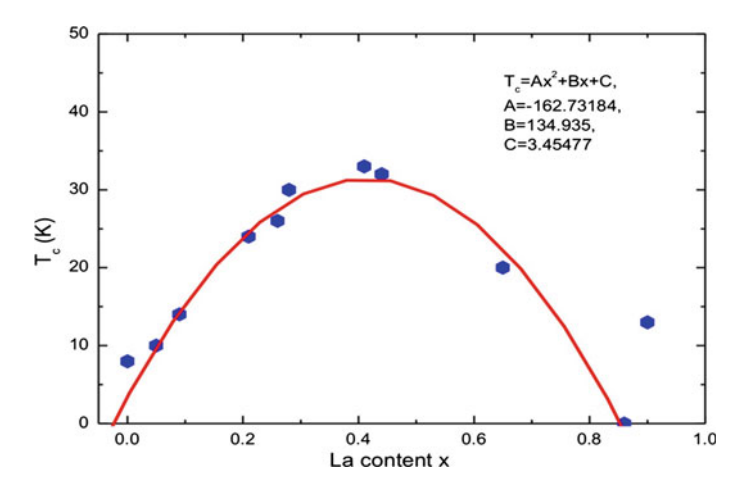


Fig. 3.15 Doping dependence of  $T_c$  for the  $Bi_2Sr_{2-x}La_xCuO_{6+\delta}$  (x = 0–0.90) single crystals [28]

## 3.4 Pb-Doped Bi-2201

It has been already mentioned that both undoped and La-doped Bi-2201 compounds demonstrate modulation structures in (a, b) plane. This effect is always visible in ARPES spectra complicating their analysis. Even more, as the strongest incommensurate modulation among all Bi-based superconductors is observed in undoped Bi-2201 material its responsibility is often assumed for a quite low  $T_c$ 

compared, for example, with Tl-2201 material which is modulation free. Concerning the doping effect on the modulation, it is known that the modulation period is almost insensitive to the La doping, while Pb substitution for Bi is a quite effective tool to supress the modulation structure [29]. It was shown in [30] that structural modulation disappears in a narrow range near Pb-solubility region of x = 0.4 at y = 0.125 in Bi<sub>2-x</sub>Pb<sub>x</sub>Sr<sub>2-y</sub>CuO<sub>z</sub>. Thus, the Pb-substitution is helpful in suppressing the incommensurate superstructure in the Bi-2201 superconductor that causes complications in band structure disentanglement. Also, superconductivity in Pb-doped Bi-2201 material is known to be highly sensitive to annealing process when one can obtain samples with different  $T_c$  by heat treatment under different conditions [31]. It has been found that by Pb<sup>2+</sup> partial doping together with annealing under different vacuum conditions lead-doped Bi-2201 crystals can cover the whole region from nearly optimally doped to heavily doped samples.

Authors could not find any report on flux growth of Pb-doped Bi-2201 in literature.

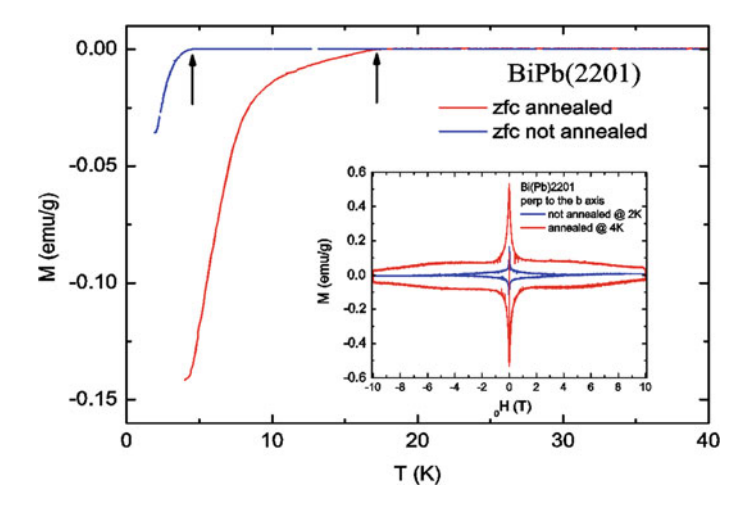
#### 3.4.1 FZ Growth

The first large-size heavily Pb-substituted Bi-2201 single crystals were grown by crucible-free FZ technique in 1997 [32]. Starting materials were Bi<sub>2</sub>O<sub>3</sub>, PbO, SrCO<sub>3</sub> and CuO for the feed rod preparation. Several different compositions were studied. The rods have been isostatically pressed and then synthesized at 840 °C for 24 h in optimal composition of the feed rod was Bi<sub>1.74</sub>Pb<sub>0.38</sub>Sr<sub>1.88</sub>CuO<sub>v</sub>. The best crystals were grown at 1.0 mm/h in air using the furnace with infra-red radiation. The image actual composition Bi<sub>1.8</sub>Pb<sub>0.38</sub>Sr<sub>2.01</sub>CuO<sub>v</sub> of the crystals was measured by EDX analysis. Based on the results of electron diffraction experiments no structural modulation was found. As-grown samples were not superconducting above 4 K from magnetization measurements, and superconductivity at  $T_c \sim 23 \; \text{K}$  was induced by vacuum annealing. Large size and thick Bi<sub>1.6</sub>Pb<sub>0.4</sub>Sr<sub>2.05</sub>CuO<sub>v</sub> single crystals have been prepared at IFW-Dresden in a similar way. The 4-mirror type image furnace (CSI, Japan) equipped with four 300 W halogen lamps was employed for the crystal growth. The growth was performed in  $Ar/O_2 = 90/10$  gas mixture, the pulling rate was 0.8-1.0 mm/h. Single crystals cleaved mechanically from the grown ingot are shown on Fig. 3.16. The largest samples have dimension up to  $15 \times 4 \times 3$  mm<sup>3</sup> with a clear cleavage plane of the (010) type.

At the same time Bi<sub>1.6</sub>Pb<sub>0.4</sub>Sr<sub>2.05</sub>CuO<sub>y</sub> samples with thickness of 2–3 mm demonstrate neutron rocking curves with shoulders around some Bragg peaks indicating the presence of small grains with slightly different misorientation. Thus, the mosaicity of thick crystals was about 2–3° only. In contrast crystals with thickness 0.3–0.5 mm show much better mosaicity about 0.5–0.7°. In all cases no traces of incommensurate superstructure was seen in reciprocal space survey. Also, preliminary ARPES measurements showed perfect ARPES spectra being free from



Fig. 3.16 As-grown Pb-doped Bi-2201 crystals



 $\begin{array}{ll} \textbf{Fig. 3.17} & \text{Superconductivity in as-grown and Ar-annealed Bi(Pb)-2201 crystals.} \ \textit{Arrows} \ \text{indicate} \\ T_c \ \text{onset} \end{array}$ 

any modulation complications. The  $T_c$  of as-grown samples was around 4 K while the Ar-annealed crystals demonstrated  $T_c \approx 17$  K (Fig. 3.17).

Also, the weak PbO and  $\rm Bi_2O_3$  evaporation was observed from the molten zone during the growth run (2–3 days). The boiling points of PbO and  $\rm Bi_2O_3$  are 1480 and 1890 °C, respectively. The deposited layer on quartz tube was very thin and didn't affect the MZ stability.

### 3.4.2 Post Growth Annealing and Superconductivity

As-grown Pb-doped Bi-2201 crystals usually demonstrate superconductivity below 3 K but post-growth annealing in vacuum drastically increases  $T_c$  up to 23 K. As shown in Table 3.4 annealing process has the strong effect on superconducting properties of  $Bi_{1.6}Pb_{0.4}Sr_{2.05}CuO_y$  crystals. Since the substitution of  $Bi^{3+}$  with  $Pb^{2+}$  is expected to introduce holes into the sample, Pb doping pushes the Bi-2201 system into heavily overdoped region.

By annealing in oxygen atmosphere, the superconducting transition disappears (below the low temperature limit of 2 K of our measurement system). On the other hand, by annealing the as-grown Pb-doped Bi-2201 crystals in vacuum ( $\sim 10^{-5}$  mbar) at 550 °C for 7 days,  $T_c$  as high as 23 K can be achieved (Table 4). This indicates that by removing the extra oxygen in the as-grown Pb-doped Bi-2201 crystals one can change the sample doping from heavily overdoped to slightly overdoped. By balancing the atmosphere and annealing temperature, different  $T_c$ 's between 0 and 23 K have been obtained. On the other hand vacuum annealing above 550 °C causes the sample partial decomposition during the heat treatment that is seen even by naked eyes. Also, the crystals annealed in vacuum at 550 °C were found to be unstable in air indicating the sample decomposition. Only samples treated either in Ar flow (5 N purity) or under vacuum conditions at 450 °C and below could be stored in air without sample and superconductivity degradation.

The crucible free floating zone technique seems to be the best tool to grow high quality and large size single crystals of pure, La-doped and Pb-doped Bi-2201 materials despite our knowledge of the melting behavior of Bi-2201 phase is still far from complete understanding. The relative simplicity of the crystal structure of the Bi-2201 phase compared with other Bi-based superconductors makes the single crystals of these compounds important for the fundamental research in the field of the high-Tc superconductivity although they possess relatively low superconducting transition temperatures.

Table 3.4 Amelaning conditions and Bi <sub>1.6</sub> 1 b <sub>0.4</sub> 51 <sub>2.05</sub> CuO <sub>y</sub> superconductivity						
Crystal composition	Annealing atmosphere	Annealing time	Superconductivity, T <sub>c</sub> (K)	Sample status		
$Bi_{1.6}Pb_{0.4}Sr_{2.05}CuO_y$	As-grown	0 days	3 K	Stable in air		
Bi <sub>1.6</sub> Pb <sub>0.4</sub> Sr <sub>2.05</sub> CuO <sub>y</sub>	450 °C in O <sub>2</sub>	7 days	Non-superconducting	Stable in air		
Bi <sub>1.6</sub> Pb <sub>0.4</sub> Sr <sub>2.05</sub> CuO <sub>y</sub>	450 °C in Ar	10 days	13 K	Stable in air		
Bi <sub>1.6</sub> Pb <sub>0.4</sub> Sr <sub>2.05</sub> CuO <sub>y</sub>	450 °C, 10 <sup>-5</sup> mbar	7 days	17 K	Stable in air		
Bi <sub>1.6</sub> Pb <sub>0.4</sub> Sr <sub>2.05</sub> CuO <sub>y</sub>	550 °C, 10 <sup>-5</sup> mbar	5 days	23 K	Non-stable in air		
$\mathrm{Bi}_{1.6}\mathrm{Pb}_{0.4}\mathrm{Sr}_{2.05}\mathrm{CuO}_{\mathrm{y}}$	650 °C, 10 <sup>-5</sup> mbar	3 days	No measurement	Sample decomposed		

Table 3.4 Annealing conditions and Bi<sub>1.6</sub>Pb<sub>0.4</sub>Sr<sub>2.05</sub>CuO<sub>y</sub> superconductivity

T<sub>c</sub> was detected from magnetization measurements

### **3.5 Bi-2212 Compound**

Among the Bi-based superconductors a  $Bi_2Sr_2CaCu_2O_{8+\delta}$  (hereafter Bi-2212) phase is the most stable one. According to [9] the stability range of Bi-2212 compound lies between 650 and 890 °C in air and spans over 300 degrees that is much higher compared with Bi-2201 and Bi-2223 phases. Many Bi-2212 single crystals have been grown using several techniques, namely the slow-cooling flux [33, 34], the Bridgeman [35, 36], the top-seeded solution growth [37] and crucible-free floating zone methods [17, 38, 39]. The large in (a, b) plane plate-like Bi-2212 crystals can be relatively easy fabricated, although it is very hard to prepare Bi-2212 samples with thickness over 0.1 mm along c-axis without low-angle grain boundaries. The reasons for this are threefold: (i) extremely high anisotropy of growth rates perpendicular and parallel to (a, b) plane; (ii) complex (incongruent) solidification behaviour of Bi-2212 compound; (iii) lack of reliable and detailed phase diagrams.

In order to study the intrinsic properties of Bi-2212 superconducting material and, in particular, the strong anisotropy behaviour of this compound, single crystals are truly indispensable. Therefore, a lot of growth efforts have been done in order to produce high quality and thick Bi-2212 crystals for the fundamental research in the past 25 years. The physical properties of Bi-2212 phase were found to be very sensitive to the oxygen content in this material. Thus, one can easily tune the superconducting properties from underdoped to overdoped regimes varying the oxygen concentration by simple argon/oxygen annealing.

### 3.5.1 Flux Growth

The results of Bi-2212 flux growth could be found in numerous publications have been done in the past 25 years. Crystal growers tested the capability of different fluxes to make high quality Bi-2212 single crystals. Although Bi-2212 crystal could be obtained from KCl flux the majority of growth experiments were done using self-flux technique, i.e. CuO and/or  $\rm Bi_2O_3$  rich melts. In some cases even stoichiometric compositions were used for the growth due to the incongruently melting behaviour of Bi-2212 compound.

For the Bi-2212 growth using KCl (m.p. = 772 °C) solvent [34] starting materials were prepared by partial melting in air of high quality Bi<sub>2</sub>O<sub>3</sub>, SrCO<sub>3</sub>, CaCO<sub>3</sub> and CuO powders with subsequent quenching to room temperature. Two different starting compositions have been prepared: BiSrCaCu<sub>2</sub>O<sub>y</sub> and Bi<sub>4</sub>Sr<sub>3</sub>Ca<sub>3</sub>Cu<sub>4</sub>O<sub>y</sub>. The product was then ground and used in growth experiments. Bi–Sr–Ca–Cu–O starting material and alkali chloride solvent were charged directly into Pt crucible with a close-fitting lid to minimize the solvent evaporation. Typical charge weights were 5 g for a starting material and 140 g for a solvent. In some cases KCl–NaCl binary eutectic (m.p. = 658 °C) was used as a solvent that reduced

a growth temperature and, in turn, suppressed a flux evaporation. The charged crucible was placed in a box-oven and heated to 920-960 °C. It was hold at this temperature for 15 h, then cooled to 600-700 °C at a rate of 4-5 °C/h and finally furnace-cooled to room temperature. The significant 1-4 g loss of alkali chloride during a growth run was observed. After the growth the solvent can be easily washed out by soaking the Pt crucible in a hot water. In all growth runs, thin Bi-2212 crystal plates about 50 μm thick were formed on the solidified solvent surface getting typical in-plane dimensions  $5 \times 5 \text{ mm}^2$ . Single crystalline samples could be obtained for the hold temperatures above 920 °C only. For the Bi<sub>4</sub>Sr<sub>3</sub>Ca<sub>3</sub>Cu<sub>4</sub>O<sub>v</sub> starting composition no superconducting phase was found, although superconducting crystals with T<sub>c</sub> about 80 K from resistivity measurements were prepared using the BiSrCaCu<sub>2</sub>O<sub>v</sub> starting composition. In the last case many CuO needle-like crystals were co-crystallized and found on the back surface of Bi-2212 plates. Single crystal X-ray diffraction gave the lattice constant c = 30.80 Å. The microprobe analysis (EPMA) of grown crystals showed a low concentration of either K or Na ions incorporated in samples. No magnetization measurements have been done.

The interesting growth approach was announced in [40]. Perfect Bi-2212 single crystals with the superconducting transition temperature  $T_c = 72-85$  K (depending on the crystallization conditions) have been obtained by free-standing growth in a gas cavity formed in a KCl flux. The specific features of the growth process are: (i) the formation of a trapped gas cavity in a KCl-based melt; (ii) the growth of free-standing Bi-2212 crystals in this encapsulated cavity. The combination of growth and in-situ high-temperature annealing in quasi-closed cavity made it possible to obtain uniform ( $\Delta T_c = 1.5 \text{ K}$ ) single crystals with high superconducting phase fraction (over 90 %). The post growth annealing in the temperature range 400-850 °C in oxygen/air confirmed that as-grown crystals were optimally doped. No potassium has been found in all analyzed samples by EPMA. The pre-sintered Bi-2212 precursor was mixed with KCl in ratio 1:4 and put in Al<sub>2</sub>O<sub>3</sub> crucible (200 ml) that placed in a tube vertical furnace. The mixture was melted and soaked at 880-920 °C for 24 h. A large 3-6 °C/cm temperature gradient has to be applied through the melt in order to get a frozen layer of Bi-2212 phase on the melt surface. Closed cavity with a lens shape and height up to 5 mm was formed during a rapid cooling from the soaking temperature by 10-15 °C at the rate 20 °C/h. Crystal growth takes place on the top of cavity by cooling at 0.1-0.3 °C/h. Number of crystals may reaches several tens with typical dimensions up to  $2 \times 2 \times 0.01 \text{ mm}^3$ .

Application of CuO and Bi<sub>2</sub>O<sub>3</sub> fluxes for the Bi-2212 crystal growth assumed the existence of Bi-2212 phase primary crystallization field (PCF) in the corresponding Bi<sub>2</sub>O<sub>3</sub>–SrO–CaO–CuO system. At the same time the Bi-2212 primary crystallization field in Bi–Sr–Ca–Cu–O system was studied in a few publications only, and the reported data are not well consistent [41–44]. For example, the Bi-Sr: Ca:Cu = 33:29:14:24 composition was reported for the reproducible Bi-2212 flux growth in Al<sub>2</sub>O<sub>3</sub> crucibles [41]. In [42] the Bi-2212 single-phase crystallization was observed for somewhat different composition 33:25:14:28 again in Al<sub>2</sub>O<sub>3</sub> crucibles. The temperature range of the Bi-2212 single-phase crystallization does not exceed

 $10~^\circ\text{C}$  for this composition being an extremely narrow for the flux method. Moreover, it was found that  $(\text{Sr,Ca})_3\text{Al}_2\text{O}_6$  compound was formed due to the reaction between the melt and the crucible material. This reaction leads to the unknown shift of the actual melt composition. The crucible-free FZ technique rules out the interaction between melt and crucible material. Usually it is assumed that the MZ composition of the steady FZ growth more or less corresponds to the PCF of Bi-2212 phase. The 31.2:23.8:12.5:32.5 solvent [44] was reported for the Bi-2212 crystal growth by the travelling solvent floating zone technique which is Bi-rich compared with flux results. According to [43], the Bi-2212 PCF lies within a wide compositional range of (24-42):(7-33):(2-27):(19-43).

The most detailed investigation of the Bi-2212 phase PCF has been done in [45]. It was demonstrated that the corrosion rate for gold crucibles is lower by one order compared with Pt and Al<sub>2</sub>O<sub>3</sub> ones [45]. Therefore, all experiments were done in gold crucibles to evade the unfavourable formation of (Sr,Ca)<sub>3</sub>Al<sub>2</sub>O<sub>6</sub> and platinate phases usually observed for Al<sub>2</sub>O<sub>3</sub> and Pt containers. The formation of these phases could easily shift the phase equilibria in a studying system. For example, 33:25:13:29 composition results in the crystallization of (Sr, Ca)<sub>2</sub>CuO<sub>3</sub> phase in Au crucibles while the same composition leads to the Bi-2212 crystallization in Pt containes. This fact well explains why the reported PCF data are being at odds. In general, the higher is the crucible corrosion rate the greater is the composition shift to the Sr-Ca-rich region [45]. As a result it was found that "Bi-2212 + melt" equilibrium exists in the narrow 859–883 °C temperature range for the 34.4:24.1:11:30.5 starting composition. Based on these data high-quality Bi-2212 crystals have been prepared by slow cooling at 0.5–3.0 °C/day in the 870–890 °C range. The extremely low cooling rates were chosen due to the very narrow (<25 °C) temperature crystallization region of Bi-2212 phase. The starting reagents were Bi<sub>2</sub>O<sub>3</sub>, SrCO<sub>3</sub>, CaCO<sub>3</sub> and CuO powders of 3 N purity. The melt homogenization was performed at 940–980 °C for 15 h in air. Then the temperature was dropped at 30 °C/h down to 890 °C. The typical dimensions of as-grown Bi-2212 crystals were  $2.0 \times 2.0 \times 0.03$  mm<sup>3</sup>. The lattice parameters were a = 5.411(1) Å, b = 5.413(1) Å and c = 30.871(1) Å (Figs. 3.18) and 3.19).

Fig. 3.18 Bi-2212 single crystal with 0.065 mm thickness showing well-developed facets [45]. Reprinted with permission from Elsevier. All rights reserved

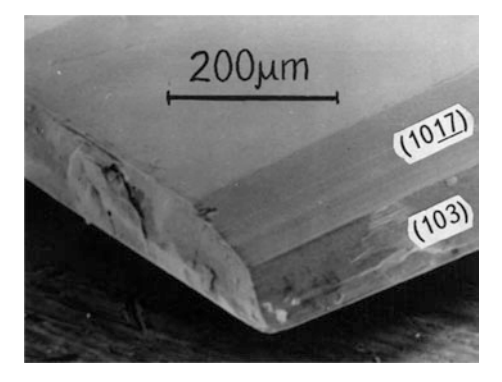
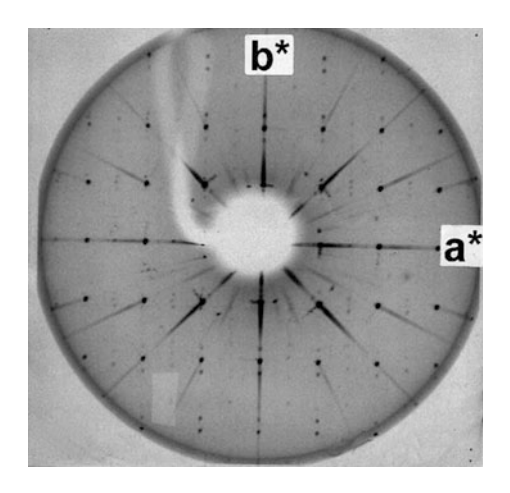


Fig. 3.19 Laue X-ray pattern of Bi-2212 single crystal [45]. Reprinted with permission from Elsevier. All rights reserved



The X-ray topography data indicate that the misorientation (about  $0.5^{\circ}$ ) in the Bi-2212 crystal mainly takes place around a-axis, and is nearly absent around b-and c-axes. The post-growth annealing at 400 °C in Ar–O<sub>2</sub> gas mixture for 20 h followed by quenching results in  $T_c = 91$  K and  $\Delta T_c = 1.5$  K from magnetization measurements. No Au traces have been found in crystals from chemical (EDX) analysis.

Nevertheless, nowadays Al<sub>2</sub>O<sub>3</sub> crucibles are widely used for the Bi-2212 flux and Bridgman growth due to the low cost compared with gold containers. Besides the shift of the melt composition caused by chemical reaction between the melt and the crucible material, the using of Al<sub>2</sub>O<sub>3</sub> crucibles may affect the superconducting properties of Bi-2212 crystals due to the Al-contamination. This effect was well studied in [46]. The Bi-2212 crystals have been grown by Bi<sub>2</sub>O<sub>3</sub>-flux method in high dense Al<sub>2</sub>O<sub>3</sub> crucibles. The starting compositions were Bi:Sr:Ca:Cu: A1 = 2.4:2:1:2:z (z = 0.0, 0.074, 0.148, 0.222, 0.296, 0.370 and 0.444). The doping material was Al<sub>2</sub>O<sub>3</sub> powder (4 N purity). The Bi<sub>2</sub>O<sub>3</sub> excess was used to compensate the Bi<sub>2</sub>O<sub>3</sub> evaporation from a melt and to act as a flux for the crystal growth. The Al content in a melt and undoped crystals (z = 0.0) derives from Al dissolution in a melt, while for the Al-doped samples (z > 0.0) it is originated from both Al dissolution and Al-doping. The formation of (Sr<sub>0.62</sub>Ca<sub>0.38</sub>)AlO<sub>v</sub> phase was observed on a melt surface for all melts, although the amount of this material was much larger for Al-doped melts. The Al concentrations caused by alumina crucible contamination in undoped Bi-2212 crystals and melts were 0.05 and 0.16 per formula unit, respectively, from EDX data. The maximum of Al solubility in Bi-2212 crystals was found to be 0.12 per formula unit. At the same time  $T_c$  of Bi<sub>2.20</sub>Sr<sub>1.95</sub>Ca<sub>0.80</sub>Cu<sub>2-</sub>  $_{\rm x}$ Al $_{\rm x}$ O $_{\rm v}$  crystals decreases with x very slowly. And this effect is almost negligible for undoped (z = 0.0) samples. Thus, the Bi-2212 crystals grown in Al<sub>2</sub>O<sub>3</sub> crucibles are slightly Al contaminated (x = 0.05), but it has very weak effect on  $T_c$ . Nevertheless, the Al contamination can affect other physical properties.

On the other hand Bi-2212 samples grown from Bi<sub>2</sub>O<sub>3</sub>-rich melts were found to be non-superconducting in [47]. According to this publication superconducting Bi-2212 crystals could be prepared from stoichiometric and/or CuO-rich melts only. The crystals were grown in Al<sub>2</sub>O<sub>3</sub> crucibles in air. Starting compositions were heated at 1200 °C, held for 2 h, cooled quickly down to 950 °C, followed by slow cooling to 800 °C at a rate of 3–4 °C/h. The authors obtained crystals as large as  $8 \times 5 \text{ mm}^2$  in (a, b) plane with  $T_c$  (onset) = 89 K from magnetization measurements.

In several publications [33, 48] Bi-2212 crystals have been obtained from stoichiometric compositions Bi:Sr:Ca:Cu = 2:2:1:2 in air. The Al<sub>2</sub>O<sub>3</sub> containers with initial compositions were heated at 960 °C for 10 h in [48]. Then the furnace was slowly cooled down to 830 °C at rates 0.5–2.0 °C/h. The effect of the cooling rate on crystal sizes and  $T_c$  has been investigated. The largest 13.5 × 12.0 mm² in-plane Bi-2212 crystal was prepared at the cooling rate of 1 °C/h. It was two times larger than any other crystal grown at different rates. Nevertheless, all as-grown Bi-2212 samples were impurity free from XRD measurements. All X-ray diffraction patterns were very similar independent from a cooling rate. At the same time, Bi-2212 samples obtained at 2 °C/h showed lowest  $T_c$  around 81 K, while Bi-2212 crystals prepared at 0.5–1.0 °C/h demonstrate highest  $T_c$  = 87 K.

Nearly all flux-grown Bi-2212 crystals have been made in air, and the effect of oxygen partial pressure on crystal growth and superconducting properties has not been investigated. From this point the results of [49] give a prompt what kind of effect might be anticipated. The authors grew Bi-2212 crystal from a stoichiometric composition. The charge was put in Al<sub>2</sub>O<sub>3</sub> crucible covered with a ceramic alumina lid. The high-temperature brick of 250 g was placed on a lid that was equivalent to the applying pressure of about 0.195 N/cm<sup>2</sup> to the cap. The crucible was heated at 990 °C for 6 h, then slowly cooled at 0.5 °C/h down to 790 °C. The temperature dependence of the Bi-2212 resistivity was measured by standard four-probe method. Surprisingly, Bi-2212 crystals grown by applying the pressure reach the zero resistance state at  $T_{c,zero}$  = 88 K, while crystals prepared without pressure show the highest  $T_{c,zero} = 77$  K with comparable  $\Delta T_c$ . The dependence between  $T_c$ . zero and pressure applied to the alumina lid is well similar to the relationship between T<sub>c</sub> and oxygen content in Bi-2212. According to [49] this result indicates that the applied pressure to the cap may control the oxygen content in the Bi-2212 crystals. The most natural explanation is the following: it seems that the pressure applied to the cap makes the junction between a crucible and a lid nearly gas-tight. According to the CuO-Cu<sub>2</sub>O phase diagram [50] the CuO melts with oxygen release. In this case the partial oxygen pressure has to be increased in the semi-closed crucible. Thus, the Bi-2212 crystal growth occurred under the oxygen pressure that allowed the fabrication of optimally doped samples instead of under-doped crystals prepared in air.

An interesting growth approach was realized in [51] in which the slow cooling flux technique was combined with the Top Seeded Solution Growth (TSSG) method. The starting composition was  $Bi_{2.4}Sr_{1.5}Ca_{1.0}Cu_{1.8}O_y$ . The mixture was slowly heated until complete melting in air. The melt was soaked for 1 h at 900 °C

**Fig. 3.20** TSSG-grown Bi-2212 boule [51]. Reprinted with permission from Elsevier. All rights reserved



and subsequently cooled to  $\approx 865$  °C. At this temperature a small seed crystal was dipped into a melt and rotated at 35 rpm. Then the melt was cooled at 1 °C/h, and the seed was pulled up at a rate of 0.3–0.5 mm/day. The temperature gradient was 10 °C/cm in a melt originated from air cooling of the upper shaft on which a seed crystal was mounted. The grown boule was taken away from the melt when the temperature became around 845 °C. The authors tried the growth along different pulling directions such as a- and c-axis, and found that the growth along c-axis was very hard. As-grown boule fabricated along a-axis was about 100 mm in diameter and 6 mm in length, and was like a lamination of thin plate-like Bi-2212 crystals (Fig. 3.20).

The composition of TSSG-grown crystals was  $Bi_{2.2}Sr_{1.8}Ca_{1.0}Cu_{2.0}O_y$  very close to the floating zone prepared samples [17, 38]. The powder X-ray patterns of cleaved samples showed only the diffraction peaks corresponded to the pure Bi-2212 phase. As-cleaved Bi-2212 crystals exhibited superconductivity transition at 86 K from magnetization measurements.

In summary, plate-like and thin Bi-2212 crystals could be grown by different fluxes in  $Al_2O_3$ , MgO, Pt and Au crucibles in air. The main drawbacks of the flux method are: (1) an average crystal thickness is about  $20{\text -}30~\mu m$  only; (2) crystals yield is small; (3) Al and Pt contamination; (4) there is no control of oxygen partial pressure during the growth; (5) flux creeping out effect observed for  $Al_2O_3$  and Pt crucibles.

## 3.5.2 Bridgman Growth

In general a temperature gradient on a crystallization front in Bridgman method is one order higher than in flux technique. Larger temperature gradient stabilizes the planar compared to cellular solid-liquid interface that results in the growth of larger and thicker crystals. Also, only a few crystal nuclei are self-selected in Bridgman method by using a crucible with a special corn-shaped bottom that suppresses well the negative effect of mass spontaneous nucleation taken place in a flux method. As a result, a lot of efforts were made in the past 25 years to prepare Bi-2212 single crystals by Bridgman method [35, 36, 52-56]. One of the most earliest and detailed investigations has been done in [35]. According to the authors [35] stoichiometric mixtures Bi:Sr:Ca:Cu = 1:1:1:z (z = 1-10) were prepared in order to study the effect of CuO excess on growth and properties of Bi-2212 crystals. All starting Bi<sub>2</sub>O<sub>3</sub>, SrCO<sub>3</sub>, Ca(OH)<sub>2</sub> and CuO powders had ACS grade. High dense Al<sub>2</sub>O<sub>3</sub> crucibles with 99.7 % purity were utilized. In all growth experiments the highest temperature was 960 °C for minimizing crystals contamination by alumina. Crucibles loaded with 1:1:1:z compositions were placed inside a tubular vertical furnace. The isothermal zone length of the furnace was 15 cm. The crucible cooling was realized by a motorized translation of the vertical furnace without any movement of the crucible holder. An effective cooling rate of 6 °C/h was got in the temperature range from 960 to 760 °C in air. It was shown that z = 1 composition melts incongruently at 960 °C, and tiny crystals of Sr<sub>0.2</sub>Ca<sub>0.8</sub>CuO<sub>v</sub>, Bi-2201, Bi-2212, Bi-2223 compounds were formed. The melting behaviour of z = 2 composition is qualitatively similar to z = 1, but mainly (Sr,Ca)CuO<sub>v</sub> and Bi-2201 compounds were crystallized. The best results were observed for z = 3 and 5 compositions. Both compositions melt congruently at 960 °C in air. The main product of well-crystallized and homogeneous ingot was Bi<sub>2.2</sub>Sr<sub>2.0</sub>Ca<sub>0.8</sub>Cu<sub>2.0</sub>O<sub>v</sub> single crystals with the largest dimensions in (a, b) plane up to 30 mm<sup>2</sup> for z = 5. The lattice parameters were  $a \approx b \approx 5.40$  Å and  $c \approx 30.6$  Å. The resistivity measurements in (a, b) plane showed a superconducting transition at about 80 K, but zero resistance was reached only around 50 K. The resistivity along c-axis demonstrated semiconductor-like behaviour. For z = 10 large fraction of Bi-2223 crystals was detected in as-prepared ingot, although Bi-2212 crystals were obtained as well.

In [36] the amount of starting material was varied and  $Al_2O_3$  crucibles with different bottom angles were used in order to enlarge the size of Bi-2212 crystals grown by vertical Bridgman (VB) method. The Bi:Sr:Ca:Cu = 2:2:1:2 starting composition has been utilized for the growth. The alumina crucibles were heated up to 985 °C, then crucibles were pulled down at 1.0 mm/h up to 830 °C. It was demonstrated that the area of plate-like Bi-2212 single crystals was proportional to the amount of starting materials, and that the optimum bottom angle of the crucible was about 60°. Optimized growth conditions allowed the fabrication of single crystals with sizes up to 25 × 5 mm². No Al was found in as-grown crystals from EDX analysis. The authors have addressed this effect to the molten zone refinement

during the Bridgman process. The average composition of Bridgman grown samples was Bi and Ca enriched but Sr deficient. Single crystal X-ray diffraction and X-ray photoelectron spectroscopy found no impurities on the surface of air-cleaved single crystals. The mosaicity of Bi-2212 samples was about 0.1 degree from single crystal XRD data. The highest  $T_c$  for as-grown samples was about 80 K, but transition width 30 K was rather large from magnetization measurements. Nevertheless,  $\Delta T_c$  can be narrowed up to 5 K by post growth annealing at 500 °C in flowing oxygen. It is worth to mention that  $T_c$  of single crystals prepared in crucibles with bottom angles 30° and 60° were 60 and 77 K, respectively. The most natural explanation is the following: the smaller bottom angle for the fixed quantity of the starting material means the longer length of a solidified ingot that, in turn, enlarges the diffusion path for oxygen because the biggest samples were located close to the crucible bottom [36]. From this point samples grown in crucibles with bottom angle of 30° have to get more pronounced oxygen deficiency being in under-doped regime with lower  $T_c$ .

In [52] effects of crucible rotation and temperature gradient on crystal quality and  $T_c$  were studied for the VB growth. The starting composition was Bi:Sr:Ca: Cu = 2.2:1:2. The authors [52] modified VB method applying a crucible rotation during the growth. Optical image of Bi-2212 ingot prepared by modified VB method is shown on Fig. 3.21. Based on this photo one can see that Bi-2212 crystals were plate-like and grew up from the crucible bottom to the top along pulling direction. The mosaicity was found to be about  $0.06^{\circ}$  for temperature gradients 2.5 and 4.0 °C/mm while it was  $0.10^{\circ}$  for 1.5 °C/mm gradient. In all cases single crystals were grown under the same growth conditions: pulling rate 1.0 mm/h, rotation speed 0–100 rpm, melting temperature 975 °C, crucible bottom angle 45°, mass of charge 25 g. The largest plate-like sample with sizes of  $18 \times 5$  mm<sup>2</sup> was obtained by using the rotation rate 25 rpm and temperature gradient 2.5 °C/mm.

It is quite interesting that samples grown at 100 rpm were more bulky compared with more plate-like samples prepared at 10, 25 and 50 rpm. The maximum crystal size in (*a*, *b*) plane increases from 50 mm<sup>2</sup> for zero rotation up to 90 mm<sup>2</sup> for rotation at 25 and 50 rpm [53] when temperature gradient and pulling rate were

Fig. 3.21 Optical image of Bi-2212 ingot grown by modified VB technique [52]. Reprinted with permission from Elsevier. All rights reserved

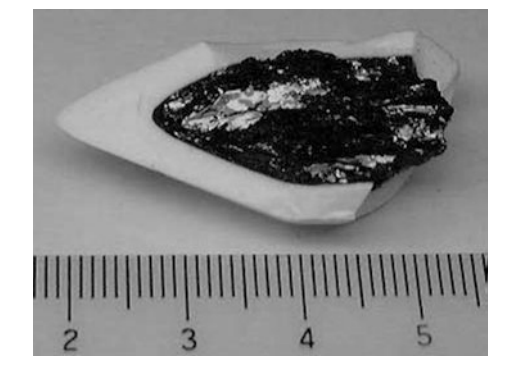
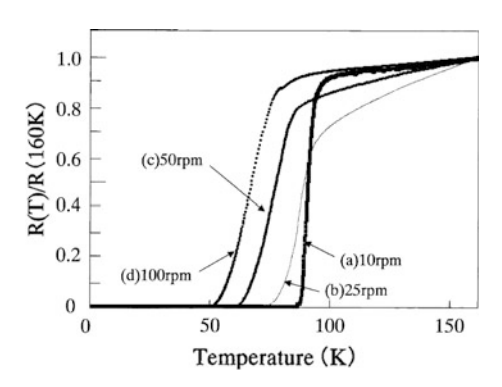


**Fig. 3.22** R–T characteristics of Bi-2212 crystals versus rotation speed [52]. Reprinted with permission from Elsevier. All rights reserved



fixed at 1.6 °C/mm and 0.75 mm/h, respectively. Effect of crucible rotation on R–T characteristics of as-grown Bi-2212 single crystals is shown on Fig. 3.22. Both  $T_c$  and  $\Delta T_c$  values strongly depend from the rotation speed although the origin of this effect is unknown [52]. Surprisingly, this effect became much weaker when the melting temperature was gained from 975 to 1000 °C [52, 53].

The effect of the crucible size on the Bi-2212 growth by VB method was studied in [53]. Two types of corn-shaped Al<sub>2</sub>O<sub>3</sub> crucibles with outer diameters 30 and 21 mm were used. It was found that much longer in b-axis Bi-2212 crystals grew continuously from a bottom to a top by using larger crucibles. Based on resistivity measurements it was demonstrated that Bi-2212 crystals prepared in crucibles with outer diameter 30 mm showed typical  $T_c$  around 85-89 K. On the other hand, Bi-2212 samples prepared in crucibles with outer diameter 21 mm possessed lower  $T_c$  of about 82 K. In all cases crystals were selected from central region of the crucibles. The authors of [53] suggested that Bi-2212 crystals fabricated in larger containers were less Al contaminated. Also, the melting temperature, T<sub>m</sub>, was varied from 950 to 1040 °C. The single crystal XRD patterns were found to be fully independent from T<sub>m</sub> and showed diffraction peaks of pure Bi-2212 phase only. At the same time the optimum melting temperature was  $T_m = 1000$  °C based on crystal size and composition [53]. Crystals with almost stoichiometric composition were obtained by using  $T_m = 1000$  °C. The superconducting temperature slightly increased from 84.5 to 88.5 K when T<sub>m</sub> grew from 950 to 1040 °C.

The effect of crucible materials on Bi-2212 vertical Bridgman growth was investigated in [54]. The crucibles of SSA–H (Al $_2O_3$  content 95 %, SiO $_2$  content 3 %), SSA–T (Al $_2O_3$  content 99.6 %) and MG–12G (MgO content 99.7 %) types were used in this study. The growth conditions for the VB method were as follows: crucible rotation at 25 rpm, melting temperature  $T_m$  = 1000 °C, crucible pulling down at 0.75 mm/h. For comparison Bi-2212 crystals were grown by self-flux technique using the same crucibles in the temperature range 830–1000 °C. The cooling rate was 1 °C/h. Single crystal XRD patterns for all Bridgman and flux grown Bi-2212 crystals prepared in alumina and magnesia crucibles showed only sharp (001) diffraction peaks which corresponded to the pure Bi-2212 phase. No impurity phases were found from these XRD patterns. The mosaicity of all Bi-2212

samples collected from Al<sub>2</sub>O<sub>3</sub> and MgO containers slightly varies from 0.05 to 0.07 degrees. Based on these data high quality Bi-2212 single crystals can be prepared in both alumina and magnesia crucibles. At the same time resistivity measurements done in (a, b) plane demonstrated a weak dependence of  $T_c$  value from crucible material for flux grown samples. For example, Bi-2212 crystals grown by flux method in Al<sub>2</sub>O<sub>3</sub> containers showed superconducting transition at 86–88 K. The higher  $T_c$  = 88 K was observed for the SSA-T crucibles while  $T_c = 86 \text{ K}$  corresponded to the SSA-H container. Moreover, Bi-2212 crystals fabricated in magnesia crucibles presented superconducting transition at 90 K. Thus,  $T_c$  of Bi-2212 single crystals prepared by flux method using alumina containers was lower than that fabricated in magnesia crucibles. Also, T<sub>c</sub> value correlated well with the purity of alumina crucibles. This decrease of superconducting temperature may be originated from Al contamination in flux grown crystals. However, all VB grown samples showed a sharp transition at 88-89 K independent from a crucible material. This may be due to the effect of molten zone refining during the Bridgman growth [54]. As a result MgO crucible was suggested for the flux method. Also, magnesia crucibles demonstrated the much less pronounced flux creeping out effect compared with Al<sub>2</sub>O<sub>3</sub> and Pt containers that played the important role for both flux and Bridgman techniques.

The role of partial oxygen pressure, p(O<sub>2</sub>), on crystal growth and superconducting properties of Bi-2212 crystals was studied in [55]. The authors used Bi:Sr: Ca:Cu = 2:2:1:2 starting composition. The Bi-2212 crystals were prepared at the p  $(O_2) = 0$ , 21, 60 and 100 kPa. Other growth conditions were as follows: the crucible rotation rate 25 rpm, the melting temperature 1000 °C, the temperature gradient 1.6 °C/mm and the pulling down rate 0.75 mm/h. The mixture of Ar and O<sub>2</sub> gases at different ratios was applied, and the total gas pressure was kept at 1 atm. It was found that large Bi-2212 crystals were not fabricated in area of 3-5 mm close to the inner crucible walls because of the alumina contamination. The crystal size in (a, b) plane depended from applied partial oxygen pressure, and the largest samples with dimensions up to  $20.5 \times 6.5 \text{ mm}^2$  were obtained at the  $p(O_2) = 21 \text{ kPa}$ . In addition single crystals grown at each p(O<sub>2</sub>) from 0 to 100 kPa showed mosaicity of 0.05°-0.06° indicating the nearly perfect crystal quality. According to the EDX data all single crystals had almost stoichiometric composition of the Bi-2212 superconductor. The  $T_c$  values of Bi-2212 single crystals grown at different  $p(O_2)$  had no significant difference and were 87-88 K, although samples prepared at 100 kPa of oxygen pressure demonstrated the narrowest superconducting transition from resistivity data. All crystals showed the metallic conductivity in (a, b) plane with temperature. The same effect of partial oxygen pressure on horizontal Bridgman growth was investigated in [56]. For the horizontal setup the average size of Bi-2212 single crystals was much smaller compared with the vertical Bridgman growth although the growth conditions were very similar. Again the largest samples with dimensions up to  $3 \times 4 \text{ mm}^2$  in (a, b) plane have been prepared at  $p(O_2) = 21$  kPa. The *c*-axis values were 30.933, 30.885 and 30.840 Å for the single crystals grown at  $p(O_2) = 0$ , 21 and 100 kPa, respectively. No impurity phases have

been detected from XRD patterns. The as-grown Bi-2212 samples demonstrated the superconducting transition at 84 K from resistivity data.

In summary, the Bridgman technique allowed the preparation of large in (a,b) plane crystals with dimensions up to 120 mm<sup>2</sup> that is about one order larger than flux-grown samples. The most bulky Bridgman grown crystals have thickness up to 0.1 mm along c-axis which is several times better compared with flux prepared samples. Also, Bi-2212 single crystals fabricated by Bridgman method demonstrated the similar mosaicity and comparable  $T_c$ , but they showed no Al contamination compared with flux-grown samples.

### 3.5.3 FZ Growth of Large-Size Crystals

It is quite easy for crystal growers to obtain thin, plate-like Bi-2212 single crystals with thickness 20–100  $\mu$ m along c-axis by both flux and Bridgman methods. Nevertheless, this size is not sufficient for neutron scattering, optical and transport experiments. In general, all studies of physical properties anisotropy have need of much thicker samples along c-axis. The dramatic progress in the fabrication of large size and thick Bi-2212 crystals has been achieved by applying the crucible-free floating zone technique [17, 38, 39, 44]. The temperature gradient on a crystalization front is one order larger for FZ method than in Bridgman growth. It allowed the preparation of Bi-2212 crystals with thickness up to 1.0 mm along c-axis. Also, the FZ method makes very easy the control of a growth atmosphere, and even gas pressures up to 10 bars can be applied for commercially available furnaces produced by CSI (Japan). Moreover, there is no crystal contamination problem because it is crucible-free growth. Therefore, a lot of growth efforts have been done since the first publication in 1988 [17].

#### 3.5.3.1 Growth Conditions and Sample Characterization

The first FZ grown Bi-2212 single crystals were prepared in [17] using the double-mirror type image furnace (NEC, Japan) equipped with 1.5 kW halogen lamps as a heat source. Powders of Bi<sub>2</sub>O<sub>3</sub>, SrCO<sub>3</sub>, CaCO<sub>3</sub> and CuO (each of 3 N purity) were used as the raw materials. They were mixed and calcined at 760 °C for 12 h in alumina crucible and subsequently treated at 860 C for 2–3 days. Thus prepared mixture was placed into a rubber tube and pressed by CIP under 1000 kg/cm<sup>2</sup>. Finally, the well-pressed rod was synthesized at 870 °C for 12 h in oxygen flow. The FZ growth conditions were as follows: pulling rate of 1 mm/h and oxygen flow rate of 0.6 l/h. The upper and lower shafts were counter-rotated at 30 rpm. The preliminary growth experiments showed that the feed rod of Bi<sub>2.2</sub>Sr<sub>1.8</sub>Ca<sub>1.0</sub>Cu<sub>2.0</sub>O<sub>y</sub> composition co-exists with the molten zone of Bi<sub>2.4</sub>Sr<sub>1.5</sub>Ca<sub>1.0</sub>Cu<sub>1.8</sub>Oy composition during the steady growth. So, a solvent pellet of this composition was placed between feed and seed rods, and then the crystal

growth was performed using this solvent as a molten zone. An as-grown ingot was an aggregate of large single crystalline  $Bi_{2.2}Sr_{1.8}Ca_{1.0}Cu_{2.0}O_y$  grains with dimensions up to  $8 \times 4 \times 0.2$  mm<sup>3</sup>. These Bi-2212 grains demonstrate well-pronounced tendency to grow along a-axis and can be easily cleaved in the (a, b) plane. As-grown samples possessed an orthorhombic symmetry with a superstructure, and unit cells parameters a, b and c were 5.43, 5.43 and 30.63 Å respectively. Two types of growth impurities have been observed by polarized optical microscope and EDX analysis. A small amount of  $(Sr_{1.5}Ca_{1.3}Bi_{0.2})Cu_{5.0}O_y$  phase was detected close to the lateral surface of as-grown ingot. Rarely Bi-2201 inclusions have been revealed in the center area of ingot. Most probably, the latter inclusions were formed due to the cellular growth. Therefore, it was concluded that the growth rate has to be lowered in order to avoid this unfavourable effect [17]. The as-grown Bi-2212 samples reached zero resistance at 92 K and showed metallic conductivity in (a, b) plane with temperature.

In [57] a significant improvement of FZ method was done by elaboration of so-called pre-melting technique allowing the densification of as-sintered feed rod. In this technique a molten zone was rapidly passed through a feed rod at a high rate of 20-50 mm/h. As a result a pre-melted feed rod got density over 90 % although initial rod density was about 48 % only [57]. In the last case molten zone was usually sucked up by the porous rod at low pulling rates (below 1 mm/h) that terminated a growth run. Thus, a pre-melting treatment was found to be very effective in maintaining a stable molten zone at low growth rates. Nowadays, the pre-melting of feed rods is always used for the growth of all Bi-based superconductors because the melting point is below 920 °C for all members of this family. Therefore, the preparation of high dense feed rods by standard solid state synthesis is fully impossible due to the low (<900 °C) sintering temperatures. The Bi-2212 single crystals were grown using NEC SC-2 (Japan) double-mirror type furnace equipped with 1.0-1.5 kW halogen lamps. The pulling rate was 0.5 mm/h. It was demonstrated that only growth rates lower 2 mm/h yielded a single phase ingot, and thickness along c-axis drastically increased with reducing of a pulling rate. At the same time the pulling rate of 0.5 mm/h was the lower limit for this NEC oven. Both upper and lower shafts were counter-rotated at 10 rpm. Partial oxygen pressure was varied in the wide range ( $p(O_2) = 0$ , 22, 60, 100 kPa) during growth experiments. Highest stability of MZ was observed at  $p(O_2) = 22$  kPa while bubbles in MZ were always observed at higher oxygen pressures that made a crystal growth completely unstable. The Sr/Ca ratio in the feed rod of Bi<sub>2.2</sub>(Sr,Ca)<sub>2.8</sub>Cu<sub>2.0</sub>O<sub>v</sub> composition was varied from 0.57 to 1.8 at  $p(O_2) = 22$  kPa. Cross sections of as-grown Bi-2212 ingots fabricated at different Sr/Ca ratios were examined using optical polarized microscope. The most thick single crystalline grains were observed at Sr/Ca = 1.4, and no single phase ingots were prepared at Sr/Ca < 0.6. As a result Bi-2212 single crystals with dimensions up to  $50 \times 5 \text{ mm}^2$  in (a, b) plane were obtained. It was claimed that as-grown crystals showed thickness up to 1.0 mm along c-axis based on optical microscope inspection. Unfortunately, no neutrons and/or X-ray rocking curves were given to support this statement. The lattice parameters were a = 5.413Å, b = 5.411 Å and c = 30.810 Å for Sr/Ca = 1.8 in Bi-2212 crystals. Based on EDX analysis the Sr/Ca ratio in Bi-2212 samples varied from 1.8 to 2.0 for different feed rod compositions and partial oxygen pressures. The  $\rm Bi_{2.2}Sr_{1.8}Ca_{1.0}Cu_{2.0}$  single crystals grown at  $\rm p(O_2)=22~kPa$  demonstrated zero resistance at 83 K from resistivity measurements. Also, significant change in density was noted among ingots reflecting a fluctuation of chemical compositions.

In [39] large size Bi-2212 single crystals were grown using the Bi<sub>2.1</sub>Sr<sub>1.9</sub>Ca<sub>1.0</sub>Cu<sub>2.0</sub>O<sub>v</sub> feed rod and Bi<sub>2.6</sub>Sr<sub>1.9</sub>Ca<sub>1.0</sub>Cu<sub>2.6</sub>O<sub>v</sub> solvent compositions at 0.35 mm/h in air. The deeply upgraded NEC SC-N35HD (Japan) image furnace was employed which allowed the using of this very low pulling rate and oxygen pressure up to 6 bars. The authors [39] used as-sintered feed rod without pre-melting. The initial Bi<sub>2</sub>O<sub>3</sub>, SrCO<sub>3</sub>, CaCO<sub>3</sub> and CuO powders of 3 N purity were well-mixed and fired at 850 °C with intermediate grindings. The feed rods were pressed by hydrostatic press under 3.5 kbars and finally sintered at 880 °C for 24 h in air. The density of feed rods was about 85 %. The Bi-2212 single crystals with dimensions up to  $15 \times 4 \times 0.12 \text{ mm}^3$  were cleaved from as-grown ingots. The EDX analysis gave the Bi<sub>2.18</sub>Sr<sub>1.87</sub>Ca<sub>0.99</sub>Cu<sub>1.97</sub>O composition for these samples. The lattice parameters were a = 5.33 Å, b = 5.48 Å and c = 30.76 Å from powder X-ray diffraction. The powder XRD analysis indicated a very small amount of foreign phases. The optical polarized microscope study combined with EDX analysis found the presence of Bi<sub>4.8</sub>Sr<sub>2.7</sub>Ca<sub>0.8</sub>Cu<sub>2.0</sub>Oy impurities. Also, the high resolution electron microscope investigation revealed a weak intergrowth of Bi-2201 phase although its amount was about 0.2 %. The magnetization measurements demonstrated superconducting transition at  $T_c = 88$  K and  $\Delta T_c = 2.2$  K. Also, Ni-doped Bi-2212 single crystals have been prepared in this work. However, the size of Ni-doped samples became smaller with increasing Ni content, and  $T_c$ was suppressed to 83 K (Cu/Ni = 1.98/0.02) and 78 K (Cu/Ni = 1.96/0.04).

Stoichiometric Bi<sub>2</sub>Sr<sub>2</sub>CaCu<sub>2</sub>O<sub>v</sub> feed rods were applied in [58] for the floating zone growth of superconducting Bi-2212 crystals. Mixture of Bi<sub>2</sub>O<sub>3</sub>, SrCO<sub>3</sub>, CaCO<sub>3</sub> and CuO powders taken in soichiometric ratio was calcined at 865 °C for 24 h in air with several intermediate grindings. The obtained powder got an average grain size between 5 and 10 µm. It was isostatically pressed at 2.5 kbars, and final sintering was performed at 865 °C in air. The density of as-sintered rods ranged between 80 and 85 % and was not enough to prevent soaking of the melt into porous ceramic bars. Therefore, feed rods were pre-melted at 80 mm/h in air. The pre-melted rods of diameter 7–8 mm were used for a FZ growth at the pulling rates of 1-2 mm/h. The upper and lower shafts were counter-rotated at 40 rpm. Air pressure was 2 bars during the growth. In this work a stable MZ with 4-5 mm in diameter and 5 mm in length was maintained between feed and seed rods. Plate-like Bi-2212 single crystals with typical dimensions of  $10 \times 3 \times 0.3 \text{ mm}^3$  were cleaved from as-grown ingots. Wet chemical analysis gave the Bi<sub>2.02</sub>Sr<sub>2.00</sub>Ca<sub>0.98</sub>Cu<sub>1.99</sub>O<sub>y</sub> crystal composition. X-ray diffraction experiments on as-grown and crushed single crystals revealed the pseudo-tetragonal structure with  $a \approx b = 5.4$  Å and c = 30.97 Å. No impurity phases were detected. For as-grown samples superconducting transition at  $T_c = 91$  K and width of the transition  $\Delta T_c = 5-6$  K were found.

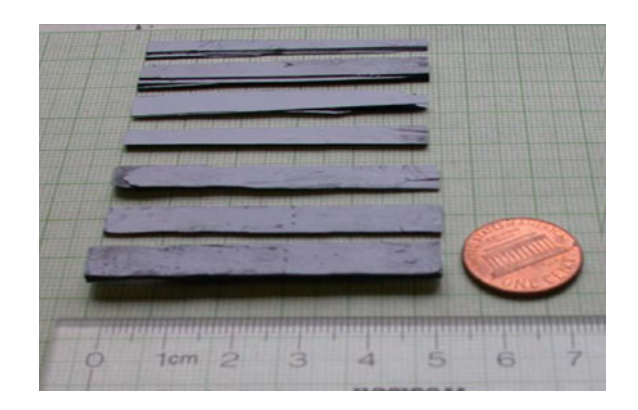
Undoped and Y-doped Bi-2212 crystals were obtained in [59]. Nominal compositions of feed rods and solvent pellets were  $Bi_{2.2}Sr_{1.8}Ca_{1-x}Y_xCu_2O_y$  (x = 0.0, 0.2, 0.4) and Bi<sub>2.4</sub>Sr<sub>1.5</sub>Ca<sub>1-x</sub>Y<sub>x</sub>Cu<sub>1.8</sub>O<sub>y</sub> (x = 0.0, 0.2, 0.4), respectively. The feed rods were pressed by hydrostatic press and sintered at 850-900 °C for 62 h. Single-crystal growth was performed using double-mirror type image furnace NEC SC-35HD (Japan) equipped with halogen lamps. Pre-melting of as-sintered feed rods was done at 7-8 mm/h, and crystal growth was carried out at 0.4-0.5 mm/h. Undoped Bi-2212 samples had average dimensions of  $5 \times 3 \text{ mm}^2$ , but the size of vttrium doped crystals decreased with Y-doping and was about  $2.0 \times 0.5 \text{ mm}^2$  in (a, b) plane. Powder X-ray diffraction patterns confirmed that x = 0 crystals consisted of almost pure Bi-2212 phase, but Bi-2201 phase was distinctly observed in Y-substituted samples. The lattice constant along c-axis decreased from 30.75 Å to 30.30 Å with Y-doping, but those along a- and b-axes did not demonstrate any noticeable changes. The high-resolution electron microscopy images showed that undoped samples were homogeneous and contained Bi-2212 phase only, but Y-substituted crystals have got many structural distortions and even an amorphous phase. The superconducting onset transition temperatures were 84, 90 and 80 K for x = 0.0, 0.2 and 0.4, respectively, based on magnetization measurements. The superconducting transition width was drastically broadened by Y-substitution suggesting non-uniform distribution of Y atoms in Bi-2212 phase.

The effect of oxygen pressure on Bi-2212 crystal growth was investigated in [60]. Powders of Bi<sub>2</sub>O<sub>3</sub>, SrCO<sub>3</sub>, CaCO<sub>3</sub> and CuO (3 N purity and better) were taken in the ratios of Bi:Sr:Ca:Cu = 2.1:1.9:1.0:2.0 and Bi:Sr:Ca:Cu = 2.6:1.9:1.0:2.6 for feed rods and solvent, respectively. The powders were pressed under hydrostatic pressure of 3.5 kbars after calcination at 820 °C and then sintered at 840 °C for 48 h in air. Prior to the crystal growth step, the feed rods were densified by pre-melting at 60-80 mm/h in air. The crystal growth was performed in the upgraded NEC SC-N35HD (Japan) double-mirror type image furnace equipped with 1.5 kW halogen lamps. Upper and lower shafts were counter rotated at 30 rpm. The growth rate was about 0.26 mm/h. The applied oxygen pressure was 22, 200 and 300 kPa during the growth. For the growth in air, "large-volume" Bi-2212 samples were prepared for neutron diffraction experiments with the largest dimensions up to  $12 \times 5 \times 1.5 \text{ mm}^3$  and the weight 690 mg. Neutron scattering results demonstrated that this big sample actually consisted of one large and one small single crystalline grains that were closely aligned along c-axis (mismatch less than 2°) and with rocking curves of 0.4° and 0.6°, respectively. Large plate-like Bi-2212 crystals with sizes up to  $16 \times 4 \times 0.5 \text{ mm}^3$  have been made at 200 and 300 kPa oxygen pressures. The Sr/Ca ratio in Bi-2212 crystals linearly increased with oxygen pressure from 1.85 (in air) to 2.10 (p(O2) = 300 kPa), although Bi and Cu contents were nearly unchangeable. According to the powder X-ray diffraction all Bi-2212 samples got the tetragonal symmetry. No change in the a-axis was detected. At the same time the c-axis enlarged from 30.78 Å (in air) to 30.88 Å at p (O2) = 200 kPa and then shortened to 30.81 Å at p(O2) = 300 kPa. Also, the results of magnetization measurements showed that superconducting temperature,  $T_c$ , depended strongly from the applied oxygen pressure. The onset  $T_c$  varied from 88 K (in air) to 95 K (p(O2) = 200 kPa) and then reduced to 91 K (p (O2) = 300 kPa). The width of superconducting transition was about 2 K independent from oxygen pressure. Thus, the pressure behaviour of both c-axis and onset  $T_c$  demonstrated well-defined similarity: both parameters got saturation at p (O2) = 200 kPa.

The dramatic effect of feed rod composition and growth rate on the thickness of Bi-2212 crystals along c-axis was reported in [38]. High quality Bi-2212 single crystals with dimensions up to  $50 \times 6 \times 1.5$  mm<sup>3</sup> have been prepared (Fig. 3.23) using the Bi<sub>2.1</sub>Sr<sub>1.9</sub>Ca<sub>1.0</sub>Cu<sub>2.0</sub>O<sub>v</sub> feed rod composition and pulling rate 0.2 mm/h [38, 61]. Based on X-ray diffraction study all Bi-2212 single crystals grew along aaxis. The Bi<sub>2.5</sub>Sr<sub>1.9</sub>Ca<sub>1.0</sub>Cu<sub>2.6</sub>O<sub>v</sub> solvent composition was always employed. Prior to the growth feed rods sintered at 860 °C were then pre-melted at 25 mm/h in air. The authors [38] studied the influence of feed rod composition and pulling rate on the morphology of the solid-liquid interface between molten zone and grown crystal. It was found that the planar crystallization front resulted in the growth of thick Bi-2212 crystals was very sensitive to the growth rate and feed rod composition. The solid-liquid interface became cellular for pulling rates larger than 0.2 mm/h that led to the growth of Bi-2212 crystals with thickness less than 0.2 mm along c-axis. Also, any deviation in the feed rod composition from the optimal Bi<sub>2.1</sub>Sr<sub>1.9</sub>Ca<sub>1.0</sub>Cu<sub>2.0</sub>O<sub>v</sub> one caused the cellular solid-liquid interface even at pulling rate of 0.2 mm/h. Thus, the low pulling rate and the optimal feed rod composition were highly demanded for maintaining the planar crystallization front that allowed the growth of bulky and impurity-free Bi-2212 samples. The cellular crystallization front always led to the presence of impurity phases on grain boundaries in as-grown Bi-2212 ingots [38].

Non-continuous parallel micro-cracks along b-direction were found in thick Bi-2212 crystals that was a serious obstacle for transport measurements along c-axis. The larger the c-axis thickness of a Bi-2212 crystal, the more pronounced was the micro-crack problem. Most probably, these micro-cracks were originated from a large thermal stress caused by very high radial and axial temperature gradients in image furnace. Neutron diffraction study performed on a large Bi-2212 crystal of

**Fig. 3.23** Bi-2212 single crystals cleaved from as-grown ingot [61]



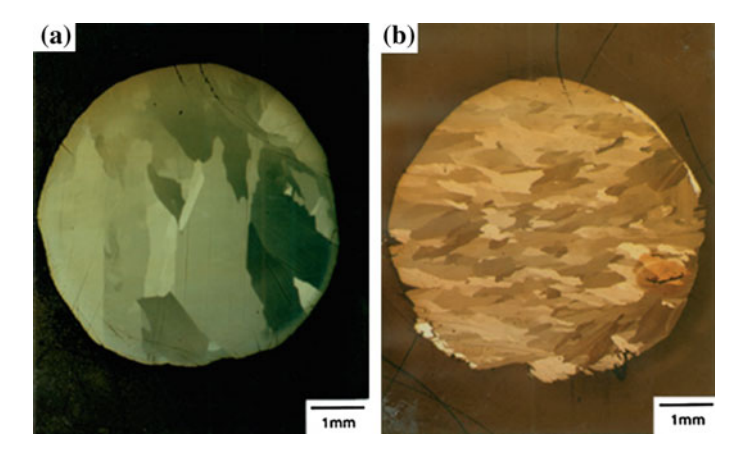


Fig. 3.24 Microstructure of Al-doped as-grown ingots prepared at 0.2 mm/h.  $\mathbf{a}$  y = 0;  $\mathbf{b}$  y = 0.1 [63]. © IOP Publishing. Reproduced with permission. All rights reserved

volume  $10 \times 5 \times 1.2$  mm<sup>3</sup> demonstrated the mosaicity of about 1° indicated the good quality of this sample [62]. For as-grown Bi-2212 crystals  $T_{c,onset}$  = 91 K and  $\Delta T_c$  = 2 K were found from magnetization measurements. The Al-doped Bi-2212 single crystals have been grown in [63] using the same low pulling rate approach. The optical polarization microscope photographs (Fig. 3.24) demonstrated the effect of Al-doping on microstructure of Bi<sub>2.1</sub>Sr<sub>1.9</sub>Ca<sub>1.0</sub>Cu<sub>2.0</sub>Al<sub>y</sub>O<sub>x</sub> ingots prepared at 0.2 mm/h. The size of Bi-2212 crystals became much smaller with increasing Al content in a feed rod. Based on the optical inspection of undoped and Al-doped ingots this effect was ascribed to the transition from the planar crystallization front to the cellular one caused by Al-doping. The results of EDX analysis showed that the solubility limit for Al in the Bi-2212 crystals was less than 0.5 %.

The FZ growth of Fe-doped Bi-2212 single crystals was performed in [64]. The feed rods were prepared by standard solid state synthesis including the hydrostatic pressing and final sintering at 860 °C for 72 h. Sintered rods were densified by pre-melting at 25 mm/h in order to maintain a stable molten zone during a growth. All experiments were done in air. The pulling rate was 0.2 mm/h, upper and lower shafts were counter-rotated at 30 rpm. The as-grown Bi<sub>2.1</sub>Sr<sub>1.9</sub>Ca<sub>1.0</sub>(Cu<sub>1-v</sub>Fe<sub>v</sub>)<sub>2</sub>O<sub>x</sub> ingots were examined by optical polarized microscope, EDX, SEM and X-ray analysis. It was revealed that the crystallization front had the planar solid-liquid (S-L) interface for  $y \le 0.01$ . The maximum thickness along c-axis for undoped samples (y = 0.0) was about 2 mm. When y > 0.01, the planar S-L interface changed its morphology to the cellular one. At the same time the thickness along caxis of single crystals reduced abruptly. The maximum thickness was 0.3 mm for y = 0.03 only. When y = 0.06, the as-grown ingot consists of very tiny multiphase grains and no Fe-doped Bi-2212 crystals were obtained. The Bi-2212 single phase ingots have been prepared for  $y \le 0.01$  only. For 0.015 < y < 0.03 the as-grown ingots consisted of almost single phase, but a small quantity of impurities was

detected on grain boundaries. Thus, the Fe doping dramatically disturbed the crystal growth conditions and consequently decreased dimensions of as-grown single crystals. This result is very similar to the effect of Al-doping on Bi-2212 crystal growth [63]. The maximum Fe solubility limit in Bi-2212 crystals is less than 0.03 at. %. It was demonstrated that Fe substitution sharply reduced not only the superconducting transition temperature, but also the homogeneity of the superconducting phase in single crystals.

In summary, it was unambiguously established in [38, 61–64] that the planar crystallization front was the indispensable condition for the growth of thick (1–2 mm) along *c*-axis Bi-2212 crystals. The planar solid-liquid interface between molten zone and grown crystal was achieved for the optimal Bi<sub>2.1</sub>Sr<sub>1.9</sub>Ca<sub>1.0</sub>Cu<sub>2.0</sub>O<sub>y</sub> feed rod composition and pulling rate of 0.2 mm/h merely. The planar S–L interface showed the strong tendency to break into a cellular one with (i) increase of the pulling rate above 0.2 mm/h and (ii) any deviation from the optimal feed rod composition. The cellular S–L interface resulted in growth of thin (<0.2 mm) along *c*-axis Bi-2212 samples.

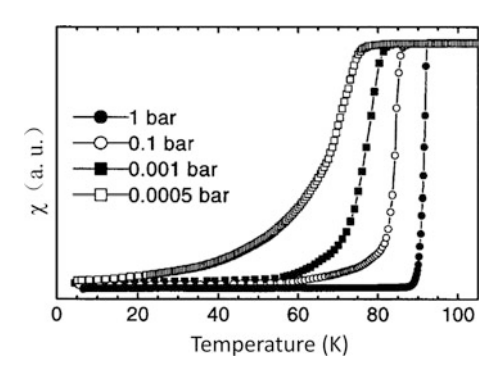
The FZ growth of under-doped Bi-2212 single crystals was carried out under low oxygen partial pressures  $p_{(O2)} = 1, 5 \times 10^{-1}, 1 \times 10^{-1}, 5 \times 10^{-2}, 1 \times 10^{-3}$  and  $5 \times 10^{-4}$  bar in [35]. Based on results of [38, 61] the Bi<sub>2.1</sub>Sr<sub>1.9</sub>CaCu<sub>2</sub>O<sub>y</sub> starting composition and slow growth rate of 0.2 mm/h were used for the growth. Prior to the crystal growth as-sintered feed rods were pre-melted at 25 mm/h. The crystal growth was carried put in four-mirror type image furnace (CSI, Japan) equipped with 300 W halogen lamps. It was found that the stability of molten zone and dimensions of Bi-2212 crystals were nearly insensitive to the oxygen pressure in the range from 1 to  $1 \times 10^{-3}$  bar. Bi-2212 single crystals with the considerable sizes up to  $15 \times 5 \times 1$  mm<sup>3</sup> have been obtained (Fig. 3.25).

At the same time the superconducting transition width,  $\Delta T_c$ , which is known to be an indication of the oxygen homogeneity, increased from 2 to 10 K when p(O<sub>2</sub>) reduced from 1 to  $1 \times 10^{-3}$  bar. The superconducting transition temperature,  $T_c$ , reduced from 92 K (optimal doped regime) to 79 K (under-doped regime) with decreasing p(O<sub>2</sub>) from 1 to  $1 \times 10^{-3}$  bar (Fig. 3.26). The results of chemical analysis (EDX and ICP) showed no remarkable difference in actual crystal compositions as compared with the starting composition except for the growth at p(O<sub>2</sub>) =  $5 \times 10^{-4}$ 

**Fig. 3.25** Typical underdoped Bi-2212 crystals [65]



**Fig. 3.26** Dependence of superconducting transition from  $p(O_2)$  [65]



bar. For this oxygen pressure the significant Bi-2212 phase decomposition was observed based on visual inspection of as-grown ingot and powder XRD data. No trace of secondary phases was detected from XRD data for  $p(O_2) = 1 \sim 5 \times 10^{-2}$  bar, which means that the Bi-2212 material remained stable in this pressure range. When  $p(O_2) = 1 \times 10^{-3}$  bar was applied, a tiny amount of Bi<sub>2</sub>O<sub>3</sub> was detected in as-grown Bi-2212 ingot. All as-grown Bi-2212 samples had orthorhombic symmetry, and c-axis increased from 30.731 Å at  $p(O_2) = 1$  bar to 30.912 Å at  $p(O_2) = 1 \times 10^{-3}$  bar.

Usually, the oxygen content of overdoped Bi-2212 crystals is controlled by oxygen annealing either in oxygen flow or under oxygen pressure. On this way several difficulties were encountered: one is oxygen inhomogeneity introduced by slow cooling of a sample after oxygen treatment that caused a broad superconducting transition. On the other hand the quenched Bi-2212 crystals always demonstrated high-temperature disorder frozen by fast cooling. This disorder led to the electron localization at low temperatures and the worsened structural quality [66, 67]. Possible way to overcome these difficulties was the FZ growth under high oxygen pressures [37] aiming the fabrication of as-grown over-doped Bi-2212 samples. The Bi<sub>2.1</sub>Sr<sub>1.9</sub>CaCu<sub>2.0</sub>O<sub>v</sub> feed rods were prepared by standard solid state synthesis. Prior to crystal growth, the feed rods have been pre-melted at 27 mm/h under different oxygen pressures from 1 to 10 bars. The crystal growth was carried out in four-mirror type image furnace (CSI, Japan) equipped with 300 W halogen lamps. The pulling rate was varied from 0.2 to 0.4 mm/h. It was found that the molten zone was much less stable under oxygen pressure compared with air growth. The MZ volume was slowly and periodically increased during the growth process. In this case both melting and solidification fronts moved up and down in contrary directions. This effect finally led to the zone collapse. When the MZ volume increased the growth direction of ingot randomly deviated of about 10°-30° from the vertical axis of the zone. The period of the stable MZ volume was dependent from applied oxygen pressure, i.e. the higher the pressure the shorter is the period of stable growth. As a result, the grown ingot has got a zigzag form. The instability of the MZ under high oxygen pressures was caused by the precipitation of impurity phases, namely Bi-2201, (Sr, Ca)<sub>2</sub>CuO<sub>3</sub> and BiO<sub>x</sub>. The small yellowish BiO<sub>x</sub> spots were

well visible even by naked eyes in ingot portions corresponding to the unstable growth. It was found from XRD data that feed rods contained the same impurity phases after pre-melting under 8-10 bars oxygen pressure while pre-melted in oxygen flow feed rods consisted of Bi-2212 phase only. Multi-phases feed rods drastically affected the MZ stability during the growth step. For example, the MZ was very unstable even under 4 bars oxygen pressure if the pre-melting was done under 10 bars. On the other hand, the MZ was well stable under oxygen pressure of 10 bars if the feed rod was pre-melted under oxygen pressure of 1–2 bars. As a result, Bi-2212 single crystals with dimension up to  $9 \times 2 \text{ mm}^2$  in (a, b) plane have been obtained under 10 bars oxygen pressure, although their thickness along c-axis was about 0.1-0.2 mm. These crystals had orthorhombic structure. The lattice parameters were a = 5.323(5) Å, b = 5.418(5) Å and c = 30.653(8) Å. The crystals grown under 10 bars oxygen pressure have got the Bi<sub>2.18</sub>Sr<sub>1.81</sub>CaO<sub>0.89</sub>Cu<sub>2.0</sub>O<sub>v</sub> composition. For comparison, samples fabricated in oxygen flow showed more stoichiometric Bi<sub>2.10</sub>Sr<sub>1.90</sub>Ca<sub>0.89</sub>Cu<sub>2.0</sub>O<sub>v</sub> composition. At the same time the *c*-axis gradually decreased from 30.890 Å (2 bars) to 30.653 Å (10 bars).

The results of magnetization measurements on as-grown overdoped Bi-2212 single crystals are shown on Fig. 3.27. The onset  $T_c$  reduced compared with optimally doped crystals from 95 K (not shown) to 81 K (10 bars). The  $\Delta T_c$  was about 12–15 K and independent on the applied pressure. This value was the same or even smaller compared with oxygen annealed samples [67]. It was found that the oxygen distribution in crystals was influenced by the applied oxygen pressure during the growth and the proceeding of feed rods.

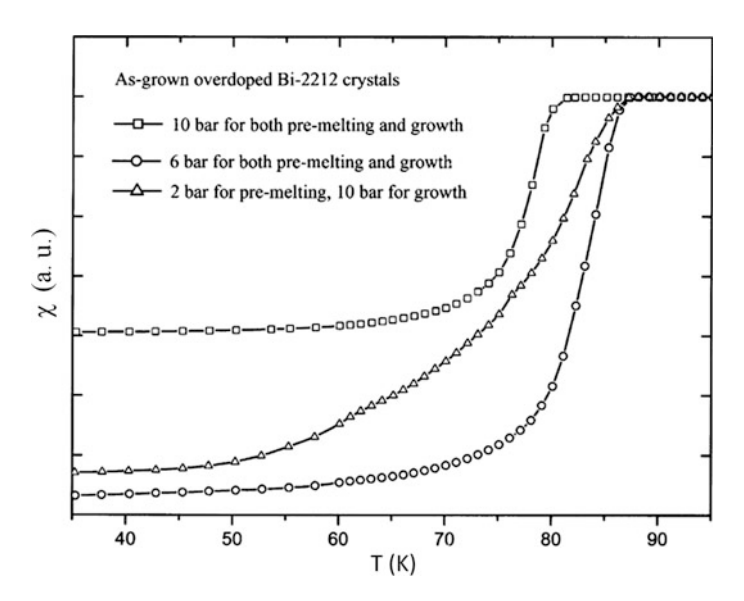


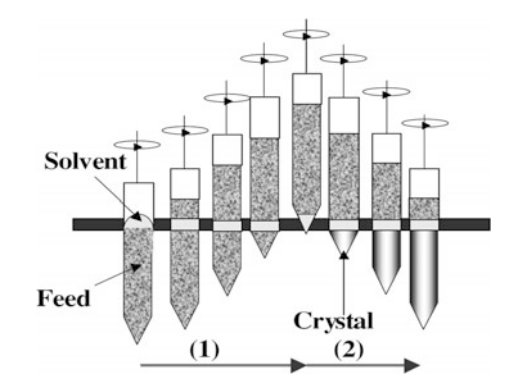
Fig. 3.27 Superconductivity of as-grown overdoped Bi-2212 crystals [67]

An interesting growth approach was realized in [68]. The authors applied FZ growth in gold crucibles due to the much less pronounced Au corrosion compared with Pt and Al<sub>2</sub>O<sub>3</sub> materials. For the growth a small amount of Bi<sub>2.1</sub>Sr<sub>1.5</sub>CaCu<sub>1.8</sub>O<sub>v</sub> solvent was put on a top of a previously melted feed rod. Both solvent disk and feed rod were charged in a gold crucible, and the molten solvent was passed through the feed rod by a zone melting technique. The main advantage of this approach compared with the crucible-free FZ method was the molten zone stabilization due to its support by crucible walls. The Bi<sub>2.1</sub>Sr<sub>1.8</sub>CaCu<sub>2.0</sub>O<sub>v</sub> feed rod was calcined at 770 °C for 24 h, and then pressed under hydrostatic pressure of 300 MPa. The cylindrical rod was finally sintered at 830 °C for 12 h. After that the sintered rod was pre-melted at 50 mm/h by using infrared image furnace. The pre-melted rod was filled into a gold crucible of a hollow pencil shape. In order to remove a void between feed rod and crucible walls the authors partly melted the rod at 915 °C. The furnace used for the crystal growth was handmade kantal wire electric resistance oven. In the furnace the coil density at the center was increased and gradually reduced towards both ends to produce a narrow hot zone. The temperature gradient in a hot zone was 25 °C/cm.

The growth process is schematically illustrated on Fig. 3.28. The crucible was first placed with its top close to the hot zone. Then the molten solvent was transferred from the top to the crucible bottom by lifting up the crucible at 1 mm/h (1st stage). After that the crystal growth (2nd stage) was performed by passing the solvent upwards at the rate of 0.2–04 mm/h. As a result the authors have obtained Bi-2212 single crystals with dimensions up to  $3\times4\times0.5$  mm<sup>3</sup>. The crystal composition was Bi<sub>1.97</sub>Sr<sub>1.75</sub>Ca<sub>0.88</sub>Cu<sub>2.0</sub>O<sub>y</sub> and no gold contamination from the crucible was detected from EDX data. The Bi-2212 samples showed superconducting transition at 85 K after annealing in air at 800 °C for 72 h.

Usually the FZ grown Bi-2212 single crystals are less stoichiometric compared with flux and Bridgman prepared samples. They are nearly always Bi-rich and Sr-deficiency according to the chemical formula  $Bi_{2.1}Sr_{1.9}Ca_{1.0}Cu_{2.0}O_y$ . Nevertheless, the high quality floating zone grown Bi-2212 crystals demonstrate the superconducting transition at around 90 K.

Fig. 3.28 The sketch of the growth process [68]. © IOP Publishing. Reproduced with permission. All rights reserved



#### 3.5.3.2 Effect of Oxygen Annealing on Superconductivity

The Bridgman and FZ grown Bi-2212 crystals were annealed in air and oxygen flow (1 bar) at 500, 600, 700 and 800 °C for 72 h in [69]. Effect of annealing temperature,  $T_{ann}$ , on  $T_c$  and  $\Delta T_c$  was studied. The  $\Delta T_c$  value is related to the homogeneity of cations composition, crystal structure, oxygen content and oxygen distribution in crystals. Usually, it is assumed that the smaller  $\Delta T_c$  is, the more homogeneous are the crystals. Annealing the Bridgman grown Bi-2212 crystals in air at 500 °C resulted in a large decrease of  $\Delta T_c$  from 35 K to 15–20 K. At the same time  $T_c$  increased from 70 K (as-grown) to 83 K (air-annealed). Further enlargement of  $T_{ann}$  from 500 to 800 °C did not lead to a large change in either  $T_c$  or  $\Delta T_c$ . Opposite to this result, air-annealing of FZ grown Bi-2212 crystals at 500 °C reduced superconducting transition temperature from 90 to 80 K and increased the transition width. Annealing in oxygen flow at temperatures in the range 500–800 °C showed no detectable differences in either  $T_c$  or  $\Delta T_c$  between air-treated and oxygen-treated samples independent from the growth pre-history.

In [70] the vacuum annealing was carried out on Bi-2212 crystals sealed in quartz ampoules under different partial oxygen pressures ranging from  $8 \times 10^{-1}$  to  $5 \times 10^{-4}$  bar. The high quality Bi-2212 single crystals were grown by FZ method similar to [38, 65]. The superconducting transition temperature was found to be affected more strongly by the applied partial oxygen pressure, p(O<sub>2</sub>), than by the annealing temperature. The optimal annealing conditions were found to be 430 °C and 220 h. The  $T_c$  value reduced significantly from 92 to 29 K with decreasing p (O<sub>2</sub>) from 1 down to  $4 \times 10^{-2}$  bar (Fig. 3.29). The transition remained relatively

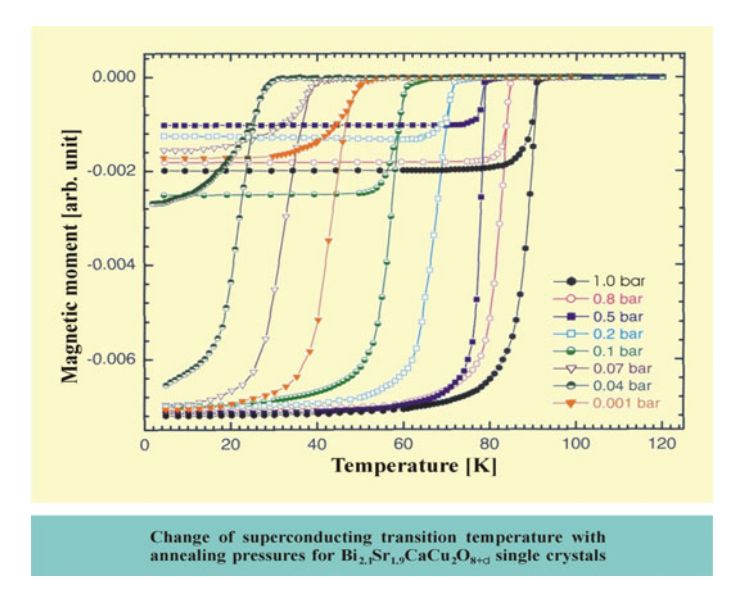


Fig. 3.29 DC susceptibility of annealed Bi-2212 samples [70]

sharp for the samples annealed under  $p(O_2) = 8 \times 10^{-1} - 4 \times 10^{-2}$  bar with no evidence of Bi-2212 phase decomposition from powder XRD data. The XRD studies demonstrated that all samples have the orthorhombic symmetry.

The refinement of XRD data showed that the c-axis expands, while both a- and b-axis shrink up slightly with decreasing p(O<sub>2</sub>). The c-axis increased from 30.731 (1) Å (as-grown) up to 30.923(1) Å (4 × 10<sup>-2</sup> bar). The relation between  $T_c$  and c-axis lattice parameter suggested that the change of superconducting temperature is well correlated with a re-distribution of holes between Bi-O layers and Cu-O planes. Impurity phases were detected for all Bi-2212 samples treated under p(O<sub>2</sub>) < 4 × 10<sup>-2</sup> bar indicating the phase instability limit of Bi-2212 compound at low partial oxygen pressures. Although vacuum annealing remarkably suppressed  $T_c$  however it hardly changed  $\Delta T_c$ . Therefore, it was rather important to select as-grown crystals with narrow superconducting transition in order to produce high-quality under-doped crystals though vacuum annealing. The results of [70] demonstrated that  $\Delta T_c$  of under-doped Bi-2212 samples was generally broader than that of over-doped crystals. Furthermore, it was argued that oxygen-deficient samples were more sensitive to chemical disorder than highly oxygen-doped crystals.

The over-doped Bi-2212 samples were prepared in [71] by oxygen annealing at 1, 5 and 12 bars at 540 °C for 18 h. The crystals were flux-grown and had dimensions along c-axis about 20–100  $\mu$ m. The typical crystal composition was Bi<sub>2.10</sub>Sr<sub>1.94</sub>Ca<sub>0.88</sub>Cu<sub>2.07</sub>O<sub>v</sub> from electron probe microanalysis (EPMA). No evidence of crystal inhomogeneity or phase separation for over-doped samples was found from XRD, magnetization and resistivity measurements. It was demonstrated that oxygen treatment produced very little change in a and b lattice parameters. However, a very distinct difference was seen in the c-axis length between as-grown samples (30.90 Å) and oxygen-annealed samples (30.81 Å). Annealing in flowing oxygen (1 bar) reproducibly reduced T<sub>c</sub> from 90 to 84 K. Further suppression of transition temperature from 84 to 79 K and finally to 77 K was observed after 5and 12-bars oxygen pressure treatments. The transition width was 2-5 K and no transition width broadening was detected as transition temperature was decreased from 90 to 77 K. The Hall-effect measurements demonstrated the increasing of carrier concentration (over-doped regime) from 0.34 mobile holes per Cu site (as-gown sample,  $T_c = 90 \text{ K}$ ) to 0.50 mobile holes per Cu site (12-bars  $O_2$ ,  $T_c = 77 \text{ K}$ ).

At the same time annealing at 750 °C in oxygen flow (1 bar) leads to the Bi-2201 phase segregation in Bridgman-grown Bi-2212 single crystals [72]. Also, it was mentioned in [77] that a surface of Bi-2212 crystal showed tiny degradation after heat treatment under 2.5 bars of oxygen pressure at 500 °C for several days. So, the temperature stability limit of Bi-2212 phase at elevated oxygen pressures is still unknown. In conclusion it is relatively easy to vary  $T_c$  of Bi-2212 samples in a wide range from 92 to 29 K in under-doped regime while it is still challenge to get over-doped samples with  $T_c$  below 80 K.

### **3.6 Bi-2223 Compound**

Both Bi-2201 and Bi-2212 superconductors have been available as sizeable high-quality single crystals and extensively studied so far. On the other hand fundamental investigations on the three-layered Bi<sub>2</sub>Sr<sub>2</sub>Ca<sub>2</sub>Cu<sub>3</sub>O<sub>y</sub> compound (hereafter Bi-2223) have been strongly embarrassed due to the lack of single crystals. Even more, the Pb-doped Bi-2223 compound is nowadays believed to be the most promising material for large scale applications of superconductivity at liquid nitrogen temperature, and has been the subject of tremendous studies in the past 20 years. But all these studies were done on powder/ceramic samples with small grain sizes and can be questioned because of significant boundary effects on sample properties. For example, the pinning characteristics of the Bi-2223 material in the absence of grain boundaries have been still largely unexplored due to the lack of high quality single crystalline samples. It is worth to mention that pinning properties play the key role in all possible commercial applications of Bi-2223 material.

Also, from the crystallographic point the three-layered Bi-2223 compound has to demonstrate highly anisotropic physical properties similar to the double-layered Bi-2212 material. And again this study strongly requires the availability of high quality and large size single crystals.

## 3.6.1 Main Growth Difficulties

Whereas the Bi-2201 and Bi-2212 compounds could be directly synthesized either from a melt or using a standard solid state reaction [4, 13, 17, 38], the Bi-2223 phase is quite difficult to prepare with acceptable purity even in powder form [73]. The question of phase formation is highly debated in literature, and different mechanisms have been proposed [73–75]:

- (i) a direct phase transformation from Bi-2212 into Bi-2223 through the insertion of additional Ca and Cu–O layers into the structure;
- (ii) a disproportionation reaction  $2 \cdot \text{Bi-}2212 \rightarrow \text{Bi-}2223 + \text{Bi-}2201$ ;
- (iii) a nucleation and growth from a liquid phase.

Therefore, even the selection of a nominal composition for a Bi-2223 solid state synthesis is not obvious. Also, the thermal stability range of Bi-2223 material is much smaller compared with Bi-2201 and Bi-2212 phases. According to [1] the Bi-2223 compound is stable only in a very narrow temperature range of about 50 °C just below the incongruent melting line. For comparison, Bi-2212 compound is stable in a wide temperature range between 650 and 895 °C [1]. Thus, the Bi-2223 phase solid state synthesis with acceptable purity has been a particularly difficult task. Moreover, the sluggish formation rate known for Bi-2223 phase makes this task even more arduous [76]. The Bi<sub>2</sub>O<sub>3</sub>(PbO)–SrO–CaO–CuO system contains

four or even five components that strongly complicates the phase equilibria investigations especially taken into account that this system has a certain tendency for a glassy behavior.

It was reported that the partial substitution of Bi by Pb can effectively enhance the phase formation kinetics as well as increase the yield of Bi-2223 phase [77]. The formation of Bi(Pb)-2223 phase is highly accelerated by the partial melting of Pb-doped samples. Nevertheless, the Pb-doped Bi-2223 samples are less attractive objects for the fundamental research because the substitution of Bi by Pb gives rise to additional complications in interpretation of physical measurements. From this point high-quality Pb-free Bi-2223 crystals are in great demand for the fundamental research.

The very interesting in-situ investigation of growth mechanism for compositions near the Bi<sub>2</sub>Sr<sub>2</sub>Ca<sub>2</sub>Cu<sub>3</sub>O<sub>v</sub> stoichiometry has been done in [78]. The authors used high-temperature optical microscope for in-situ observation of melting and crystallization processes. The solidified bodies were studied by EDX/SEM analysis. The authors made a conclusion that no nucleation and no growth of Bi-2223 was directly observed from a melt in all experiments independent from a starting composition. The Bi-2223 crystals were formed peritectically at 870 °C for 6.5 %  $O_2/93.5$  % Ar atmosphere according to reaction: (Sr, Ca)CuO<sub>x</sub> + Bi-rich melt  $\rightarrow$ Bi-2223. In air Bi-2223 phase was formed according to another peritectic reaction:  $(Sr,Ca)_{14}Cu_{24}O_x + Bi$ -rich melt  $\rightarrow$  Bi-2223. In both cases long-lasting annealing of about 50 h was required to observe the formation of Bi-2223 compound when Bi<sub>2.5</sub>Sr<sub>2</sub>Ca<sub>1.3</sub>Cu<sub>3.2</sub>O<sub>v</sub> starting composition has been used. No Bi-2223 crystals were found when stoichiometric Bi-2223 composition was utilized. These results are fully inconsistent with data given in [7, 73] where Bi-2223 material could be formed throughout the normal nucleation and growth within the primary crystallization phase field. This peritectic growth and the absence of a primary crystallization field could explain well why extremely low growth rates of 0.05 mm/h are necessary for the FZ growth of Bi-2223 crystals [79] compared with other Bi-based superconductors. It seems that the question of phase formation and thermal stability of Bi-2223 compound is still unclear and requires further investigations. All together it makes well understandable why the growth of Bi-2223 crystals has been a main challenge for crystal growers since the discovery of Bi-2223 compound in 1988 although a numerous efforts were done including flux and FZ growth.

Another commonly observed problem is Bi-2212 intergrowth lamellae in Bi-2223 matrix. Most of intergrowth lamellae have the thickness of unit cell or half-unit cell. Figure 3.30a shows the typical HRTEM image of Bi-2223 single crystal grown by FZ method with electron beam parallel to the b-axis [79]. One can see intergrowth of two different phases as dark lamellae. The scale is magnified in Fig. 3.30b to clarify this intergrowth. The spacing denoted as "3" is about 19 Å, which corresponds to a half-unit cell of Bi-2223 phase. At the same time the spacing denoted as "2" is a bit narrower ( $\sim$ 15 Å), indicating the presence of Bi-2212 phase. According to numerous observations, there is no regularity in the sequence of intergrowth phases. In low-quality Bi-2223 crystals the amount of

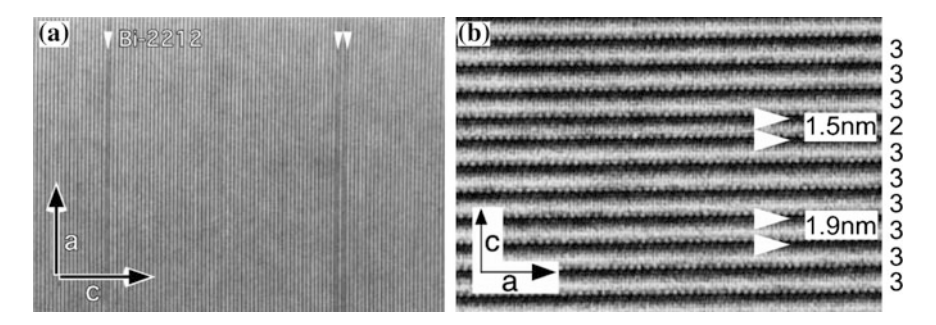


**Fig. 3.30** a HRTEM image of Bi-2223 crystal [79], showing the coexistence of Bi-2223 and Bi-2212 phases (Bi-2212 phase is seen as dark lamellae pointed out by the *arrows*). **b** Magnified picture: Bi-2212 marked as "2" is intergrowth in Bi-2223 matrix marked as "3". Reprinted with permission from Elsevier. All rights reserved

Bi-2212 phase might be up to 20 wt% due to the intergrowth problem, while the good quality crystals contain 2–3 wt% of Bi-2212 only.

Although the HRTEM is a nice tool to observe the intergrowth, the preparation of samples by ion-beam milling after cut perpendicular to Bi-2223 layers is special, sophisticated and time-consuming procedure. Also HRTEM technique is a local probe. Another method to identify a possible Bi-2212 intergrowth in Bi-2223 sample is magnetic measurements of SC transition in zero-field cooled (ZFC) regime. Researchers observed a small (usually <2%) step-like decrease in the magnetization at around 80 K [76, 79] on the good quality samples originated from Bi-2212 intergrowth. It was shown in [80] that XRD technique is a more sensitive tool for the intergrowth detection than ZFC magnetic measurements. Effects of oscillated broadening and peak shift of the (0 0 L) Bragg reflections were demonstrated for the Bi-2223 crystals [80]. This diffraction phenomena is well known for a random intergrowth of a secondary phase (here is Bi-2212). The oscillation amplitude is proportional to the defects concentration if it is relatively low. It enables the authors to estimate the content of intergrowth defects to be about 2 wt% even for the "intergrowth-free" samples according to ZFC measurements. This approach was found to be rather universal being applicable for other layered Bi-based superconductors [81]. Thus, not only the growth of Bi-2223 crystals is a hard task but the correct characterization of as-grown samples requires a special attention, too.

#### 3.6.2 Flux Growth

The self-flux method is often used to grow high-Tc superconductors because of its simplicity. However, in systems getting a narrow primary crystallization field the flux method allows the preparation of tiny crystals embedded in a solidified melt. Since Bi-2223 has a very narrow crystallization field [1, 7], growth by self-flux was thought to be almost impossible. There were a few attempts to prepare Pb-free and

Pb-doped Bi-2223 single crystals by using the molten KCl salt [82, 83]. Only very small samples with dimensions up to  $100 \times 100 \text{ um}^2$  in (a, b) plane and thickness of 1–5 µm along c-axis were obtained. In general B-2223 crystals contained 2–3 wt % of Bi-2212 phase due to the intergrowth problem. The presence of Bi-2212 intergrowth was detected by both XRD and ZFC magnetic measurements [83]. Also, the presence of impurity (Ca, Sr)CuO<sub>2</sub> and CuO phases was often observed in XRD patterns. The SC transition temperature was close to 110 K based on magnetic susceptibility and resistivity data. It is worth to mention that from the growth point it is more correctly to talk about accelerated transformation of Bi-2212 phase to Bi-2223 one in the presence of KCl melt than about the flux growth. It has been already discussed in Sect. 3.6.1 that the main problem of Pb-free Bi-2223 phase formation is related to the very sluggish transformation of 2212 phase into 2223 one. At present, there is no experimental evidence of possibility to complete this transformation through conventional solid-state reaction or using self-flux method [84]. On another hand it was demonstrated in [82, 83] that the using of molten KCl salt drastically enhances the kinetics of Bi-2223 phase formation. The most detailed investigation of this synthetic route is given in [84]. The authors used pre-sintered at 880 °C precursors getting the cation compositions Bi:Sr:Ca:Cu = 2:2:2:3 and 2:2:2:4. The obtained oxide powders (solute) were mixed with KCl (solvent) in ratio 1:4 and 1:10 and used as a charge for the crystal growth. The synthesis was performed in Al<sub>2</sub>O<sub>3</sub>, MgO and Pt containers. The crystals were grown by isothermal heat treatment of charge material at 800-880 °C for 15 and 100 h. In some cases a low cooling rate of 0.5-1.0 °C/h was applied to reduce the effect of KCl evaporation. It was found that the best samples were obtained in high-density MgO crucibles. It was shown that the interaction of MgO with the KCl melt and components of oxide precursor, as well as Bi-2223 contamination by Mg is negligible. The optimal temperature range for the Bi-2223 phase formation and crystal growth was found to be very narrow (860-870 °C) and located just below the peritectic melting of oxide precursor in the KCl melt. At the first stage of isothermal heat treatment (<15 h) rapid formation of almost pure Bi-2223 phase was demonstrated by X-ray diffraction. The same process without KCl leads to the formation of samples dominated by the Bi-2212 phase. The rapid formation of Bi-2223 material in presence of molten KCl was explained based on the "dissolution-precipitation" mechanism and high activity of Cu in the KCl melt [84]. Since the transformation of Bi-2212 into Bi-2223 phase needs a long-lasting annealing, the fast KCl evaporation is not favorable for the Bi-2223 crystal growth. In order to reduce the flux evaporation the very effective tool was the crucible covering with a lid and increasing of solute/solvent ratio. It was shown that individual crystals with dimensions of about  $100 \times 100 \ \mu m^2$  and thickness of 5  $\mu m$ have been prepared after isothermal treatment for 15 h, while the samples larger than  $500 \times 500 \,\mu\text{m}^2$  in (a, b) plane were obtained after 100 h treatment. After growth the solidified KCl melt was washed out by the distilled water and further rinsing in acetone. For the as-grown samples, a superconducting transition at  $T_c$ (onset) = 109 K was detected by magnetization and resistivity measurements.

#### 3.6.3 FZ Growth

Usually the flux method is not suitable for materials with a narrow primary crystallization field when the control of nucleation and growth is rather hard. Also, it is important to keep the solvent composition and quantity at the specific optimal values for the flux steady growth. The last one requires the detailed knowledge of a corresponding phase diagram. Unfortunately, it is not a case for nearly all four-component systems including Bi<sub>2</sub>O<sub>3</sub>-SrO-CaO-CuO one. Thus, flux-grown Bi-2223 crystals were very thin with dimensions  $1.0 \times 1.0 \times 0.005$  mm<sup>3</sup>. From this point the crucible-free FZ method is much more suitable for the growth of larger crystals, because, in general, the crystal growth is performed continuously at one point on the temperature-composition phase diagram. In this case there is no need in detailed knowledge of primary crystallization field. Moreover, in FZ growth of Bi-based superconductors the molten zone (MZ) composition is self-adjusted during the growth if molten zone is well stable against the compositional and temperature fluctuations [76, 79]. The stability of MZ depends from many factors: quality of feed rod, pulling rate, temperature gradient along MZ, applied gas pressure. Usually it is expected that the MZ can be kept more stable if its length is reduced, because the MZ is supported only by surface tension against gravity. For the image furnaces equipped with halogen lamps the length of MZ mainly depends from the thickness of lamp filament. Thus, the higher is a nominal lamp power the larger is the zone length. Also, it was found in [79] that a steep temperature gradient along the MZ plays the very important role in maintaining a stable zone for Bi-2223 growth. Another crucial condition for the growth of large single crystals is a planar growth front. Both slow pulling rate and large temperature gradient are expected to prevent a constitutional supercooling which is the origin of the opposite cellular crystallization front. From this point it is quite interesting to compare the technical specifications of image furnaces produced by different companies. The NEC (Japan) image oven is equipped with 500 and 1500 W halogen lamps, and the lower limit of pulling rate is 0.5 mm/h for a standard setup. The CSI (Japan) image furnaces got halogen lamps with nominal lamp power ranging from 150 to 1500 W. Also, the lowest pulling rate is about 0.04-0.05 mm/h. The comparison obviously demonstrates that the CSI image furnace provides better growth conditions than the NEC one. Moreover, the four-mirror CSI optical setup gives much less pronounced thermal fluctuations in a horizontal plane compared with double-mirror NEC optics. The SciDre GmbH (Germany) produced an image oven that allows one to reach extremely high gas pressures up to 150 bars. The last value is the world record for all image furnaces. For example, the CSI and NEC machines have the upper gas pressure limit of 10 bars. The lowest pulling rate for SciDre oven is 0.1 mm/h that makes it suitable for the growth of Bi-based superconductors. On the other hand the SciDre furnace is equipped with an arc lamp. In general an arc lamp provides less stable molten zone at low pulling rates (≤1.0 mm/h) compared with a halogen lamp due to the tiny position fluctuations of the arc hottest point. This is the main reason why image furnaces equipped with arc lamps have been never used successfully for the growth of high-T<sub>c</sub> cuprates. And up to the author's experience the CSI image furnace is the best one for the growth of all Bi-based superconductors.

The large Bi-2223 single crystals have been grown successfully by the FZ method for the first time in 2001 [79]. The main clue of this success was (i) applying an extremely low growth rate of 0.04–0.5 mm/h and (ii) using 300 W halogen lamps. The authors found that the temperature gradient was 350 °C/cm in the hot zone, which was two times larger than that with 1500 W lamps. Thus, the length of MZ was reduced from 4.0–4.5 mm of 1500 W lamps to 3.5–4.0 mm of 300 W lamps, and the MZ was quite stable over the whole growth time (3–4 weeks). The most detailed investigations of the Bi-2223 crystal growth by FZ method has been done in [76, 80, 85, 86] and discussed in the next section.

#### 3.6.3.1 Growth of Pure and Pb-Doped Samples

According to [9, 19] Bi<sub>2.1</sub>Sr<sub>1.9</sub>Ca<sub>2.0</sub>Cu<sub>3.0</sub>O<sub>y</sub> is the best feed rod composition that is slightly Bi-rich similar to the Bi-2212 growth. The feed rods for the crystal growth were prepared by the conventional solid state method. Powders of Bi<sub>2</sub>O<sub>3</sub>, SrCO<sub>3</sub>, CaCO<sub>3</sub> and CuO (all of 99.9 % purity) with cation ratio Bi:Sr:Ca:Cu = 2.1:1.9:2.0:3.0 were well mixed and calcined at 780 °C for 48 h in air with intermediate grindings. The calcined powder was formed into cylindrical rods ( $\sim \phi$  6 × 80 mm). The rods were hydrostatically pressed under a pressure of  $\sim 70$  MPa and sintered at 850 °C for 50 h in air. Prior to the crystal growth the high-density feed rod ( $\sim 90$  % of the crystal density) was obtained by pre-melting the as-sintered rod at a rapid rate of 25 mm/h. The quality of the pre-melted feed rods is critical to the FZ technique because during the crystal growth the molten zone is sustained by the feed rod through surface tension. A straight, long and equal-diameter feed rod is required to stabilize the molten zone over a long growth period.

Single crystals were grown using the CSI image furnace equipped with four halogen lamps as an infrared radiation source. A sharp temperature gradient of  $\sim 300$  °C/cm along the molten zone was obtained using 300 W halogen lamps. A short pre-melted feed rod ( $\sim 20$  mm in length) was used as a seed rod in the crystal growth. Both the feed and seed rods were counter rotating (25 and 15 rpm) to ensure efficient mixing of the liquid. The mixed gas flow of argon and oxygen was applied. Due to the highly anisotropic crystallization rates for Bi-based superconductors, it is very difficult to obtain thick single crystals along the c-axis direction. Therefore, slow growth rates of 0.20, 0.10, 0.06 and 0.04 mm/h were used in an attempt to obtain large crystals. The experimental conditions are summarized in Table 3.5.

It has been already discussed in Sect. 3.6.1 that the Bi-2223 phase melts incongruently, and it is stable within a narrow temperature range of about 50 °C only. A minor variation in composition can cause major changes in the phase contents, leading to a significant decrease of the volume fraction of Bi-2223 phase. For a narrow crystallization field a constitutional supercooling readily causes the

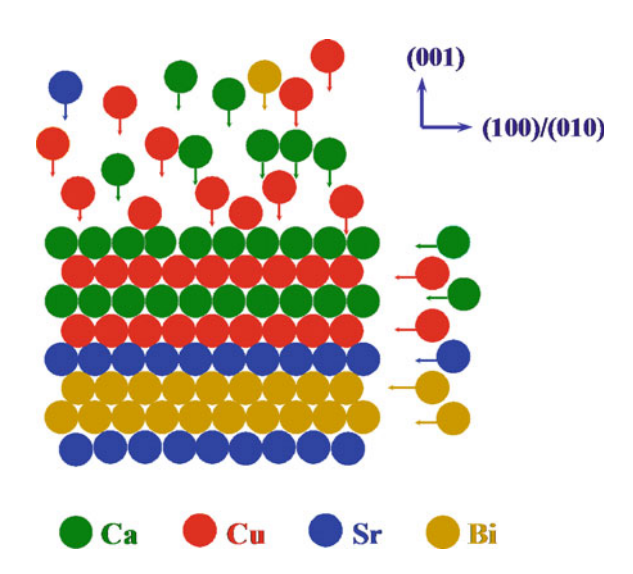
Feed rod composition	Crystal composition	Growth atmosphere	Growth rate (mm/h)	Dominant phase	T <sub>c,</sub> onset (K)
$Bi_{2.1}Sr_{1.9}Ca_2Cu_3O_{10+\delta}$	$Bi_{2.18}Sr_{1.82}Ca_{1.27}Cu_{2.15}O_{10} \\ +\delta$	80 % Ar + 20 % O <sub>2</sub>	0.20	Bi-2212	80
Bi <sub>2.1</sub> Sr <sub>1.9</sub> Ca <sub>2</sub> Cu <sub>3</sub> O <sub>10+δ</sub>	Bi <sub>2.16</sub> Sr <sub>1.84</sub> Ca <sub>1.32</sub> Cu <sub>2.34</sub> O <sub>10</sub> +δ	80 % Ar + 20 % O <sub>2</sub>	0.10	Bi-2212	93
$Bi_{2.1}Sr_{1.9}Ca_2Cu_3O_{10+\delta}$	Bi <sub>2.08</sub> Sr <sub>1.92</sub> Ca <sub>1.69</sub> Cu <sub>2.69</sub> O <sub>10</sub> +δ	80 % Ar + 20 % O <sub>2</sub>	0.06	Bi-2223	102
$Bi_{2.1}Sr_{1.9}Ca_2Cu_3O_{10+\delta}$	$Bi_{2.11}Sr_{1.89}Ca_{1.83}Cu_{2.87}O_{10} \\ +\delta$	20 % Ar + 80 % O <sub>2</sub>	0.04	Bi-2223	103

 $\textbf{Table 3.5} \ \ \text{Growth conditions, crystal compositions from EDX analysis, presence of dominant phase determined from XRD and ZFC measurements, and $T_c$ of Bi-2223 single crystals$ 

cellular growth front, which results in the formation of multi phases. To overcome this problem, a slow zone-travelling rate and a sharp temperature gradient along the molten zone have to be applied during the growth.

According to the Bi-2223 lattice structure, it might be assumed that the growth of (001) plane is a layer-by-layer process and a whole (001) face requires exposure to only one species of atom at a given instant for a layer to propagate. Other atoms in the vicinity of the (001) growth plane, therefore, cannot be adsorbed and diffuse to a 'kink' site in the lattice. Figure 3.31 schematically illustrates an instantaneous growth contour for layer-by-layer growth, along the (001) crystallographic axis. Growth of the Bi layers commence once the Sr layer is complete and Sr layer commences after Bi. The layer growth runs in cycles according to the growth contour of the layer structure, -Sr-Bi-Bi-Sr-Cu-Ca-Cu-Ca-Cu-, therefore, for (001) growth the diffusion of the relatively few Ca (Sr or Bi or Cu) atoms to the surface of the crystals is hindered by a large amount of Sr, Bi and Cu (Ca, Bi and Cu

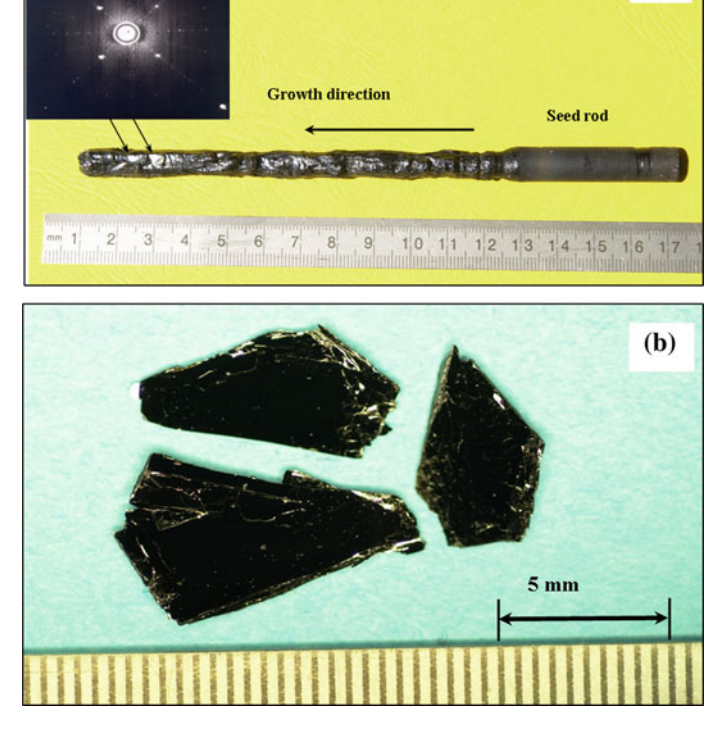
**Fig. 3.31** Growth contour of the layer structure of Bi-2223 crystals



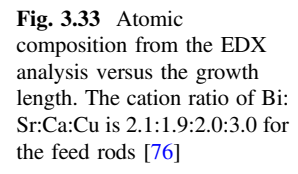
(a)

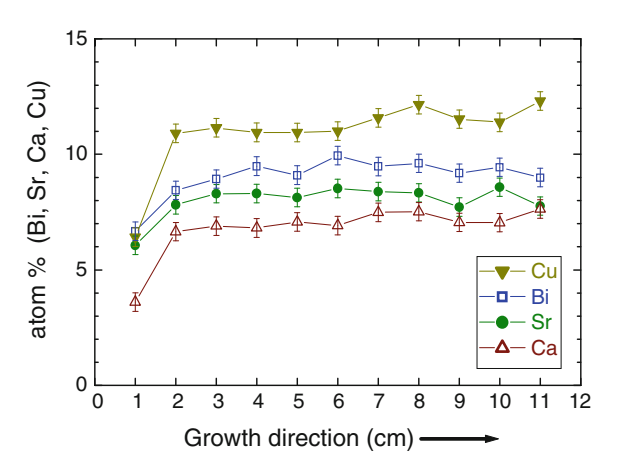
or Ca, Sr and Cu or Bi, Sr and Ca) atoms. This results in an extended diffusion layer formed above the (001) plane. Because of the relatively long diffusion path along the (001) direction, a slow growth rate is thus desired for obtaining a thick crystal. Such diffusion phenomena do not exist for the (100) growth face since growth interface can directly adsorbed Bi, Sr, Ca or Cu atoms. Therefore, the crystallization rate along the (100) direction is much faster ( $\sim 10^3$  times) than that in the c direction leading to the plate-like Bi-2223 crystals, which exhibit large (a, b) planes but small dimensions along c-axis.

Figure 3.32a shows an as-grown Bi-2223 ingot prepared at the growth rate of 0.06 mm/h. Many shiny facets can be seen from the cylindrical surface of the ingot. Laue X-ray back-reflection photography revealed that these facets are along the (001) crystallographic plane. Since the crystal growth was initiated on a polycrystalline seed rod, only needle-shaped crystallites were observed in the initial part when the ingot was cleaved. The crystallites became gradually larger as the ingot grew. However, the continuous growth of these grains was periodically interrupted when new planar growth fronts were created. This indicates that a frequent self-adjusted flux composition took place during the growth. As a result, the cleaved



**Fig. 3.32** a Bi-2223 as-grown ingot exhibiting the (001) facets on the surface [76]. b Typical Bi-2223 single crystals cleaved from the ingot grown with a rate of 0.06 mm/h





crystals exhibit 'V' shape, as shown in Fig. 3.32b. The largest single crystal obtained was approximately  $10 \times 6 \times 0.5$  mm<sup>3</sup>, which is the largest ever reported.

The composition of each ingot was determined by EDX analysis. The results are summarized in Table 3.5. The compositions of crystals grown at slow rates of 0.04–0.06 mm/h are close to Bi-2223 phase. These two ingots are Ca- and Cu-poor due to the intergrowth of the Bi-2212 phase. However, the compositions of crystals obtained at rates of 0.10–0.20 mm/h are closer to Bi-2212 phase, indicating that the faster growth rates are unfavorable for the formation of Bi-2223 phase.

To examine the homogeneity of composition throughout as-grown ingots, crystals were selected at intervals of 1 cm along the ingots and measured by EDX analysis. The atomic compositions of each crystal were derived by averaging data measured on three or four points of each crystal. Figure 3.33 shows the atomic percentages of Bi, Sr, Ca, and Cu at different positions of the ingot obtained with growth rate of 0.06 mm/h under mixed gas flow of 80 % Ar and 20 % O<sub>2</sub>. It can be seen that the fluctuation of the composition is quite low except for the initial part of the ingot. This implies that the molten zone was quite stable during the growth except for the beginning. Indeed, it was observed during the growth that the stability of the molten zone of Bi-2223 is higher than those of the Bi-2201 and Bi-2212, which reflects that the self-adjustability of the Bi-2223 melt composition is rather high.

The composition of MZ during the Bi-2223 growth was studied in [80]. Two specimens were frozen by quenching the molten zones after running 3 and 20 days, respectively. The composition of each frozen zone was measured by ICP-AES analysis. The results of the chemical analysis are listed in Table 3.6. The data indicate that the molten zone composition comes into equilibrium after 3-days run already, remaining practically invariable thereafter.

When compared with the initial feed rod composition one can easily see that the liquid zone content of Sr and Cu remains invariant, whereas the content of Ca in the molten zone is definitely lower compensated by an increased concentration of Bi.

Composition (at. %)	3-day's specimen	20-day's specimen	Bi <sub>2.1</sub> Sr <sub>1.9</sub> Ca <sub>2.0</sub> Cu <sub>3.0</sub> O <sub>y</sub>
Bi	$32.6 \pm 0.5$	$32.0 \pm 0.6$	23.3
Sr	$19.9 \pm 0.4$	$20.8 \pm 0.4$	21.1
Ca	$13.3 \pm 0.4$	$13.5 \pm 0.5$	22.2
Cu	$34.2 \pm 0.4$	$33.7 \pm 0.5$	33.4

Table 3.6 MZ composition after 3- and 20-day's FZ growth compared with feed rod composition

As a result the composition of the liquid in the equilibrium with the Bi-2223 phase is Ca-depleted in the course of FZ run. Also, the results of [80] showed that the Bi-2223 crystal growth at 0.06 mm/h is quite sensitive to the oxygen content in gas environment, and the low-oxygen limit is about 2.5 %. According to the magnetic measurements the majority of crystals grown at 2.5 % oxygen content are Bi-2212 while the same growth procedure at 5, 10 and 20 % oxygen content leads to the Bi-2223 growth. Also, the ingot prepared at 2.5% oxygen content contained a visible amount of  $\text{Ca}_2\text{CuO}_3$  impurity phase.

For growing the Pb-doped crystals, the commonly used image furnace setup was modified by adding an internal source of Pb [87]. According to [88, 89] a Pb loss at high temperatures has to be minimized in order to keep the stoichiometry of the sample close to the nominal one, thus promoting equilibrium phase formation. This can be done either by applying a high pressure [88] to prevent Pb evaporation or by enclosing samples in sealed tubes [89] to saturate the atmosphere with Pb vapour. Unfortunately, neither of these methods can be utilized in FZ growth. For these reasons, the authors in [87] developed a new technique called as VA-FZ (Vapour Assisted Floating Zone) by adding an internal source of Pb vapour. An Al<sub>2</sub>O ring crucible containing PbO encircling the seed rod was placed inside the quartz tube close to the molten zone. The position of the PbO source was accurately chosen so that the temperature of the ring crucible was around 750 °C, and the PbO evaporation rate was about 2 ×  $10^{-8}$  mol/h, determined by preliminary TG experiments. This allowed the authors [87] to compensate the Pb loss from the MZ by means of a lead evaporation from the PbO source.

The feed rod composition was Bi:Pb:Sr:Ca:Cu = 1.84:0.32:1.84:1.97:3.00. The crystal growth was performed at low travelling rates ranging from 0.03 to 0.20 mm/h, and the best samples have been grown at 0.05–0.06 mm/h. Both pre-melting and crystal growth were carried out under flowing 93 % Ar – 7%  $O_2$  gas mixture. Pre-melting of as-sintered feed rod was done at 25 mm/h. Large (Bi, Pb)-2223 crystals with typical dimensions up to  $2.0 \times 3.0 \times 0.1$  mm<sup>3</sup> have been prepared by VA-FZ method. The Pb content in as-grown samples was found to be Bi:Pb:Sr:Ca:Cu = 2.16:0.26:2.08:1.95:2.65. This indicates that this growth technique was successful in compensation of Pb evaporation from the molten zone during the long-lasting growth run. The superconducting transition was observed at  $T_c = 106$  K, and the width of transition,  $\Delta T_c = 3$  K, was smaller compared with Pb-free Bi-2223 crystals. The Pb-doped crystals have orthorhombic structure, but the orthorhombic distortion is enhanced and the c-axis cell parameter is found to be

slightly larger compared with Pb-free Bi-2223 samples. The lattice parameters are the following: a = 5.395(1) Å, b = 5.413(1) Å and c = 37.04(1) Å. The structure of lead-doped samples was modulated with a modulation vector  $q \sim 0.21a$ , as confirmed by the presence of satellites in the diffraction pattern. The high quality of as-grown crystals allowed the observation of satellites of up to the third order.

#### 3.6.3.2 Sample Characterization

Single-crystal XRD measurements were made on a number of Pb-free as-grown Bi-2223 crystals [85] chosen from each ingot to check the crystallinity of as-grown samples. Figure 3.34 shows a single-crystal XRD patterns for the crystal grown at a rate of 0.04 mm/h. Only sharp (00l) peaks are observed, indicating the good crystallinity of the sample. All diffraction peaks can be indexed into the Bi-2223 phase with the c-axis lattice parameter of 36.552(6) Å.

Powder XRD measurements were performed on ground crystals in order to examine the presence of impurity phases as well as to determine the crystal structure and lattice parameters. Figure 3.35a–c present the powder XRD patterns for three as-grown crystals obtained using growth rates of 0.20, 0.10 and 0.04 mm/h, respectively. It is noteworthy that the growth rate dramatically influences the phase formation of crystals. The crystals obtained at a rate of 0.20 mm/h exhibit majority phase of Bi-2212 and small amount of Ca<sub>2</sub>CuO<sub>3</sub> and some unidentified phases, as shown in Fig. 3.35a. No Bi-2223 phase could be detected from this crystal. The crystals grown at a slower rate of 0.10 mm/h consist of Bi-2212, Ca<sub>2</sub>CuO<sub>3</sub> as well as a small amount of Bi-2223 phase, as shown in Fig. 3.35b. When growth was performed at a very slow rate of 0.04 mm/h, nearly

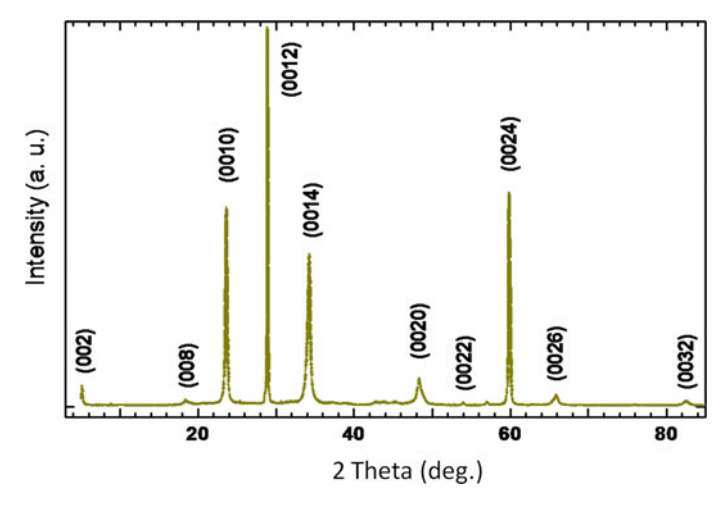
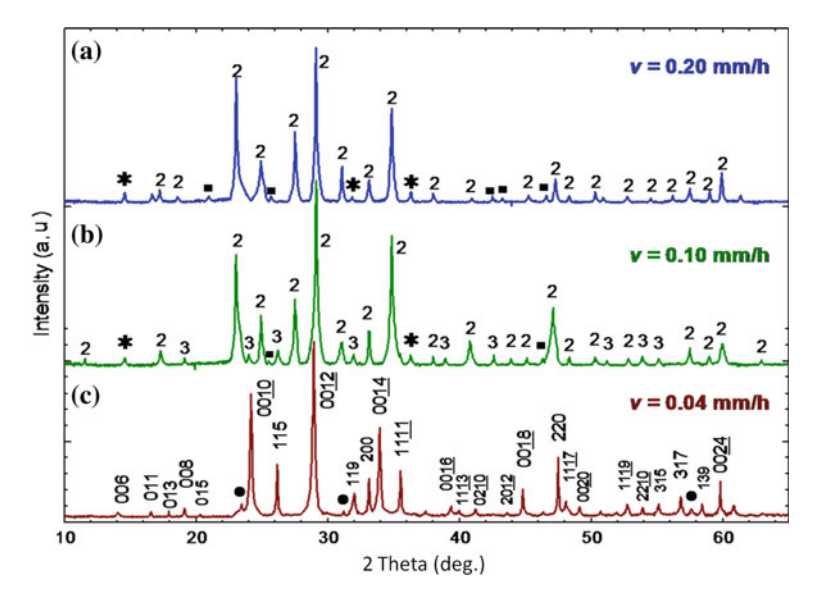


Fig. 3.34 Single-crystal XRD pattern of as-grown Bi-2223 crystal prepared at 0.04 mm/h rate [76]

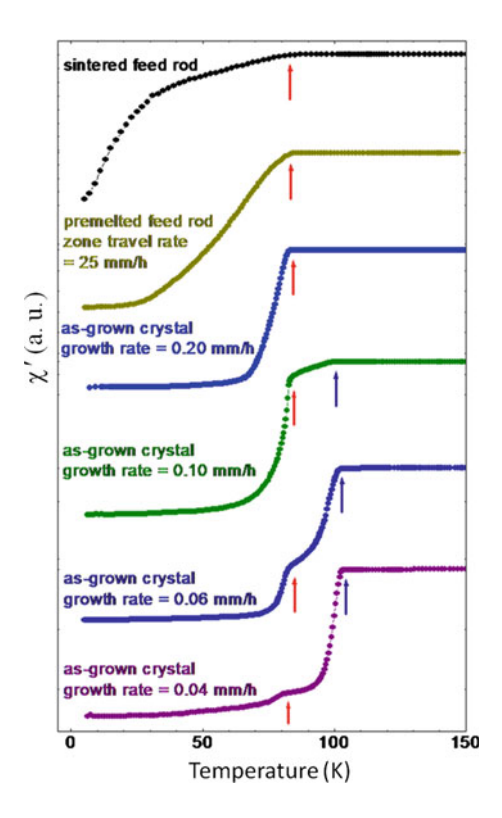


**Fig. 3.35** Powder XRD patterns of crystals grown at different rates, revealing the effect of growth rate on the phase formation in crystals. **a** 0.20 mm/h, majority phase Bi-2212; **b** 0.10 mm/h, Bi-2223 phase appeared; **c** 0.04 mm/h, nearly pure Bi-2223 phase. "3", "2", "\*" and "■" indicate Bi-2223, Bi-2212, Ca<sub>2</sub>CuO<sub>3</sub> and unidentified phases, respectively. The diffraction peaks of Bi-2223 phase in Fig. 3.6c are indexed with respect to the space group A2aa. A few weak peaks corresponding to the Bi-2212 phase are marked with "•" in this pattern [76]

single-phase crystals which have >90 % Bi-2223 phase were obtained from the as-grown ingot, as shown in Fig. 3.35c. Using a least-square refinement program the nearly single-phase Bi-2223 crystals were determined to be of orthorhombic structure with the lattice parameters a = 5.408(2) Å, b = 5.413(7) Å and c = 36.868(1) Å (space group A2aa). These results demonstrate that a faster growth rate is unfavorable for the formation of Bi-2223 phase due to the extremely narrow crystallization field and complex melting behaviour. A large number of as-grown crystals from each ingot were checked using magnetic susceptibility measurements. Sintered and pre-melted feed rods were also measured for comparison.

These results also reveal that the crystal growth rate apparently influences the phase formation in crystals. Figure 3.36 shows the temperature dependence of the real part of AC susceptibility measured on sintered and pre-melted feed rod as well as on as-grown crystals obtained at different growth rates. Both sintered and pre-melted feed rods exhibit very broad superconducting transitions with onset  $T_{\rm c} \sim 80~{\rm K}$ , indicating that the principal superconducting phase in feed rods is Bi-2212 phase with an inhomogeneous oxygen distribution. The crystal grown at a rate of 0.20 mm/h exhibits a relatively sharp transition also around 80 K. No trace of a transition around 110 K could be seen, implying that the majority superconducting phase in fast-grown crystals is still Bi-2212 with relatively homogeneous oxygen distribution.

Fig. 3.36 Temperature dependence of AC susceptibility measured on sintered feed rod, premelted feed rod and crystals grown with different rates, showing the effect of growth rate on the phase formation of Bi-2223 crystals. Only the real part ( $\chi'$ ) of AC susceptibility is plotted [76]



When the growth rate decreases to 0.10 mm/h, the as-grown crystal displays two superconducting transitions around 100 and 80 K, corresponding to Bi-2223 and Bi-2212 phases, respectively. When the growth rate slows down further to 0.06 mm/h, the Bi-2223 phase has become the dominant phase in crystals. When an extremely slow growth rate of 0.04 mm/h was used, the as-grown crystals have >90 % of Bi-2223 phase.

The  $T_c$  of as-grown Bi-2223 crystals was found to be around 102 K from ZFC measurements, but it was drastically enhanced by pressure-driven doping reaching 136 K at 36.4 GPa [90]. This result provides the first evidence for pressure-induced superconductivity in the inner  $CuO_2$  plane of high- $T_c$  cuprates.

Also, it is worth to compare the results of HREM on Bi-2212 and Bi-2223 crystals grown by FZ method (Fig. 3.37). Obviously, the Bi-2223 sample has a number of intergrowth defects visible as Bi-2201 and Bi-2212 half-unit cells compared with single phase Bi-2212 sample.

This result reflects the much more complicated crystallization behaviour of Bi-2223 phase and its less thermal stability compared with other Bi-based superconductors. All together the FZ growth of nearly pure Bi-2223 compound required almost one order less pulling rates (0.04–0.06 mm/h) than the growth of Bi-2201 (0.5–1.0 mm/h) and Bi-2212 (0.2–0.5 mm/h) materials.

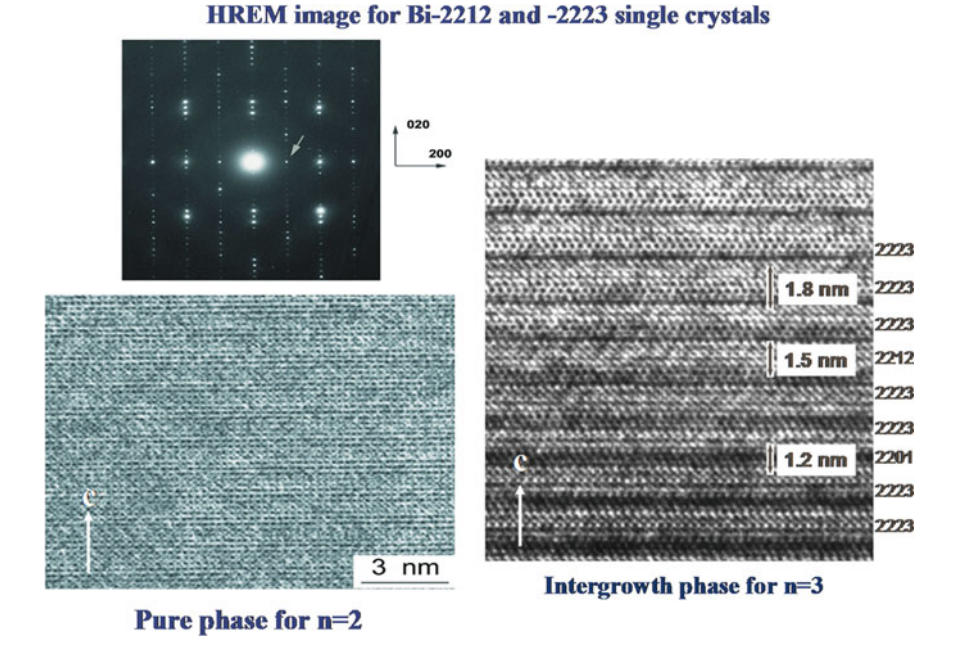


## Fig. 3.37 HREM images of Bi-2212 (left) and Bi-2223 (right) crystals [76]

## 3.6.3.3 Effect of Post-growth Treatment on Superconductivity

Post-annealing experiments were carried out at 500–850 °C for 120–500 h to improve the crystal quality with respect to phase purity and oxygen homogeneity [91]. The annealing conditions are listed in Table 3.7. The effect of oxygen annealing was studied by both XRD and magnetic susceptibility measurements. A phase-transform process from Bi-2212 to Bi-2223 was observed.

Such a phase transformation might be explained via a layer-intercalation mechanism, which suggests that Bi-2212 phase can be transformed to Bi-2223 phase through layer-by-layer intercalation of the Ca-Cu-O bi-layers into the

8 8				
Temperature (°C)	Time (h)	Atmosphere	Phases	T <sub>c,onset</sub> (K)
500	120	O <sub>2</sub> flow	Bi-2223, Bi-2212, Ca <sub>2</sub> CuO <sub>3</sub>	105
600	120	air	Bi-2223, Bi-2212, Ca <sub>2</sub> CuO <sub>3</sub>	105
650	120	O <sub>2</sub> flow	Bi-2223, Bi-2212, Ca <sub>2</sub> CuO <sub>3</sub>	106
750	120	O <sub>2</sub> flow	Bi-2223, minor Bi-2212	106
850	360	O <sub>2</sub> flow	Bi-2223	108
850	500	O <sub>2</sub> flow	Bi-2223	110

Table 3.7 Annealing conditions and results for Bi-2223 single crystals

existing Bi-2212 structure. Figure 3.38 shows the temperature dependence of AC susceptibility measured on Bi-2223 as-grown and annealed crystals. The as-grown crystal shows two superconducting transitions around 102 and 80 K, corresponding to Bi-2223 and Bi-2212 phases, respectively. As the annealing temperature is elevated and/or the annealing time increased, the transition at 80 K is gradually suppressed, indicating a decrease of the Bi-2212 phase. The crystal annealed at 850 °C for 500 h shows a sharp transition at 110 K with only a small remnant at 80 K. This indicates that nearly single-phase Bi-2223 crystals were obtained using slow growth rates (≤0.06 mm/h) and subsequent long-time annealing. The result of susceptibility measurements does not only demonstrate the influence of annealing on the phase transformation in crystals but also shows the effect of annealing on the superconductivity of Bi-2223 crystals. As shown in the inset of Fig. 3.38, the onset  $T_c$  increases from 102 K for the as-grown crystal to 110 K for the crystal annealed at 850 °C for 500 h. Usually it is difficult to precisely determine the oxygen content for single crystals, particularly for the large ones; however, from the tendency of  $T_{\rm c}$ 's change observed from our annealing experiments, one can suggest that the as-grown Bi-2223 crystals are in the slightly underdoped region. It is interesting that further increasing of oxygen pressure up to 500 bars during the annealing remains the T<sub>c</sub> to be unchangeable around 110 K.

In order to demonstrate more clearly the phase evolution with annealing temperature and/or time powder XRD measurements were performed on a ground crystal before and after oxygen annealing. The results are presented on Fig. 3.39a–d. Prior to annealing, Bi-2223 was the dominant phase in the as-grown sample. However, considerable amounts of Bi-2212 and Ca<sub>2</sub>CuO<sub>3</sub> phases were also observed, as shown in Fig. 3.39a. After being annealed in O<sub>2</sub> flow at 600 °C for 120 h, the intensity of the Bi-2212 and Ca<sub>2</sub>CuO<sub>3</sub> peaks decreased, as shown in

Fig. 3.38 Temperature dependence of AC susceptibility measured on an as-grown crystal grown with a rate of 0.06 mm/h ( $\Delta$ ) and crystals annealed: at 600 °C for 120 h ( $\blacksquare$ ), 850 °C for 360 h ( $\bigcirc$ ) and 850 °C for 500 h ( $\bigcirc$ ). Only the real part ( $\chi$ ') of AC susceptibility is plotted. The curves have been mass normalized to unity for the sake of comparison [76]

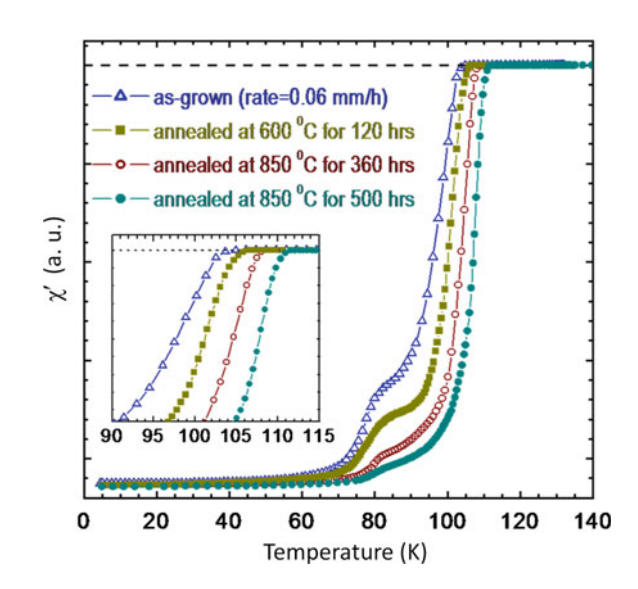


Fig. 3.39 Powder XRD patterns of as-grown and annealed in oxygen flow Bi-2223 crystals: a as-grown sample; b 600 °C for 120 h; c 850 °C for 360 h; d 850 °C for 500 h. "3", "2" and "□" indicate Bi-2223, Bi.2212 and Ca<sub>2</sub>CuO<sub>3</sub> phases, respectively. The Bi-2223 diffraction peaks in (d) are indexed in the space group A2aa. A few weak Bi-2212 peaks are shown with "+" [9, 25]

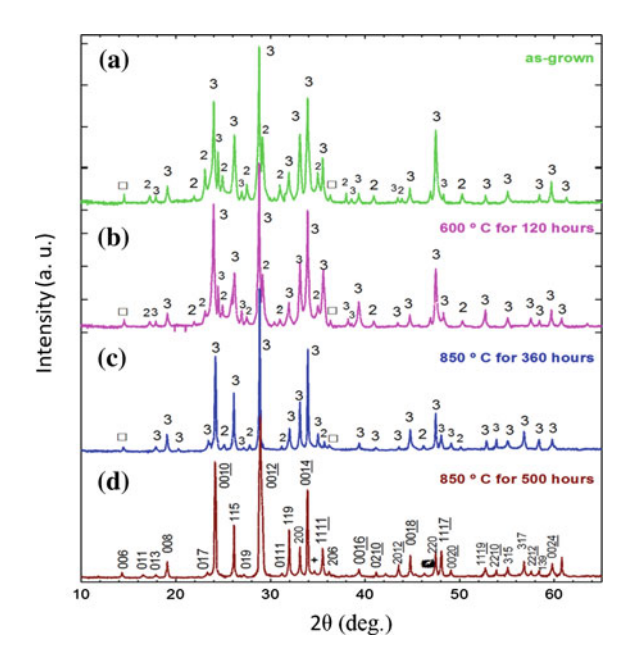
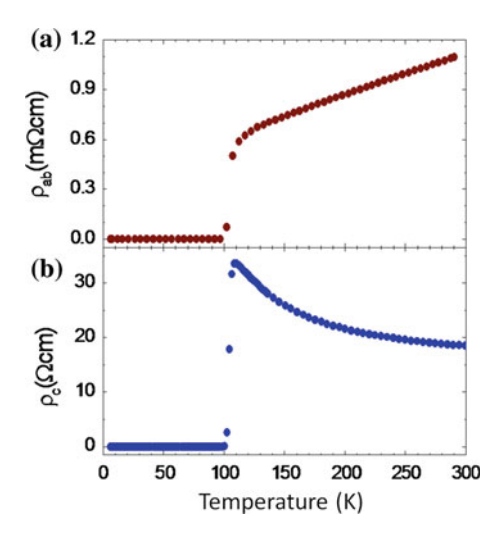


Fig. 3.39b. At the high temperature annealing at 850 °C for 500 h a nearly single-phase Bi-2223 crystal was obtained (Fig. 3.39d). All diffraction peaks in Fig. 3.39d can be assigned to the Bi-2223 phase with orthorhombic symmetry. These results confirmed a nearly complete conversion of Bi-2212 into Bi-2223 (Bi-2223 content >99 %) because no trace of Bi-2212 phase can be detected from the powder XRD pattern on Fig. 3.39d. The transformation from one member of the structural family into another can be understood via a layer-intercalation mechanism [92]. According to this mechanism, the Bi-2212 phase could be transformed into the Bi-2223 compound via intercalating the CuO<sub>2</sub>/Ca bi-layers into the CuO<sub>2</sub>/Ca/CuO<sub>2</sub> blocks of the existing Bi-2212 structure. This kind of phase conversion is diffusion limited and, consequently, is very sluggish even at high temperatures that can be directly seen from Fig. 3.39c–d.

The in-plane and out-of-plane resistances as a function of temperature were measured on selected annealed crystals composed of almost pure Bi-2223 phase. The measured resistance was transformed to the respective resistivity  $\rho_{ab}$  and  $\rho_c$  using the crystal dimension. Figure 3.40a, b show the typical in-plane resistivity  $\rho_{ab}$  and out-of-plane resistivity  $\rho_c$  as a function of temperature, both of which show very sharp transition at 110 K. The typical T-linear behaviour for  $\rho_{ab}$  and semi-conductive upturn for  $\rho_c$  can be seen. The values of the resistivity for Bi-2223 crystals are of the same order of magnitude as those for Bi-2212 crystals.

Thus, a Bi-2223 crystal quality can be improved after a long-lasting post-growth annealing either in oxygen flow or under oxygen pressure. On the other hand, the superconducting transition temperature of the Bi-2223 phase is found to be much less sensitive to oxygen doping than Bi-2212, and only small variations of  $T_{\rm c}$  are

**Fig. 3.40** Temperature dependence of (a) in-plane and (b) out-of-plane resistivity for Bi-2223 crystals annealed at 850 °C for 360 h in oxygen flow [76, 91]



observed after different oxygen/argon post-growth treatments. For example, argon annealing at 650 °C for 120 h slightly decreases  $T_c$  up to 100 K. The dependence of  $T_c$  on oxygen content has been reported in [91, 93]. For both publications authors reported a flat  $T_c$  against oxygen doping dependence in the overdoped regime and did not measure any decrease of  $T_c$  upon annealing under high oxygen pressures (up to 500 bars). The independence of  $T_c$  against oxygen content in the overdoped regime has been interpreted as being compatible with different carrier doping levels in the outer and inner  $CuO_2$  layers [91, 93], which would be a unique property of  $n \ge 3$  Bi-cuprates (n = 100 number of  $CuO_2$  planes).

Thus, among all non-toxic high-Tc cuprates the Bi-2223 material is the most hardly grown one. The reasons for this are threefold: (i) a low thermal stability of Bi-2223 phase; (ii) a high anisotropy of growth rates; (iii) a tricks' melting/solidification behavior. At the same time the crucible-free floating zone method allows a crystal grower to make nearly single-phase Bi-2223 crystals with dimensions up to  $10 \times 6 \times 0.5 \text{ mm}^3$  suitable for the majority of physical measurements. Nevertheless, even the "best" samples contain a few weight percents of Bi-2212 phase due to the intergrowth problem and complications in crystallization process. It is necessary to acknowledge that a melting behavior and a growth mechanism of Bi-2223 material are still far from our complete understanding, and this calls for further investigations in Bi-2223 crystal growth.

# References

- T. Jacobs, S.O. Katterwe, H. Motzkau, A. Rydh, A. Maljuk, T. Helm, C. Putzke, E. Kampert, M.V. Kartsovnik, V.M. Krasnov, Phys. Rev. B 86, 214506 (2012)
- 2. S.O. Katterwe, T. Jacobs, A. Maljuk, V.M. Krasnov, Phys. Rev. B 89, 214516 (2014)

References 111

 Y.-D. Chuang, A.D. Gromko, A. Fedorov, Y. Aiura, K. Oka, Y. Ando, H. Eisaki, S.I. Uchida, D.S. Dessau, Phys. Rev. Lett. 87, 117002 (2001)

- 4. N.R. Khasanova, E.V. Antipov, Physica C 246, 241 (1995)
- 5. R.S. Roth, C.J. Rawn, L.A. Bendersky, J. Mater. Res. 5, 46 (1990)
- 6. Y. Gao, P. Lee, J. Ye, P. Bush, V. Petricek, P. Coppens, Physica C 160, 431 (1989)
- 7. H. Komatsu, Yu. Kato, S. Miyashita, T. Inoue, Sh Hayashi, Physica C 190, 14 (1991)
- 8. T. Suzuki, K. Yumoto, M. Mamiya, M. Hasegawa, H.Takei, Physica C 301, 173 (1998)
- 9. P. Majewski, J. Mater. Res. 15, 854 (2000)
- 10. K. Remschnig, J.M. Tarascon, R. Ramesh, G.W. Hull, Physica C 175, 261 (1991)
- J.I. Gorina, G.A. Kaljushnaia, V.P. Martovitsky, V.V. Rodin, N.N. Sentjurina, Solid State Commun. 108, 275 (1998)
- 12. N.L. Wang, B. Buschinger, C. Geibel, F. Steglich, Phys. Rev. B 54, 7449 (1996)
- 13. B. Liang, A. Maljuk, C.T. Lin, Physica C **361**, 156 (2001)
- 14. E. Sonder, B.C. Chakoumakos, B.C. Sales, Phys. Rev. B 40, 6872 (1989)
- M. Mansori, A. Yoshikawa, C. Favotto, P. Satre, T. Nojima, M. Kikuchi, T. Fukuda, Physica C 449, 9 (2006)
- 16. I. Tanaka, H. Kojima, Nature **337**, 21 (1989)
- S. Takekawa, H. Nozaki, A. Umezono, K. Kosuda, M. Kobayashi, J. Cryst. Growth 92, 687 (1988)
- M. Matsumoto, J. Shirafuji, K. Kitahama, S. Kawai, I. Shigaki, Y. Kawate, Physica C 185– 189, 455 (1991)
- J.H.P. Emmen, V.A.M. Brabers, W.J.M. de Jonge, M. Nevriva, J. Sramek, J. Alloy. Compd. 195, 15 (1993)
- 20. P.V.P.S.S. Sastry, A.R. West, Physica C 225, 173 (1994)
- A. Maeda, M. Hase, I. Tsukada, K. Noda, S. Takebayashi, K. Uchinokura, Phys. Rev. B 41, 6418 (1990)
- 22. J. Zhang, C. Zhang, H. Xie, Yu. Zhang, J. Cryst. Growth 222, 518 (2001)
- W.L. Yang, H.H. Wen, Y.M. Ni, J.W. Xiong, H. Chen, C. Dong, F. Wu, Y.L. Qin, Z.X. Zhao, Physica C 308, 294 (1998)
- A.E. Schlögl, J.J. Neumeier, J. Diederichs, C. Allgeier, J.S. Schilling, W. Yelon, Physica C 216, 417 (1993)
- H. Faqir, M. Kikuchi, Y. Syono, M. Mansori, P. Satre, A. Sebaoun, G. Vacquier, Supercond. Sci. Technol. 13, 1155 (2000)
- 26. Y. Ando, T. Murayama, Phys. Rev. B 60, R6991 (1999)
- 27. B. Liang, C.T. Lin, J. Crystal Growth 267, 510 (2004)
- 28. J.B. Peng, C.T. Lin, J. Supercond. Nov. Magn. 23, 591 (2010)
- T. Amano, M. Tange, M. Yokoshima, T. Kizuka, S. Nishizaki, R. Yoshizaki, Physica C 412–414, 230 (2004)
- 30. Y. Ikeda, Z. Hiroi, H. Ito, S. Shimomura, M. Takano, Y. Bando, Physica C 165, 189 (1989)
- Z. Lin, Z. Wen-Tao, L. Hai-Yun, M. Jian-Qiao, L. Guo-Dong, L. Wei, D. Xiao-Li, Z. Xing-Jiang, Chin. Rhys. Lett. 27, 087401 (2010)
- 32. I. Chong, T. Terashima, Y. Bando, M. Takano, Y. Matsuda, T. Nagaoka, K. Kumagai, Physica C **290**, 57 (1997)
- 33. S. Kishida, E. Hosokawa, W.Y. Liang, J. Cryst. Growth 205, 284 (1999)
- 34. A. Katsui, H. Ohtsuka, J. Cryst. Growth 91, 261 (1988)
- 35. S. Pinol, J. Fontcuberta, C. Miravitlles, J. Cryst. Growth 100, 286 (1990)
- 36. S. Kishida, M. Nakamura, W.Y. Liang, J. Cryst. Growth 216, 220 (2000)
- K. Shigematsu, H. Takei, I. Higashi, K. Hoshino, H. Takahara, J. Cryst. Growth 100, 661 (1990)
- 38. G.D. Gu, K. Takamuku, N. Koshizuka, S. Tanaka, J. Cryst. Growth 130, 325 (1993)
- 39. M.J.V. Menken, A.J.M. Winkelman, A.A. Menovsky, J. Cryst. Growth 113, 9 (1991)
- YuI Gorina, G.A. Kalyuzhnaya, N.N. Sentyurina, V.A. Stepanov, S.G. Chernook, Crystallogr. Rep. 50, 142 (2005)
- 41. Y. Huang, M.-H. Huang, J.M. Jiang, J. Cryst. Growth 166, 867 (1996)

- A.B. Kulakov, A.V. Kosenko, S.A. Zver'kov, G.A. Emel'chenko, I. Ponahlo, Supercond. Sci. Technol. 9, 859 (1996)
- 43. W.K. Wong-Ng, L.P. Cook, F. Jiang, J. Am. Ceram. Soc. 81, 1829 (1998)
- G.D. Gu, T. Egi, N. Koshizuka, P.A. Miles, G.J. Russell, S.J. Kennedy, Physica C 263, 180 (1996)
- A.B. Kulakov, I.G. Naumenko, S.A. Zver'kov, A.V. Kosenko, S.S. Khasanov, I.K. Bdikin, G. A. Emel'chenko, M. Fehlmann, L.J. Gauckler, G. Yang, J.S. Abell, J. Cryst. Growth 231, 194 (2001)
- 46. Y. He, F. Zhou, Z.X. Zhao, Physica C 328, 207 (1999)
- 47. R. Zhifeng, Y. Xiuli, J. Yandao, G. Weiyan, J. Cryst. Growth 92, 677 (1988)
- 48. H. Imao, S. Kishida, Physica C **378–381**, 660 (2002)
- 49. H. Funabiki, K. Okanoue, C. Takano, K. Hamasaki, J. Cryst. Growth 259, 85 (2003)
- 50. A.M.M. Gadalla, W.E. Ford, J. White. Trans. Br. Ceram. Soc. 62, 45 (1963)
- 51. K. Oka, T.-S. Han, D.-H. Ha, F. Iga, H. Unoki, Physica C 215, 407 (1993)
- 52. H. Tanaka, M. Nakamura, S. Kishida, Physica C 357-360, 722 (2001)
- 53. Y. Echizen, H. Tanaka, S. Kishida, Physica C 426-431, 583 (2005)
- 54. S. Adachi, H. Tanaka, M. Fujiwara, T. Ishigaki, S. Kishida, Physica C 463-465, 449 (2007)
- 55. Y. Echizen, H. Tanaka, S. Adachi, T. Ishigaki, S. Kishida, Physica C 445-448, 455 (2006)
- M. Fujiwara, T. Makino, T. Nakabayashi, H. Tanaka, K. Kinoshita, S. Kishida, Physica C 469, 1178 (2009)
- I. Shigaki, K. Kitahama, K. Shibutani, S. Hayashi, R. Ogawa, Y. Kawate, T. Kawai, S. Kawai,
   M. Matsumoto, J. Shirafuji. Jpn. J. Appl. Phys. 29, L2013 (1990)
- J.H.P.M. Emmen, S.K.J. Lenczowski, J.H.J. Dalderop, V.A.M. Brabers, J. Cryst. Growth 118, 477 (1992)
- 59. D.H. Ha, I.S. Kim, Y.K. Park, K. Oka, Y. Nishihara, Physica C 222, 252 (1994)
- T.W. Li, P.H. Kes, N.T. Hien, J.J.M. Franse, A.A. Menovsky, J. Cryst. Growth 135, 481 (1994)
- 61. J.S. Wen, Z.J. Xu, G.Y. Xu, M. Hücker, J.M. Tranquada, G.D. Gu. (unpublished)
- 62. H.F. Fong, P. Bourges, Y. Sidis, L.P. Regnault, A. Ivanov, G.D. Gu, N. Koshizuka, B. Keimer, Nature 398, 588 (1999)
- 63. G.D. Gu, Z.W. Lin, Supercond. Sci. Technol. 13, 1197 (2000)
- 64. G.D. Gu, K. Takamuku, N. Koshizuka, S. Tanaka, J. Cryst. Growth 137, 472 (1994)
- 65. B. Liang, C.T. Lin, J. Cryst. Growth 237-239, 756 (2002)
- 66. T. Watanabe, T. Fujii, A. Matsuda, Phys. Rev. Lett. 84, 5848 (2000)
- 67. A. Maljuk, B. Liang, C.T. Lin, G.A. Emel'chenko, Physica C 355, 140 (2001)
- 68. I. Tanaka, T. Iwamoto, A.T.M.N. Islam, S. Watauchi, Supercond. Sci. Technol. 15, 458 (2002)
- G.D. Gu, S.H. Han, Z.W. Lin, Y. Zhao, G.J. Russell, Supercond. Sci. Technol. 11, 1118 (1998)
- 70. B. Liang, C.T. Lin, A. Maljuk, Y. Yan, Physica C 366, 254 (2002)
- D.B. Mitzi, L.W. Lombardo, A. Kapitulnik, S.S. Laderman, R.D. Jacowitz, Phys. Rev. B 41, 6564 (1990)
- 72. X. Sun, W. Wu, X. Zhao, L. Zheng, G. Zhou, X.-G. Li, Y. Zhang, Physica C 279, 47 (1997)
- 73. J.-C. Grivel, R. Flükiger, Supercond. Sci. Technol. 11, 288 (1998)
- 74. S. Horiuchi, K. Shoda, X.-J. Wu, H. Nozaki, M. Tsutsumi, Physica C 168, 205 (1990)
- 75. J.-C. Grivel, R. Flükiger, Supercond. Sci. Technol. 9, 555 (1996)
- 76. B. Liang, C.T. Lin, P. Shang, G. Yang, Physica C 383, 75 (2002)
- N. Knauf, J. Harnischmacher, R. Müller, R. Borowski, B. Roden, D. Wohlleben, Physica C 173, 414 (1991)
- 78. D. Maier, A.B. Kulakov, Cryst. Growth Des. 5, 1751 (2005)
- 79. T. Fujii, T. Watanabe, A. Matsuda, J. Cryst. Growth 223, 175 (2001)
- 80. A.B. Kulakov, D. Maier, A. Maljuk, I.K. Bdikin, C.T. Lin, J. Cryst. Growth 296, 69 (2006)
- 81. L.A. Novomliskii, B.Z. Narymbetov, S.A. Zverkov, V.S. Shekhtman, A.A. Bush, B.N. Romanov, S.A. Ivanov, V.V. Zhurov, Phys. Solid State 37, 463 (1995)

References 113

82. G. Balestrino, E. Milani, A. Paoletti, A. Tebano, Y.H. Wang, A. Ruosi, R. Vaglio, M. Valentino, P. Paroli, Appl. Phys. Lett. **64**, 1735 (1994)

- 83. S. Chu, M.E. McHenry, J. Mater. Res. 13, 589 (1998)
- 84. S. Lee, A. Yamamoto, S. Tajima, Physica C **357–360**, 341 (2001)
- 85. C.T. Lin, B. Liang, *Growth of a Hard-Grown Single Crystal: Bi*<sub>2</sub>*Sr*<sub>2</sub>*Ca*<sub>2</sub>*Cu*<sub>3</sub>*O*<sub>3</sub>, *New Trends in Superconductivity*, ed. by J.F. Annett, S. Kruchinin II. Mathematics, Physics and Chemistry, vol. 67, (NATO Science Series, Kluwer/Boston/London, 2002), p. 19
- E. Giannini, R. Gladyshevskii, N. Clayton, N. Musolino, V. Garnier, A. Piriou, R. Flükiger, Curr. Appl. Phys. 8, 115 (2008)
- 87. E. Giannini, V. Garnier, R. Gladyshevskii, R. Flükiger, Supercond. Sci. Technol. 17, 220 (2004)
- 88. M. Lomello-Tafin, E. Giannini, E. Walker, P. Cerutti, B. Seeber, R. Flükiger, IEEE Trans. Appl. Supercond. 11, 3438 (2001)
- 89. E. Giannini, I. Savysyuk, V. Garnier, R. Passerini, P. Toulemonde, R. Flükiger, Supercond. Sci. Technol. 15, 1577 (2002)
- 90. C.T. Lin et al., Enhanced superconductivity in Bi-2223 by pressure-induced inhomogeneity
- 91. B. Liang, C. Bernhard, T. Wolf, C.T. Lin, Supercond. Sci. Technol. 17, 731 (2004)
- 92. Z.X. Cai, Y. Zhu, D.O. Welch, Phys. Rev. B 52, 13035 (1995)
- 93. T. Fujii, I. Terasaki, T. Watanabe, A. Matsuda, Phys. Rev. B 66, 024507 (2002)

# Chapter 4 Crystal Growth and Characterization of Na<sub>x</sub>CoO<sub>2</sub> and Na<sub>x</sub>CoO<sub>2</sub>·yH<sub>2</sub>O

**Dapeng Chen and Chengtian Lin** 

**Abstract** This chapter reviews the single crystal growth of  $Na_xCoO_2$  family and the superconductivity is obtained by hydration of the compounds  $Na_xCoO_2 \cdot yH_2O$ . The large crystals of  $Na_xCoO_2$  are grown by optical floating zone method. A systematic study of Na-extraction and hydration process in  $Na_xCoO_2$  (x = 0.32-1.00) and  $Na_xCoO_2 \cdot yH_2O$  (x = 0.22-0.47, y = 1.3) is demonstrated with the pure phase of  $\alpha$  ( $\alpha$  = 0.90–1.00) and  $\alpha$  ( $\alpha$  = 0.75) and the detailed procedures are presented.

#### 4.1 Introduction

 $A_x M X_2$  type compounds (A = alkaline metal, M = transition metal, X = O, S, Se) have attracted much attention as cathode materials for many years [1]. These compounds have a layered structure, and among them, there is an extensive group of oxides involving 3d transition-metals that have been investigated as a reference for HTSCs. In 1997, I. Terasaki et al. discovered the coexistence of a large in-plane thermoelectric (TE) power ( $\sim 100 \ \mu V/K$ ) and low resistivity (200  $\mu \Omega$ ) at room temperature in NaCo<sub>2</sub>O<sub>4</sub> (or Na<sub>0.5</sub>CoO<sub>2</sub>), which made the sodium cobaltate an attractive material for thermoelectric applications [2–6].

 $NaCo_2O_4$  belongs to a family of bronze-type compounds expressed as  $A_xMO_2$  (0.5 < x < 1), which was first identified by Jansen and Hoppe [7]. An important similarity to HTSCs is that  $NaCo_2O_4$  is a layered transition-metal oxide, where Na sites are  $\sim 50$  % occupied and  $CoO_2$  units are alternately stacked along the c axis. Thus, the physical properties are expected to be highly two dimensional (2D). However, the  $CoO_2$  layer is different in structure from the  $CuO_2$  layer of HTSCs: the former is a 2D triangular lattice, and the latter is a 2D square lattice. Early investigation by Tanaka, Nakamura, and Iida [8] has shown that polycrystalline  $NaCo_2O_4$  is a good metal down to 12 K, although it shows Curie-Weiss-like

D. Chen (⋈) · C. Lin

susceptibility instead of the Pauli paramagnetism. According to their results, NaCo<sub>2</sub>O<sub>4</sub> can be regarded as a doped 2D triangular spin lattice, which is worth comparing with the CuO<sub>2</sub> layer HTSCs.

Superconductor  $Na_{0.35}CoO_2 \cdot 1.3H_2O$  has attracted considerable attention as being the first layered superconductor to replace copper with cobalt and as evidence that important electronic correlations exist [9]. Its superconducting transition temperature of maximum  $T_c < 5$  K exhibits composition dependence, with  $T_c$  decreasing for both under-doped and over-doped materials, as observed in the cuprates. Despite the major differences in their geometry and bond filling, there is the intriguing similarity that the cobalt superconductor has low spin  $Co^{4+}$  with  $S = \frac{1}{2}$ , just as cuprate superconductors have  $Cu^{2+}$  with S = 1/2.

However, the transport and magnetic properties of  $Na_xCoO_2$  are strongly dependent on the Na content. It has been found that as x increases from 0.3, the ground state of these compounds goes from a paramagnetic metal through a charge ordered insulator (at x=0.5) to a 'Curie-Weiss metal' (around x=0.70), and finally to a weak-moment magnetically ordered state (x>0.75) [10]. Muon spin rotation ( $\mu$ SR) and nuclear magnetic resonance (NMR) measurements have identified the stoichiometric three-layer  $Na_1CoO_2$  phase to be a non-magnetic insulator [11, 12]. Thus the phase diagram of  $Na_xCoO_2$  is different from that of cuprates. The superconducting 'dome' of  $Na_xCoO_2$  is closer to  $Co^{3+}$  (S=0) rather than  $Co^{4+}$  (S=1/2) [13–15], and  $Na_xCoO_2$  even shows magnetic ordering at  $x \ge 0.75$ , except for a special one at x=0.5 [10, 16]. These interesting behaviours clearly indicate that the origin and functionality of strong correlations in these two materials are very different.

Whatever the relationship between these two types of superconductor may be, the cobalt superconductor at least could provide insight into the relationship between dimensionality and superconductivity. This suggests that a detailed characterization of the electronic and magnetic behavior of this new family of materials and their interplay with structural peculiarities may contribute to a more fundamental understanding of the high  $T_{\rm c}$  superconductivity in cuprates and even lead to thermoelectronic applications.

This chapter deals with all the phases of sodium cobaltate. With sodium content x increasing to 1.0, there are four thermodynamically stable phases in the Na<sub>x</sub>CoO<sub>2</sub> system that have been previously reported [17]. In all the phases, sheets of edge-sharing CoO<sub>6</sub> octahedra are interleaved by sodium ions along the c-axis direction, delineated as (i)  $\alpha$ -Na<sub>x</sub>CoO<sub>2</sub> (0.9  $\leq$  x  $\leq$  1) having the O3 structure (with O referring to the octahedral coordination of the Na ions and 3 the number of layers in a repeat), (ii)  $\alpha$ -Na<sub>x</sub>CoO<sub>2</sub> (0.55  $\leq$  x  $\leq$  0.6) having the P3 structure (with P referring to the trigonal prismatic coordination of the Na ions and 3 the number of layers in a repeat), and (iv)  $\gamma$ -Na<sub>x</sub>CoO<sub>2</sub> (0.55  $\leq$  x  $\leq$  0.74) having a P2 phase. For these phases, chemical or electrochemical methods can be used to adjust the sodium composition within these structures. Thus, lower Na content phases have been

4.1 Introduction 117

obtained by de-intercalation of their higher x counterparts [18]. In addition, intercalation can be used to increase the sodium content of the higher Na phases to even higher phases. For example,  $\gamma$  phase from x = 0.7 up to x = 1.0 [18].

# 4.2 Two-Layer Na<sub>x</sub>CoO<sub>2</sub>

In March 2003, Takada et al. announced the discovery of superconductivity in a compound in this family with two-dimensional  $CoO_2$  layers [9]. They reported that by using a chemical oxidation process (as shown in Fig. 4.1) from  $Na_{0.7}CoO_2$ , a superconductor,  $Na_{0.3}CoO_2$  1.3H<sub>2</sub>O with a T<sub>c</sub> of about 5 K, was obtained. This discovery has generated enormous interest in the research community. Earlier interest was focused on the understanding of the surprisingly high thermoelectric power of the metallic conductor  $Na_{0.7}CoO_2$  [19, 20].

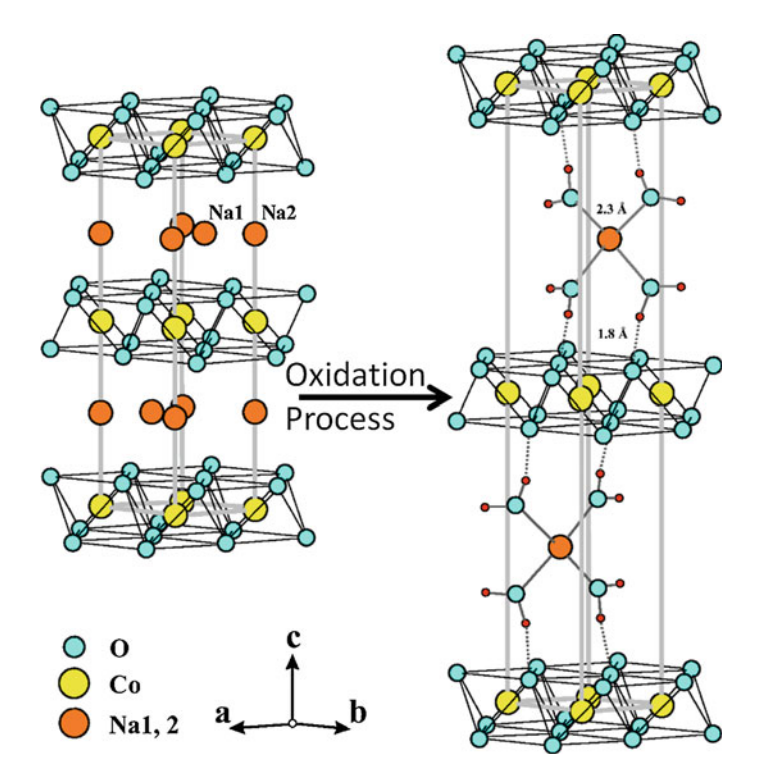


**Fig. 4.1** Structural views of Na<sub>0.7</sub>CoO<sub>2</sub> (*left*) and Na<sub>x</sub>CoO<sub>2</sub> yH<sub>2</sub>O (*right*), where Na and H<sub>2</sub>O sites are partially occupied. Na<sub>0.7</sub>CoO<sub>2</sub> was prepared by solid-state reaction under oxygen gas flow. A fivefold excess of Br<sub>2</sub> with respect to the Na content was dissolved in acetonitrile (CH<sub>3</sub>CN). A well pulverized powder of Na<sub>0.7</sub>CoO<sub>2</sub> was immersed in the Br<sub>2</sub>/CH<sub>3</sub>CN solution for 5 days to de-intercalate Na ions; then the product was filtered, washed with CH<sub>3</sub>CN and distilled water, and finally dried in ambient atmosphere [9]

Two-layer  $\gamma$ -Na<sub>x</sub>CoO<sub>2</sub> has a hexagonal structure with the space group symmetry of P6<sub>3</sub>/mmc and lattice parameters a = b = 2.840 Å and c = 10.811 Å [7]. The in-plane direction of the CoO<sub>6</sub> octahedron in CoO<sub>2</sub> alternates with the nearest CoO<sub>2</sub> layers, as shown on the left of Fig. 4.1.

# 4.2.1 Single Crystal Growth

It is of particular interest that the Na<sub>x</sub>CoO<sub>2</sub> compounds can be transformed into a superconductor with water molecules intercalated between the CoO<sub>2</sub> layers [9, 20, 21], as the observation of superconductivity in a transition metal oxide is a rare and exceptional phenomenon. To obtain superconductivity in the compound, a controlled doping level or a particular ratio of Co<sup>3+</sup>/Co<sup>4+</sup> has to be achieved, and the intercalated water should also be considered as an important parameter. Although neutron and X-ray powder diffraction (XRD) were used to determine the crystal structure and the arrangement of water molecules in the sodium layer [22–24], it is rather difficult to fix the local coordination of the water molecules. Furthermore, the intercalated water in the crystal is extremely unstable; hence, the accurate characterization of the compound becomes another problem to be solved [25–28]. Several models have been proposed [23, 24] to interpret the structure of the compound. There are several plausible scenarios of unconventional, non-phonon superconductivity in Na<sub>0.3</sub>CoO<sub>2</sub> yH<sub>2</sub>O, and it is expected that the water coordination also affects the electronic properties of the CoO<sub>2</sub> planes. Therefore, the availability of single crystals is important, since they allow an accurate characterization of the compound with respect to its physical, chemical, electrical, and thermal properties.

When growing  $Na_xCoO_2$  single crystals, considerable difficulties appear on account of the high  $Na_2O$  vapor pressure, which increases exponentially from  $10^{-5}$  to  $10^{-3}$  Torr with heating to temperatures between 500 and 800 °C, followed by a noticeable evaporation. Therefore ceramic powders were synthesized using additional  $Na_2CoO_3$  to compensate for the Na loss during heating [26, 27], or a "rapid heat-up" technique was used [29, 30] to avoid the formation of a non-stoichiometric compound. Solution growth using NaCl flux [31] was performed, but unfortunately, that led only to thin crystals (<0.03 mm) or to non-stoichiometric and possibly contaminated samples.

#### 4.2.1.1 Single Crystal Growth by the Flux Method

Large single crystals are required for measuring the thermoelectric properties and other anisotropic properties of these sorts of compounds. However, it is difficult to grow large  $Na_xCoO_2$  crystals. In 1997, Terasaki et al. first grew  $NaCo_2O_4$  single crystals by the flux method, with the largest size  $1.5 \times 1.5 \times 0.01$  mm<sup>3</sup>. Since then, the flux method has been widely used in the single crystal growth of  $Na_xCoO_2$  [31–39].

Fujita et al. [31, 33] studied the flux growth of two-layer γ-Na<sub>x</sub>CoO<sub>2</sub> and its high-temperature thermoelectric properties. Single crystals were grown from the molten materials using NaCl as the flux. The starting materials were well mixed in the ratio of Na<sub>2</sub>CO<sub>3</sub>:CO<sub>3</sub>O<sub>4</sub>:NaCl = 1:1:7. The mixture was heated in an Al<sub>2</sub>O<sub>3</sub> crucible at 1223 K for 12 h in air and slowly cooled down to 1123 K at the rate of -0.5 K/h. This was followed by washing away of the NaCl flux with pure water. The largest size of the flaky resultant samples was about  $5 \times 3 \times 0.05$  mm<sup>3</sup>; the typical size was  $1.5 \times 1.5 \times 0.03$  mm<sup>3</sup>. These single crystals with metallic luster are thin in the c-axis direction and can be cleaved along the ab plane. Single crystals grown by the same procedure were used in many studies [36-38]. The in-plane resistivity and thermal conductivity of single crystal Na<sub>0.7</sub>CoO<sub>2</sub> were measured down to 40 mK. A Fermi-liquid state at low temperature is characterized by the largest Kadowaki-Woods ratio ever observed. Comparison with other materials suggests that the giant electron-electron scattering is due to magnetic frustration or to the proximity of a nearby magnetic quantum critical point [37]. Wang et al. [36] investigated the electronic structure and charge for Na<sub>0.7</sub>CoO<sub>2</sub> single crystals by means of an optical spectroscopy probe. The in-plane optical conductivity spectra show two broad interband transition peaks at 1.6 and 3.1 eV, and a weak mid-infrared peak at 0.4 eV. The origin of the interband transitions and the low-frequency charge dynamics is also discussed [36].

Single  $\gamma$ -Na<sub>0.7</sub>CoO<sub>2</sub> crystals can be grown from a higher flux ratio (Na:Co: NaCl = 1:1:10) mixture by the same procedure [40]. The resultant hexagonal thin platelets with a typical size of  $3 \times 3 \times 0.1$  mm<sup>3</sup> seem have better morphology than the crystals grown from the lower flux ration (as shown on the right of Fig. 2.5). When B<sub>2</sub>O<sub>3</sub> was used as the flux with Na<sub>2</sub>CO<sub>3</sub>:B<sub>2</sub>O<sub>3</sub> = 8:1 [35],  $\gamma$ -Na<sub>0.6</sub>CoO<sub>2</sub> single crystals were grown with a typical size of  $3 \times 3 \times 0.1$  mm<sup>3</sup>. (The Na content is inaccurate; however, as otherwise the compound would be  $\beta$ -phase.)

## 4.2.1.2 Single Crystal Growth by Optical Floating Zone Method

Using NaCl (or B<sub>2</sub>O<sub>3</sub>) flux can grow millimeter sized Na<sub>x</sub>CoO<sub>2</sub>, but that unfortunately led only to thin crystals, when the flux washed in water will lead to non-stoichiometric and possibly contaminated samples. This kind of crystal can't be used for superconducting phase studies, for the compound can be partially decomposed during the intercalation process, resulting in highly defective crystals containing Na-poor phases.

Large and high quality single crystals of two-layer  $Na_xCoO_2$  can be grown by the floating zone method in an image furnace [25, 31, 32, 41–43]. Starting feed and seed materials were prepared from  $Na_2Co_3$  and  $Co_3O_4$  of 99.9 % purity, with the nominal composition of  $Na_xCoO_2$ , where x = 0.50, 0.60, 0.70, 0.75, 0.80, 0.85, and 0.90, respectively. Well-mixed powders were loaded into alumina crucibles, heated to 750 °C, and kept at that temperature for one day. The heated powders were reground and calcined at 850 °C for another day. They were then shaped into cylindrical bars about 6 mm in diameter and 100 mm long by pressing at an

Sample	Feed rod	Comments	Crystal	Lattice	Lattice
no.	composition	(phases, impurities)	formula	parameters a (Å)	parameters b (Å)
A	Na <sub>0.50</sub> CoO <sub>2</sub>	Na-poor phase, Co <sub>3</sub> O <sub>4</sub>	Na <sub>0.55</sub> CoO <sub>2</sub>	-	-
В	Na <sub>0.60</sub> CoO <sub>2</sub>	Na-poor-, β phase, Co <sub>3</sub> O <sub>4</sub>	Na <sub>0.60</sub> CoO <sub>2</sub>	2.819(3)	11.111(8)
С	Na <sub>0.65</sub> CoO <sub>2</sub>	ά-, β-phase, Co <sub>3</sub> O <sub>4</sub>	Na <sub>0.65</sub> CoO <sub>2</sub>	2.828(5)	10.921(2)
D	Na <sub>0.70</sub> CoO <sub>2</sub>	ά-, β-phase, Co <sub>3</sub> O <sub>4</sub>	Na <sub>0.75</sub> CoO <sub>2</sub>	2.842(5)	10.814(7)
Е	Na <sub>0.75</sub> CoO <sub>2</sub>	ά-, γ-phase, Co <sub>3</sub> O <sub>4</sub>	Na <sub>0.72</sub> CoO <sub>2</sub>	2.843(6)	10.808(5)
F	Na <sub>0.80</sub> CoO <sub>2</sub>	α-,ά-phase, Co <sub>3</sub> O <sub>4</sub>	Na <sub>0.87</sub> CoO <sub>2</sub>	2.841(4)	10.839(5)
G	Na <sub>0.82</sub> CoO <sub>2</sub>	γ-phase, Co <sub>3</sub> O <sub>4</sub>	Na <sub>0.73</sub> CoO <sub>2</sub>	2.843(0)	10.817(0)
Н	Na <sub>0.90</sub> CoO <sub>2</sub>	α-,ά-phase, Co <sub>3</sub> O <sub>4</sub>	Na <sub>0.82</sub> CoO <sub>2</sub>	2.841(9)	10.820(7)

Table 4.1 Possible co-existent phases in the Na<sub>x</sub>CoO<sub>2</sub> single crystals and their crystallographic

ά-phase: x = 0.75; β-phase:  $0.60 \ge x \ge 0.55$ ; γ-phase:  $0.74 \ge x \ge 0.55$ ; (0.75 < x < 0.90): α + ά phases; (0.60 < x < 0.75): ά-phase + Na<sub>0.6</sub>CoO<sub>2</sub> [45]

isostatic pressure of  $\sim 70$  Mpa and then sintering at 850 °C for 1 day in flowing oxygen to form the feed rods.

Each sintered feed rod was pre-melted with a mirror scanning velocity of 27 mm/h, while traveling the upper and lower shafts to densify the feed rod. After pre-melting, the  $\sim 20$  mm long rod was cut and used as the first seed, and thereafter the grown crystal was used as the seed. The feed rod and the growing crystal were rotated at 15–30 rpm in opposite directions. In an attempt to reduce the volatilization of Na and obtain large and stoichiometric crystals, traveling rates of 1–2 mm/h under pure oxygen flow of 200 ml/min were applied throughout the growing procedure. The initial growth compositions together with the analyzed crystal data are given in Table 4.1.

To obtain superconductivity, the Na was partly extracted by placing crystals in a  $6.6 \text{ mol } \mathrm{Br_2/CH_3CN}$  solution for 100 h and then washing them out with  $\mathrm{H_2O}$  or  $\mathrm{D_2O}$  solution [9]. Alternatively, the electrochemical technique was also applied, using an aqueous solution of NaOH as an electrolyte to partially extract the Na [44]. This technique needs a longer time for de-intercalation, and the resulting superconducting transitions are generally sharper.

# 4.2.2 Melting Behavior of Two-Layer Na<sub>x</sub>CoO<sub>2</sub>

The melting behavior of two-layer Na<sub>x</sub>CoO<sub>2</sub> crystal was investigated by differential thermal analysis and thermogravimetric (DTA-TG) measurements and with a high

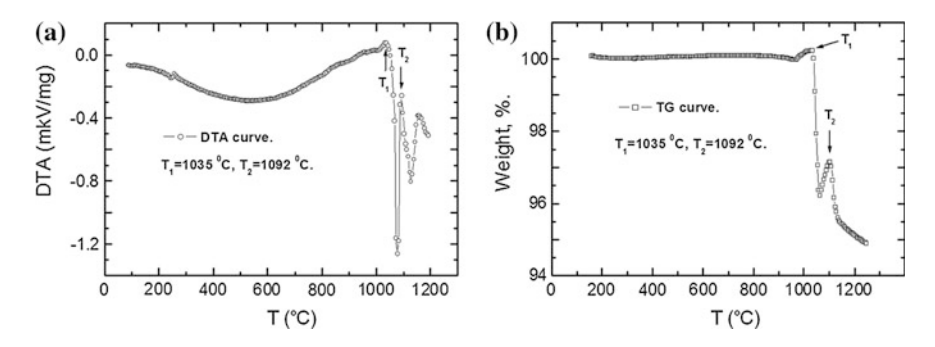


**Fig. 4.2** DTA-TG analysis by melting single crystalline  $Na_{0.7}CoO_2$ , with heating at 7.5 °C/min up to 1200–1250 °C in flowing oxygen.  $T_1 = 1035$  °C,  $T_2 = 1092$  °C. **a** The melting behavior of the compound, and **b** the temperature dependence of the weight loss [25]

temperature optical microscope. A small single crystal of  $Na_{0.7}CoO_2$  was placed in a Pt crucible and then heated in the DTA-TG apparatus at 7.5 °C/min up to 1200–1250 °C in flowing oxygen. Two peaks with onset  $T_1$  = 1035 °C and  $T_2$  = 1092 °C on the DTA curve correlate very well with the weight loss observed by TG, as shown in Fig. 4.2a, b, respectively. No weight changes were observed below 980 °C.

A high temperature optical microscope study of the crystal reveals that the liquid phase appears at  $T_1 = 1035~{}^{\circ}\text{C}$ , but the solid phase (crystal) still remains up to  $T_2 = 1092~{}^{\circ}\text{C}$ , so that there is a coexistence of solid and liquid phases. The investigations indicate that thermal decomposition of  $Na_{0.7}CoO_2$  is accompanied by a weight loss down to 96.2 wt% and the compound decomposes into a sodium-rich liquid and a cobalt-rich solid phase [45, 46], assuming that the chemical reaction of the melt proceeds as follows:

$$Na_xCoO_2 \rightarrow CoO + liquid (Na-rich) + xO_2 - (T > 1100 \,^{\circ}C) \rightarrow [Na_xCoO_{1.65}]*$$

$$* = homogeneous melt.$$

The dissolution of CoO occurs in the Na-rich melt by taking up oxygen from the environment. Thus, it results in an increase of weight, because the oxidation state of cobalt is significantly higher in the melt, i.e.,  $Co^{+2.7}$ , according to the chemical reaction equation shown above. A sharp weight loss down to 95.5 wt% occurs at  $T_2 = 1092~^{\circ}C$ , and the melt starts to become homogeneous and stable. A nearly constant weight of 95.5–94.9 wt% is obtained in the temperature range of 1120–1200  $^{\circ}C$ , where the melt becomes homogeneous. A monotonic weight loss in the melt may occur under constant heating. Evidently, the melting behavior described so far indicates that the compound melts incongruently.

## 4.2.2.1 Crystal Growth, Morphology, and Composition

When sintering Na<sub>x</sub>CoO<sub>2</sub> at high temperatures, the decomposition of Na<sub>2</sub>O can cause weight loss and lead to an inhomogeneous compound. During growth, a

**Fig. 4.3** Typical Na<sub>0.82</sub>CoO<sub>2</sub> (*upper*) and Na<sub>0.75</sub>CoO<sub>2</sub> (*lower*) single crystal ingots obtained by the optical floating zone technique



white powder consisting of  $Na_2O$  is observed to volatilize and be deposited on the inner wall of the quartz tube. From weighing, a total weight loss of  $\sim 6$  wt% is estimated. This value is in agreement with the data shown in Fig. 4.2b, neglecting the tiny loss of oxygen caused by the change in the cobalt valence state. The main loss of  $Na_2O$  is found during the pre-melting procedure and is estimated to be  $\sim 5$  wt%. This is probably caused by incompletely reacted  $Na_2O$  when the mixtures are calcined and sintered prior to pre-melting. An additional  $\sim 1$  wt% loss is estimated after the crystal growth.

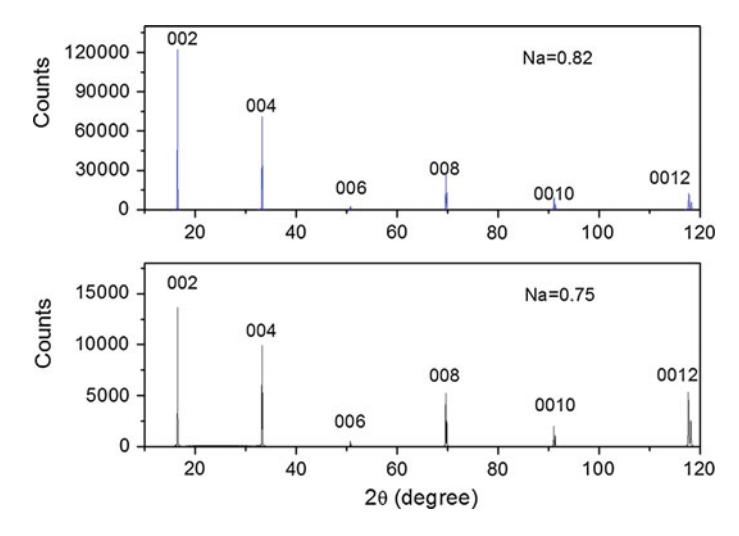
Large single crystals of  $Na_xCoO_2$  were obtained with variable Na content, using a growth rate of 2 mm/h in flowing oxygen atmosphere. During growth, it has been observed that the molten zone was stable and that it was easy to form the  $\alpha$ -phase of  $Na_xCoO_2$  with sodium content x=0.75, while it was hard to grow the  $\beta$ -phase with x=0.55 and 0.60, and  $\gamma$ -phase with x=0.65 and 0.70. Energy dispersive X-ray analysis (EDX) results indicated that as-grown  $Na_xCoO_2$  with the lower sodium content of x=0.65 consists of multi-phases such as  $Na_2O$ ,  $Co_3O_4$ , and Na-poor phases. Co-existent phases and inhomogeneous composition are always observed in the compounds with initial x=0.70, 0.80, and 0.82, as listed in Table 4.1.

Figure 4.3 shows typical as-grown crystal ingots of  $Na_{0.82}CoO_2$  and  $Na_{0.75}CoO_2$ . The XRD 00l diffraction patterns indicate nearly pure phases of both  $\gamma$ - and  $4Na_xCoO_2$  crystals, as shown in Fig. 4.4.

Both crystals were identified to have a hexagonal structure with two sheets (prismatic, P2) of edge-shared  $CoO_6$  octahedra in a unit cell for the  $\gamma$ - and  $\alpha$ -phase, respectively. The lattice parameters and cell volumes were determined by least squares refinement of the XRD data and correspond to the space group P6<sub>3</sub>/mmc (P2), respectively. The crystallographic data are given in Table 4.1.

Figure 4.5a displays one-half of an ingot showing crystal platelets with the 00l face of several  $\rm cm^2$  areas cleaved from the ingot with a sharp scalpel. Figure 4.5b shows the other half after water intercalation. Crystal grains were found to grow preferentially along the a crystallographic axis, parallel to the rod axis.

A convex growth interface is observed to be the boundary between the regions of smaller and larger diameter of the crystal ingot, as shown in Fig. 4.5. The smaller diameter part was formed when the molten zone was at lower temperatures, and the larger diameter one was formed at higher temperatures. Therefore, the unequal diameter for an ingot indicates that temperature fluctuations occurred at the molten zone during growth. According to the temperature-composition relationship, a fluctuation in the heating temperature may result in a composition change of the molten zone, leading to an inhomogeneous compound. Figure 4.5a, c show that



**Fig. 4.4** 001 XRD patterns showing pure  $\gamma$ -phase Na<sub>0.82</sub>CoO<sub>2</sub> (*upper panel*) and  $\gamma$ -phase Na<sub>0.75</sub>CoO<sub>2</sub> (*lower panel*). The split peaks are CuKa<sub>1</sub> and CuKa<sub>2</sub> for the higher and lower intensity, respectively

many tiny crystal grains of  $CoO_2$  gather at the boundary of the growth front. These grains can be removed by the de-intercalation treatment, as shown in Fig. 4.5b. It is important to maintain a stable molten zone by applying a constant heating temperature to grow a high quality single crystal.

Fig. 4.5 Two halves of an as-grown crystal ingot with a cleaved 001 surface: **a** As-cleaved half ingot of Na<sub>0.7</sub>CoO<sub>2</sub>, showing CoO<sub>2</sub> inclusions gathered at the growth boundary **b** The other half of the ingot transformed to Na<sub>0.3</sub>CoO<sub>2</sub> yH<sub>2</sub>O, showing the removal of the CoO<sub>2</sub> inclusions after de-intercalation followed by hydration. **c** The enlarged CoO<sub>2</sub> inclusions [25]





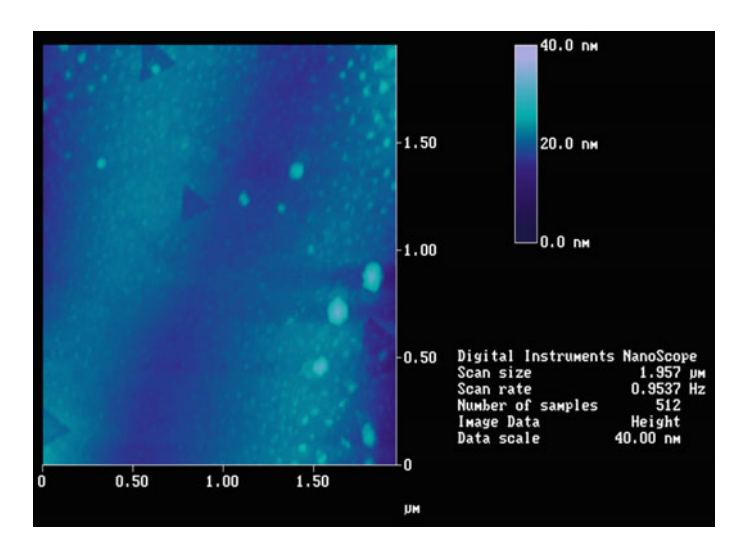


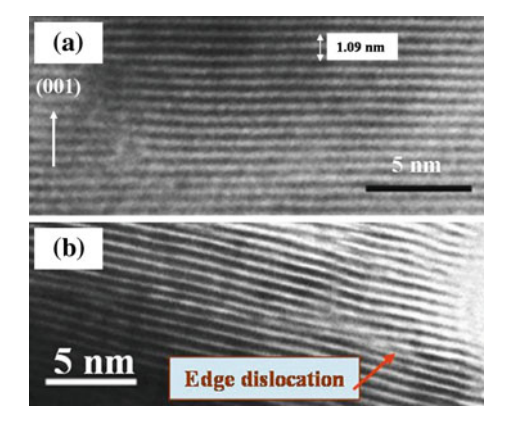
Fig. 4.6 Typical terraced pits on the (110) face of as-grown Na<sub>0.7</sub>CoO<sub>2</sub> single crystal

In order to understand the detailed structures of these materials, atomic force microscopy (AFM) and transmission electron microscopy (TEM) were used. Figure 4.6 shows an AFM image taken from the freshly cleaved (110) face of  $Na_{0.7}CoO_2$  single crystal. It can be seen that there are some triangular pits at specific sites, which may be attributed to the defects in the as-grown crystal.

High-resolution TEM (HRTEM) images taken from the ingot in Fig. 4.5a are shown in Fig. 4.7. The identical d-spacing of 1.09 nm is consistent with the d-value of (001), indicating single-crystal characteristics, with a cleavage surface along [001].

The composition distribution along the ingot of Na<sub>0.75</sub>CoO<sub>2</sub> was determined using EDX. The crystal was scanned through a 3 mm segment along the growth direction in order to determine the Na/Co compositions. The average value of the

**Fig. 4.7 a** HRTEM image showing the layered structure of a Na<sub>0.7</sub>CoO<sub>2</sub> single crystal; **b** HRTEM image of an edge dislocation in the same crystal



Na composition was calculated from four measured points in the central and edge regions of the crystal. It was found that the Na content varied with the temperature fluctuations during the growth. At the beginning of the growth the temperature fluctuations were high and caused a high variation of the composition,  $\Delta x \approx 0.11$ , determined within 2 cm from the seeding part of the ingot. Further away from the seeding part, the variation of Na content is smaller,  $\Delta x \approx 0.06$ , when the molten zone is maintained in a stable state by a constant temperature. A volatilized white Na<sub>2</sub>O powder accumulates on the inner wall of the quartz tube after the growth is completed. The loss of Na may result in a reduction of its concentration in the as-grown crystal. White Na<sub>2</sub>O powders also form on the surfaces of crystals if the samples are stored under ambient conditions. Therefore, the freshly grown crystals must be stored in an evacuated container or a desiccator to avoid decomposition.

# 4.2.3 Sodium Extraction and Hydration

By chemically extracting additional sodium from the structure of  $Na_xCoO_2$  and following this by hydration, one can obtained the superconducting phase of the compound with the composition  $Na_xCoO_2$  yH<sub>2</sub>O (0.26  $\leq$  x  $\leq$  0.42, y = 1.3). Crystals of  $Na_xCoO_2$  with x = 0.3 resulted from a treatment in 6.6 mol Br<sub>2</sub>/ CH<sub>3</sub>CN, and the details of the oxidation process are described in [25]. Na extraction from the crystals was also can be carried out by the electrochemical method. The composition  $Na_{0.3}CoO_2$  could be achieved in an aqueous solution of NaOH using a constant current of 0.5 mA and a voltage of 1.0 V for over 10 days. Compared to the published 1–5 days extraction time for  $Na_{0.7}CoO_2$  powders [9, 21], a longer time is needed for single crystal samples to complete the extraction, it also depending on the dimensions of the sample. This can be attributed to the fact that the Na extraction process takes place along the 100 direction, and the chemical bonding period of Na–O–Na in the NaO layer for single crystal is an order of magnitude greater and more perfect than that of nanoscale powders, which are randomly distributed.

Before and after the extraction treatment, the sodium composition distribution across the crystals was determined by EDX. Figure 4.8 shows a plot of the sodium distribution in the central area along the crystal growth direction. This analysis indicates that the change in the sodium content of the resulting crystals after de-intercalation was  $\Delta x \approx 0.3$ . The sodium intercalant layer expanded with decreasing Na content, because the Na removal results in Co oxidation (where  $\text{Co}^{3+}$  ions are oxidized to the smaller  $\text{Co}^{4+}$  ions), and thus the  $\text{CoO}_2$  layers are expected to shrink [27]. This suggests that a decreased bonding interaction between the layers with decreasing Na content may result in a readily cleaved plane.

The Na-extracted samples are then hydrated by immersing them in de-ionized water at room temperature to obtain the superconducting phase. After hydration a large increase in thickness is visible to the naked eye, and the morphology exhibits

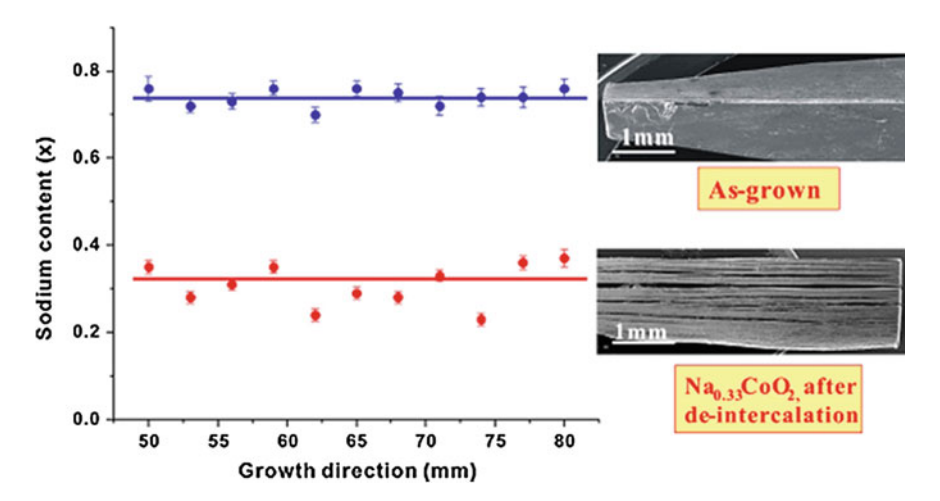


Fig. 4.8 Sodium distributions along the growth direction for the as-grown Na<sub>0.75</sub>CoO<sub>2</sub> single crystal before and after Na-extraction [47]

layered cracks perpendicular to the c-axis. The typical crystal morphologies are shown in Fig. 4.9a, c and b, d show morphologies formed by Na-extraction and  $\rm H_2O$ -intercalation, respectively.

# 4.2.4 Hydration Dynamics

The high sensitivity of the X-ray diffraction procedure allows us to observe the phase formation as well as its dissolution during the hydration and dehydration of Na<sub>0.3</sub>CoO<sub>2</sub>. Figure 4.10 shows the 002 reflections obtained from a crystal with hydration time from 0 min up to 10 days. It is not surprising to observe the coexistence of the two phases with y = 0 and 0.6 (Fig. 4.10, 0 min) prior to hydration, since the non-hydrated sample of Na<sub>0.3</sub>CoO<sub>2</sub> was stored in air and readily absorbs water to form a partial hydrate under ambient conditions (Fig. 4.11c). After heating the sample at 150 °C for 15 min, the y = 0.6 phase could be removed. As hydration proceeded, the y = 0.6 phase reformed and vanished after 10 days, when the fully hydrated phase of y = 1.3 was formed. Assuming that the initial diffusion paths of the water molecules ran along the Na-plane to fill the partially occupied sites, this process would not stop until water saturation occurred in these planes. According to the 002 reflection patterns, the expansion of the c-axis per intercalant layer is about 1.3 Å, averaged between the non-hydrated Na<sub>0.3</sub>CoO<sub>2</sub> (11.2 Å) and the partially hydrated Na<sub>0.3</sub>CoO<sub>2</sub> 0.6H<sub>2</sub>O (13.8 Å). This value is smaller than the diameter of an oxygen ion ( $\sim$ 2.8 Å),

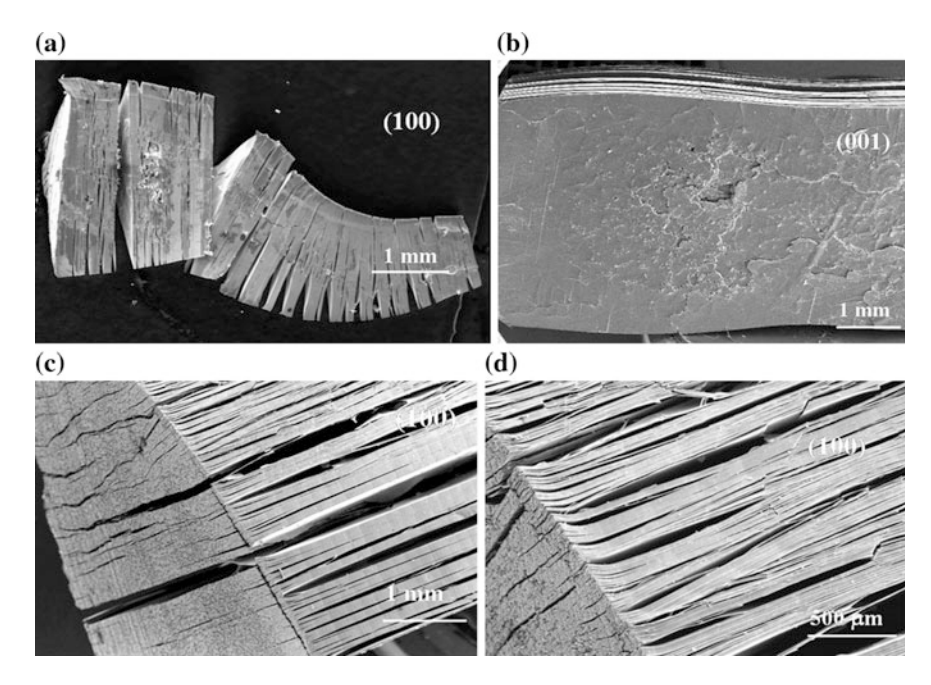
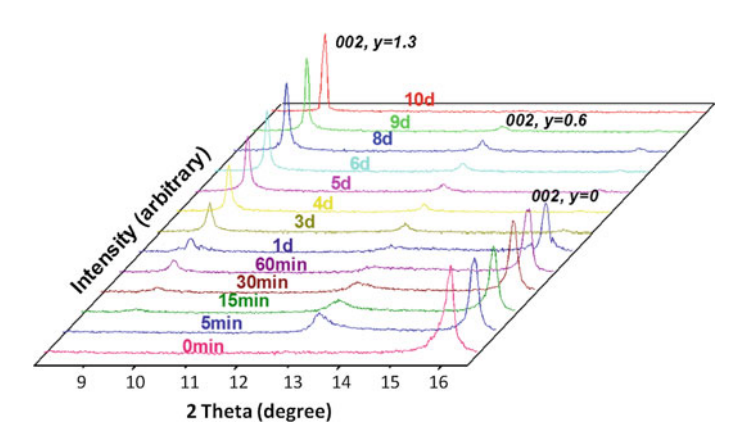
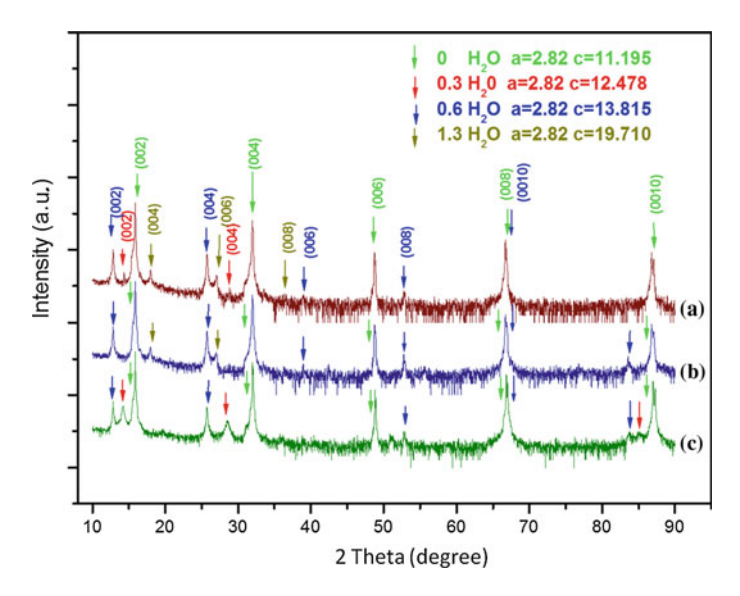


Fig. 4.9 Typical crystal morphologies showing the layered structure of  $Na_xCoO_2$  single crystals. Intercalant layers appeared after de-intercalation using a  $Br_2/CH_3CN$  solution (2 days) and b  $H_2O$  to wash out Na ions. c "Booklet"-like crystals obtained by the electrochemistry method using NaOH solution (7 days); d the same electrochemistry method crystals after a further washing with  $D_2O$ 



**Fig. 4.10** The 002 reflections show the hydration dynamics of the water molecule intercalation in  $Na_{0.3}CoO_2$ . The process indicates that two water molecules (y = 0.6, n = 2) are inserted into a formula unit initially and that this is followed by a group of four to form a fully hydrated phase (y = 1.3, n = 4) [40]



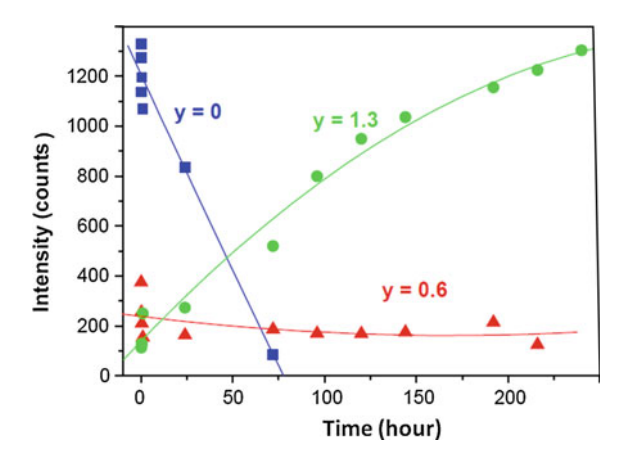
**Fig. 4.11** XRD patterns and lattice constants for  $Na_{0.3}CoO_2$  yH<sub>2</sub>O under changing ambient conditions: **a** From humid to dry air for 2 days after full hydration. **b** From humid to dry air for 5 days after full hydration. **c** From dry to humid air for 5 days before hydration [25]

suggesting that in this partial hydrate, the Na ions and the H<sub>2</sub>O molecules are accommodated in the same plane.

As shown by the hydration process in Fig. 4.10, the y=1.3 phase is formed predominantly and becomes the sole phase within 10 days, with nearly complete elimination of both the y=0 and y=0.6 phases. These results suggest that the sample is fully hydrated with four water molecules, forming clusters of Na(H<sub>2</sub>O)<sub>4</sub> in the structure. Thus, the optimal superconducting phase of Na<sub>0.3</sub>CoO<sub>2</sub> yH<sub>2</sub>O (y=1.3, n=4) is achieved with  $T_c\approx 4.9$  K [25]. No evidence of the formation of the phases with y=0.3 (n=1), 0.9 (n=3), or 1.8 (n=6) is observed during the 10-day hydration process. This clearly demonstrates that the initial intercalation process takes place with two water molecules, followed by a group of four to form two additional layers between the Na and the CoO<sub>2</sub>. Increasing the hydration time further, beyond 15 days, may lead to an additional phase of y=1.8 [47].

With increasing intercalation time, the y = 1.3 phase starts to form after a hydration time of 15 min. The diffraction data in Fig. 4.12 show that the 002 intensity of this phase tends to be stronger, indicating that more water molecules are accommodated in the lattice, resulting in an increase in the phase volume, while the opposite is true for the non-hydrated y = 0 phase. The fully hydrated sample will lose water after being moved to ambient conditions, and mixture phases are formed with y = 0, 0.3 (n = 1), 0.6 (n = 2), or 1.3 (n = 4) (see Fig. 4.11a, b).

Fig. 4.12 Time dependence of the 002 counts for y = 0, 0.6 and 1.3, respectively, indicating that the volume of the fully hydrated y = 1.3 phase increases while the y = 0 phase rapidly decreases. The y = 0.6 phase is rather stable [40]



## 4.2.5 Deintercalation Process

After a specimen of Na<sub>0.3</sub>CoO<sub>2</sub> was treated by an over-hydrating time of 15 days, the dehydration process was then carried out by heating the sample and monitored by the thermogravimetric measurement. The result in Fig. 4.13a is the thermogravimetric curve obtained by the sample heated at 0.3 °C/min in flowing oxygen environment. There are five plateaus observed in the change of weight via heating sample. Analysis of XRD data suggests that each plateau corresponds to certain dehydrate phases with different water contents, i.e., y values. The y values are calculated from the weight loss. Turning points between every two plateaus at elevated heating temperature are noticeable, which is similar to a phase transition. The study of XRD revealed the existence of a majority phase corresponding to each turning point.

The first sharp loss of weight is estimated to be about 13 mg, observed between 28 and 50 °C. This value resulted from the initial water content y  $\sim 1.8$ , indicating that the sample is over-hydrated with composition Na<sub>0.3</sub>CoO<sub>2</sub> 1.8H<sub>2</sub>O. For an over-hydrated sample, it is assumed that six water molecules are filled below, in and above the Na ion site to form a cluster of Na(H<sub>2</sub>O)<sub>6</sub>. The over-hydrated structure model is presented with y = 1.8; n = 6 in Fig. 4.14. It was reported by Jin et al. [22] that for y = 1.3 and 1.8 phases, the lattice parameters are very close, and hence they are difficult to be identified by X-ray diffraction. The XRD data in Fig. 4.10 show the reflections of 0 0 2, 0 0 4 and 0 0 8 at  $2\theta = 8.051$ ; 16.081 and 31.991, which result from the phase y = 1.8 with the lattice constant c = 22.38 (Å) This process deintercalated water from y = 1.8 (n = 6) to y = 0.9 (n = 3), corresponding to a loss of about three water molecules from each sodium site. It is noted that the y = 1.3 phase is not observable by a turning point in Fig. 4.13. The indication of this rapid loss of water confirms that both phases of over-hydrate (y = 1.8; n = 6) and optimum hydrate (y = 1.3; n = 4) are extremely unstable around room temperature.

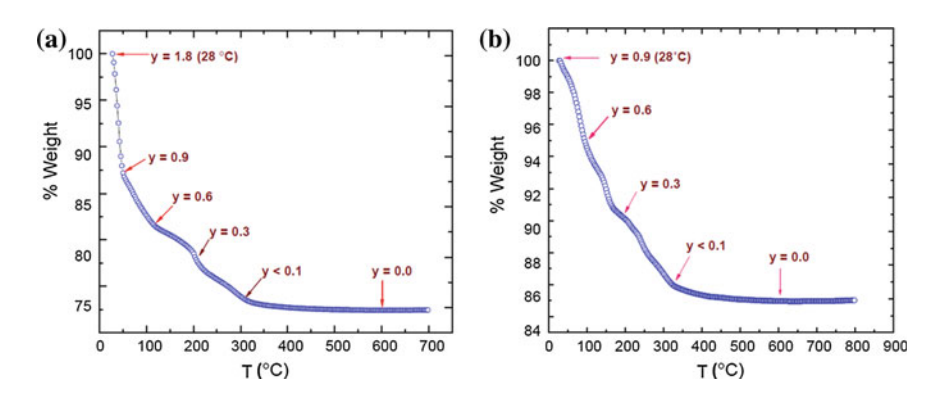


**Fig. 4.13** Thermogravimetric analysis of **a** over-hydrated (15 days) Na<sub>0.3</sub>CoO<sub>2</sub> 1.8H<sub>2</sub>O (112.9650 mg) sample, showing the temperature dependence of the weight loss for the compound heated at 0.3 °C/min in flowing oxygen. **b** The result is reproduced from another sample of partial hydrate Na<sub>0.3</sub>CoO<sub>2</sub>·0.9H<sub>2</sub>O (107.7800 mg) [47]

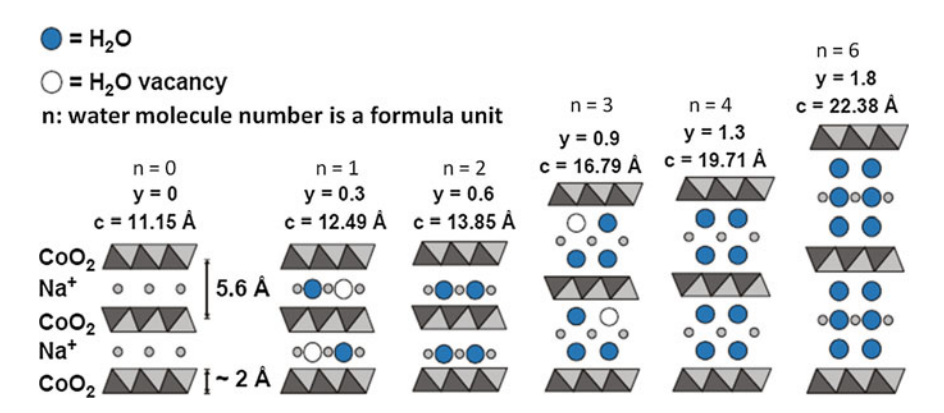


Fig. 4.14 Schematic representation of the structures of the possible ordered phases with y = 0, 0.3, 0.6, 0.9, and 1.3, respectively [47]

The following deintercalation processes take place by stages identified as phase transitions from one to another majority phase. At elevated temperatures of approximately 50, 100, 200 and 300 °C, the loss of water is estimated to be one molecule per formula unit, corresponding to y = 0.9 (n = 3), y = 0.6 (n = 2), 0.3 (n = 1) and < 0.1 (n = 0; only trace water), respectively. Their corresponding phase transitions are: Na<sub>0.3</sub>CoO<sub>2</sub>·0.9H<sub>2</sub>O (50 °C)  $\rightarrow$  Na<sub>0.3</sub>CoO<sub>2</sub>·0.6H<sub>2</sub>O (100 °C)  $\rightarrow$  Na<sub>0.3</sub>CoO<sub>2</sub>·0.3H<sub>2</sub>O (200 °C)  $\rightarrow$  Na<sub>0.3</sub>CoO<sub>2</sub> (> 300 °C). Entire removal of water from the crystal occurs at about 600 °C. These results are in excellent agreement with a further deintercalation study starting from the partially hydrated phase Na<sub>0.3</sub>CoO<sub>2</sub>·0.9H<sub>2</sub>O. The corresponding data are shown in Fig. 4.13b. There is an important feature in Fig. 4.13a, b given by the stepwise decrease of plateau slopes

with elevated temperature or progressive deintercalation. This reduction of the slope marks a generally higher stability of the compound with lower content of water.

## 4.3 Three-Layer Na<sub>x</sub>CoO<sub>2</sub>

Compared with the widely studied aforementioned phases of  $Na_xCoO_2$ , there has only been little research focus on three-layer sodium cobaltates. The research has been hampered by difficulties in single crystal growth, as well as by phase separation effects for high Na content samples [3]. Some physical properties are even decided by the sample preparation process. For instance, no superconductivity has been found in sodium cobalt oxyhydrates obtained from a parent polycrystalline sample of  $\beta$ -Na<sub>0.6</sub>CoO<sub>2</sub> [48], but sodium cobalt oxyhydrates obtained from both single crystal and powder samples of  $\beta$ -Na<sub>0.6</sub>CoO<sub>2</sub> have shown superconductivity with a T<sub>c</sub> of about 4–5 K [22, 49].

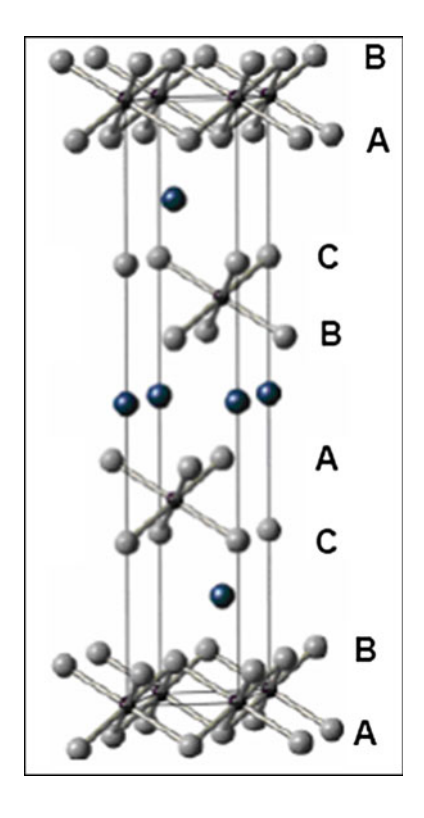
## 4.3.1 Crystal Structure

In three-layer structured  $Na_xCoO_2$ , crystallographic studies have been reported for x=1 (single crystals [50], polycrystalline powder [51]), x=0.92 (polycrystalline powder) [52], and x=0.60 [48], 0.61 [23], and 0.67 [53] (polycrystalline powder). At x=1 and 0.92, the reported three-layer structure is trigonal (R-3 m with a=2.889 Å and c=15.60 Å), and at x=0.6, the reported structure is also trigonal (R-3 m with a=2.8256(4) Å and c=16.466(2) Å), while at x=0.61, the crystal structure is two-layer hexagonal (P63/mmc, with a=2.83287(2) Å, c=10.8969(1) Å). However, at x=0.67, the crystal structure is single-layer monoclinic (C2/m, with a=4.9023(4) Å, b=2.8280(2) Å, c=5.7198(6) Å, and  $b=105.964^\circ$ ). The three-layer structure is shown in Fig. 4.15, where the unit cell is defined by three CoO2 identically orientated planes in an ACBACB [52].

# 4.3.2 Single Crystal Growth

The sample preparation method strongly impacts on the structure and physical properties. Small  $\beta$ -Na $_{0.57}$ CoO $_2$  single crystals (1.5 × 1.5 × 0.01 mm $^3$ ) can be grown from a NaCl flux, where the NaCl is mixed in a molar ratio Na:Co: NaCl = 1:1:7. The mixture is then fired at 950 °C for 12 h and then slowly cooled down to 850 °C [26].  $\alpha$ -Na $_x$ CO $_2$  single crystals also can be grown from a NaCl flux with a molar ratio Na:Co:NaCl = 1:1:4 or 1:1:5 [50, 54]. Bigger single crystals of Na $_x$ CoO $_2$  were grown by a flux technique [35, 55] using Na $_2$ CO $_3$  and Co $_3$ O $_4$  powders as the starting materials. A mixture of NaCl, Na $_2$ CO $_3$ , and B $_2$ O $_3$  was used

Fig. 4.15 The crystal structure of Na<sub>0.92</sub>CoO<sub>2</sub> (R-3 m). *Smaller* and *larger black spheres* represent Co and sodium ions, respectively, while the *grey spheres* are the oxygen ions [52]



as the flux. The typical dimensions of the obtained Na<sub>0.9</sub>CoO<sub>2</sub> crystal were  $3\times3\times0.1~\text{mm}^3$ , while those of Na<sub>0.6</sub>CoO<sub>2</sub> were  $6\times6\times0.1~\text{mm}^3$ . Investigation [56] on an as-grown Na<sub>0.9</sub>CoO<sub>2</sub> crystal indicated a transition from a paramagnetic to an incommensurate spin-density wave state (IC-SDW) at 19 K and suggested that the oscillating moments of the IC-SDW are directed along the c axis. The Na<sub>0.6</sub>CoO<sub>2</sub> crystal is paramagnetic down to 1.8 K, and the magnitude of the electronic specific-heat parameter indicates that Na<sub>x</sub>CoO<sub>2</sub> is unlikely to be a typical strongly correlated electron system.

The growth of large  $\beta$ -Na<sub>x</sub>CO<sub>2</sub> single crystals still remains a big challenge for the researcher, even using the FZ method, and only poor quality ingots, including mixtures of Na-poor phase,  $\beta$ -Na<sub>x</sub>CO<sub>2</sub>, and Co<sub>3</sub>O<sub>4</sub> can be obtained [57]. High quality large single crystals of  $\alpha$ -Na<sub>x</sub>CO<sub>2</sub> can be grown by the FZ method [58]. For the  $\alpha$ -Na<sub>x</sub>CoO<sub>2</sub> single crystal with  $x \approx 1$ , crystallographic, magnetic, and NMR measurements indicated that the stoichiometric Na<sub>1</sub>CoO<sub>2</sub> was a non-magnetic insulator, as expected for homogeneous planes of Co<sup>3+</sup> ions with S = 0. Because of a slight average Na deficiency, phase separation led to a segregation of Na vacancies into the well-defined, magnetic, Na<sub>0.8</sub>CoO<sub>2</sub> phase [12]. With x ≤ 0.97, no detectable phase segregation was found [58, 59].

Single crystals of  $Na_xCoO_2$  with nominal Na content from 0.50 to 1.00 have also been grown successfully using the TSFZ method [25, 57, 58, 60]. In this section, we present a detailed study on the crystal growth of large and high quality three-layer  $Na_xCoO_2$  (x = 0.91, 0.92 and 0.93) single crystals by the floating zone method.

When preparing the polycrystalline  $Na_xCoO_2$  by the solid state method, sintering the feed rods, pre-melting the feed rods, and growing the crystals at high temperatures, the sodium loss caused by high  $Na_2O$  vapor pressure has to be considered. Therefore, ceramic powders were synthesized using additional  $Na_2O_2$  for compensation. Sintered powders were observed by X-ray powder diffraction (XRD) to consist of a main phase of  $\alpha$ -NaCoO<sub>2</sub> mixed with a small amount of  $Co_3O_4$  impurity, due to the slow reaction in the core of the rod compared to the outside area; this is what normally happens in this series of compounds. Crystals grown using the impure feed rod did not contain any impurities, since Na has a large solubility range in the  $\alpha$ -phase in this system, and the Na loss is corrected by homogeneous mixing in the following molten process.

Crystals grown under different conditions follow the aforementioned procedures. The quality of the pre-melted feed rods is one of the critical conditions of the TSFZ technique, because during the crystal growth the molten zone is sustained by the feed rod through surface tension. A straight, long, and equal-diameter feed rod is required to stabilize the molten zone over a long growth period. It was found that it was very difficult to stabilize the molten zone during the atmospheric flow, due to the evaporation of Na, which can be observed as white Na<sub>2</sub>O deposited on the inner wall of the quartz tube, with the molten zone collapse being the result of the composition change. Application of low-pressure oxygen (2 atm) during growth was found to greatly reduce the Na evaporation. Under these conditions, zone travel rates of 1.0, 2.0, 3.0 and 5.0 mm/h were employed. It was found that the zone travel rates in this range have no detectable influence on the crystal quality. However, it has been observed that the slower rate stabilized the molten zone. Considering the evaporation of Na ions during the growth, much slower rates were not applied.

Figure 4.16 (right) presents a typical  $\alpha$ -Na<sub>x</sub>CoO<sub>2</sub> boule, which was grown at the moderate rate of 2 mm/h under an oxygen pressure of 2 atm in an attempt to reduce the volatilization of Na and obtain large crystals. The boule was black with a metallic luster and was 5 mm in diameter and 37 mm in length. The arrow indicates the crystal growth direction. Due to the layer growth mechanism, the crystal grains were found to grow preferentially along the crystallographic ab-plane, parallel to the rod axis. It was found that the cleaved surface of the as-grown crystal was shiny, but unstable under atmospheric conditions, in contrast to  $\gamma$ -phase Na<sub>x</sub>CoO<sub>2</sub> crystal. The cleaved surface became dull just 20 min after cleavage due to its reaction with moisture and CO<sub>2</sub> in the air. The crystal samples must be quickly removed after processing and stored in a clean and dry container to prevent the absorption of moisture.

The crystal wafers were cut from the last grown part and polished to a mirror face. Under a polarized light microscope, only a few separate grains were found in the peripheral area. No inclusions, cracks, or grain boundaries were observed in the

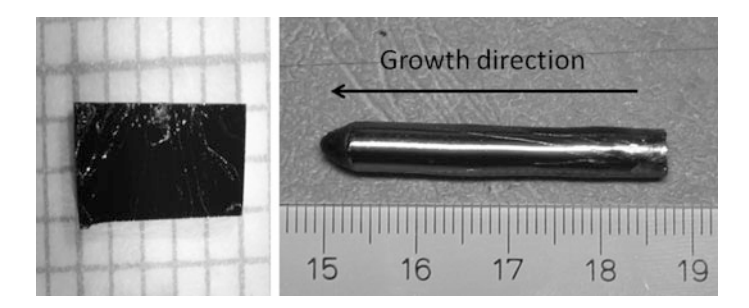


Fig. 4.16 As-grown single crystal of  $\alpha$ -NaCoO<sub>2</sub> (*right*) and the cleaved crystal from the last grown part of the ingot (*left*) [58]

inner area of about 4 mm diameter. Figure 4.16 (left) displays a  $5 \times 2 \times 1$  mm<sup>3</sup> crystal. This crystal was mechanically cleaved from the central region of the last grown part of the ingot using a sharp steel pin.

There can be a concentration gradient of Na either along or across the crystal growth direction. In order to minimize this possibility, the crystal wafers were cut from the last grown part, in the range of 2 to 3 mm from the end. Three pieces of crystal were cut from the same crystal wafer, and all three pieces were analyzed by ICP-AES. It was found that the Na concentrations of the three pieces of crystal are very close. The average values of Na determined from the three pieces of crystal are x = 0.91, 0.92, and 0.93 for the starting compositions of  $Na_{1.00}CoO_2$ ,  $Na_{1.05}CoO_2$ , and Na<sub>1.10</sub>CoO<sub>2</sub>, respectively. Single crystal XRD measurements were made on both as-grown crystals. Plate-like crystals were cleaved along the growth direction. Typical XRD patterns are shown in Fig. 4.17. All the peaks were indexed to the (00l) peaks of α-NaCoO<sub>2</sub>. Using a fitting method based on the Nelson–Riley (N–R) function, the c-axis lattice constant is estimated to be 15.597(2) Å for Na<sub>0.92</sub>CoO<sub>2</sub>, and 15.5928 (9) Å for Na<sub>0.93</sub>CoO<sub>2</sub>. The cell parameters derived from the single crystals agrees with the reported powder samples. No traces of impurities or inclusions were observed in these samples. The crystal quality was determined to be high, with the full width at half maximum (FWHM) < 0.05°, as shown in the inset of Fig. 4.17.

Superconducting sodium cobalt oxyhydrates can be derived from  $\alpha$ -NaCoO<sub>2</sub>, the procedures for sodium extraction and water hydration is same as the descriptions in Sect. 4.2.4.

# 4.4 Sodium Cobalt Oxyhydrates Superconductor

Motivated by the discovery of superconductivity in two-dimensional  $CoO_2$  layers [9], many efforts have been made to investigate the structural details of the water intercalated superconductor  $Na_xCoO_2 \cdot yH_2O$ , for an understanding of the crystal structure is fundamental to interpreting the physical and chemical properties. It has

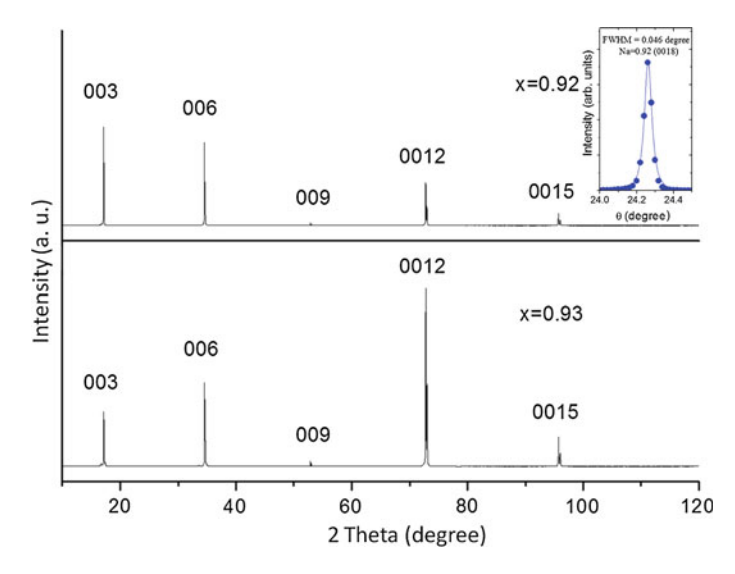


Fig. 4.17 X-ray diffraction patterns for  $\alpha$ -NaCoO<sub>2</sub> single crystals cleaved along the growth direction. All the peaks can be attributed to (00l) [58]. X-ray rocking curves for the as-grown Na<sub>0.91</sub>CoO<sub>2</sub> crystal (Mo K<sub> $\alpha$ </sub>-radiation)

been found that no superconductivity was found in a new series of sodium cobalt oxyhydrates obtained from the parent compound  $\beta$ -Na<sub>0.6</sub>CoO<sub>2</sub> [48], whereas the sodium cobalt oxyhydrates formed from  $\alpha$ -NaCoO<sub>2</sub> show superconducting transitions at 4.3–4.6 K [61, 62]. Both parent materials have three CoO<sub>2</sub> layers per unit cell, in contrast to the first superconductor, Na<sub>x</sub>CoO<sub>2</sub>·yH<sub>2</sub>O, which was obtained from a parent  $\gamma$ -Na<sub>x</sub>CoO<sub>2</sub> containing only two CoO<sub>2</sub> layers per unit cell. This indicates that the geometrical shape of the site for the Na ions and the number of CoO<sub>2</sub> sheets play an important role in the resultant electronic and magnetic properties.

# 4.4.1 Crystal Structure

The crystal structure of superconducting  $Na_xCoO_2 \cdot yH_2O$  differs from the parent material's crystal structure, and the structural details differ from the model for structure refinement. Even different data (XRD data or neutron data) for refinement may result in differences in the structural details. In general, superconducting  $Na_xCoO_2 \cdot yH_2O$  derived from  $\gamma$ - $Na_xCoO_2$  and  $\beta$ - $Na_xCoO_2$  has a hexagonal P6<sub>3</sub>/mmc space group structure (No. 194), while that from  $\alpha$ - $Na_xCoO_2$  has a trigonal R-3 m space group structure (No. 166). All superconducting phases have two layers of  $H_2O/D_2O$  between the  $CoO_2$  layers. The crystallographic symmetry does not change during the Na de-intercalation and  $H_2O$  intercalation processes. The

Parent phase	β [123]	γ [9]	γ [124]	γ [13]	α [61]
Space group	P63/mmc	P63/mmc	P63/mmc	P63/mmc	R-3 m
Data source	Neutron	XRD	neutron	XRD	XRD
Co site	2a	2a	2a	2a	3b
O site	4f	4f	4f	4f	6c
M1 site	6 h(Na)	2d(Na)	2b(Na)	4e(Na/H <sub>2</sub> 0)	6c(Na/H <sub>2</sub> 0)
M2 site	2b(Na)	2b(Na)	2c(Na)	2d(Na)	
W1 site	24 l(D <sub>2</sub> O)	12 k(H <sub>2</sub> O)	12 k(D <sub>2</sub> O)	12 k(H <sub>2</sub> O)	18 h(H <sub>2</sub> O)
W2 site	24 l(D <sub>2</sub> O)	12 k(H <sub>2</sub> O)	12 k(D <sub>2</sub> O)	12 k(H <sub>2</sub> O)	18 h(H <sub>2</sub> O)
a(Å)	2.81693(5)	2.8230(2)	2.8232(1)	2.81693(5)	2.8231(9)
b(Å)	19.6449(6)	19.6207(14)	19.530(1)	19.6449(6)	29.506(7)

Table 4.2 Structure details and unit cell parameters of Na<sub>x</sub>CoO<sub>2</sub>·yH<sub>2</sub>O at room temperature

small differences in the unit cell parameters shown in Table 4.2 may come from errors in the Na and  $H_2O$  content determination.

Takada et al. systematically studied the oxidation state of cobalt in the  $Na_xCoO_2\cdot yH_2O$  superconductors [13, 15, 61, 63], and it was found that the oxidation number of cobalt is about 3.46, which is significantly lower than the value (3.64) deduced from the Na to Co stoichiometry ratio, x. This may be explained by the presence of an oxygen deficiency or excess protons. They also found that the Na content decreased during the water intercalation process, Raman spectroscopy indicated that the ingoing species substituting for the Na1 ion is the  $H_3O^+$  ion, therefore, the reaction corresponding to the water intercalation should be as follows:

$$Na_{0.406}CoO_2 + (0.140 + n) H_2O \rightarrow Na_{0.337}(H_3O)_{0.070}CoO_2 nH_2O + 0.069 Na^+ + 0.069 OH^-$$

 $Na_xCoO_2$  also experienced reductive insertion of  $H_3O^+$  ions according to the following reaction:

$$Na_{0.337}(H_3O)_{0.070}CoO_2\ nH_2O + 0.246H_2O \rightarrow Na_{0.337}(H_3O)_{0.234}CoO_2\ nH_2O + 0.041\ O_2$$

Although it is not clear whether the reactions occurred sequentially or simultaneously, they modified the refinement structure model by the occupation of the M sites not only by Na<sup>+</sup> ions, but also by oxonium (H<sub>3</sub>O<sup>+</sup>) ions.

The two typical superconductor structures are given in Fig. 4.18. The figure in the left shows the P6<sub>3</sub>/mmc space group structure superconductors, it also revealed that the dimensions of the water block are close to those found in free ice [24]. The crystal structure of the  $\alpha$ -Na<sub>x</sub>CoO<sub>2</sub> derived superconductor (R-3 m) is shown in the right figure.

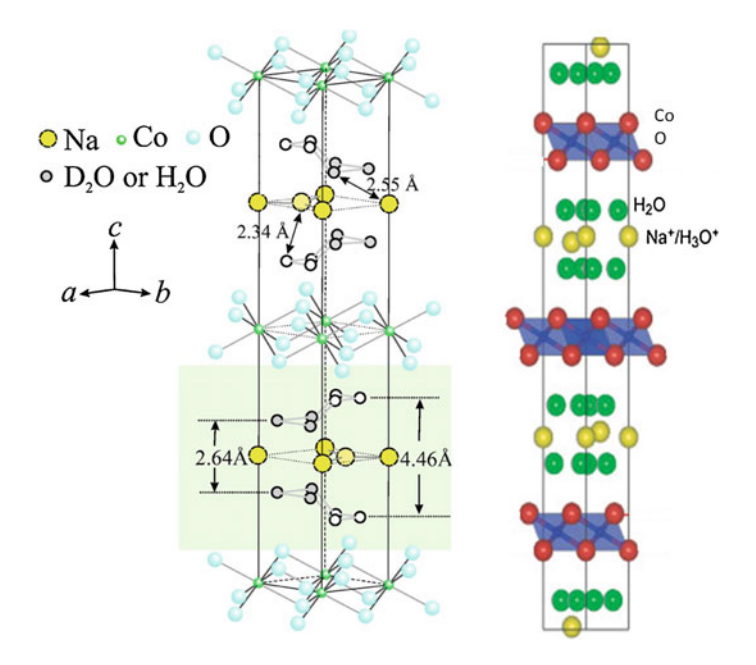


Fig. 4.18 Structural models for the  $Na_xCoO\cdot 1.4(D/H_2O)$  superconductor. *Left* P6<sub>3</sub>/mmc structure of the γ-Na<sub>x</sub>CoO<sub>2</sub> derived superconductor [24]. The figure on the *right* shows the crystal structure of the α-Na<sub>x</sub>CoO<sub>2</sub> derived superconductor (R-3 m) [61]

In contrast to the well known fact that the parent materials only show a significant expansion along the c-axis with increasing temperature, the unit cell parameters for the P6<sub>3</sub>/mmc superconductor show expansion in both the a- and c-axis parameters with increasing T [13, 24].

### 4.4.2 Superconductivity and Phase Diagram

The superconducting properties of the fully hydrated single crystals obtained from two-layer parent compounds were characterized by susceptibility measurements. Zero field cooling (ZFC) measurements with 10 Oe applied field are presented in Fig. 4.19 [25]. Superconducting transition temperatures  $T_c = 2.8$ –4.9 K with  $x \approx 0.28$ –0.42 were observed, respectively. The transition width for each sample is different, which is very likely caused by an inhomogeneous sodium concentration and partial hydration, which affect the superconducting state of  $Na_xCoO_2\cdot 1.3H_2O$ .

Figure 4.20 depicts the magnetic susceptibility of the polycrystalline sample measured under zfc and fc conditions, it shows a steep drop at 4.6 K [61]. The magnetic susceptibility at 1.8 K, measure under zfc condition, was  $-3.4 \times 10^{-3}$  emug<sup>-1</sup>, which can be converted to  $-1.0 \times 10^{-2}$  emu cm<sup>-3</sup> based on the unit-cell

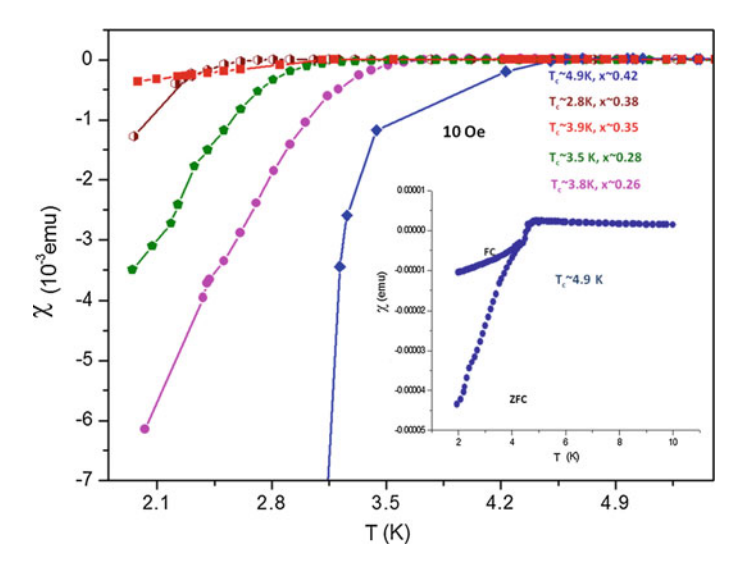
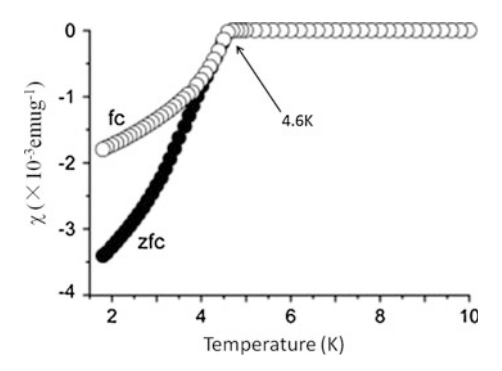


Fig. 4.19 Zero field Cooling (ZFC) magnetic characterization of the Na<sub>x</sub>CoO<sub>2</sub> 1.3H<sub>2</sub>O single crystals showing the onset  $T_c(x)$ . Inset: ZFC and FC measurements showing that the optimum  $T_c \approx 4.9$  K with x=0.42 [25]



**Fig. 4.20** Magnetic susceptibility as a function of temperature for three-layer  $Na_{0.35}(H_3O)_{0.17}(H_2O)_{1.22}CoO_2$  [61]

dimensions. This value was 13% of theoretically predicted diamagnetism, and large enough to conclude the presence of bulk superconductivity in this phase. The oxidation state of Co was +3.48, comparable to those two-layer derived superconductors.

Figure 4.21 shows a plot of  $T_c$  as a function of the sodium concentration of  $Na_xCoO_2$ . For samples with  $0.47 \ge x \ge 0.22$  there is no superconducting transition detectable. These data agree to some extent with a recent study that shows a constant  $T_c$  for Na contents up to 0.37. However, they conflict with the superconducting "dome" of  $T_c$  (x) demonstrated for powder samples [21]. This latter

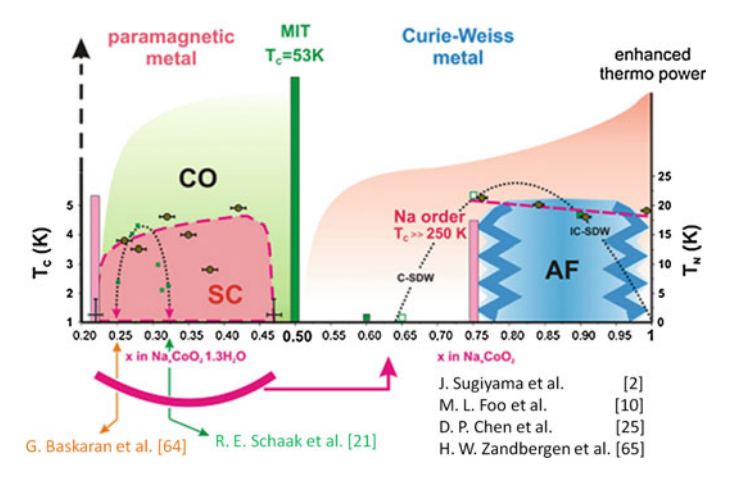


Fig. 4.21 Revised superconducting  $(Na_xCoO_2 \cdot 1.3H_2O)$  and non-superconducting  $(Na_xCoO_2)$  phase diagrams schematically combined. Susceptibility data [25] (open circles) is compared to earlier data (small solid squares) and theoretical estimations (thin dashed curve). The arrows in red SC area mark a proposed charge ordering instability at x = 1/4 and x = 1/3 [21] that is not evident in data from [25]. Green bars mark the report of charged ordered phases at x = 0.5, 0.60, and 0.65. For x = 0.5, a metal–insulator transition (MIT) is observed. The composition x = 0.5 separates the behavior of the magnetic susceptibility into a paramagnetic metallic and a Curie–Weiss-like regime. The antiferromagnetic (AF) phase shows an approximately composition-independent critical temperature  $T_N$  and fades out for a composition of  $x \le 0.75$  [57]

dependence motivated the proposal that there are intrinsic critical concentrations  $x_{cr1} \approx 1/4$  and  $x_{cr2} \approx 1/3$  related to charge ordering instabilities of the  $Co^{3+}/Co^{4+}$ . In the single crystal study the upper limit is shifted to much higher concentrations,  $x_{cr2} \approx 0.45$  [64]. This implies that a possible charge ordering at  $x_{cr2} \approx 1/3$  is not relevant to the suppression of  $T_c$ .

However, the superconducting phase now extends close to the phase line where non-hydrated Na $_{0.5}$ CoO $_2$  shows a metal–insulator transition [65]. This is evidence for the importance of electronic correlations at higher x in the hydrated system. It is interesting to note that the Néel transition at  $T_N \approx 20~K$  is also only observed for higher Na concentrations with x > 0.75 in non-hydrated crystals and that this ordering temperature does not change appreciably with x. Bulk antiferromagnetic order has been proven using muon spin rotation (MSR) and other thermodynamic experimental techniques [66]. The exact nature of the ordering, however, still needs to be investigated further.

Evidence for superlattice formation and electronic instabilities, either due to Na or  $\mathrm{Co^{3+}/Co^{4+}}$  charge ordering, has recently been accumulating for non-hydrated  $\mathrm{Na_{x}CoO_{2}}$  with  $\mathrm{x}=0.5$ , but also to some extent for other stoichiometries [67, 68]. Hydration contributes to the charge redistribution due to its effect on the  $\mathrm{CoO_{2}}$  layer thickness and the formation of  $\mathrm{Na(H_{2}O)_{4}}$  clusters that shield disorder of the

partially occupied Na sites. The above-mentioned instabilities should influence the superconducting state, as they modulate the electronic density of states and change the nesting properties of the Fermi surface.

#### 4.5 Conclusion

Sodium cobaltate is an attractive material for thermoelectric applications and the parent compound of superconducting sodium cobalt oxyhydrates. The best way to grow large single crystal growth of  $Na_xCoO_2$  is the optical floating zone technique. The experiments demonstrate that nearly pure  $\alpha$ - (x=0.90--1.00) and  $\acute{\alpha}$ - (x=0.75) phases of  $Na_xCoO_2$  large crystals could be obtained using the optical floating zone method, while other phases with lower sodium content, x<0.70 ( $\beta$ -phase with  $x=0.55,\ 0.60$  and  $\gamma$ -phase with x=0.65 and 0.70, respectively), are observed always to contain  $Na_2O,\ Co_3O_4,$  and Na-poor phases. Na-extraction can be carried out on the  $\alpha$ - and  $\acute{\alpha}$ -crystals to obtain the other phases with lower sodium content. Na content and the following hydration process need to be carefully controlled in order to obtain superconducting phase. Further studies are needed to investigate a possible interrelation of Na content, hydration, and structural details on well-characterized samples with the highest  $T_c$ .

#### References

- 1. J. Molenda, Solid State Ionics 21, 263 (1986)
- 2. J. Sugiyama et al., Phys. Rev. Lett. **92**, 017602 (2005)
- P.M. Lee, L. Viciu, L. Li, Y. Wang, M.L. Foo, S. Watauchi, R.A. Pascal Jr, R.J. Cava, N. P. Ong, Nat. Mater. 5, 537 (2006)
- 4. R. Berthelot, D. Carlier, C. Delmas, Nat. Mater. **10**(1), 74–80 (2011)
- 5. P. Brinks et al, Adv. Energy Mater. 4(8) (2014)
- 6. M.H.N. Assadi, H. Katayama-Yoshida, Funct. Mater. Lett. 1540016 (2015)
- 7. M. Von Jansen, R. Hoppe, Z. Anorg, Allg. Chem. 408, 104 (1974)
- 8. T. Tanaka, S. Nakamura, S. Iida, Jpn. J. Appl. Phys. 33, 581 (1994)
- K. Takada, H. Sakurai, E. Takayama-Muromachi, F. Izumi, R. Dilanian, T. Sasaki, Nature 422, 53 (2003)
- M.L. Foo, Y. Wang, S. Watauchi, H.W. Zandbergen, T. He, R.J. Cava, N.P. Ong, Phys. Rev. Lett. 92, 247001 (2004)
- G. Lang, J. Bobroff, H. Alloul, P. Mandels, N. Blanchard, G. Collin, Phys. Rev. B 72, 094404 (2005)
- C. de Vaulx, M.-H. Julien, C. Berthier, M. Horvatic, P. Bordet, V. Simonet, D.P. Chen, C.T. Lin, Phys. Rev. Lett. 95, 186405 (2005)
- K. Takada, K. Fukuda, M. Osada, I. Nakai, F. Izumi, R.A. Dilanian, K. Kato, M. Takata, H. Sakurai, E. Takayama-Muromachi, T. Sasaki, J. Mater. Chem. 14, 1448 (2004)
- C.J. Milne, D.N. Argyriou, A. Chemseddine, N. Aliouane, J. Veira, S. Landsgesell, D. Alber, Phys. Rev. Lett. 93, 247007 (2004)
- 15. M. Karppinen, I. Asako, T. Motohashi, H. Yamauchi, Chem. Mater. 16, 1693 (2004)

References 141

 G. Gašparović, R.A. Ott, J.-H. Cho, F.C. Chou, Y. Chu, J.W. Lynn, Y.S. Lee, Phys. Rev. Lett. 96, 046403 (2006)

- Claude Fouassier, Guy Matejka, Jean-Maurice Reau, Paul Hagenmuller, J. Solid State Chem. 6, 532 (1973)
- Q. Huang, M.L. Foo, R.A. Pascal Jr, J.W. Lynn, B.H. Toby, T. He, H.W. Zandbergen, R. J. Cava, Phys. Rev B 70, 184110 (2004)
- 19. I. Terasaki, Y. Sasago, K. Uchinokura, Phys. Rev. B 56, R12 685 (1997)
- 20. Yayu Wang, N. S. Rogado, R. J. Cava, and N. P. Ong. Nature 423, 425 (2003)
- 21. R.E. Schaak, T. Klimczuk, M.L. Foo, R.J. Cava, Nature 424, 527 (2003)
- 22. R. Jin, B.C. Sales, P. Khalifah, D. Mandrus, Phys. Rev. Lett. 91, 217001 (2003)
- J.D. Jorgensen, M. Avdeev, D.G. Hinks, J.C. Burley, S. Short, Phys. Rev. B 68, 214517 (2003)
- J.W. Lynn, Q. Huang, C.M. Brown, V.L. Miller, M.L. Foo, R.E. Schaak, C.Y. Jones, E.A. Mackey, R.J. Cava, Phys. Rev. B 68, 214516 (2003)
- D.P. Chen, H.C. Chen, A. Maljuk, A. Kulakov, H. Zhang, P. Lemmens, C.T. Lin, Phys. Rev. B 70, 024506 (2004)
- 26. F. Rivadulla, J.-S. Zhou, J.B. Goodenough, Phys. Rev. B 68, 075108 (2003)
- M.L. Foo, R.E. Schaak, V.L. Miller, T. Klimczuk, N.S. Rogadoa, Y. Wange, G.C. Lau, C. Craley, H.W. Zandbergen, N.P. Ong, R.J. Cava, Solid State Commun. 127, 33 (2003)
- 28. M.D. Johannes, D.J. Singh, Phys. Rev. B **70**, 014507 (2004)
- T. Motohashi, E. Naujalis, R. Ueda, K. Isawa, M. Karppinen, H. Yamauchi, Appl. Phys. Lett. 79, 1480 (2001)
- 30. Qiuhang Li, Yuanyuan Zhang, Xu Mingxiang, Unconventional Magnetic Transition in Na<sub>x</sub>CoO<sub>2</sub> (x > 0.7) Single Crystals. J. Supercond. Novel Magn. **27**(5), 1235–1238 (2014)
- 31. K. Fujita, T. Mochida, K. Nakamura, Jpn. J. Appl. Phys. 40, 4644 (2001)
- 32. I. Terasaki, Y. Sasago, K. Uchinokura, Phys. Rev. B 56, R12685 (1997)
- 33. K. Fujita, T. Mochida, K. Nakamura, in *Proceedings of the 20th International Conference on Thermoelectricity* (ICT'01), 2001 (The Institute of Electrical and Electronics Engineers, Piscataway, 2001), p. 168
- 34. Hongtao Wang, Zhangzhang Chen, Qingli Jin, Mater. Lett. 59, 3917 (2005)
- 35. M. Mikami, M. Yoshimura, Y. Mori, T. Sasaki, Jpn. J. Appl. Phys. 42, 7383 (2003)
- N.L. Wang, P. Zheng, D. Wu, Y.C. Ma, T. Xiang, R.Y. Jin, D. Mandrus, Phys. Rev. Lett. 93, 237007 (2004)
- S.Y. Li, L. Taillefer, D.G. Hawthorn, M.A. Tanatar, J. Paglione, M. Sutherland, R.W. Hill, C. H. Wang, X.H. Chen, Phys. Rev. Lett. 93, 056401 (2004)
- 38. R. Jin, B.C. Sales, S. Li, D. Mandrus, Phys. Rev. B 72, 060512(R) (2005)
- M. Mikami et al., in *Proceedings of the 20th International Conference on Thermoelectricity* (ICT'01), 2001 (The Institute of Electrical and Electronics Engineers, Piscataway, 2001), p. 195
- M.N. Iliev, A.P. Litvinchuk, R.L. Meng, Y.Y. Sun, J. Cmaidalka, C.W. Chu, Physica C 402, 239 (2004)
- 41. L.B. Luo, Y.G. Zhao, G.M. Zhang, S.M. Guo, L. Cui, Phys. Rev. B 73, 245113 (2006)
- 42. H. Ohta, S.-W. Kim, S. Ohta, K. Koumoto, M. Hirano, H. Hosono, Cryst. Growth Des. 5, 25 (2005)
- 43. W.J. Chang, C.C. Hsieh, T.Y. Chung, S.Y. Hsu, K.H. Wu, T.M. Uen et al., Appl. Phys. Lett. **90**, 061917 (2007)
- F.C. Chou, J.H. Cho, P.A. Lee, E.T. Abel, K. Matan, Y.S. Lee, Phys. Rev. Lett. 92, 157004 (2004)
- 45. M. Chen, B. Hallstedt, L.J. Gauckler, J. Phase Equilib. 24, 212 (2003)
- 46. H.A. Wriedt, Bull. Alloy Phase Diagrams 8, 234 (1987)
- 47. C.T. Lin, D.P. Chen, P. Lemmens, X.N. Zhang, A. Maljuk, P.X. Zhang, J. Crystal Growth 275, 606 (2005)
- 48. Sundip Mistry, Donna C. Arnold, Chris J. Nuttall, Alexandros Lappas, Mark A. Green, Chem. Commun. 21, 2440 (2004)

- 49. Y.G. Shi, H.X. Yang, H, Huang, X. Liu, and J. Q. Li. Phys. Rev. B 73, 094505 (2006)
- 50. Y. Takahashi, Y. Gotoh, J. Akimoto, J. Solid State Chem. 172, 22 (2003)
- 51. R. Siegel, J. Hirschinger, D. Carlier, M. Menetrier, C. Demas, Solid State Nucl. Magn. Reson. 23, 243 (2003)
- 52. L. Viciu, J.W. Bos, H.W. Zandbergen, Q. Huang, M.L. Foo, S. Ishiwata, A.P. Ramirez, M. Lee, N.P. Ong, R.J. Cava, Phys. Rev. B 73, 174104 (2006)
- Y. Ono, R. Ishikawa, Y. Miyazaki, Y. Ishii, Y. Morii, T. Kajitani, J. Solid State Chem. 166, 177 (2002)
- C. Thinaharan, D.K. Aswal, A. Singh, S. Bhattacharya, N. Joshi, S.K. Gupta, J.V. Yakhmi, Cryst. Res. Technol. 39, 572 (2004)
- 55. M. Mikami, M. Yoshimura, Y. Mori, T. Sasaki, R. Funahashi, M. Shikano, in *Proceedings of 21st International Conference on Thermoelectrics*, Long Beach, 2002 (Institute of Electrical and Electronics Engineers, Piscataway, 2002), pp. 223–225
- J. Sugiyama, J.H. Brewer, E.J. Ansaldo, B. Hitti, M. Mikami, Y. Mori, T. Sasaki, Phys. Rev. B 69, 214423 (2004)
- 57. C.T. Lin, D.P. Chen, A. Maljuk, P. Lemmens, J. Cryst. Growth 292, 422 (2006)
- 58. D.P. Chen, Xiaolin Wang, C. T. Lin, and S. X. Dou. Phys. Rev. B 76, 134511 (2007)
- C. Bernhard, Ch. Niedermayer, A. Drew, G. Khaliullin, S. Bayrakci, J. Strempfer, R.K. Kremer, D.P. Chen, C.T. Lin, B. Keimer, Europhys. Lett. 80, 27005 (2007)
- 60. D. Prabhakaran, A.T. Boothroyd, R. Coldea, N.R. Charnley, J. Cryst. Growth 271, 74 (2004)
- K. Takada, H. Sakurai, T.-M. Eiji, F. Izumi, R.A. Dilamian, T. Sasaki, Adv. Mater. 16, 1901 (2004)
- 62. M.L. Foo, T. Klimczuka, Lu Li, N.P. Ong, R.J. Cava, Solid State Commun. 133, 407 (2005)
- K. Takada, M. Osada, F. Izumi, H. Sakurai, T.-M. Eiji, T. Sasaki, Chem. Mater. 17, 2040 (2005)
- 64. G. Baskaran, Phys. Rev. Lett. 91, 097003 (2003)
- 65. Q. Huang, M.L. Foo, J.W. Lynn, H.W. Zandbergen, G. Lawes, Y. Wang, B.H. Toby, A. P. Ramirez, N.P. Ong, R.J. Cava, J. Phys.: Condens. Matter 16, 5803 (2004)
- S. Bayrakci, C. Bernhard, D.P. Chen, B. Keimer, P. Lemmens, C.T. Lin, C. Niedermayer, J. Strempfer, Phys. Rev. B 69, 100410 (2004)
- 67. H.W. Zandbergen et al., Phys. Rev. B **70**(2), 024101 (2004)
- 68. J.L. Gavilano, D. Rau, B. Pedrini, J. Hinderer, H.R. Ott, S.M. Kazakov, J. Karpinski, Phys. Rev. B 69, 100404 (2004)

# Chapter 5 Crystal Growth and Characterization of Iron-Based Superconductor

Dapeng Chen, Chengtian Lin, Andrey Maljuk and Fang Zhou

**Abstract** This chapter focuses on the various single crystal growth techniques applied to the new class of high temperature superconductors of iron-based layered pnictides, such as the parent compounds  $AFe_2As_2$  (A=Ba, Sr, Ca) (122), hole-doped  $A_{1-x}K_xFe_2As_2$ , electron/hole-doped  $AFe_{2-x}M_xAs_2$  (M=Co, Ni, Mn, Cr), isovalently doped  $AFe_2As_{2-x}P_x$ , the chalcogenides  $A_xFe_{2-y}Se_2(A=K, Rb, Cs)$  (122), binary FeSe and  $Fe_{1-x}Te_{1-x}Se_x$  (11), AFePn (A=Li and Na; Pn=P and As) (111), Ln (O/F)FePn (1111) and ( $Li_{1-x}Fe_x$ )OHFe<sub>1-y</sub>Se (11111). Detailed single crystal growth methods (fluxes, Bridgman, floating zone), the associated procedures, and their impact on crystal size, quality and physical properties are presented.

#### 5.1 Introduction

The first new high  $T_c$  superconductor that do not contain copper was found in February 2008, LaFeAs( $O_{1-x}F_x$ ), which shows superconductivity at 26 K [1]. Reports on higher  $T_c$  iron-based compound have quickly emerged [2–4], and the  $T_c$  was optimized to 55 K by replacing lanthanum with rare earth ions that had smaller atomic radii [5]. This discovery has been regarded as one of the most important breakthroughs in the materials science and solid state research communities [6]. It triggered a worldwide race to find new high  $T_c$  superconductors based on iron. Almost all of the achievements gained from research on the copper-based superconductors have been applied to the investigation of the new materials. Figure 5.1 shows a schematic illustration of the progress in iron-based superconductors.

D. Chen  $\cdot$  C. Lin  $(\boxtimes)$ 

Max Planck Institute for Solid State Research, Stuttgart, Germany e-mail: ct.lin@fkf.mpg.de

A. Maljuk

Leibniz Institute for Solid State and Materials Research, Dresden, Germany

F. Zhou

Institute of Physics, Chinese Academy of Sciences, University of Chinese Academy of Sciences, 100190, 100049 Beijing, China

<sup>©</sup> Springer International Publishing Switzerland 2016

D. Chen et al., *Growth and Characterization of Bulk Superconductor Material*,

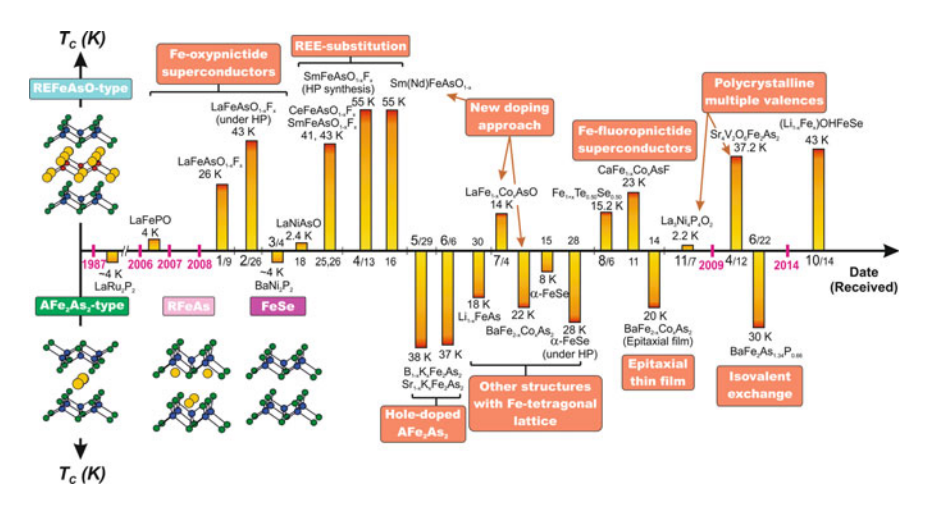


Fig. 5.1 Progress in Fe-based superconductors

Early research revealed that there are several similarities between the iron-based and copper-oxide-based superconductors, such as both of them being layered systems, both systems start with the antiferromagnetic (AFM) order as the parent phase, and in both systems, doping into the functioning layers will lead to the systematic evolution of magnetism and superconductivity. In just a few years, without changing the basic structural unit supporting the superconductivity, i.e. the edge-shared FeX<sub>4</sub> tetrahedral layer, more than 50 compounds among the iron-based pnictides and chalcogenides were found to be superconducting. They have been categorized into six families by the ratio of elements in their chemical formula: the 1111 type of Ln(O/F)FePn (Ln= rare earth elements; Pn=P and As) [1–4], the 111 type of AFePn (A=Li and Na; Pn=P and As) [7–11], the 122 type of AFe<sub>2</sub>As<sub>2</sub> (A=Ca, Sr, Eu, and Ba) [12–18], the defect structured A<sub>0.8</sub>Fe<sub>1.6</sub>Se<sub>2</sub> (A=K, Rb, Cs, Tl, Tl/K, Tl/Rb) related to the 122 structure (also called "122") [19–24], the 11 type of FeCh (Ch=S, Se, and Te) [25–29], the 21311 type of A<sub>2</sub>MO<sub>3</sub>FePn (A=Ca, Sr, and Ba; M=Sc, V, Cr Ti, and Al; Pn=P and As) [30–34], and the 11111 type of Li<sub>1.x</sub>Fe<sub>x</sub>)OHFe<sub>1-x</sub>Se [35, 36].

Once more and more iron-based superconductors had been studied, it was found that they apparently belong to a different class of materials from the copper based superconductors. They are also different from other superconductors such as MgB<sub>2</sub>, which are well explained in the Bardeen-Cooper-Schrieffer (BCS) framework. Despite the significant progress that has been achieved since the iron-based superconductors were discovered, a large number of experimental results are controversial or contradict each other due to the sample quality, and the limitations of or differences in the preparation methods that were used. The understanding of many important superconducting properties is still a mystery and requires further thorough investigation through wide collaborations between researchers with complementary expertise. Further refined experimental studies performed on high quality single crystals will help us to develop the physical understanding of

5.1 Introduction 145

iron-based superconductors, especially in experimental techniques where size, purity, and volume are essential parameters for the samples.

The researchers have so far extensively studied the 11 and 122 type superconductors, due to the impressive progress in large single crystal growth of these two types. The single crystal growth of iron-based superconductors is more difficult than that of copper-based superconductors, because these materials involve a trickier chemistry. The process design needs to consider the high toxicity of arsenic and selenium, the high volatility of arsenic, the high moisture/oxygen reactivity and low melting points of alkali metals and alkaline-earth metals, and the oxygen sensitivity of rare earth metals. The growth is complicated by the need to seal the reactions in vacuum or inert atmospheres, and by the need to make sure that there is no health risk and that harm to the environment is under control.

Although high quality and large size single crystals of 11 and 122 type can now be grown, including the defect-structured iron chalcogenide superconductors, there are still some unknowns and controversies awaiting further research on cleaner crystals. In this chapter, we present detailed single crystal growth procedures and their impact on crystal size and quality, as well as on their physical properties. Various attempts to improve the superconducting quality will be described, including post-annealing treatment and doping effects on the crystal structure, and the magnetic and electric properties. Finally, we will briefly present the future prospects for single crystal growth studies on iron-based superconductor.

# 5.2 122 Type AFe<sub>2</sub>As<sub>2</sub> (A=Ba, Sr)

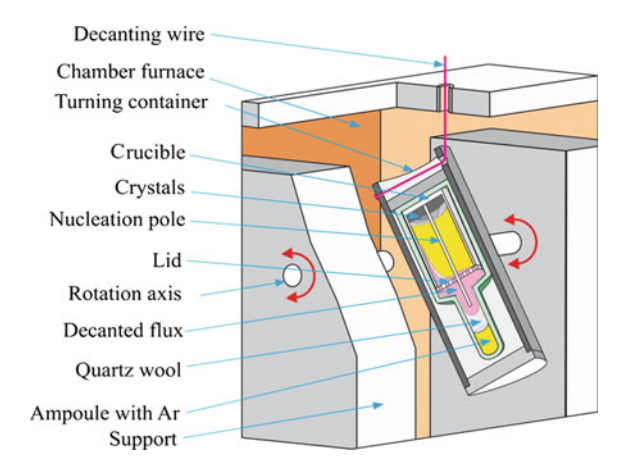
The discovery of superconducting Ba<sub>1-x</sub>K<sub>x</sub>Fe<sub>2</sub>As<sub>2</sub> was very important for both theoretical and practical reasons [37]. Similar to the high  $T_c$  cuprates, magnesium diboride (MgB<sub>2</sub>), and sodium cobalt oxide (Na<sub>x</sub>CoO<sub>2</sub>), this type of iron-based superconductor had sandwich structure characteristics, but did not contain any oxygen. The parent compound AFe<sub>2</sub>As<sub>2</sub> shows a spin-density-wave (SDW) ground state. On introducing charge carriers by electron or hole doping, the SDW transition is suppressed, while a superconducting transition takes place instead, which is reminiscent of the situation for copper-based superconductors. A superconducting dome can be established with increasing doping level in the phase diagram, as observed for Ba<sub>1-x</sub>K<sub>x</sub>Fe<sub>2</sub>As<sub>2</sub> [38]. In addition to doping in the A layer, superconductivity can also be induced by doping ions into the FeAs conducting layer, such as in BaFe<sub>2-x</sub>Co<sub>x</sub>As<sub>2</sub> [39, 40], BaFe<sub>2-x</sub>Ni<sub>x</sub>As<sub>2</sub> [41], and BaFe<sub>2</sub>( $As_{1-x}P_x$ )<sub>2</sub> [42], as well as by application of pressure [43, 44]. This behavior indicates that the iron-based superconductivity is different from that in the copper-oxide-based high  $T_c$  superconductors, which are sensitive to the perturbations of the Cu sublattice. To study the superconductivity, the electrical and magnetic anisotropic behavior, and the inelastic neutron diffraction experiments of this type superconductor, high quality and large single crystals are desperately required. By thoroughly studying the doping effects on accurately characterized single crystal 122 type samples, it is hoped that a universal picture of the physics will emerge.

### 5.2.1 Single Crystal Growth by the Flux Method

The growth of oxygen-free iron arsenide single crystals was reported by using the flux method, and a reasonable size was achieved [39, 41, 45–49]. Several groups reported the growth of AFe<sub>2</sub>As<sub>2</sub> single crystals by using the Sn flux or FeAs self-flux methods, obtaining sizes as large as  $12 \times 8 \times 1$  mm [50]. The crystals grown from Sn flux, however, are contaminated with Sn at about  $1 \sim 2$  at.% [46]. It has been proved that the Sn is incorporated into the Fe sites, as detected by atomic spectroscopy, and this leads to a decrease in the SDW transition temperature [47]. Therefore, the FeAs self-flux method is preferred for the growth to prevent contamination of the crystal [47–49]. The typical flux growth method for 122 type single crystals was reviewed by Stewart [51]. In order to avoid adherence of the residual flux to the crystal surface, which leads to contamination or damage to the crystals that are being grown, a decanting method was developed using specially designed apparatus [46], and centimeter-sized crystals were obtained using either the Sn flux or FeAs self-flux methods. By using an alumina stick as a nucleation center in the melt during growth, larger and high quality doped 122 type single crystals with sizes up to  $\emptyset$  40  $\times$  5 mm were obtained [52–55].

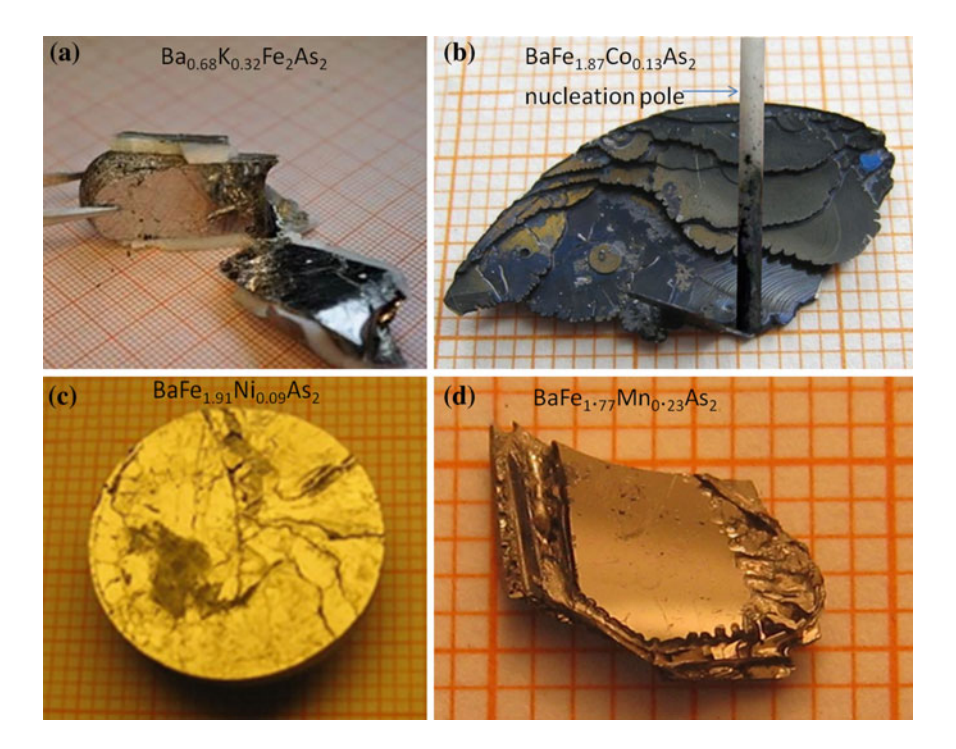
Figure 5.2 shows a schematic illustration of the apparatus used to grow doped 122 type single crystals by using a nucleation pole. The starting materials, high purity (>4 N) Ba lump, K ingot, and Fe, Co, Ni or Mn, As, and Sn powders were weighed and mixed in a ratio of [(Ba/Sr)<sub>1-x</sub>K<sub>x</sub>Fe<sub>2</sub>As<sub>2</sub>]: Sn = 1:45–50, or in the ratio of Ba<sub>1-x</sub>K<sub>3x</sub>Fe<sub>4</sub>As<sub>4</sub> or BaFe<sub>5-3.5x</sub>M<sub>3.5x</sub>As<sub>5</sub> (M=Co, Ni, and Mn). Usually, 90 g of the mixture for Sn flux or 15 g for self-flux were used for the growth. The mixtures were loaded into a ZrO<sub>2</sub> crucible, and an Al<sub>2</sub>O<sub>3</sub> stick of Ø 0.1 cm × 7 cm was then inserted into the crucible and positioned well above the mixture to serve as a nucleation center during growth. The whole preparation procedure was performed in a glove box filled with argon atmosphere. The loaded crucible was then sealed in a quartz ampoule containing 250 mbar argon atmosphere. The ampoule was heated up to 1080 °C for

**Fig. 5.2** Schematic drawing of the apparatus used to grow doped single crystals of AFe<sub>2</sub>As<sub>2</sub> (A=Ba, Sr) [56]



K-doped or 1190 °C for Co, Ni, and Mn-doped crystals for 10 h, and then slowly cooled down at the rate of 2 °C/h, followed by decanting of the flux at 980 °C for K-doped or 1090 °C for Co, Ni, or Mn-doped compounds. It should be noted that to obtain crystals mostly free from flux, a temperature of 980 °C or 1090 °C had to be maintained for 2 h after decanting, followed by cooling to room temperature. This allows the residual flux to flow out completely and leaves free-standing crystals inside the crucible.

By the use of the nucleation pole, together with the low cooling rate of  $\sim\!2~^\circ\text{C}~\text{h}^{-1}$  that was applied, the spontaneous appearance of numerous nuclei can be minimized during growth, and the biggest crystals can be grown as large as Ø  $40\times5$  mm, where the diameter depends on the crucible size and the thickness depends on the amount of source materials. Figure 5.3b shows the nucleation pole located in the center of the crystal disk and a broken part of the crystal measuring  $20\times10\times2~\text{mm}^3$ , the size of which is one third of the disk size. It is emphasized that the decanting device is specially designed with a movable nickel wire for tilting the crucible on its top and releasing the residual flux at the high decanting temperatures out of the furnace. This can avoid any poisoning from arsenic if cracking of the quartz tube occurs.



Large and high quality single crystals of hole-doped  $Ba_{1-x}K_xFe_2As_2$  and  $BaFe_{2-x}Mn_xAs_2$ , and electron-doped  $BaFe_{2-x}M_xAs_2$  (M=Co and Ni) can be grown by using this modified self-flux method.

# 5.2.2 Features of K Doped Crystals Grown from Sn Flux and Self-flux

The parent compounds of AFe<sub>2</sub>As<sub>2</sub> (A=Ba, Sr) are intermetallic and non-superconducting. One important finding is the existence of a spin density wave (SDW) anomaly at the critical temperature,  $T_s$ , at  $\sim 140$  K for BaFe<sub>2</sub>As<sub>2</sub> and  $\sim 200$  K for SrFe<sub>2</sub>As<sub>2</sub> [57, 58]. This SDW is linked to abrupt changes in the electrical resistivity and magnetic susceptibility, as well as a structural transition from the high-temperature tetragonal to a low-temperature orthorhombic phase [57–60]. By the changing of the electron density in the FeAs layers, the compounds can be made superconducting, which is believed to be associated with the suppression of the SDW anomaly [59]. Large single crystals can be grown by the flux method, but they all have some defects, such as flux inclusions, twinning, and element substitution from the flux. The crystal quality is closely related to the growth process parameters and the flux materials employed. It has been revealed that the Sn flux or self-flux has an important influence on the properties of the AFe<sub>2</sub>As<sub>2</sub> (A=Ba, Sr) parent compounds and their doped crystals [45, 46, 61]. Here, we will review the flux effects on the properties of parent and potassium doped 122 type crystals.

#### 5.2.2.1 Crystal Morphology and Crystal Structure

Owing to the layered structure, the pnictide  $A_{1-x}K_xFe_2As_2$  crystals exhibit a platelet-like morphology, and the c-axis is normal to the (001) face. The crystal facets can be well developed according to the crystallographic orientation. The growth rate along the [010] direction is faster than along the [001], because the atomic bonding energy is higher for the a-axis than for the c-axis. Doping of  $K^+$  (1.51 Å) causes a decrease in the As-Fe-As bond angle and an increase in the bond length, leading to a weakening of the bonding energy. This can result in a lower growth rate. The crystals grown by using self-flux exhibit small and thin platelets, particularly potassium-doped  $Ba_{1-x}K_xFe_2As_2$ , but they have high quality as characterized by the resistivity and magnetic measurements.

There is an interesting crystal habit for all such pnictide compounds: they exhibit multilayer stacks, macrosteps, step bunches, and inclusions in the (001) face. These typical features are shown in Fig. 5.4a–c, where all the crystals were obtained by the Sn flux method. Figure 5.4a shows an edge of the crystal, exposing multiple layers, each with a thickness of  $\sim 5$  µm. These crystal layers are readily cleaved mechanically. Macro-steps are observed on the (001) plane, as shown in Fig. 5.4b.

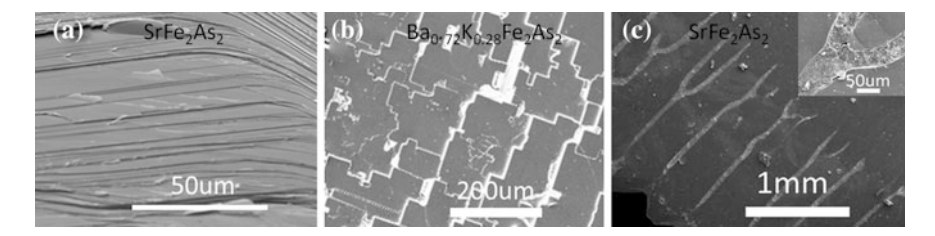


**Fig. 5.4** SEM micrographs of crystals obtained by the Sn flux method: **a** SrFe<sub>2</sub>As<sub>2</sub> with multilayer stacks, **b** macrosteps on the (001) face of Ba<sub>0.72</sub>K<sub>0.28</sub>Fe<sub>2</sub>As<sub>2</sub>, **c** inclusions of Sn formed in the (001) plane of SrFe<sub>2</sub>As<sub>2</sub> crystal. *Inset* is an enlarged part [56]

Figure 5.4c shows the Sn inclusion lines as impurities formed in the (001) face of the SrFe<sub>2</sub>As<sub>2</sub> crystal grown from the melt in a supercooled state. The content of Sn impurities in the crystals is determined to be <1.0 at.% by both energy dispersive X-ray spectroscopy (EDX) and inductively coupled plasma (ICP) measurements. No growth spirals were observed in the (001) faces. This indicates that the crystal growth on the (001) face occurs at a relatively high supersaturation according to a layer-by-layer growth mechanism.

#### 5.2.2.2 Transport and Magnetic Properties

The electronic and magnetic properties of the  $A_{1-x}K_xFe_2As_2$  family are extremely sensitive to the extrinsic influence of the Sn impurities. This restricts the universal role of the SDW in explaining superconductivity. The discrepant spin density wave anomaly at  $T_s \approx 138$  and 85 K, which occurs in BaFe<sub>2</sub>As<sub>2</sub> crystals grown using self-flux and Sn flux, respectively, is suggested to be based on the substitution of Fe within the FeAs basal plane. The presence of Sn impurities not only suppresses the ordering temperature, but also transforms the first-order transition to a second-order one. Doping with K suppresses the spin density wave and induces superconductivity in the doped  $A_{1-x}K_xFe_2As_2$ .

The temperature dependence of the in-plane resistivity for BaFe<sub>2</sub>As<sub>2</sub> single crystals is shown in Fig. 5.5a. Weak temperature dependence is seen from 138 to 300 and 85 to 300 K, indicating metallic behavior at higher temperatures for BaFe<sub>2</sub>As<sub>2</sub> crystals formed in both self-flux and Sn flux, respectively. A sharp decrease is seen at 138 K for the crystals grown by self-flux, while an anomaly occurs at 85 K for the crystals obtained by Sn flux. Such behavior is similar to the transition in LaFeAsO that is driven by the SDW instability in the iron layers [10, 11]. A pronounced difference in the spin density wave anomaly is observed on comparing the two crystals, which might be attributed to the tiny amount of Sn incorporated into the crystals and might be related to a reduction in  $T_s$ . A very sharp superconducting transition temperature  $T_c$  occurs at 38.5 K for the doped Ba<sub>0.68</sub>K<sub>0.32</sub>Fe<sub>2</sub>As<sub>2</sub> single crystal grown using self-flux.

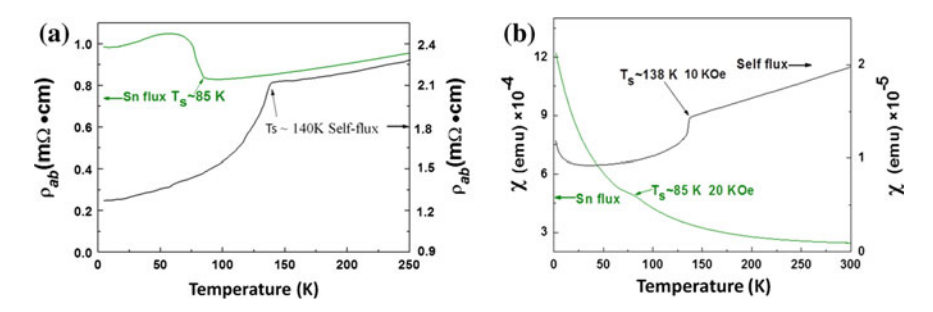


Fig. 5.5 a Temperature dependence of the in-plane resistivity and b magnetization data with the field H/lab for BaFe<sub>2</sub>As<sub>2</sub> single crystals formed by self-flux and Sn flux, respectively. Different features are observed at  $T_s$  in crystals obtained using different flux [56]

The magnetic susceptibility data in Fig. 5.5b show a clear transition at 85 K in the H/lab curve. This is indicative of an effect on the structural phase transition, assumed to be a change in the nature of the in-plane magnetic interactions [45], and due to the substitution by Sn. This behavior is observed for the crystals grown using Sn flux, but not for self-flux or polycrystalline samples, which exhibit a SDW transition at  $\sim 140$  K [38, 45, 49, 62]. This pronounced discrepancy may be an effect associated with Sn insertion into the crystal.

No change in the SDW transition has been observed in  $SrFe_2As_2$  crystals formed by Sn flux or self-flux. Sun et al. performed the in-plane resistivity measurements on the single crystals grown by Sn flux [55]. For the pure  $SrFe_2As_2$  crystal, it shows linear temperature dependence for temperatures above 202 K with metallic behavior. The observed kink is attributed to the onset of the SDW transition associated with a structural transition from tetragonal to orthorhombic at  $\sim 200$  K. For the potassium-doped  $Sr_{0.85}K_{0.15}Fe_2As_2$ , there is an anomaly occurring at 178 K for the SDW transition and at 32 K for the superconducting transition. This suggests the coexistence of superconductivity and SDW in the weakly doped regime, which is consistent with angle resolved photoemission spectroscopy (ARPES) data [63].

#### 5.2.2.3 Sn in the Crystal Structure and Dopant Distribution

It is well known that Sn is included into the crystal structure when the crystal growth is by Sn flux, and it leads to a modification of the SDW state. It is not known which site Sn occupies in the structure, however. Sun et al. studied the Sn 3d photoelectron spectra for BaFe<sub>2</sub>As<sub>2</sub>, SrFe<sub>2</sub>As<sub>2</sub>, and Ba<sub>0.72</sub>K<sub>0.28</sub>Fe<sub>2</sub>As<sub>2</sub> grown by Sn flux. All the measured crystals formed by Sn flux contain  $\sim 1$  at.% Sn [55]. Sn  $3d_{5/2}$  photoelectron peaks were observed for all samples, which suggest that Sn occupies the Fe<sup>2+</sup> sites in the basal plane of the crystals, and Sn is likely to be incorporated onto the Fe sites during the crystal formation in Sn solvent. While Ni et al. [45] claim that Sn is most likely incorporated on the As sites, and Su et al. [61]

concluded that Sn was doped into Ba sites. Nevertheless, the effect of Sn on  $T_s$  and the local structure [64] is not understood so far, and a further investigation of the details, for instance, the bonding distances for Sn-As and Sn-Ba, is required.

Impurities in the samples such as dopant distributions, have been confirmed to alter the physical properties [65]. Studies on the local dopant atom distribution are highly desirable. Atom probe tomography (APT) provides three-dimensional (3D) chemical mapping with near-atomic resolution and is ideally suited to investigate dopant distributions [66]. The nanoscale distribution of K and Ba was investigated using frequency distribution analysis, and these results strongly support the suggestion that K atoms in the crystal grown from the self-flux are not randomly distributed—rather, these atoms are clustered in a way that produces local nanoscale regions of both low and high K concentrations. Systematic investigation of the dopant distribution in more 122 type compounds will help to clarify some of these issues, which have aroused controversy on this family of superconductors.

# **5.2.2.4** Relationship Between Antiferromagnetic Order and Superconductivity

The relationship between AFM and SC is of great importance for understanding the physics of iron-based superconductors. It has been proposed that elucidating this relationship can serve to determine the pairing symmetry. The conclusions on this question, as well as other important features, are still controversial, however, due to the lack of a suitable experimental probe or sufficiently clean samples. Early experiments on the iron-pnictide superconductor Ba<sub>1-x</sub>K<sub>x</sub>Fe<sub>2</sub>As<sub>2</sub> have suggested that AFM and SC are microscopically separated [67, 68], while on the other hand, there are also suggestions and some evidence that SC and AFM may coexist in Ba<sub>2</sub>Fe<sub>2</sub>As<sub>2</sub> replaced by various elements such as Ca, K (to replace Ba) [69–72], Co (to replace Fe) [67, 73], or P (to replace As) [74], or in SmFeAsO<sub>1-x</sub>F<sub>x</sub> [75]. It is instructive to compare the results in samples of underdoped Ba<sub>1-x</sub>K<sub>x</sub>Fe<sub>2</sub>As<sub>2</sub> (BKFA) to gain an idea of how the AFM and SC at a microscopic scale can vary with differences in the flux.

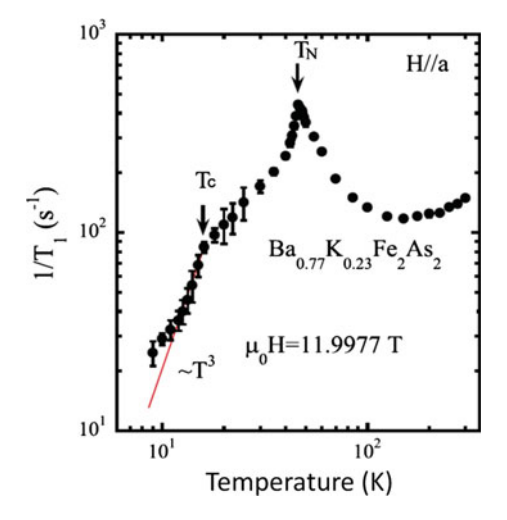
For single crystals grown from Sn flux, Park et al. performed dc susceptibility, x-ray powder diffraction (XRPD), neutron scattering, and muon spin rotation ( $\mu$ SR) measurements on the same samples [68]. In these measurements, a phase-separated coexistence between static magnetic order and nonmagnetic regions (either SC below  $T_c$  or normal-state above  $T_c$ ) was observed, and they suggest that this phase separation is an intrinsic property of underdoped BKFA. They also observed mesoscopic phase separated coexistence of magnetically ordered and nonmagnetic states on the lateral scale of 65 × 10 nm in a slightly underdoped iron pnictide superconductor, as estimated from magnetic force microscope (MFM) imaging, in agreement with the  $\mu$ SR measurements. Their findings indicate that such electronic phase separation is an intrinsic property of the studied material, as both the XRPD and the susceptibility measurements indicate the absence of chemical inhomogeneities in the samples.

Further study was conducted on the same sample by means of neutron scattering and XRPD, along with theoretical calculations [76]. Their experimental evidence indicates that macroscopically, the sample preserves its tetragonal symmetry down to 15 K, well below the magnetic phase transition temperature,  $T_{\rm m}$ . The lattice reacts to the magnetic order only microscopically, by an increase in the microstrain, as observed in XRPD measurements, without a macroscopic breakdown of the lattice symmetry.

They argue that such an effect is most probably related to a softening of the lattice below the magnetic phase transition, in comparison to the high-temperature nonmagnetic state, whereas the phase-separated coexistence of twinned magnetic domains and the nonmagnetic phase [68] suppresses the structural phase transition beyond the experimentally detectable limit, in spite of a relatively high SDW transition temperature.

For the single crystals grown form self-flux, a high quality sample with surface size of  $4 \times 1.5$  mm was measured by using nuclear magnetic resonance (NMR). Figure 5.6 shows the <sup>75</sup>As NMR measurements on under-doped single crystal Ba<sub>0.77</sub>K<sub>0.23</sub>Fe<sub>2</sub>As<sub>2</sub>. The spin-lattice relaxation rate,  $1/T_1$ , shows an upturn with decreasing T and forms a peak at the Néel temperature,  $T_N = 46$  K, due to a critical slowing down of the magnetic moments. Below  $T_N = 46$  K,  $1/T_1$  decreases and becomes nearly proportional to T before superconductivity sets in. Below  $T_c$  ( $\mu_0 H = 12$  T) = 16 K,  $1/T_1$  shows another sharp reduction, and follows a  $T^3$  relation. At even lower temperatures, the decrease in  $1/T_1$  becomes gradual. The sharp decrease in  $1/T_1$  below  $T_c$  indicates that the electrons that are hyperfine coupled to the nuclei produce both the magnetic order and the superconductivity. The results are clear and direct evidence that AFM coexists microscopically with superconductivity [77].

Fig. 5.6 Temperature dependence of the spin-lattice relaxation rate  $1/T_1$ . The straight line indicates the  $1/T_1 \propto T^3$  relation [77]



# 5.3 Electron/Hole-Doped BaFe<sub>2-x</sub>M<sub>x</sub>As<sub>2</sub> (M=Mn, Cr, Co, and Ni)

The structure of the 122 phase is commonly recognized as comprising the A layers, the charge reservoir blocks, and the FeAs conducting layers, alternatively stacked along the c-axis. By out-of-plane doping with aliovalentions in the A layer, namely, hole doping, charge carriers can be introduced into the FeAs layer and lead to superconductivity. In addition to doping into the A layer, superconductivity can also be induced by the in-plane doping of aliovalent ions in the FeAs conducting layer, namely, electron doping, such as in BaFe<sub>2-x</sub>Co<sub>x</sub>As<sub>2</sub> and BaFe<sub>2-x</sub>Ni<sub>x</sub>As<sub>2</sub> [52–55, 78–82]. Remarkably, substitutions on the Fe sites by hole-dopant atoms, namely Cr or Mn, do not lead to a superconducting state [83–86].

It is feasible to grow transition metal (TM) doped 122 type single crystals with large dimensions and high quality by the decanting flux method. Centimeter-size as-grown  $BaFe_{1.85}Co_{0.15}As_2$  and  $BaFe_{1.91}Ni_{0.09}As_2$  single crystals were used for inelastic neutron-scattering (INS) measurements. Magnetization measurements on several small pieces of each sample revealed sharp SC transitions at  $T_c = 18$  K and 25 K, respectively, as shown in Fig. 5.7a. In both the (hhl) and (hk0) planes, the

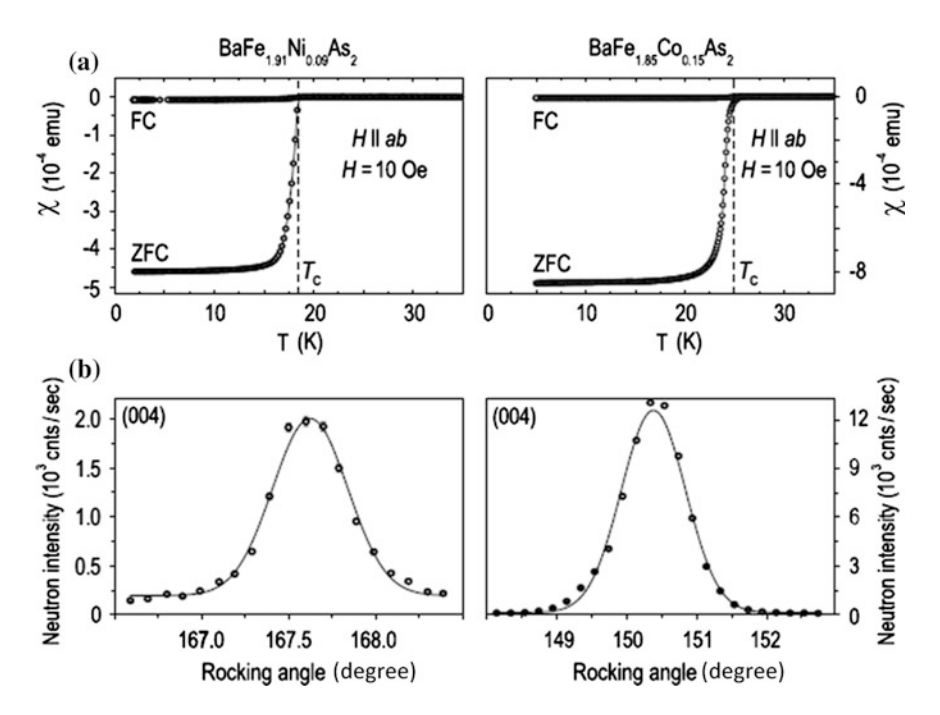


**Fig. 5.7** Characterization of the samples used for INS study: **a** Magnetization curves measured in magnetic field of 10 Oe, applied in-plane, after cooling in field (FC) and in zero field (ZFC). Insets show photographs of the samples. **b** Rocking curves measured on the (004) reflection in the (hhl) scattering plane with a triple-axis spectrometer [79]

neutron-diffraction patterns exhibit well defined Bragg spots with narrow mosaicity <1° (Fig. 5.7b), with no signatures of multiple single-crystalline grains, but with some polycrystalline contamination originating both from the main phase and, to a lesser extent, from traces of the (Fe, Co)As flux.

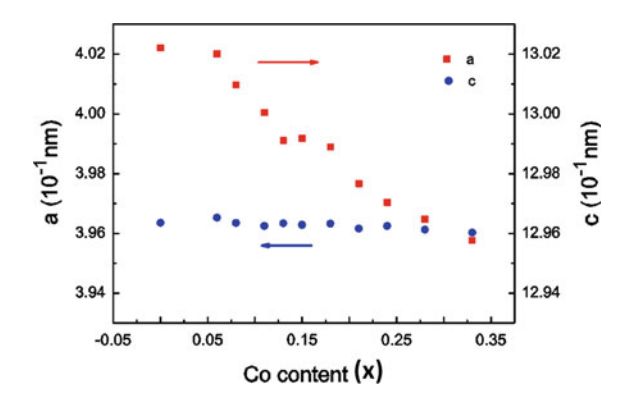
Researchers therefore had to optimize the scattering conditions in their INS measurements by avoiding the appearance of spurious inelastic peaks caused by such contamination. No structural or SDW transitions were detected down to 2 K in either sample, consistent with the known phase diagrams [53]. In order to improve the quality of the as-grown single crystals, segregation of dopants related to Fe and the effects of annealing on the properties of the crystals were carefully studied [54, 82].

### 5.3.1 Crystal Structure and Segregation Coefficient

The space group of the TM doped  $BaFe_2As_2$  single crystals were I4/mmm. Compared to the undoped  $BaFe_2As_2$  with a=3.9635(5) Å, c=13.022(2) Å, the a-axis lattice constants of the Co and Ni doped crystals exhibit near invariance within the experimental uncertainty, while the c-axis values shrink in a nearly linear way with increasing x, which is owing to the partial replacement of  $Fe^{2+}$  in the basal plane of  $BaFe_2As_2$  by the dopent ions, with the ionic radius of the dopants less than that of Fe [41, 54, 81]. Figure 5.8 shows the variation of the lattice parameters with Co content x.

For Mn doped BaFe<sub>2</sub>As<sub>2</sub> single crystal, the in-plane a-axis lattice parameter slightly increases with increasing x, but the c-axis lattice parameter shows a linear decrease [87]. The Cr doped BaFe<sub>2</sub>As<sub>2</sub> single crystal shows different behavior, with both a and c-axis lattice parameters increasing with increasing Cr concentration x, at a larger rate for the c-axis than for the a-axis parameter. The incorporation of x = 0.75 Cr in the Fe sites increases the cell volume by 2.6 %, mainly due to the increase in the c lattice constant [84]. The behavior of the lattice parameters changes

Fig. 5.8 Variation of lattice parameters of single crystals as a function of Co concentration x in BaFe<sub>2-x</sub>Co<sub>x</sub>As<sub>2</sub> [54]



with hole-dopant concentration in a way that cannot be simply attributed to the different ionic sizes of the substituted atoms.

The segregation coefficient of doping ions is an important parameter for growing a single crystal with an anticipated concentration. It should be noted that the concentration of dopants in the crystals is always lower than in the melt. The relationship between the TM composition x in the crystal and y in the melt varies with the initial flux ratio. It is found that the ratio of Ba:Fe:TM:As = 1:(5-y):y:5 is more suitable for growing large and high quality crystals, and the segregation coefficient of Co relative to Fe is about 0.78 [52–55].

### 5.3.2 Annealing Effect on the Superconductivity

It has been reported that there are annealing effects that improve the superconducting properties of LnFeOP (Ln=La, Pr, Nd) single crystals [88], which is correlated with the fact that high temperature  $O_2$  annealing improves the crystallinity and chemical homogeneity of samples. Due to the residual strain in the samples at room temperature and chemical inhomogeneity, post-annealing treatment studies were performed on the TM doped 122 type single crystals [54, 82]. It was found that annealing can enhance the  $T_c$  as much as  $\sim 50$  %, which could be an indication of improved crystallinity due to release of residual strain and/or improved microscopic chemical homogeneity of the dopant content, thereby enhancing the stability of the superconductor. Figure 5.9 shows a "dome" shaped diagram of the doping dependence of  $T_c$  in BaFe<sub>2-x</sub>Co<sub>x</sub>As<sub>2</sub> single crystals before and after annealing in argon atmosphere. It should be noted that the annealing treatment can result in an increase of  $T_c$  value of about 1–3 K for all the samples, underdoped, optimally doped and overdoped, respectively.

When the as-grown samples were annealed in air atmosphere and a vacuum environment at 750 °C for 7 days, even the surface of the air annealed sample remained shiny, suggesting that the BaFe<sub>2-x</sub>Co<sub>x</sub>As<sub>2</sub> single crystals are stable and do

**Fig. 5.9** Doping dependence of  $T_c$  for BaFe<sub>2-x</sub>Co<sub>x</sub>As<sub>2</sub> single crystals before and after annealing in argon atmosphere. Reprinted with permission from [54]

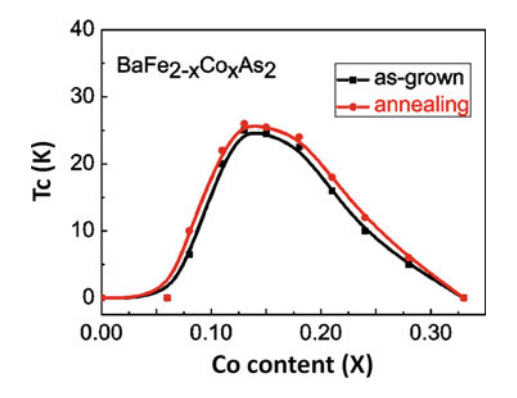
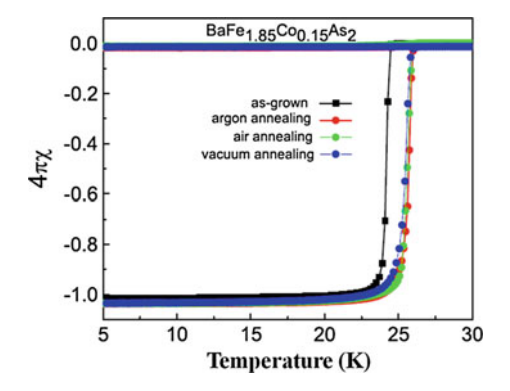


Fig. 5.10 Susceptibility curves of BaFe<sub>1.85</sub>Co<sub>0·15</sub>As<sub>2</sub> sample, showing a sharp transition of at  $T_c \approx 23$  K before annealing and increasing to  $\sim 25$  K after annealing in three different atmospheres, respectively [54]



not easily react with oxygen at 750 °C. Figure 5.10 shows the  $T_{\rm c}$  evolution of a BaFe<sub>1.85</sub>Co<sub>0.15</sub>As<sub>2</sub> sample annealed in three different atmospheres, i.e., argon, air, and vacuum. Compared to the sharp superconducting transition temperature  $T_{\rm c} \approx 23$  K of the as-grown sample, the results indicate that the different annealing atmospheres have an identical effect towards the enhancement of  $T_{\rm c}$  ( $\sim 25$  K), which is about 2 K. The study of the samples obtained from decanting also shows that it is difficult to completely remove the broad or double transition behavior by the high temperature annealing treatment. Annealing for longer times, such as 21 and 28 days, does not enhance the  $T_{\rm c}$  further, while it gradually reduces the superconducting volume fraction; there is an optimal annealing time for specific as-grown BaFe<sub>2-x</sub>TM<sub>x</sub>As<sub>2</sub> single crystals that is related to the growth conditions and doping levels.

# 5.4 Isovalently Doped $BaFe_2(As_{1-X}P_x)_2$ Single Crystals Grown by the Bridgman Method

BaFe<sub>2</sub>(As<sub>1-x</sub>P<sub>x</sub>)<sub>2</sub> is a characteristic system, in that the substitution of isovalent P for As does not change the carrier number. Therefore, it is expected that the systematic study of BaFe<sub>2</sub>(As<sub>1-x</sub>P<sub>x</sub>)<sub>2</sub> will unravel the effects of chemical pressure on the electronic structure of the iron-based superconductors [42, 89–91].

Before 2012, owing to the difficulty in synthesizing sizable single crystals with a wide doping range, experimental studies on  $BaFe_2(As_{1-x}P_x)_2$  were limited. Kasahara et al. grew 0.9-mm<sup>3</sup>-sized  $BaFe_2(As_{1-x}P_x)_2$  single crystals with  $0 \le x \le 0.71$  [91, 92]. In their method, stoichiometric mixtures of Ba (flakes), and FeAs, Fe, P, or FeP (powders) were placed in an alumina crucible and sealed in an evacuated quartz tube. The sample was heated up to 1150–1200 °C, kept for 12 h, and then cooled slowly down to  $\sim 800$  °C at the rate of 1.5 °C/h.

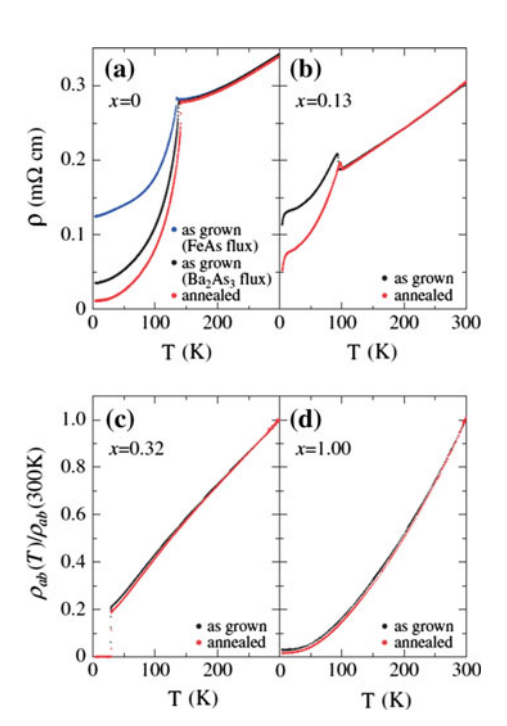
Self-flux of FeAs and FeP was used to grow high quality single crystals. The mixed powders were placed in Al<sub>2</sub>O<sub>3</sub> crucible. The crucible was sealed in an

evacuated quartz tube under vacuum, heated up to 1180 °C and cooled down to 900 °C at the rate of 2 °C/min. This method yielded hundreds of crystals with platelet shapes. The largest size is  $\sim 1$  mm, with most crystals ranging in size between 300 and 600 µm [93, 94]. Nakajima et al. reported a breakthrough in crystal growth using Ba<sub>2</sub>As<sub>3</sub>/Ba<sub>2</sub>P<sub>3</sub> flux for growing centimeter-sized crystals of BaFe<sub>2</sub>(As<sub>1-x</sub>P<sub>x</sub>)<sub>2</sub>, covering the entire *x* range from 0 to 1 [95]. Large single crystals ( $\sim 7 \times 7$  mm<sup>2</sup>) with controlled P concentrations were successfully obtained by decanting the flux.

The resistivity curve of BaFe<sub>2</sub>(As<sub>1-x</sub>P<sub>x</sub>)<sub>2</sub> grown in Ba<sub>2</sub>As<sub>3</sub>-flux is distinct from the crystals grown in FeAs flux. As shown in Fig. 5.11a, the residual resistivity ratio (RRR) of the Ba<sub>2</sub>As<sub>3</sub>-flux crystal is about 10, higher than the typical value of  $\sim$ 3 for the crystals grown by the FeAs-flux method. In addition, the transition temperature  $T_{\rm AFO}$  from the paramagnetic-tetragonal (PT) phase to an antiferromagnetic-orthorhombic (AFO) phase of the Ba<sub>2</sub>As<sub>3</sub>-flux crystal is 139 K, higher than that of the FeAs-flux samples at 135 K. The higher RRR and  $T_{\rm AFO}$  presumably indicate that the crystals grown by the Ba<sub>2</sub>As<sub>3</sub>-flux method have fewer defects and/or lattice dislocations than the ordinary crystals grown by the FeAs-flux method [96, 97].

It is also found that the quality of the as-grown crystals is improved by post-annealing, as evidenced by the increase in  $T_{\rm c}$  and  $T_{\rm AFO}$ , as well as the significant reduction in residual resistivity in the AFO phase in the underdoped regime.

**Fig. 5.11** Temperature dependence of the resistivity in the *ab*-plane,  $\rho_{ab}$ , before and after annealing for  $\mathbf{a} \times (0.32)$ , and  $\mathbf{d} \times (0.32)$ , and  $\mathbf{d} \times (0.32)$ , and  $\mathbf{d} \times (0.32)$ , the results obtained from crystals grown by the FeAs-flux method are also shown. The normalized data are plotted for  $\mathbf{a} \times (0.32)$  and 0.32 and 0.32 and 0.32 and 0.33 where a small but definite decrease in resistivity at low temperatures is observed after annealing [95]



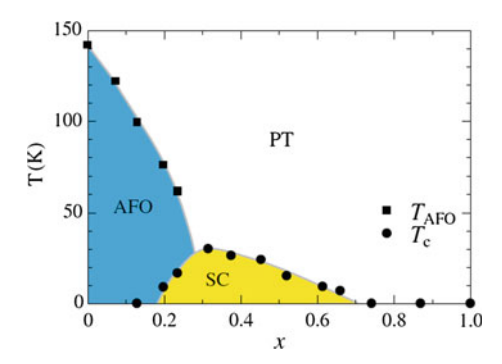


Fig. 5.12 Phase diagram obtained from the annealed BaFe<sub>2</sub>(As<sub>1-x</sub>P<sub>x</sub>)<sub>2</sub> single crystals.  $T_{AFO}$  is defined as the temperature at which the T derivative of resistivity shows a peak.  $T_c$  is determined by the zero-resistivity temperature that coincides with the temperature corresponding to the onset of the  $\chi(T)$  curve [95]

In order to extract the intrinsic properties of  $BaFe_2(As_{1-x}P_x)_2$ , refinement of the sample quality, which can be achieved by annealing, is a prerequisite. The phase diagram obtained from the annealed  $BaFe_2(As_{1-x}P_x)_2$  single crystals is shown in Fig. 5.12.

# 5.5 122 Type Iron Chalcogenides A<sub>x</sub>Fe<sub>2-y</sub>Se<sub>2</sub> (A=K, Rb and Cs)

The discovery of superconductivity at temperatures above 30 K in  $A_xFe_{2-y}Se_2$  (A=K, Rb, Cs, (Tl, K), and (Tl, Rb)) compounds has attracted considerable attention [19–22, 98–105]. The crystal structure of  $A_xFe_{2-y}Se_2$  descends from the ThCr<sub>2</sub>Si<sub>2</sub> structure with vacancies at the Fe sites. It has been revealed that some of these selenides are magnetic insulators. This behavior is distinct from that of the FeAs based 122 type but close to that of the cuprates superconductors.

Early investigations have indicated that Fe vacancy orders and phase separation occur in these compounds [105–107]. So far, large single crystals are easily grown for the iron-chalcogenide compounds; different techniques such as flux growth, the Bridgman method, and the modified floating zone (FZ) method have been successfully used to grow  $A_x Fe_{2-y} Se_2$  single crystals [108–113]. The complex microstructures, however, make it difficult to grow phase-pure superconducting single crystals. Nearly all the resulting crystals show either inhomogeneous composition or a low superconducting volume fraction. The major obstacle that limits our understanding of the intrinsic properties of  $A_x Fe_{2-y} Se_2$  is still the difficulty in preparing phase-pure superconducting samples.

### 5.5.1 Single Crystal Growth

#### 5.5.1.1 Self-flux Method

Success in obtaining superconducting samples strongly depends on the ratios of the starting chemical components, particularly on the initial Fe content, as well as heating, cooling, and growth rates. The typical procedure for A<sub>x</sub>Fe<sub>y</sub>Se<sub>2</sub> (A=K, Rb, and Cs) single crystal growth is as follows: first, FeSe precursor is synthesized at 700 °C in an evacuated quartz tube. Then, the FeSe precursor is ground into powder and mixed with K(Rb, Cs) at a ratio of K(Rb, Cs): Fe: Se = 0.8:2:2. The mixtures were loaded into a double-sealed quartz ampule, and then heated to 1030 °C and kept at this temperature for 2 h. A fast cooling rate of 6 °C h<sup>-1</sup> or a quenching method is applied before turning off the furnace at 750 °C. The composition of the as-grown crystals can be determined by energy dispersive X-ray (EDX) analysis, wave dispersive X-ray spectroscopy (WDX), or inductively-coupled plasma (ICP) analysis. All the methods of compositional analysis have revealed a different stoichiometry compared to the starting materials. The actual composition of the as-grown crystals produced by this method showed fluctuation, with the iron content fluctuating between 1.59 and 1.76, while the alkaline iron A content fluctuated between 0.75 and 0.88 [98, 113–116]. The results also showed that there are two transition steps in K<sub>0.84</sub>Fe<sub>1.59</sub>Se<sub>2</sub> crystal obtained from the flux growth, one at about 38 K and another at about 44 K, and the phases corresponding to these transition steps need to be carefully studied.

In order to optimize the growth parameters, Peng et al. investigated the melting behavior of alkaline iron selenide compounds by thermogravimetry/differential thermal analysis (TG/DTA) and high temperature optical microscopy (HTOM) [110]. The results indicated that all of the compounds melt incongruently, with complete melting occurring at 902, 927, and 900 °C, while a Fe-vacancy-ordered/disordered transition occurs at 267, 261, and 241 °C for A=K, Rb, and Cs, respectively. The starting material mixtures, with a molar ratio of 0.8A:2Fe:2Se were sealed in a quartz tube under vacuum. By shortening the soaking and growth time to minimize the volatilization of alkaline and Se components, larger crystals (millimeter-size) with homogeneous composition were grown.

#### 5.5.1.2 Floating Zone Method

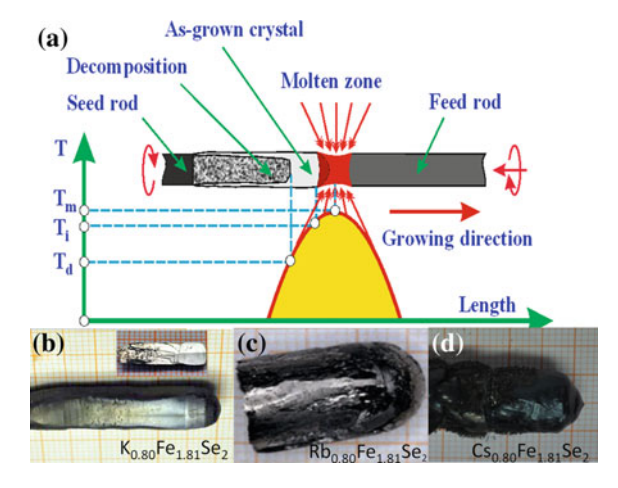
Superconducting  $A_xFe_{2-y}Se_2$  single crystals can be reproducibly grown by the optical floating-zone (FZ) technique [23]. This method enables us to obtain high quality single crystals with a mass of up to  $\sim 1.8$  g, offering sufficient material for measurements where large samples are required, such as inelastic neutron-scattering experiments. In [23], the feed rod was synthesized by the one-step solid-state reaction method. Elemental A, Fe, and Se were weighed at a ratio of A:Fe:Se = 0.8:2:2, and this was followed by sintering of the mixture at 850 °C for 10 h. The sintered mixture

was ground into a powder, and the powder was pressed into a cylindrical rod 6–7 mm in diameter and 70–80 mm in length under 600 bar of hydrostatic pressure. The rod was used to grow the crystal directly without the conventional process of sintering and pre-melting. A seed rod 2 cm in length was cut from the feed rod.

Figure 5.13a shows a schematic illustration of the growth process for the  $A_xFe_{2-y}Se_2$  single crystals. Homogeneous crystals could be grown at a traveling velocity of  $\sim 0.8$  mm h<sup>-1</sup> under 8 bar of argon pressure. It was observed that as the molten zone moved up, the already formed crystal continuously passed through a temperature zone,  $T_{\rm d}$ , where the crystal begins to decompose. Thus, to avoid passing through the decomposition zone, the lamp power was switched off towards the end of the growth process, resulting in non-decomposed crystal phase at the terminal part of the ingot.

Typical as-grown single-crystal ingots of  $A_xFe_{2-y}Se_2$  are shown in Fig. 5.13b–d. As can be seen in the inset of Fig. 5.13b, the cleaved termination of the  $\sim 1$  cm ingot displays a large crystal grain with a shiny surface. It is interesting to note that the iron content in the samples is approximately 1.81, which is higher than for the single crystals grown by the flux and Bridgman methods. It was also found that the Fe content can be tuned by using different growth atmospheres.

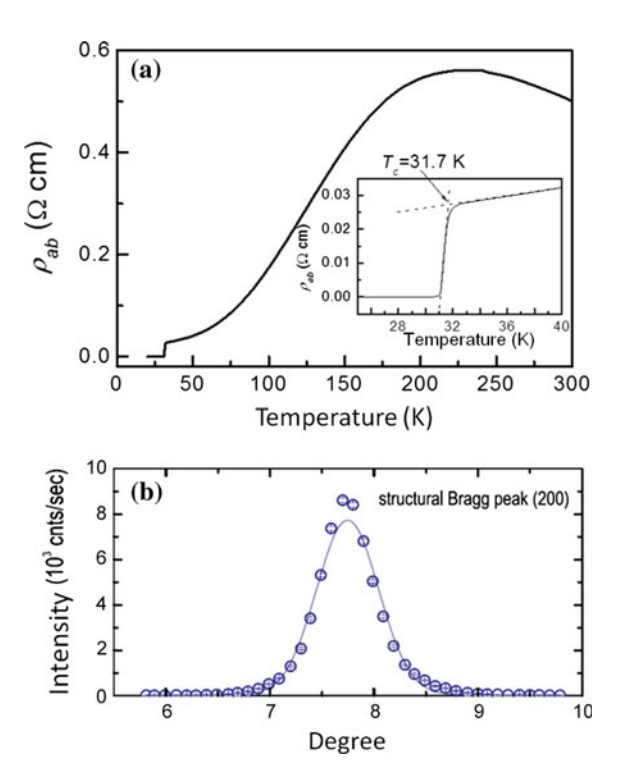
Systematic measurements, such as X-ray diffraction (XRD), neutron diffraction, EDX, resistivity, and magnetization, have been carried out to characterize the as-grown crystals. Figure 5.14 shows the XRD reflections in the (00*l*) plane, with all of the single crystals representing an intergrowth of two sets of *c*-axes, characterized by slightly different lattice constants. It assumed that the stronger reflections that have shorter *c*-axes are responsible for the superstructure phase with



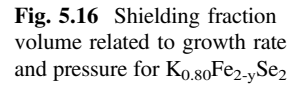
**Fig. 5.13** a Schematic drawing illustrates the growth process of the  $A_x$ Fe<sub>2-y</sub>Se<sub>2</sub> single crystals, which form between the solid?liquid interface temperature,  $T_i$ , and the decomposition temperature,  $T_d$ , below which the crystals undergo a continuous decomposition during crystal traveling [23]. **b** As-grown K<sub>0.80</sub>Fe<sub>1.81</sub>Se<sub>2</sub> single-crystal ingot. **c** and **d** single crystals cut off from ingots of Rb<sub>0.80</sub>Fe<sub>1.81</sub>Se<sub>2</sub> and Cs<sub>0.80</sub>Fe<sub>1.81</sub>Se<sub>2</sub>, respectively [56]

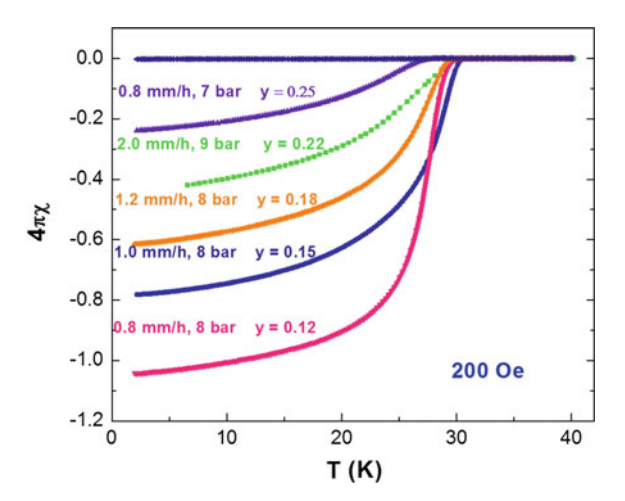
Fig. 5.14 (00*l*) X-ray diffraction patterns of the  $A_{0.80}$ Fe<sub>1·81</sub>Se<sub>2</sub> (A=K, Rb, and Cs) single crystals grown by FZ method. The c-axis lattice parameter is reduced with increasing alkaline ionic radius  $R_{\rm Cs+}$  (1.74 Å) >  $R_{\rm Rb+}$  (1.61 Å) >  $R_{\rm K+}$  (1.51 Å). The shoulders located beside the main reflections are indicated by the *asterisks*, which correspond to the possible superconducting phase [110]

Fig. 5.15 a Temperature dependence of in-plane resistivity  $\rho_{ab}$  of a  $K_{0.80}$ Fe<sub>1.81</sub>Se<sub>2</sub> single crystal. Inset shows a superconducting transition temperature at around  $T_c = 31.7$  K, with  $\Delta T_c \sim 1$  K. b Rocking curve of the (200) structural Bragg peak [23]



the iron-vacancy-ordered states, while the second phase (asterisks) with longer c-axes should be responsible for the superconducting phase with the iron-vacancy-disordered states. The EDX results and the transition width of about 1 K (inset of Fig. 5.15a) indicates that the as-grown  $K_{0.80}Fe_{1.81}Se_2$  crystal is





homogeneous. From neutron diffraction measurements, the sample shows a mosaic spread of 0.5 °C or better in the *ab*-plane (Fig. 5.15b). These results demonstrate that high quality and large single crystals of  $A_x Fe_{2-y} Se_2$  can be grown by using the FZ method.

The superconductivity of the crystals strongly depends on the ratios of the starting chemical components, as well as the growth parameters such as growth rate and pressure. Magnetization measurements were performed under a 200 Oe field, and all crystals were obtained from the same starting mixture with a ratio of K:Fe: Se = 0.8:2:2. As shown in Fig. 5.16, the general feature of the magnetic susceptibility are quite similar to each other, and the shielding fraction volume increases with increasing Fe content in the crystals. When crystal growth was performed under 8 bar Ar atmosphere, the Fe content decreased with increasing growth rate. The results also demonstrate that higher pressure and a slower growth rate will result in higher Fe content. The  $K_{0.80}Fe_{1.88}Se_2$  crystal has its superconducting transition temperature at  $T_c = 31.6$  K, having a near 100 % shielding fraction at low magnetic field. It is worth noting that in cases of non-uniform morphology, shielding will not provide the superconducting volume fraction, and a true Meissner experiment must be performed [106].

# 5.5.2 Microstructure and Phase Separation

The  $A_xFe_{2-y}Se_2$  single crystals tend to grow in a composition which is deficient both in iron and in the alkali atoms. They exhibit a main phase with  $\sqrt{5} \times \sqrt{5}$  superstructure, which corresponds to the  $A_{0.8}Fe_{1.6}Se_2$  stoichiometry. However, this phase is insulating and a number of experimental probes have shown that the minority

superconducting (SC) phase is spatially separated from this magnetic phase. The precise stoichiometry and the structure of the SC phase are unclear up to now.

Accumulated evidence indicates that phase separation occurs in superconducting  $A_x Fe_{2-y} Se_2$ . It has been evidenced by tunneling electron microscopy (TEM) [100], muon spin rotation ( $\mu$ SR) [117], scanning electron microscopy (SEM) [114], scanning tunneling microscopy (STM) [118], angle resolved photoemission spectroscopy (ARPES) measurements [117, 119], and scanning nanofocus single-crystal X-ray diffraction [182]. The nature of the phase separation indicates that Fe-vacancy-free or low Fe-vacancy  $A_x Fe_{2-y} Se_2$  is responsible for the superconductivity, while Fe-vacancy-ordered  $A_2 Fe_4 Se_5$  corresponds to the insulating/semiconducting phase.

Microstructure analysis by means of transmission electron microscopy (TEM) on  $K_xFe_{2-y}Se_{2-z}Te_z$  single crystals grown by the FZ method demonstrates a clear phase separation and its evolution with Te concentration on the nanoscale. As shown in Fig. 5.17a and b, two phases in the form of parallel lamellae, namely, an iron vacancy ordered state (OS) and disordered state (DOS), stack along the c axis of the crystal, and the results agree well with a previous study performed on  $KFe_{1.8}Se_2$  crystals grown by the flux method [100]. While in Te = 0.51 crystal, there are two phases in the form of randomly distributed domains (Fig. 5.17c), the results are consistent with a previous report and can be interpreted in terms of the coexistence of different phases separated mesoscopically [117].

The micrometer-scale phase separation was investigated by using SEM in order to analyze the correlation between the microstructures and the superconductivity, and to gain a better understanding of the dependence of superconductivity on the thermal history [111, 114, 120–123]. Figure 5.18 shows clear evidence of the coexistence of two phases in  $K_xFe_{2-y}Se_2$  single crystals. SEM images were collected on the surfaces of newly cleaved samples in the ab-plane. The images clearly demonstrate that  $K_xFe_{2-y}Se_2$  crystals have complex microstructures, consisting of a network throughout the matrix. This network is woven from stripes perpendicular to each other, and orientation analysis indicates that these stripes are aligned along the crystallographic  $\langle 110 \rangle$  directions. Each individual stripe consists of regularly

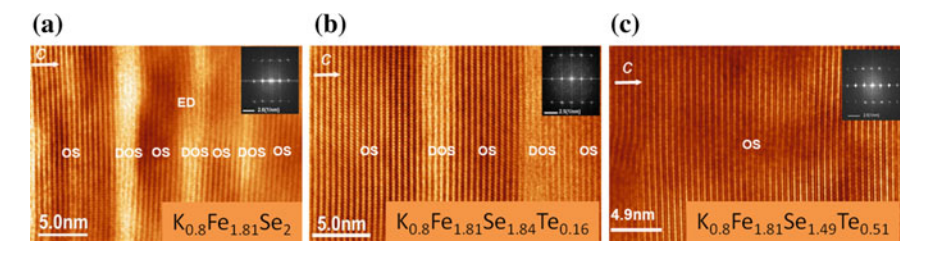


**Fig. 5.17** High-resolution TEM images of superconducting  $K_xFe_{2-y}Se_{2-z}Te_z$  crystals grown by the FZ method under 8 bar pressure: (a), (b) and (c) show complex domains along the *c*-axis direction in crystals of  $K_{0.8}Fe_{1.81}Se_2$ ,  $K_{0.8}Fe_{1.81}Se_{1.84}Te_{0.16}$ , and  $K_{0.8}Fe_{1.81}Se_{1.49}Te_{0.51}$ , respectively. The mesoscopic phase separation of vacancy-ordered (*brighter*) and vacancy-disordered (*darker*) regions is clearly illustrated [56]

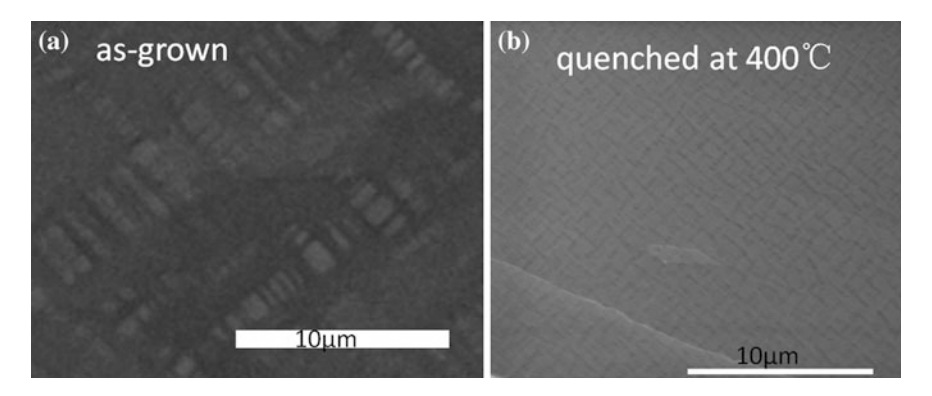


**Fig. 5.18** Typical SEM images of the *ab*-plane reveal the microstructural phase separation characteristic in  $K_{0.8}$ Fe<sub>2-v</sub>Se<sub>2</sub> samples: **a** As-grown, **b** quenched at 400 °C

ordered small rectangular bars for the as-grown samples (Fig. 5.18a). The morphology of the stripes as well as the superconductivity of the single crystals can be tuned by a post-annealing and quenching technique (Fig. 5.18b). A similar stripe pattern and its development by post treatment have also been demonstrated in  $Cs_xFe_{2-v}Se_2$  samples [122].

The chemical and structural analysis led to the conclusion that the minor Fe-rich phase was responsible for superconductivity in these crystals, but the precise stoichiometry for this SC phase is still unclear. Early research suggested that the SC phase consists of the pure FeSe structure without iron vacancies, but recent research has also suggested a new superconducting phase consisting of a single Fe vacancy for every eight Fe-sites arranged in a  $\sqrt{8} \times \sqrt{10}$  parallelogram structure [123].

It is worth noting that since accurate chemical analysis of the minor phase is difficult due to both the sensitivity of the EDX technique and the spatial resolution in the bulk samples in the SEM, so further studies using complementary techniques such as TEM and STM are necessary to investigate this nanoscale phase separation. Alternatively, single crystal growth studies are even more necessary in order to achieve the predictable synthesis of samples with larger superconducting volumes, and the achievements of these will greatly help to solve the puzzles in this family of materials.

# 5.6 11 Type Iron Chalcogenides

The tetragonal PbO-type FeSe, i.e. the  $\beta$ -FeSe (11 tpye), is the simplest member of the iron-based superconductor family. The  $\beta$ -FeSe, having a layered structure formed by a stacking of edge-sharing FeSe<sub>4</sub>-tetrahedra layers, superconducts at  $\sim$ 8 K [25, 124]. By the substitution of Te for Se, the  $T_{\rm c}$  value increases up to 15 K [125–127]. Moreover, it displays a strong positive pressure effect on  $T_{\rm c}$ , enhancing

 $T_{\rm c}$  to 36.7 K under a pressure of 8.9 GPa [128] and even fascinatingly well above 65 K in a FeSe-monoplayer grown on a SrTiO<sub>3</sub> substrate by molecular beam epitaxy [29, 129–131]. The common structural feature for iron selenide superconductors is the FeSe<sub>4</sub>-tetrahedron layers which serves as a basic unit for the superconductivity. Other iron selenide superconductors, like  $A_y$ Fe<sub>2-x</sub>Se<sub>2</sub> and  $(Li_{1-x}Fe_x)$ OHFe<sub>1-y</sub>Se for example, can be viewed as derived from the binary FeSe by intercalating in between its FeSe-layers the alkali metal ions A and the spacer layer  $(Li_{1-x}Fe_x)$ OH, respectively. The unusual properties, the similarity in structure and the simplicity in chemical composition, all make the binary FeSe an important prototype for investigating the underlying physics of the iron-based family.

# 5.6.1 Binary FeSe Crystal Growth by Flux and TSFZ Methods

Many efforts have been made to prepare superconducting FeSe crystals. However, it is not possible to directly grow the FeSe crystal from the melt, because, as shown in the phase diagram of Fe-Se system (Fig. 5.19) [132], the  $\beta$ -FeSe phase decomposes at 457 °C before melting. Consequently, the slow-cooling flux technique was commonly used to grow the crystals from various flux solutions. However, the as-grown crystals always exhibit a small size. For instance, FeSe<sub>x</sub> crystals with a size

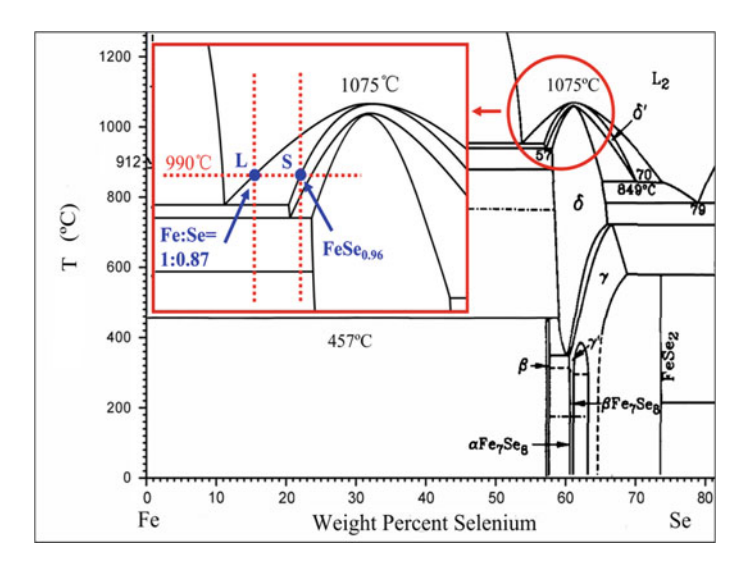


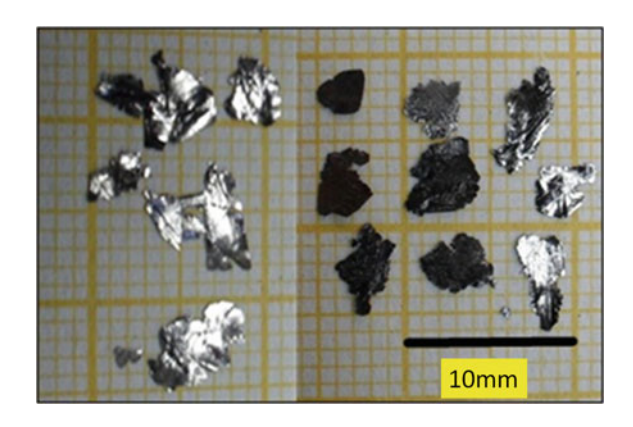
**Fig. 5.19** Fragment of Fe-Se phase diagram from [132]. The superconducting tetragonal β-FeSe phase forms in the narrow composition region near 57.5 wt% of Se below 457 °C. The inset is a magnified local area showing the solid-liquid equilibrium at 990 °C between S (δ'-FeSe<sub>0.96</sub>) on the solidus and L (Fe:Se = 1:0.87) on the liquidus

of about 500  $\mu$ m was grown using NaCl/KCl as flux [133, 134], single crystalline samples of about 4  $\times$  4  $\times$  0.1 mm³ in dimensions using KCl-AlCl₃ flux [135], FeSe<sub>0.88</sub> crystals of 2–4 mm across and 0.1–0.3 mm thickness and bigger FeSe<sub>0.94</sub> crystals with dimensions of 6  $\times$  3  $\times$  0.1–0.2 mm³ were prepared from KCl solutions [136–139]. A growth from a specially chosen LiCl-CsCl flux, with a low-temperature eutectic at 326 °C well below the decomposition temperature, yielded β-FeSe crystal of 1.5  $\times$  0.5  $\times$  0.05 mm³ dimensions [140]. Besides, vapor transport growth, a very time-consuming process, produced FeSe<sub>1-x</sub> crystals with similarly small lateral sizes of 0.5–3.5 mm [141, 142]. It is noted that in most cases the FeSe crystals grown from flux solutions display a (101) orientation, except for those synthesized from KCl-AlCl₃ flux [135] or via vapor transport [142] which orientate along (001) plane.

Relatively bigger superconducting FeSe<sub>0.94</sub> crystals were grown from a KCl solution [139], by improving the dissolution and convection (the mass transportation) of Fe solute in the flux solution and the temperature gradient and by optimizing the KCl content (the experimental conditions were detailed in [139]). The as-grown crystal pieces orientating along (101) plane are up to  $6 \times 3 \times 0.1$ – $0.2 \text{ mm}^3$  or  $5 \times 5 \times 0.1$ – $0.2 \text{ mm}^3$  in dimensions, as shown in Fig. 5.20. The optimal composition for the starting materials was found to be Fe:Se: KCl = 1:0.94:10, with a necessarily higher KCl content than earlier reports. The FeSe<sub>0.94</sub> crystals were grown by a slow-cooling process at a rate of 2 °C/h, after soaked at 850 °C for 24 h to dissolve the Fe powder to the most extent. The superconducting transition temperature ( $T_c$ ) of as-grown FeSe<sub>0.94</sub> crystals was determined to be  $\sim 10 \text{ K}$  by both magnetic and electronic transport measurements.

Generally speaking, a low solubility of the Fe solute in the flux solutions is the main cause for the small size of the crystals grown by the flux methods. To obtain larger FeSe crystals highly demanded by important measurements like, for example, neutron scattering, a crystal growth from a melt, instead of from the flux solutions, is necessary.

**Fig. 5.20** Photographs of typical FeSe<sub>0.94</sub> crystal pieces grown from KCl solution [139]



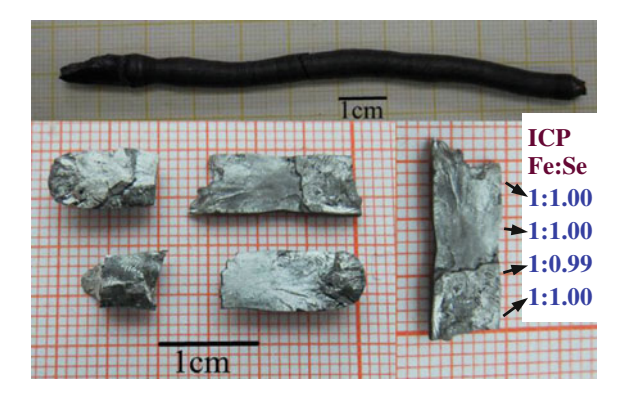


**Fig. 5.21** Photographs for an as-grown ingot 5–6 mm in diameter and 100 mm in length (the upper one) and for some typical large FeSe crystal pieces separated from the as-grown ingots (the lower ones). The biggest crystal is of  $15 \times 6 \times 2$  mm<sup>3</sup> dimensions. The composition of the crystals is very uniform as evidenced by the ICP-AES results given in the lower right part, showing almost the same composition at four different locations along the biggest crystal of FeSe. From [143]

Most recently, large and composition homogeneous superconducting tetragonal FeSe crystals (Fig. 5.21) have been successfully prepared via a specially designed flux-free traveling-solvent floating-zone approach [143]. The size of obtained crystal pieces is up to  $15 \times 6 \times 2 \text{ mm}^3$ , far bigger than previously reported in all dimensions. The thermodynamic phase relations underlying this growth process are sketched as follows. In a common flux growth using, e.g. KCl as the flux like the case of [139], the crystallization of FeSe proceeds through a slow cooling from a soaking temperature about 850 °C to about 770 °C, the melting point of KCl. Therefore the crystal directly grown at this temperature range is the non-superconducting δ-FeSe phase according to the Fe-Se phase diagram (Fig. 5.19). At lower temperatures below 457 °C, the most part of as-grown  $\delta$ -FeSe is phase transformed into the superconducting β-FeSe. The flux-free TSFZ growth is carried out, however, at an elevated temperature ~990 °C without any flux but using a solvent of the composition Fe:Se = 1:0.87. As illustrated in the inset of Fig. 5.19, the incongruent solid S (i.e.  $\delta'$ -FeSe<sub>0.96</sub>) at 990 °C is in equilibrium with the liquid L (the solvent) with Fe:Se = 1:0.87. Note that the slope of the liquidus line near the liquid L is not steep, which is beneficial for the crystallization of the liquid. The unique advantage of the TSFZ growth lies in that the solid-liquid equilibrium between S and L can be maintained during a stable TSFZ process, so that a big and composition homogeneous crystal S can be grown. And the superconducting β-FeSe phase is subsequently obtained due to the phase transformation at lower temperatures below 457 °C.

The lattice parameters for the tetragonal main phase ( $\beta$ -FeSe) of the crystals grown by the flux-free TSFZ are determined to be a = 3.771 Å and c = 5.522 Å by powder XRD (Fig. 5.22a). The crystal samples are of a single preferred orientation along (101) plane (Fig. 5.22b), which displays a crystal mosaic of 5.3° in terms of

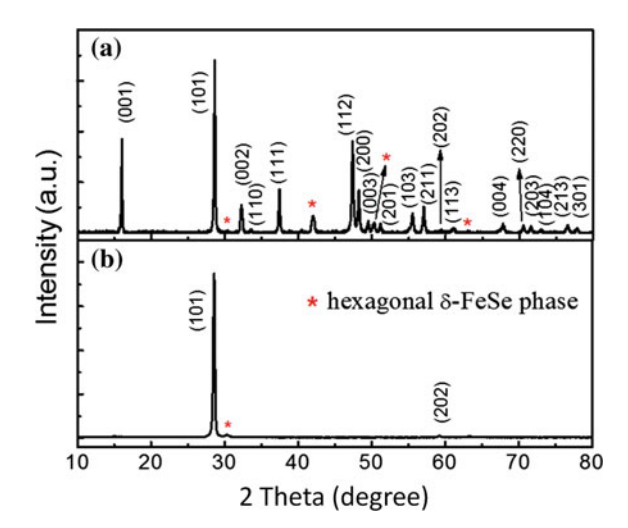


**Fig. 5.22** a Powder x-ray diffraction pattern of FeSe crystal. All the main diffraction peaks can be well indexed, except for some weak peaks from a second hexagonal phase as indicated by red asterisks. **b** A typical XRD pattern on a FeSe crystal showing the orientation along (101) crystal plane. Again a very weak peak from the second hexagonal phase is detected. From [143]

the FWHM for double-crystal x-ray rocking curve (Fig. 4 of [143]). The considerable mosaicity is the same as that observed on the crystal grown from KCl flux (Fig. 4 of [139]), suggesting it is intrinsic for the crystallization of this material. The superconducting transition temperature for the FeSe crystal is measured to be 9.4 K by ac magnetic susceptibility and electronic transport. A nearly perfect diamagnetic shielding signal (97 %) from the real part of the ac susceptibility indicates its bulk superconductivity.

The successful flux-free TSFZ growth of large superconducting FeSe crystals has made possible the important neutron scatterings on FeSe crystal samples, which clearly exhibit a tetragonal to orthorhombic phase transition at 90 K in the absence of an antiferromagnetic order. A most recent study by both elastic and inelastic neutron scatterings on these large FeSe crystal samples [144] has revealed the presence of stripe spin fluctuations coupled with the nematicity, which is substantially enhanced at  $\sim 4$  meV, but suppressed at 2.5 meV, on entering the superconducting state. The redistribution of the magnetic spectral weight across  $T_{\rm c}$  indicates a close relation between the spin fluctuations and superconductivity. The energy scale ( $\sim 4$  meV) for the sharp spin resonance below  $T_{\rm c}$  is consistent with an electron-boson coupling mode, suggesting a strong coupling between the electrons and spin fluctuations. The magnetic spectral weight in FeSe is found to be comparable to that of iron arsenide superconductors. The neutron scattering results strongly support that both nematicity and superconductivity are driven by spin fluctuations.

# 5.6.2 $Fe_{1-\delta}Te_{1-x}Se_x$ Crystals Grown by the Bridgman and Self-flux Method

Se-doped crystals of  $Fe_{1+\delta}Te_{1-x}Se_x$  with tetrahedral PbO-type structure could be successfully grown via melt growth methods, such as Bridgman [145], optical zone-melting [146] and self-flux methods [147]. Single crystal growth investigations have indicated that the self-flux grown crystals are superior to those grown by the Bridgman method, because the former contain less excess iron. Schematic drawings of the Bridgman and self-flux growth methods are shown in the Fig. 5.23a and b, respectively. To start with, high purity (4 N) Fe pieces, Te lump, and Se shot were weighed, mixed, and loaded into an alumina crucible. For the Bridgman method, mixtures with the nominal compositions of FeTe<sub>1-x</sub>Se<sub>x</sub> (x = 0, 0.2, 0.3, and0.4) were sealed in an evacuated quartz ampoule, which was then filled with 200 mbar argon atmosphere. Single crystals of  $Fe_{1+\delta}Te_{1-x}Se_x$  were obtained when the melt was soaked at 1050 °C for 12 h and a slow traveling speed of 1 mm/h was applied. In the self-flux method, various initial compositions of  $Fe_{1-y}Te_{1-x}Se_x$  (y = 0 and 0.05, and x = 0.3, 0.4, 0.5, 0.6, and 0.7) together with argon atmosphere from 200 to 800 mbar were introduced into evacuated ampoules. The ampoules were heated at 970-1000 °C for 12 h, and then slowly cooled down to 400 °C at a cooling rate of 2 °C/h.

The obtained bulk crystals were identified by Laue X-ray diffraction, which suggests good crystallization of the samples. All of the crystals are naturally cleaved along the ab-plane, as confirmed by X-ray  $\theta$ -2 $\theta$  scans. The crystal compositions were determined by the energy dispersive X-ray spectroscopy (EDX) within an error of  $\pm 2$  at.%. The compositional analysis revealed a different stoichiometry compared to the starting materials. For the crystals grown by the Bridgman method, the ratios of Te/Se slightly deviate from the nominal compositions. For the crystals grown with the self-flux method, the ratios of Te/Se vary

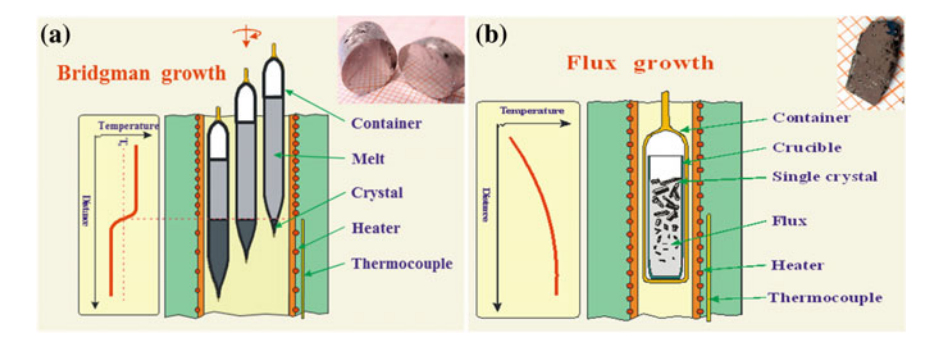


**Fig. 5.23** a Schematic diagram of the Bridgman growth. The inset shows the large  $Fe_{1+\delta}Te_{1-x}Se_x$  crystal, which can be readily cleaved along the *ab*-plane. **b** Schematic diagram of the flux growth. The inset shows the thin plates of as-grown  $Fe_{1+\delta}Te_{1-x}Se_x$  crystal grown by the self-flux method [56]

between  $0.37 \le x \le 0.40$ , though various ratios of initial mixtures were used. Most importantly, EDX analysis showed that the crystals grown by the Bridgman method contain more excess iron ( $\delta \ge 0.07$ ) compared to those ( $\delta \le 0.04$ ) grown by the self-flux method.

The transport and magnetic susceptibility measurements on as-grown crystals demonstrated that the samples have different properties. Figure 5.24 shows typical transport and magnetic properties of  $\text{Fe}_{1+\delta}\text{Te}_{1-x}\text{Se}_x$  (x=0,0.28, and 0.37) crystals grown by the Bridgman method. The parent compound  $\text{Fe}_{1+\delta}\text{Te}$  exhibits an antiferromagnetic (AFM) phase transition at  $T_N \approx 66.7\,$  K, accompanied by a tetragonal to monoclinic structural transition. Meanwhile the resistivity  $\rho_{ab}$  shows a sudden drop at  $T_N$ , below which, it evolves into a metallic state. With increasing Se doping level, superconductivity is introduced, and the AFM transition is suppressed. This indicates that  $\text{Fe}_{1+\delta}\text{Te}_{1-x}\text{Se}_x$  crystals ( $x=0.28\,$  and 0.37) display a Curie-Weiss-like behavior above  $T_c$ . However, the superconducting volume fraction is only around 0.8 % for these samples, suggesting a percolated superconducting behavior. Figure 5.24b shows that one of the crystals (x=0.37) exhibits semiconducting behavior above  $T_c\approx 15.4\,$  K. The paramagnetic state at high temperatures and the semiconducting behavior are likely to be related to the enhanced magnetic interactions resulting from the excess of iron.

Interestingly, dramatic changes are observed in the transport and magnetic properties of the crystals grown by the self-flux method. Fe $_{1+\delta}$ Te $_{0\cdot60}$ Se $_{0\cdot40}$  crystal displays a very sharp superconducting transition at  $T_c\approx 14$  K, and the shielding fraction is as high as 80 %, confirming the bulk nature of the superconductor. In contrast to the semiconducting behavior observed in the crystals grown by the Bridgman method, the normal state resistivity of the crystals grown via the self-flux method displays a large hump, as in Fig. 5.25a. The magnetic susceptibility measured in 7 T magnetic field is displayed in Fig. 5.25b. It monotonically decreases

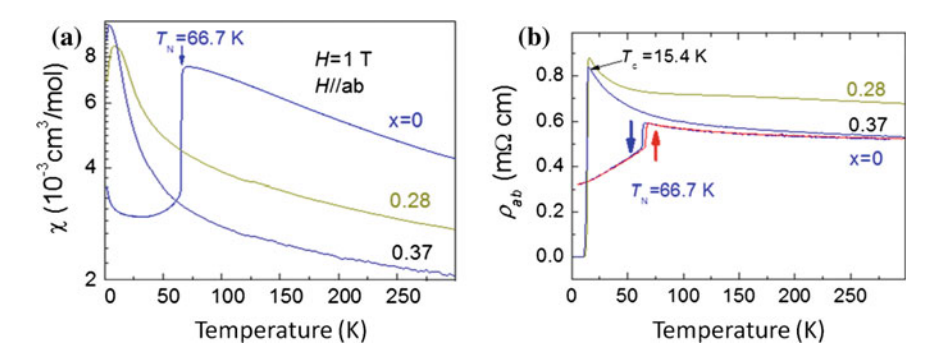


Fig. 5.24 a Magnetic susceptibility displays a Curie-Weiss-like behavior at high temperatures for  $Fe_{1+\delta}Te_{1-x}Se_x$  crystals ( $x=0,\ 0.28,\$ and 0.37) grown by the Bridgman method. **b** Temperature dependence of the resistivity for  $Fe_{1+\delta}Te_{1-x}Se_x$  crystals ( $x=0,\ 0.28,\$ and 0.37). Thermal hysteresis behavior is observed at  $T_N\approx 66.7$  K, indicating the existence of the first order structure phase transition. The *blue* and *red arrows* indicate the directions of the cooling and warming processes, respectively [56]

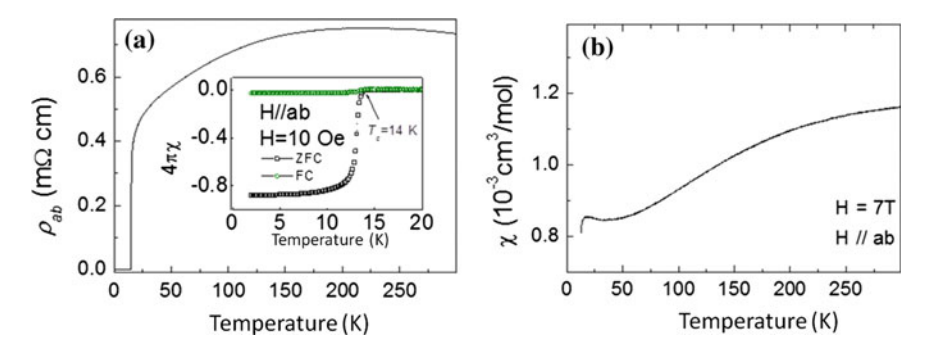


Fig. 5.25 a Temperature dependence of the resistivity of a Fe $_{1+\delta}$ Te $_{0-60}$ Se $_{0-40}$  crystal grown by the self-flux method. The inset shows the magnetic susceptibility; displaying a superconducting transition at  $T_c \approx 14$  K. b The magnetic susceptibility decreases with decreasing temperature and exhibits an upturn below 40 K

with decreasing temperature, and then displays an upturn below 40 K. It is estimated that the ratios of  $\rho(300 \text{ K})/\rho(50 \text{ K})$  and  $\chi(300 \text{ K})/\chi(50 \text{ K})$  are 1.30 and 1.36, respectively. This result confirms that the large hump in the resistivity is strongly correlated with the evolution of magnetic susceptibility for the self-flux-grown sample, which appears more ?clean? than that obtained by the Bridgman method.

The phase diagrams of  $Fe_{1-x}Te_{1-x}Se_x$  single crystal grown by the modified Bridgman method and self-flux method were established through different measurements [148–151]. Three regions in the phase diagram of  $Fe_{1.03}(Se_xTe_{1-x})$  single crystal grown by the Bridgman method can be identified as: (i) commensurate magnetic order for  $x \le 0.1$ , (ii) bulk superconductivity for  $x \approx 0.5$ , and (iii) for the range between 0.25 < x < 0.45, the coexistence of superconductivity and incommensurate magnetic order [148]. For the  $Fe_{1.02}(Te_{1-x}Se_x)$  ( $0 \le x < 0.5$ ) single crystal grown by the flux method, three composition regions with distinct physical properties. Region I ( $0 \le x < 0.09$ ) exhibits long-range AFM order with a wave vector ( $\pi$ , 0). Region II (0.09 < x < 0.29) exhibits neither long-range AFM order nor bulk superconductivity. Only in region III ( $x \ge 0.29$ ) evidence of bulk superconductivity [149]. Despite the minor differences on the doping regions, the reported phase diagrams show similar features.

# 5.7 111 Type of AFePn (A=Li and Na; Pn=P and As)

After the discovery of 1111 and 122 types iron-based superconductors, Superconductivity was also discovered in LiFeAs [8, 9, 152] and Na<sub>1- $\delta$ </sub>FeAs [153] (111 type materials), which crystallize in a PbFCl structure type and containing Fe<sub>2</sub>As<sub>2</sub> tetrahedral layers. Transition temperatures of 18 K (for LiFeAs) and 12? 25 K (for Na<sub>1- $\delta$ </sub>FeAs) [153] have been observed dependent on the precise Na concentration. Interestingly, superconductivity seems to appear in the 111 materials

in purely stoichiometric material without chemical doping. Despite the lower  $T_{\rm c}$  than the 1111 and 122 type, the structural simplicity of the 111 type makes it a convenient model to examine the superconducting mechanism.

However, there are few reports on the growth of 111 type of single crystals due to the difficulty in handling, reactivity with air and sensitivity to moisture of lithium and sodium. Even more, it is difficult to growth the stoichiometric LiFeAs and NaFeAs single crystals, because of the evaporation loss of Li/Na during the high-temperature reaction. Na<sub>1</sub>FeAs crystals have been grown from self-flux [154] while LiFeAs crystals have been grown by a Bridgman technique [155] and from both self-flux and Sn flux [156].

High quality single crystals of Na<sub>1-8</sub>FeAs have been grown by the self-flux technique. The starting compositions were selected as Na<sub>1.5</sub>FeAs. The mixtures of Na, and FeAs were put into an alumina crucible and sealed in Ta crucible under 2 atmosphere of argon gas. The Ta crucible was then sealed in an evacuated quartz ampoule and heated to 1100 °C and cooled slowly (at 5 °C/h) to grow single crystals. The obtained crystals with sizes up to  $8 \times 5 \times 0.5$  mm have the form of platelets with shinny surface. These crystals were characterized by X-ray diffraction (XRD). Figure 5.26 shows the X-ray diffraction pattern of  $Na_{1-\delta}FeAs$  with the  $00\ell$ reflections. The lattice constant c = 7.028 Å was calculated from the higher order peaks, comparable to that of polycrystalline sample. The elemental composition of the single crystal was checked by Inductively Coupled Plasma (ICP) analysis. Several crystals from the same batch were analyzed and the deficiency of sodium was found to be less than 1 %; that is, the elemental composition of the single crystal is very close to a stoichiometric 1:1:1. The crystals were found to undergo three successive phase transitions at around 52, 41, and 23 K, which correspond to structural, magnetic and superconducting transitions, respectively.

LiFeAs single crystal with onset  $T_c \sim 19.7$  K can be grown by using the Bridgeman method [155]. Approximately 3 g of FeAs<sub>1.2</sub> was prepared by a solid reaction of Fe powder and As chips. The mixture was sealed twice in an evacuated quartz tube and placed in a box furnace. The furnace was heated to 1050 °C at a rate of 100 °C/h and kept at that temperature for 40 h. The sample was then cooled

Fig. 5.26 Single crystal X-ray diffraction pattern for Na<sub>1- $\delta$ </sub>FeAs. The inset shows the photograph of a Na<sub>1- $\delta$ </sub>FeAs single crystal (length scale 1 mm) [154]

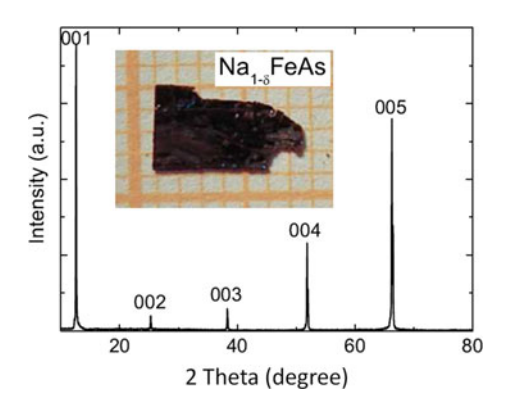
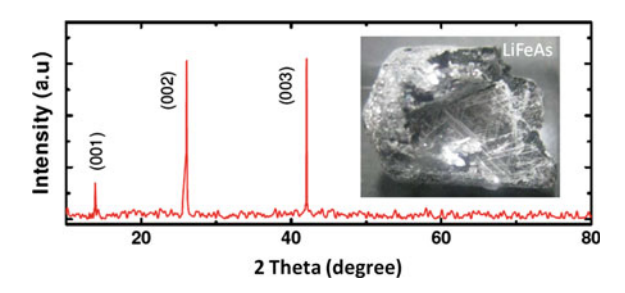


Fig. 5.27 X-ray diffraction pattern of a LiFeAs crystal grown by Bridgeman method. The inset is photography of the LiFeAs single crystal with a well cleaved plane [155]



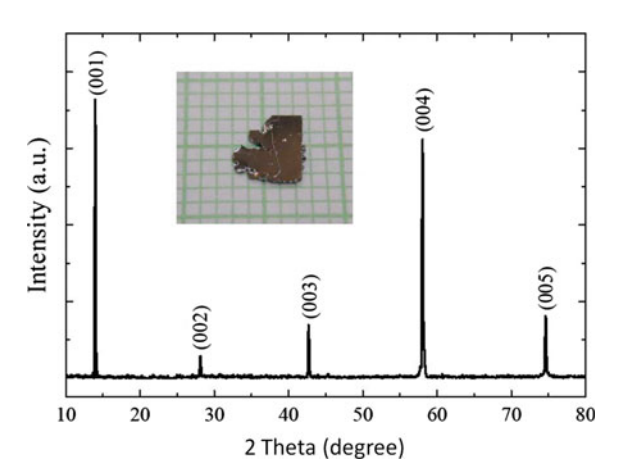
to room temp at a rate of  $100\,^{\circ}\text{C/h}$ . Under an Ar atmosphere, precursors of FeAs<sub>1.2</sub> and Li with nominal composition ratio 1:1.9 were loaded into a small BN crucible, which was put in a W crucible. A BN crucible was used to avoid a reaction between the starting materials (especially Fe) and W crucible. The cap covering the W crucible was welded with an arc welder and filled with Ar gas to prevent the escape of volatile As and Li. The welded W crucible was placed in a vacuum furnace with a tungsten mesh heater (VFTMH), heated slowly to  $1500\,^{\circ}\text{C}$  over a  $12\,^{\circ}\text{h}$  period and held at that temperature for  $102\,^{\circ}\text{h}$ . When the temperature reached  $1500\,^{\circ}\text{C}$ , the crucible was held its position for  $12\,^{\circ}\text{h}$ , and then slowly moved downward out of the heater in the furnace at a rate of  $1.6\,^{\circ}\text{mm/h}$ . The obtained bulk sample contained a  $\sim 6 \times 6 \times 3\,^{\circ}\text{mm}^3$  single crystal as shown the inset of Fig. 5.27.

Figure 5.27 shows the XRD pattern of a LiFeAs crystal selected from the well cleaved bulk sample, and only (001), (002) and (003) peaks were observed. This indicates a well oriented single crystal.

LiFeAs crystal with lateral sizes up to  $5 \times 5$  mm<sup>2</sup> can been grown by using Sn-flux method [157]. Stoichiometric amount of Li, Fe and As were weighed and kept in a pair of alumina crucibles, and Sn was added as a flux with a molar ratio [LiFeAs]:Sn = 1:10. The alumina crucible was put into a quartz ampoule, which was sealed under partial Ar atmosphere ( $\sim 0.7$  bar) to minimize Li evaporation during the reaction. To avoid oxidation, all the processes for handling chemicals were performed inside a glove box, where the levels of oxygen and moisture were maintained less than 1 ppm. The sealed quartz ampoule was heated up with a rate of 50 °C/h to be kept at 250 °C for 24 h and subsequently at 500 °C for 4 h to fully dissolve Li and As into the Sn flux. Later, the ampoule was heated up to 850 °C to stay for 4 h and then cooled down to 500 °C with a rate of 3.5 °C/h. At 500 °C, centrifuging was performed to remove the Sn-flux from the crystal surfaces. The crystals thus harvested showed a plate-like shape and the maximum lateral size reached up to  $5 \times 5$  mm<sup>2</sup> (Inset of Fig. 5.28).

X-ray diffraction results are shown in Fig. 5.28. All the peaks can be indexed with a tetragonal *P4/nmm* group, being consistent with previous reports on polycrystalline LiFeAs and other impurity phases were not detected. Electrical resistivity studies show that the superconducting onset temperature is 18.2 K with a transition width less than 1.1 K, showing the higher quality than the crystals growth by Bridgeman method [155].

Fig. 5.28 X-ray diffraction pattern of the LiFeAs single crystal grown by Sn-flux method. The inset shows a photograph of a piece of grown crystal. One grid in the photograph represents 1 mm [157]



LiFeAs and NaFeAs crystals up to  $5 \times 5 \times 0.5$  mm in size can be grown by self-flux methods [11]. The Li<sub>3</sub>As or Na<sub>3</sub>As, FeAs and As powders were mixed according to the stoichiometric ratio of LiFe<sub>0.3</sub>As or NaFe<sub>0.3</sub>As. The powder mixture was pressed into a pellet in an alumina oxide tube and sealed in a Nb tube with argon gas at a pressure of 1 atm before being sealed in an evacuated quartz tube. This quartz tube was then heated up to a temperature of 1100 °C for the LiFe<sub>0.3</sub>As compound or 0.950 °C for NaFe<sub>0.3</sub>As) for 10 h and then cooled down to 700 °C at a rate of 5 °C/h. Although the NaFeAs crystals exhibit a superconducting transition around 8 K, the superconducting volume fraction is minimal.

# 5.8 1111 Type of Ln(O/F)FePn (Ln=Rare Earth Elements; Pn=P and As)

Iron-based superconductivity was first discovered in LaFePO in 2006 [1], the superconducting transition temperature Tc was only 3.2 K. The breakthrough of superconductivity at 26 K in LaFeAsO<sub>1-x</sub>F<sub>x</sub> [158] immediately aroused great research interests in the condensed matter physics community, since the element-selective feature at the four crystallographic sites allows various kinds of successful chemical doping for inducing superconductivity. By replacing the La atoms with other rare-earth elements, the superconducting transition temperature was quickly enhanced. Further study shown that both the F doped and oxygen deficient samples show the same trend for  $T_{\rm C}$  as a function of rare earth ion [159–162]. Figure 5.29 shows the temperature dependence of resistivity for some typical 1111 type oxygen-deficient superconductors found by high-pressure synthesis [163].

The growth of large single crystals of the 1111 system has been proven to be difficult so that the largest crystals are still in submillimeter size despite extensive

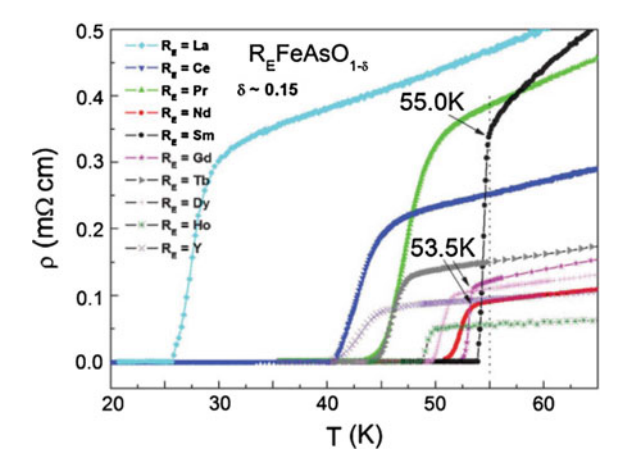


Fig. 5.29 The temperature dependence of resistivity for some typical 1111-type oxygen-deficient superconductors [163]

efforts. Zhigadlo et al. succeeded in growing single crystals of SmFeAsO<sub>1-x</sub> $F_x$  in the 100  $\mu$ m size regime using a NaCl/KCl flux technique at high (3 GPa) pressure [164].

Single crystals of RFeAsO<sub>0.9</sub>F<sub>0.1</sub> (nominal O and F composition) were extracted from 5 mm diameter pellets obtained using high pressure synthesis. Individual superconducting single crystals have dimensions up to  $650 \times 180 \times 120 \ \mu m^3$  for Nd-1111 (Fig. 5.30a) and  $330 \times 240 \times 10 \ \mu m^3$  for La-1111 (Fig. 5.30b) [165].

After the first single crystals  $(3 \times 3 \times 0.2 \text{ mm}^3)$  of the 122 superconducting compound  $Ba_{1-x}K_xFe_2As_2$  were grown by using Sn flux [45], Sn flux has been used quite successfully in the crystal growth of various other MFe<sub>2</sub>As<sub>2</sub>, 1111, and 111 compounds, such as large CeFeAsO single crystal as show in Fig. 5.30c [166], number of other fluxes were quickly tried.

In 2009, millimeter-sized single crystals of 1111 type were successfully grown in NaAs flux at ambient pressure [167]. The as-grown LaFeAsO, LaFe<sub>1-x</sub>Co<sub>x</sub>AsO, and LaFeAsO<sub>1-x</sub>F<sub>x</sub> crystals have typical dimensions of  $3 \times 4 \times 0.05$ –0.3 mm<sup>3</sup> with the crystallographic *c*-axis perpendicular to the plane of the plate-like single crystals (Fig. 5.31). The NaAs flux then been applied to crystal growth of other *RM*AsO (M = transition metal) members.

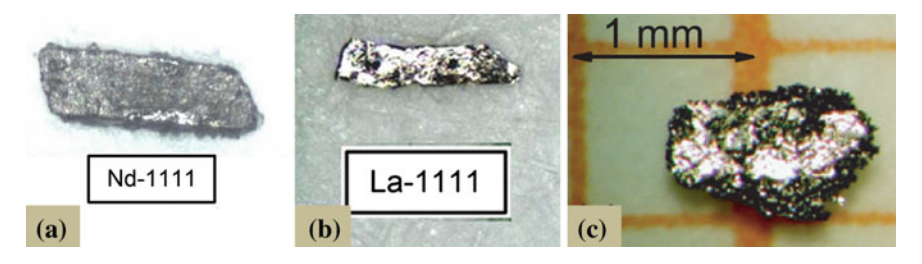


Fig. 5.30 Photographs of single crystals. a Nd-1111 [165], b La-1111 [165], c CeFeAsO [166]

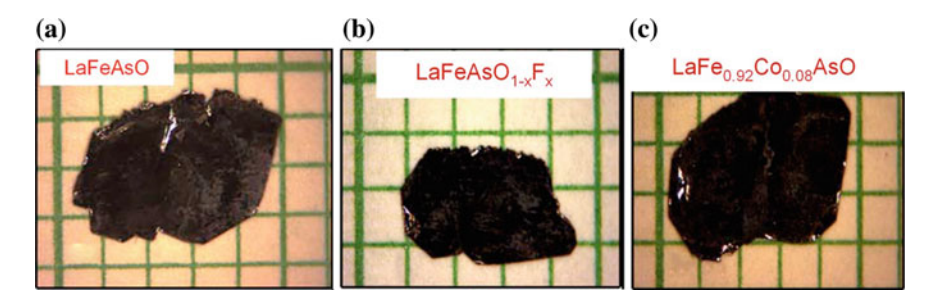
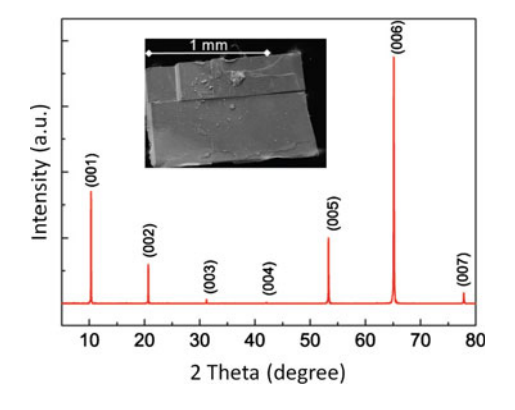


Fig. 5.31 Photographs of single crystals growth from NaAs flux [167]

Recently, millimeter-sized CaFeAsF single crystal was grown by using the self-flux method with CaAs as the flux [168]. First, the starting materials Ca granules and As grains were mixed in 1:1 ratio. Then the mixture was sealed in an evacuated quartz tube and followed by a heating process at 700 °C for 10 h to get the CaAs precursor. CaAs, FeF<sub>2</sub> powder and Fe powder were mixed together in the stoichiometric ratio 10:1:1, and the mixture were placed in a crucible. Finally, the crucible was sealed in a quartz tube with vacuum. All the weighing and mixing procedures were carried out in a glove box with a protective argon atmosphere. The quartz tube was heated at 950 °C for 40 h firstly, and then it was heated up to 1230 °C and stay for 20 h. Finally it was cooled down to 900 °C at a rate of 2 °C/h and followed by a quick cooling down to room temperature.

A typical dimension of the single crystals is  $1.2 \times 1.0 \times 0.1 \text{ mm}^3$ . The morphology was examined by the scanning electron microscopy. An SEM picture for the CaFeAsF single crystal can be seen in inset of Fig. 5.32, which shows the flat surface and some terrace-like features. The structure of the crystals was first check by a powder x-ray diffractometer, where the x-ray was incident on the *ab*-plane of the crystal. The diffraction pattern is shown in Fig. 5.32. All the diffraction peaks can be indexed to the tetragonal ZrCuSiAs-type structure. Only sharp peaks along (001) orientation can be observed, suggesting a high c-axis orientation. The full

Fig. 5.32 X-ray diffraction pattern measured on the CaFeAsF single crystal with the x-ray incident on the ab-plane. The inset is SEM picture of a CaFeAsF crystal with the lateral size larger than 1 mm [168]



width at half maximum (FWHM) of the diffraction peaks is only about  $0.10^{\circ}$  after deducting the  $K_{\alpha 2}$  contribution, indicating a rather fine crystalline quality.

At present, most of the 1111 type Ln(O/F)FePn can be grown in mm-sized single crystal form by using flux method.

# 5.9 11111-Type (Li<sub>1-x</sub>Fe<sub>x</sub>)OHFe<sub>1-y</sub>Se and Its Implication for Iron-Based Family

### 5.9.1 Electronic Phase Diagram

Iron selenide and arsenide superconductors, as the two subgroups of iron-based family, contain similar edge-sharing FeSe<sub>4</sub>- or FeAs<sub>4</sub>-tetrahedra layers as their superconducting blocks, respectively. However, previous reports have shown that the typical FeSe-based superconductors A<sub>v</sub>Fe<sub>2-x</sub>Se<sub>2</sub> (A=alkali metal ions) exhibit quite different physical properties in the parent and normal states from the FeAs-based ones, despite sharing the similar structural skeleton. In contrast to the FeAs-based superconductors, A<sub>v</sub>Fe<sub>2-x</sub>Se<sub>2</sub> compounds always manifest themselves as a mixture of high-T<sub>c</sub> superconducting (SC) phase, strongly antiferromagnetic (AFM) phase, and various cation/iron vacancy ordered phases [169-176]. For example, the superconducting phase is always intergrown with a well-known insulating 245 phase of a  $\sqrt{5} \times \sqrt{5}$  Fe vacancy order accounting for a strong cluster AFM order at about 500 K. Unlike a metallic background in iron arsenide materials, the electric resistivity of  $A_v Fe_{2-x} Se_2$  shows a broad hump between  $\sim 70$  and 300 K, a signal of the mixed electronic states. Because of the phase separation in the FeSe-based superconductors [107, 109, 172], a domelike doping dependence of  $T_{\rm c}$  was not as commonly observed as in the FeAs-based superconductors. Another important difference is that the correlated AFM SDW (spin density wave) ordering temperature for FeAs-based parent compounds (100–150 K [51, 65, 177–179]) is much lower than that for the FeSe-based counterparts ( $\sim 500$  K), owing to significantly different magnetic coupling strengths in the two material systems. These results seem to suggest different electronic ground states for the FeSe- and FeAs-based materials. It thus raises the question of whether the iron-based family would share a universal underlying physics for the high- $T_c$  superconductivity. To resolve this issue is of fundamental importance for understanding the physical mechanism of all classes of high- $T_c$  superconductors. But in  $A_v Fe_{2-v} Se_2$ , the presence of the insulating AFM 245 phase obstructs the experimental observation on the intrinsic electronic properties of the normal and superconducting states. The appearance of a new FeSe-based superconductor Li<sub>0.8</sub>Fe<sub>0.2</sub>OHFeSe [35], however, where the troublesome  $\sqrt{5} \times \sqrt{5}$  Fe vacancy ordered phase is absent [36], marks a turning point in the experimental studies.

The new FeSe-based superconductor system, generalized by the chemical formula  $(\text{Li}_{1-x}\text{Fe}_x)\text{OHFe}_{1-y}\text{Se}$  (short for FeSe11111 here) and showing a  $T_c$  up to 40–43 K,

have recently been synthesized by hydrothermal approaches [35, 36, 180, 181]. Based on a series of powder samples prepared by the hydrothermal reactions, a complete electronic phase diagram of FeSe11111 (Fig. 5.33a) has been established, which indicates that the physical properties of FeSe11111 in both the AFM-SDW and SC regimes closely resemble those of FeAs-based superconductors [36]. Like the parent compounds of FeAs-based superconductors, the non-SC FeSe11111 samples displays an AFM-SDW order below 127 K, in the absence of the  $\sqrt{5} \times \sqrt{5}$  superstructure and the associated strong AFM order at  $\sim 500$  K otherwise present in FeSe-based A<sub>y</sub>Fe<sub>2-x</sub>Se<sub>2</sub>. Moreover, in the SC regime, an optimal  $T_c = 40$  K and a dominant superstructure with a unique modulation wave vector q = 1/2(1, 1, 0) (Fig. 5.33c) are very similar and identical, respectively, to those reported for A<sub>y</sub>Fe<sub>2-x</sub>Se<sub>2</sub> and K<sub>y</sub>Fe<sub>2-x</sub>Se<sub>2</sub> superconductors. Hence, the unusual (Li<sub>1-x</sub>Fe<sub>x</sub>)OHFe<sub>1-y</sub>Se system bridges the gap between iron selenide and arsenide superconductors [36], and a common mechanism for high- $T_c$  superconductivity is thus expected.

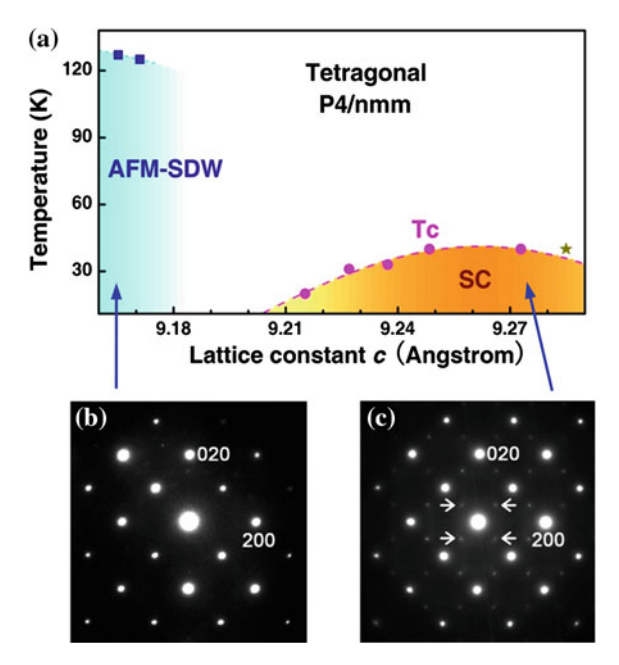


**Fig. 5.33 a** Phase diagram versus lattice parameter c for  $(\text{Li}_{1-x}\text{Fe}_x)\text{OHFe}_{1-y}\text{Se}$ . Similar to FeAs-based superconductors, when the AFM SDW order is suppressed, an SC dome appears concomitantly, with an optimal  $T_c = 40$  K. **b** and **c** are selected area diffraction patterns taken along the [001] zone axis direction. The former is for the non-superconducting sample with the AFM-SDW order at 127 K, showing only the basic tetragonal structure, and the latter is for the optimal superconducting sample  $(T_c = 40 \text{ K})$ , showing evident satellite spots characterized by a unique modulation wave vector of q = 1/2(1, 1, 0). From [36]

# 5.9.2 Crystal Synthesis via Ion/Cluster Exchange and Strong Two Dimensionality

The binary Fe<sub>1+δ</sub>Se compound, structured with FeSe<sub>4</sub>-tetrahedron layers of the maximum interlayer compactness, exhibits superconductivity only at  $\sim 8$  K under ambient pressure [25, 124]. In contrast to that, in a highly two-dimensional single unit-cell FeSe film on a SrTiO<sub>3</sub> substrate, the superconducting transition temperature  $T_c$  can be increased up to a value above 65 K [29, 129–131]. In other intercalated FeSe-based superconductors with a larger interlayer spacing of the FeSe<sub>4</sub>-tetrahedron layers, the superconductivity of a higher  $T_c$  than the binary bulk  $Fe_{1+\delta}Se$  is always realized. In A<sub>v</sub>Fe<sub>2-v</sub>Se<sub>2</sub> compounds, for example, the intercalation of alkali metal ions A into between the adjacent FeSe<sub>4</sub>-tetrahedron layers expands the interlayer separation and yields superconductivity at  $T_c \sim 30$  K. It seems that the superconductivity is enhanced with the degree of the structural and/or electronic two dimensionalities. Since FeSe11111 has a larger interlayer spacing than that of A<sub>v</sub>Fe<sub>2</sub> <sub>x</sub>Se<sub>2</sub>, the correlation between the adjacent FeSe layers becomes even weaker. Such a quasi-two-dimensional structure is propitious for unveiling the interplay of electronic anisotropy and high- $T_c$  superconductivity. For in-depth investigations on the anisotropic, intrinsic electronic properties of FeSe11111, high-quality large crystal samples are indispensable.

The common hydrothermal synthesis using commercially available reagents and prepared FeSe as starting materials have produced only powder samples of FeSe11111 [35, 36, 180, 181]. A development in the synthesis technique has recently been made, and large and high quality single-phased crystals of FeSe11111 have been successfully prepared by using specially grown big crystals of K<sub>0.8</sub>Fe<sub>1.6</sub>Se<sub>2</sub> (nominal 245 phase, KFS245 for short) as a kind of matrix for a hydrothermal ion/cluster exchange reaction [182]. The KFS245 structure consists of an alternative stacking of K-monolayers and Fe<sub>0.8</sub>Se-monolayers similar to the target compound, so as to be the best matrix for the ion/cluster exchange. The cartoon in Fig. 5.34a illustrates such an ionic exchange process. The K ions in KFS245 are completely released into solution after the ion-exchange reaction process. Simultaneously, (Li/Fe)OH layers constructed by ions from the solution are squashed into the matrix, linking the adjacent FeSe<sub>4</sub>-tetrahedra via a weak hydrogen bonding. The separation between the neighboring FeSe<sub>4</sub>-tertahedron layers is consequently enlarged by  $\sim 32 \%$  (from  $\sim 7.067$  to  $\sim 9.318$  Å), resulting in an enhanced two dimensionality of the crystalline and electronic structures compared to the bulk FeSe and A<sub>v</sub>Fe<sub>2-x</sub>Se<sub>2</sub> superconductors. It is noted that a most recent work [183] has shown that this ion/cluster exchange synthesis of FeSe11111 crystals is reproducible for precursor crystals of Rb<sub>0.80</sub>Fe<sub>1.81</sub>Se<sub>2</sub> and Cs<sub>0.80</sub>Fe<sub>1.81</sub>Se<sub>2</sub> besides K<sub>0.80</sub>Fe<sub>1.81</sub>Se<sub>2</sub>, all showing similar matrix structures. Based on thus-derived FeSe11111 crystals, an electronic phase diagram (Fig. 5.35) similar to previously reported for poly-crystalline FeSe11111 samples (Fig. 5.33a) is obtained.

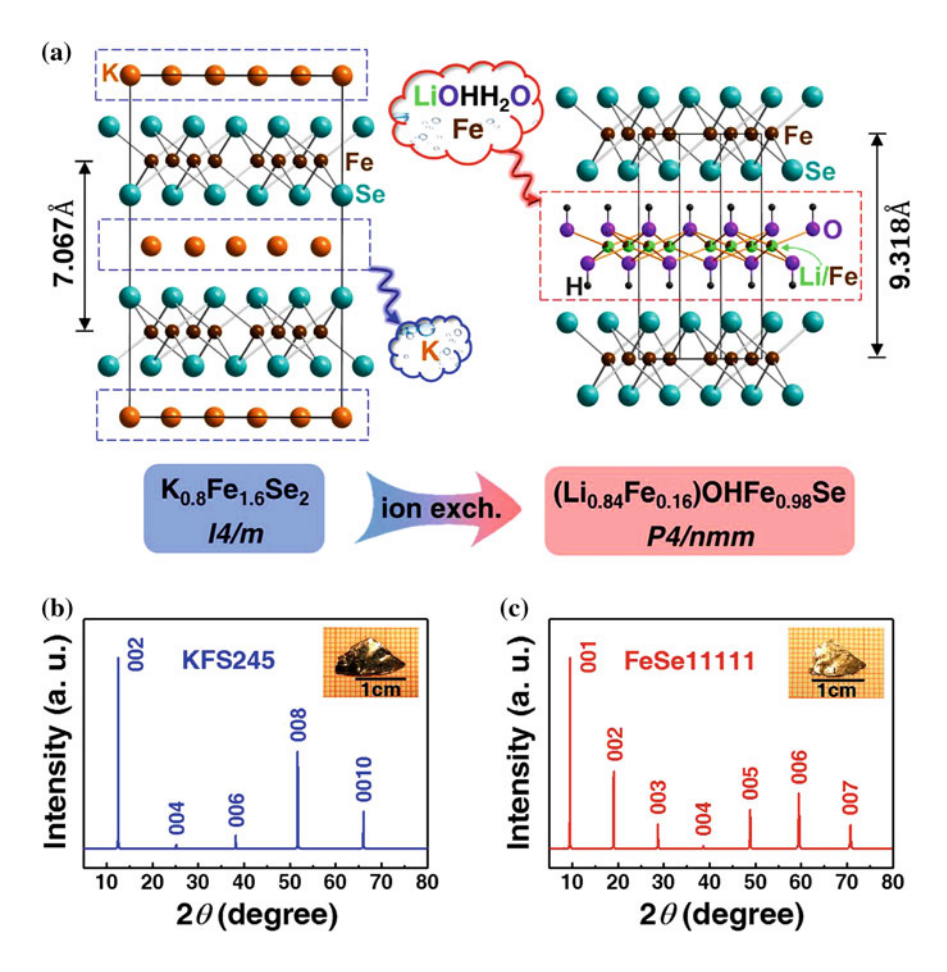


**Fig. 5.34** a A schematic illustration of the hydrothermal ion-cluster exchange reaction using the starting materials of big matrix crystals  $K_{0.8}Fe_{1.6}Se_2$ , LiOHH<sub>2</sub>O, Fe, and CH<sub>4</sub>N<sub>2</sub>Se. For clarity, the H-Se and K-Se bondings in the structures are not shown. **b** and **c** are the (00*l*) type XRD patterns for the precursor crystal  $K_{0.8}Fe_{1.6}Se_2$  and the derived end crystal  $(Li_{0.84}Fe_{0.16})OHFe_{0.98}Se$ , respectively, with l = 2n (n = integer) for the former and without the systematic extinction for the latter. The insets in **b** and **c** are the photographs for the typical precursor and end crystals, respectively. Interestingly, the as-derived  $(Li_{0.84}Fe_{0.16})OHFe_{0.98}Se$  crystal roughly inherits the original shape of its precursor. From [182]

As-synthesized high-quality FeSe11111 crystals are of a size over 10 mm in length and about 0.4 mm in thickness (inset of Fig. 5.34c). The structure refinement, performed by single crystal XRD on the FeSe11111 sample in light of the reported structure model [35, 181], yields the chemical formula of ( $\text{Li}_{0.84}\text{Fe}_{0.16}$ )OHFe<sub>0.98</sub>Se in perfect agreement with the result of ICP-AES. No impurity phases are detectable by powder XRD, and the least-squares refined unit cell dimensions are a = 3.7827(4) Å and c = 9.3184(7) Å for ( $\text{Li}_{0.84}\text{Fe}_{0.16}$ )OHFe<sub>0.98</sub>Se and a = 8.7248(6) Å and

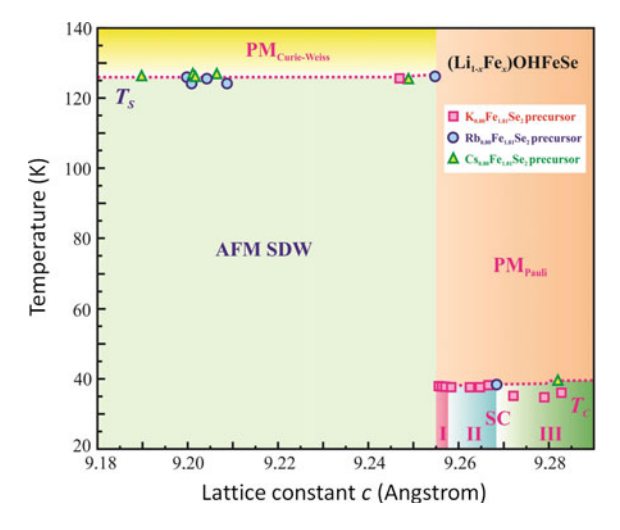


**Fig. 5.35** Phase diagram of  $(\text{Li}_{1-x}\text{Fe}_x)\text{OHFeSe}$  single crystals. The values of Ts and Tc were derived from the  $4\pi\chi$ –T curves [183]

c=14.1339(12) Å for KFS245. While the  $\sqrt{5} \times \sqrt{5}$  ordered vacant Fe sites in the Fe<sub>0.8</sub>Se-layers of K<sub>0.8</sub>Fe<sub>1.6</sub>Se<sub>2</sub> are of  $\sim 20$  % in amount [184], most of them are occupied by Fe introduced during the ionic exchange process, leaving over there only 2 % disordered Fe vacancies in the end crystal (Li<sub>0.84</sub>Fe<sub>0.16</sub>)OHFe<sub>0.98</sub>Se.

Figure 5.36a displays the magnetic susceptibility data for the insulating KFS245 precursor crystal, showing an AFM phase transition at 538 K consistent with the

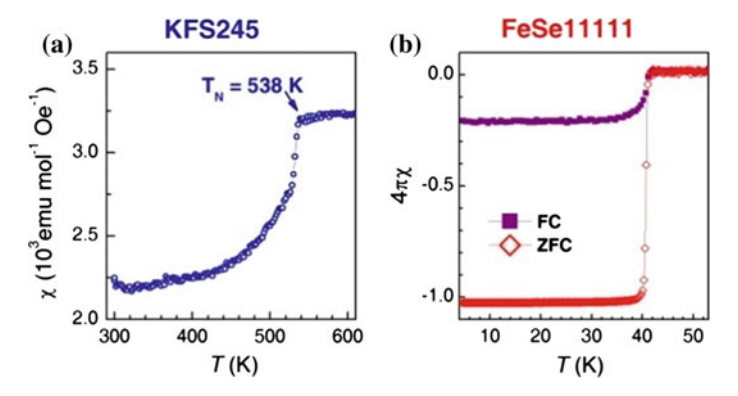
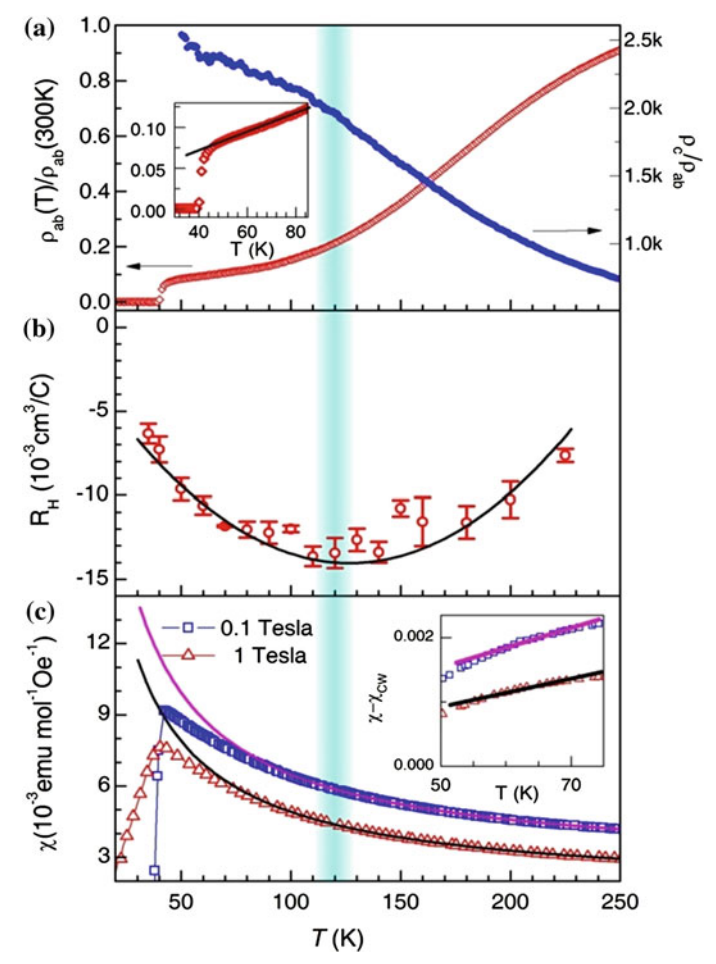


Fig. 5.36 a Temperature dependence of the static magnetic susceptibility for the precursor crystal  $K_{0.8}Fe_{1.6}Se_2$ , showing an AFM transition at 538 K. b The magnetic susceptibilities, corrected for demagnetization factor, under zero-field cooling (ZFC) and field cooling (FC, 1 Oe along the c axis) for ( $Li_{0.84}Fe_{0.16}$ )OHFe $_{0.98}$ Se crystal exhibit a sharp diamagnetic transition at 42 K. The ZFC curve shows a 100 % superconducting shielding and the FC one a Meissner signal up to  $\sim$ 21 %. From [182]

earlier reports [184]. By contrast, the ion-exchange synthesized (Li $_{0.84}$ Fe $_{0.16}$ ) OHFe $_{0.98}$ Se crystal exhibits a bulk superconductivity, as evidenced by its magnetic susceptibilities drop at 42 K (Fig. 5.36b), within a narrow temperature range  $\Delta T \sim 1$  K between 10 and 90 % shielding signals. The sharp diamagnetic transition along with its 100 % diamagnetic shielding demonstrates a high quality of the (Li $_{0.84}$ Fe $_{0.16}$ )OHFe $_{0.98}$ Se crystal

Strong anisotropy in both the superconducting and normal states has been found by electron transport and magnetic studies on (Li<sub>0.84</sub>Fe<sub>0.16</sub>)OHFe<sub>0.98</sub>Se crystal samples. The zero-temperature upper critical field  $H_{c2}$  evaluated from the WHH formula [185] for the field along the c axis (79 T) is merely a quarter of the value for the field along the ab plane (313 T). In the normal state, the ratio of out-of-plane to in-plane electric resistivity,  $\rho_c/\rho_{ab}$ , is found to increase with decreasing temperature and to reach a high value of 2500 at 50 K (Fig. 5.37a). It is clear that, prior to the superconducting transition, the normal state electronic interaction of (Li<sub>0.84</sub>Fe<sub>0.16</sub>)OHFe<sub>0.98</sub>Se is getting highly two dimensional. A common temperature scale  $T^* = 120 \text{ K}$  has been observed, which characterizes the prominent reduction in the slope of the in-plane electric resistivity (Fig. 5.37a), the kink in the ratio  $\rho_c/\rho_{ab}$  (Fig. 5.37a), the dip in the in-plane Hall coefficient (Fig. 5.37b), and the deviation in the static magnetic susceptibility from the Curie-Weiss law (Fig. 5.37c). Below this characteristic  $T^*$ , the two dimensional AFM spin fluctuations in the FeSe layers set in, manifested by the anomalous linear in-plane electric resistivity (inset of Fig. 5.37a) and nearly linear magnetic susceptibility deduced for the FeSe layers (inset of Fig. 5.37c). The negative Hall coefficient (Fig. 5.37b) indicates an electron-dominant charge transport. Its dip feature implies that above  $T^*$  the mobility of holes is reduced with lowering temperature ( $\mu_h < \mu_e$ ) and below  $T^*$  the electron carriers govern the charge transport ( $\mu_h \ll \mu_e$ ) with an enhanced carrier density. Therefore, the prominent slope reduction in the  $\rho_{ab}$ -T curve around T\* is likely related to the additional scattering mechanism brought about by the emergent two-dimensional AFM spin fluctuations and the vanishing mobility of holes below  $T^*$ . It is important to note that a most recent neutron scattering study on large binary FeSe crystal samples strongly suggests a close relation between the spin fluctuations and superconductivity [144], as introduced in Sect. 5.6.1.

The in-plane lattice constants a and b determined as  $\sim 3.78$  Å for (Li<sub>0.84</sub>Fe<sub>0.16</sub>) OHFe<sub>0.98</sub>Se are comparable to the primary bulk FeSe ( $\sim 3.77$  Å) and A<sub>y</sub>Fe<sub>2-x</sub>Se<sub>2</sub> ( $\sim 3.90$  Å) superconductors. In contrast, its FeSe<sub>4</sub>-tetrahedron layers weakly bonded to the (Li/Fe)OH layers via hydrogen ions have a larger interlayer spacing ( $\sim 9.32$  Å) compared to the bulk FeSe ( $\sim 5.52$  Å) and A<sub>y</sub>Fe<sub>2-x</sub>Se<sub>2</sub> ( $\sim 7.02$  Å) superconductors. Consequently, (Li<sub>0.84</sub>Fe<sub>0.16</sub>)OHFe<sub>0.98</sub>Se exhibits an enhanced two dimensionality of the electronic structure and a higher superconducting transition temperature (42 K) than bulk FeSe ( $\sim 8$  K) and A<sub>y</sub>Fe<sub>2-x</sub>Se<sub>2</sub> ( $\sim 30$  K). In particular, (Li<sub>0.84</sub>Fe<sub>0.16</sub>)OHFe<sub>0.98</sub>Se system is closely analogous to the strictly tow-dimensional interface superconductor of single unit-cell FeSe film on SrTiO<sub>3</sub> substrate, which shows a  $T_c$  above 65 K. The two-dimensional electron-electron interaction is crucial to the electron pairing of superconductivity, as commonly believed in optimal iron arsenide [186–188] and copper-oxide high- $T_c$ 



**Fig. 5.37** The electric resistivity, Hall coefficient, and magnetic susceptibility of  $(\text{Li}_{0.84}\text{Fe}_{0.16})$  OHFe<sub>0.98</sub>Se crystal, showing a common characteristic temperature  $T^*=120~\text{K}$ . **a** The in-plane electric resistivity and the ratio of the out-of-plane resistivity to the in-plane one as functions of temperature. The inset shows the linearly temperature dependent range from 80 K down to  $T_c$  for  $\rho_{ab}$ . **b** The in-plane Hall coefficient  $R_H$  as a function of temperature exhibits a dip feature. The black curve is a guide to the eye. **c** The temperature dependencies of magnetic susceptibility  $\chi = M/H$  under fields along the c axis. The results slightly depend on the magnitude of the field. The sudden drops in the magnetic susceptibility are due to the appearance of the superconductivity. At higher temperatures, all the data can be fitted to a modified Curie-Weiss law  $\chi_m = \chi_0 + \chi_{CW}$ . But a deviation is clearly visible below  $T^* = 120~\text{K}$ . Further lowering temperature, the rest magnetic susceptibility in which the Curie-Weiss term is subtracted shows the nearly linear temperature dependence (the inset). From [182]

superconductors [189–191], as well as in heavy fermion [192, 193] and organic superconductors [194]. Hence the  $(Li_{0.84}Fe_{0.16})OHFe_{0.98}Se$  superconductor falls under the same universality class.

### 5.9.3 Recent Results by ARPES and STS

So far the majority of iron-based superconductors show common electronic structure with hole-like bands near the Brillouin zone center ( $\Gamma$  point) and electron-like bands near the Brillouin zone corners (M point). The superconducting A<sub>y</sub>Fe<sub>2-y</sub>Se<sub>2</sub> compounds and single-layer FeSe film on SrTiO3 substrate are the only two exceptions before the appearance of (Li<sub>1-x</sub>Fe<sub>x</sub>)OHFe<sub>1-y</sub>Se system. It has recently been found by high-resolution ARPES measurements [195] that the (Li<sub>0.84</sub>Fe<sub>0.16</sub>) OHFe<sub>0.98</sub>Se superconductor exhibits electronic behaviors closely analogous to the superconducting single-layer FeSe/SrTiO<sub>3</sub> film, in terms of the Fermi surface topology, band structure and nearly isotropic superconducting gap without nodes. The measured Fermi surface for (Li<sub>0.84</sub>Fe<sub>0.16</sub>)OHFe<sub>0.98</sub>Se contains only a nearly circular electron-like Fermi surface around M points but shows no indication of Fermi crossing around the  $\Gamma$  (0, 0) point (Fig. 5.38d), very similar to that found in the superconducting single-layer FeSe/SrTiO<sub>3</sub> film (Fig. 5.38e). Similar ARPES results have been observed on a (Li<sub>0.8</sub>Fe<sub>0.2</sub>)OHFeSe crystal sample [196]. These observations are of important implications for the iron-based family, because (Li<sub>0.84</sub>Fe<sub>0.16</sub>)OHFe<sub>0.98</sub>Se is a single-phased bulk high-T<sub>c</sub> superconductor, free from the complications of phase separation and interface effect otherwise present in superconducting bulk A<sub>x</sub>Fe<sub>2-v</sub>Se<sub>2</sub> and single-layer FeSe/SrTiO<sub>3</sub> film.

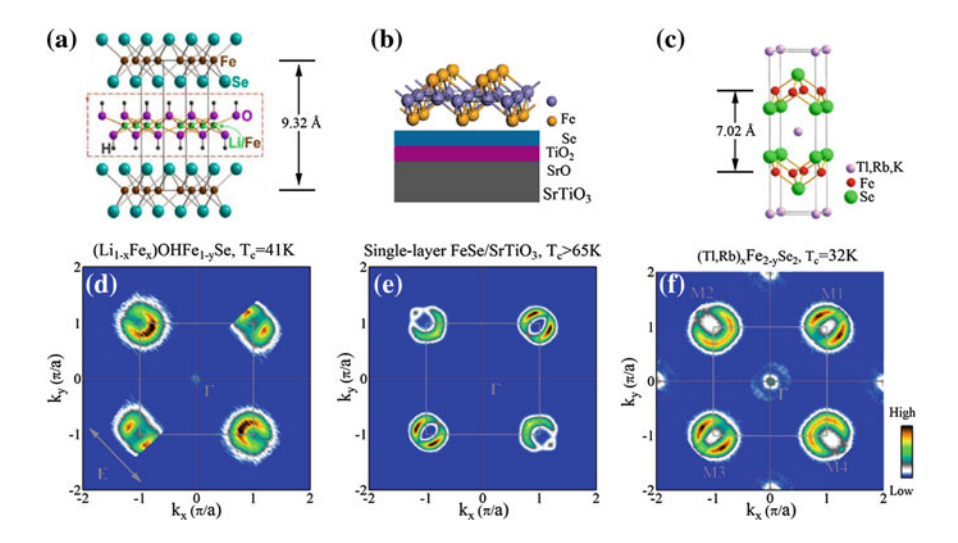


**Fig. 5.38** Fermi surface comparison between (Li<sub>0.84</sub>Fe<sub>0.16</sub>)OHFe<sub>0.98</sub>Se, single-layer FeSe/SrTiO<sub>3</sub> film and (Tl,Rb)<sub>x</sub>Fe<sub>2-y</sub>Se<sub>2</sub> superconductors. **a** The crystal structure of (Li<sub>0.84</sub>Fe<sub>0.16</sub>)OHFe<sub>0.98</sub>Se. **b** Schematic structure of single-layer FeSe/SrTiO<sub>3</sub> film **c** Schematic structure of (Tl,Rb)<sub>x</sub>Fe<sub>2-y</sub>Se<sub>2</sub>. **d** Fermi surface mapping of (Li<sub>0.84</sub>Fe<sub>0.16</sub>)OHFe<sub>0.98</sub>Se measured at 20 K. **e**, **f** Fermi surfaces of a superconducting single-layer FeSe/SrTiO<sub>3</sub> film and (Tl,Rb)<sub>x</sub>Fe<sub>2?y</sub>Se<sub>2</sub>, respectively. From [195]

On the other hand, a recent STS (scanning tunneling spectroscopy) study [197] on (Li<sub>1-x</sub>Fe<sub>x</sub>OH)FeSe crystal samples indicates the presence of double nodeless superconducting gaps, each showing a significant anisotropy with a maximum magnitude of  $\Delta_1 \sim 14.3$  meV and  $\Delta_2 \sim 8.6$  meV, respectively. This two-gap feature is reminiscent of that reported for the monolayer FeSe film on SrTiO<sub>3</sub> substrate.

#### 5.10 Conclusion

Iron-based superconductors have been studied extensively for both theoretical and practical reasons. The progress on single crystal growth has brought many important achievements, which help to develop our physical understanding and bring their applications closer. Many important superconducting properties are still a mystery, however, and require further thorough investigation. Further experimental studies performed on higher quality single crystals are still desperately needed.

This chapter reviews the single crystal growth of iron-based superconductors and the most recent developments in this family of materials, especially the large size single crystal growth. The effects of crystal defects and post-treatments on the physical properties are described.

Large single crystals can be grown by using the flux, Bridgman or floating zone methods for most compounds except the 21311 type. Crystal growth study to enhance the size and the compositional homogeneity remains much work to be done in the future.

#### References

- 1. Y. Kamihara, T. Watanabe, M. Hirano, H. Hosono, J. Am. Chem. Soc. 130, 3296 (2008)
- H. Takahashi, K. Igawa, K. Arii, Y. Kamihara, M. Hirano, H. Hosono, Nature 453, 376 (2008)
- 3. X.H. Chen, T. Wu, G. Wu, R.H. Liu, H. Chen, D.F. Fang, Nature 453, 761 (2008)
- 4. H. Kito, H. Eisaki, A. Iyo, J. Phys. Soc. Jpn. 77, 063707 (2008)
- Z.A. Ren, W. Lu, J. Yang, W. Yi, X.L. Shen, Z.C. Li, G.C. Che, X.L. Dong, L.L. Sun, F. Zhou, Z.X. Zhao, Chin. Phys. Lett. 25, 2215 (2008)
- 6. I.I. Mazin, Nature 464, 183 (2010)
- X.C. Wang, Q.Q. Liu, Y.X. Lv, W.B. Gao, L.X. Yang, R.C. Yu, F.Y. Li, C.Q. Jin, Solid State Commun. 148, 538 (2008)
- 8. J.H. Tapp, Z.J. Tang, B. Lv, K. Sasmal, B. Lorenz, P.C.W. Chu, A.M. Guloy, Phys. Rev. B 78, 060505(R) (2008)
- 9. M. Mito, M.J. Pitcher, W. Crichton, G. Garbarino, P.J. Baker, S.J. Blundell, P. Adamson, D. R. Parker, S.J. Clarke, J. Am. Chem. Soc. 131, 2986 (2009)
- 10. J.T. Park et al., Phys. Rev. B 86, 024437 (2012)

- E.P. Rosenthal, E.F. Andrade, C.J. Arguello, R.M. Fernandes, L.Y. Xing, X.C. Wang, C.Q. Jin, A.J. Millis, A.N. Pasupathy, Nat. Phys. 10, 225 (2014)
- 12. T. Park, E. Park, H. Lee, T. Klimczuk, E.D. Bauer, F. Ronning, J.D. Thompson, J. Phys.: Condens. Matter 20, 322204 (2008)
- G. Wu, H. Chen, T. Wu, Y.L. Xie, Y.J. Yan, R.H. Liu, X.H. Chen, J. Phys.: Condens. Matter 20, 422201 (2008)
- M. Tegel, M. Rotter, V. Weiß, F.M. Schappacher, R. Pöttgen, D. Johrendt, J. Phys.: Condens. Matter 20, 452201 (2008)
- P.L. Alireza, Y.T Ko J. Gillett, C.M. Petrone, J.M. Cole, S.E. Sebastian, G.G. Lonzarich, arXiv preprint arXiv 080.1896 (2008)
- 16. V.B. Zabolotnyy et al., Nature **457**, 569 (2009)
- S. Lee, J. Jiang, Y. Zhang, C.W. Bark, J.D. Weiss, C. Tarantini, C.B. Eom, Nat. Mater. 9, 397 (2010)
- D.S. Inosov, J.T. Park, P. Bourges, D.L. Sun, Y. Sidis, A. Schneidewind, K. Hradil, D. Haug, C.T. Lin, B. Keimer, V. Hinkov, Nat. Phys. 6, 178 (2010)
- J.G. Guo, S.F. Jin, G. Wang, S.C. Wang, K.X. Zhu, T.T. Zhou, M. He, X.L. Chen, Phys. Rev. B 82, 180520(R) (2010)
- A.F. Wang, J.J. Ying, Y.J. Yan, R.H. Liu, X.G. Luo, Z.Y. Li, X.H. Chen, Phys. Rev. B 83, 060512 (2011)
- F. Ye, S. Chi, W. Bao, X.F. Wang, J.J. Ying, X.H. Chen, M. Fang, Phys. Rev. Lett. 107, 137003 (2011)
- A. Krzton-Maziopa, Z. Shermadini, E. Pomjakushina, V. Pomjakushin, M. Bendele, A. Amato, K. Conder, J. Phys.: Condens. Matter 23, 052203 (2011)
- Y. Liu, Z.C. Li, W.P. Liu, G. Friemel, D.S. Inosov, R.E. Dinnebier, C.T. Lin, Supercond. Sci. Technol. 25, 075001 (2012)
- G. Friemel, W.P. Liu, E.A. Goremychkin, Y. Liu, J.T. Park, O. Sobolev, D.S. Inosov, EPL 99, 67004 (2012)
- 25. F.C. Hsu et al., Proc. Natl. Acad. Sci. U.S.A. 105, 14262 (2008)
- 26. K.-W. Yeh et al., EPL **84**, 37002 (2008)
- Y. Mizuguchi, F. Tomioka, S. Tsuda, T. Yamaguchi, Y. Takano, Appl. Phys. Lett. 94, 012503 (2009)
- 28. Y. Liu, R.K. Kremer, C.T. Lin, Supercond. Sci. Technol. 24, 035012 (2011)
- 29. S. He, J. He, W. Zhang, L. Zhao, D. Liu, X. Liu, X.J. Zhou, Nat. Mater. 12, 605 (2013)
- H. Ogino, Y. Matsumura, Y. Katsura, K. Ushiyama, S. Horii, K. Kishio, J.I. Shimoyama, Supercond. Sci. Technol. 22, 075008 (2009)
- H. Ogino, K. Machida, A. Yamamoto, K. Kishio, J.I. Shimoyama, T. Tohei, Y. Ikuhara, Supercond. Sci. Technol. 23, 115005 (2010)
- T. Nakano, N. Fujiwara, S. Tsutsumi, H. Ogino, K. Kishio, J. Shimoyama, Phys. Rev. B 84, 060502 (2011)
- Q.P. Ding, Y. Tsuchiya, S. Mohan, T. Taen, Y. Nakajima, T. Tamegai, Phys. Rev. B 85, 104512 (2012)
- Y. Tomita, H. Kotegawa, Y. Tao, H. Tou, H. Ogino, S. Horii, J. Shimoyama, Phys. Rev. B 86, 134527 (2012)
- X.F. Lu, N.Z. Wang, H. Wu, Y.P. Wu, D. Zhao, X.Z. Zeng, X.G. Luo, T. Wu, W. Bao, G.H. Zhang, F.Q. Huang, Q.Z. Huang, X.H. Chen, Nat. Mater. 14, 325 (2014)
- X. Dong, H. Zhou, H. Yang, J. Yuan, K. Jin, F. Zhou, D. Yuan, L. Wei, J. Li, X. Wang, G. Zhang, Z. Zhao, J. Am. Chem. Soc. 137, 66 (2015)
- 37. M. Rotter, M. Tegel, D. Johrendt, Phys. Rev. Lett. **101**, 107006 (2008)
- 38. M. Rotter, M. Pangerl, M. Tegel, D. Johrendt, Angew. Chem. Int. Ed. 47, 7949 (2008)
- A.S. Sefat, R. Jin, M.A. McGuire, B.C. Sales, D.J. Singh, D. Mandrus, Phys. Rev. Lett. 101, 117004 (2008)
- 40. A. Leithe-Jasper, W. Schnelle, C. Geibel, H. Rosner, Phys. Rev. Lett. 101, 207004 (2008)
- 41. L.J. Li, Y.K. Luo, Q.B. Wang, H. Chen, Z. Ren, Q. Tao, Z.A. Xu, New J. Phys. 11, 025008 (2009)

References 187

 S. Jiang, H. Xing, G. Xuan, C. Wang, Z. Ren, C. Feng, G. Cao, J. Phys.: Condens. Matter 21, 382203 (2009)

- 43. P.L. Alireza, Y.T. Ko, J. Gillett, C.M. Petrone, J.M. Cole, S.E. Sebastian, G.G. Lonzarich, arXiv preprint arXiv:0807.1896 (2008)
- 44. S.A. Kimber, A. Kreyssig, Y.Z. Zhang, H.O. Jeschke, R. Valentí, F. Yokaichiya, D.N. Argyriou, Nat. Mater. 8, 471 (2009)
- N. Ni, S.L. Bud?ko, A. Kreyssig, S. Nandi, G.E. Rustan, A.I. Goldman, P.C. Canfield, Phys. Rev. B 78, 014507 (2008)
- G.L. Sun, D.L. Sun, M. Konuma, P. Popovich, A. Boris, J.B. Peng, K.Y. Choi, P. Lemmens, C.T. Lin, arXiv:0901.2728 (2009)
- H. Luo, Z. Wang, H. Yang, P. Cheng, X. Zhu, H.H. Wen, Supercond. Sci. Technol. 21, 125014 (2008)
- 48. G.F. Chen, Z. Li, J. Dong, G. Li, W.Z. Hu, X.D. Zhang, J.L. Luo, Phys. Rev. B **78**, 224512 (2008)
- X.F. Wang, T. Wu, G. Wu, H. Chen, Y.L. Xie, J.J. Ying, X.H. Chen, Phys. Rev. Lett. 102, 117005 (2009)
- R. Prozorov, N. Ni, M.A. Tanatar, V.G. Kogan, R.T. Gordon, C. Martin, P.C. Canfield, Phys. Rev. B 78, 224506 (2008)
- 51. G.R. Stewart, Rev. Mod. Phys. 83, 1589 (2011)
- 52. D.L. Sun, Y. Liu, J.T. Park, C.T. Lin, Supercond. Sci. Technol. 22, 105006 (2009)
- 53. Y. Liu, D.L. Sun, J.T. Park, C.T. Lin, Physica C 470, S513 (2010)
- 54. D.L. Sun, J.Z. Xiao, C.T. Lin, J. Cryst. Growth 321, 55 (2011)
- G.L. Sun, D.L. Sun, M. Konuma, P. Popovich, A. Boris, J.B. Peng, K.-Y. Choi, P. Lemmens, C.T. Lin, J. Supercond. Nov. Magn. 24, 1773 (2011)
- 56. D.P. Chen, C.T. Lin, Supercond. Sci. Technol. 27(10), 103002 (2014)
- M. Rotter, M. Tegel, D. Johrendt, I. Schellenberg, W. Hermes, R. Pöttgen, Phys. Rev. B 78, 020503 (2008)
- J.Q. Yan, A. Kreyssig, S. Nandi, N. Ni, S.L. Budko, A. Kracher, P.C. Canfield, Phys. Rev. B 78, 024516 (2008)
- 59. M. Tegel, M. Rotter, V. Weiß, F.M. Schappacher, R. Pöttgen, D. Johrendt, J. Phys.: Condens. Matter 20, 452201 (2008)
- Q. Huang, Y. Qiu, W. Bao, M.A. Green, J.W. Lynn, Y.C. Gasparovic, X.H. Chen, Phys. Rev. Lett. 101, 257003 (2008)
- Y. Su, P. Link, A. Schneidewind, T. Wolf, P. Adelmann, Y. Xiao, M. Loewenhaupt, Phys. Rev. B 79, 064504 (2009)
- K. Sasmal, B. Lv, B. Lorenz, A.M. Guloy, F. Chen, Y.Y. Xue, C.W. Chu, Phys. Rev. Lett. 101, 107007 (2008)
- Y. Zhang, J. Wei, H.W. Ou, J.F. Zhao, B. Zhou, F. Chen, D.L. Feng, Phys. Rev. Lett. 102, 127003 (2009)
- Z. Bukowski, S. Weyeneth, R. Puzniak, P. Moll, S. Katrych, N.D. Zhigadlo, B. Batlogg, Phys. Rev. B 79, 104521 (2009)
- 65. D.C. Johnston, Adv. Phys. 59, 803 (2010)
- 66. W.K. Yeoh et al., Phys. Rev. Lett. 106, 247002 (2011)
- 67. M.H. Julien, H. Mayaffre, M. Horvati?, C. Berthier, X.D. Zhang, W. Wu, G.F. Chen, N.L. Wang, J.L. Luo, EPL 87, 37001 (2009)
- 68. J.T. Park et al., Phys. Rev. Lett. **102**, 117006 (2009)
- S.H. Baek, H. Lee, S.E. Brown, N.J. Curro, E.D. Bauer, F. Ronning, T. Park, J.D. Thompson, Phys. Rev. Lett. 102, 227601 (2009)
- R.R. Urbano, E.L. Green, W.G. Moulton, A.P. Reyes, P.L. Kuhns, E.M. Bittar, C. Adriano, T.M. Garitezi, L. Bufaiçal, P.G. Pagliuso, Phys. Rev. Lett. 105, 107001 (2010)
- E. Wiesenmayer, H. Luetkens, G. Pascua, R. Khasanov, A. Amato, H. Potts, B. Banusch, H.-H. Klauss, D. Johrendt, Phys. Rev. Lett. 107, 237001 (2011)
- 72. S. Avci et al., Phys. Rev. B 83, 172503 (2011)

- Y. Laplace, J. Bobroff, F. Rullier-Albenque, D. Colson, A. Forget, Phys. Rev. B 80, 140501 (2009)
- T. Iye, Y. Nakai, S. Kitagawa, K. Ishida, S. Kasahara, T. Shibauchi, Y. Matsuda, T. Terashima, J. Phys. Soc. Jpn. 81, 033701 (2012)
- S. Sanna, R. De Renzi, G. Lamura, C. Ferdeghini, A. Palenzona, M. Putti, M. Tropeano, T. Shiroka, Phys. Rev. B 80, 052503 (2009)
- D.S. Inosov, A. Leineweber, X. Yang, J.T. Park, N.B. Christensen, R. Dinnebier, J. Stahn, Phys. Rev. B, 79(22), 224503 (2009)
- Z. Li, R. Zhou, Y. Liu, D.L. Sun, J. Yang, C.T. Lin, G.Q. Zheng, Phys. Rev. B 86, 180501 (2012)
- 78. D.S. Inosov et al., Phys. Rev. B 81, 014513 (2010)
- 79. J.T. Park et al., Phys. Rev. B 82, 134503 (2010)
- 80. V.A. Gasparov, L. Drigo, A. Audouard, D.L. Sun, C.T. Lin, S.L. Bud?ko, P.C. Canfield, F. Wolff-Fabris, J. Wosnitz, JETP Lett. 93, 667 (2011)
- N. Ni, M.E. Tillman, J.Q. Yan, A. Kracher, S.T. Hannahs, S.L. Budko, P.C. Canfield, Phys. Rev. B 78, 214515 (2008)
- 82. S.R. Saha, N.P. Butch, K. Kirshenbaum J. Paglione, Physica C 470, S379 (2010)
- 83. P. Popovich, A.V. Boris, O.V. Dolgov, A.A. Golubov, D.L. Sun, C.T. Lin, R.K. Kremer, B. Keimer, Phys. Rev. Lett. **105**, 027003 (2010)
- 84. A.S. Sefat, D.J. Singh, L.H. VanBebber, Y. Mozharivskyj, M.A. McGuire, R. Jin, B.C. Sales, V. Keppens, D. Mandrus, Phys. Rev. B **79**, 224524 (2009)
- 85. J.P. Clancy, B.D. Gaulin, A.S. Sefat, Phys. Rev. B 85, 054115 (2012)
- 86. D.S. Inosov et al., Phys. Rev. B 87, 224425 (2013)
- J.S. Kim, S. Khim, H.J. Kim, M.J. Eom, J.M. Law, R.K. Kremer, J.H. Shim, K.H. Kim, Phys. Rev. B 82, 024510 (2010)
- 88. R.E. Baumbach, J.J. Hamlin, L. Shu, D.A. Zocco, N.M. Crisosto, M.B. Maple, New J. Phys. 11, 025018 (2009)
- 89. S. Kasahara et al., Nature 486, 382 (2012)
- 90. K. Hashimoto et al., Science **336**, 1554 (2012)
- 91. S. Kasahara et al., Phys. Rev. B 81, 184519 (2010)
- 92. K. Hashimoto et al., Phys. Rev. B 81, 220501 (2010)
- J.G. Analytis, J.H. Chu, R.D. McDonald, S.C. Riggs, I.R. Fisher, Phys. Rev. Lett. 105, 207004 (2010)
- C. Chaparro, L. Fang, H. Claus, A. Rydh, G.W. Crabtree, V. Stanev, W.K. Kwok, U. Welp, Phys. Rev. B 85, 184525 (2012)
- M. Nakajima, S.I. Uchida, K. Kihou, C.H. Lee, A. Iyo, H. Eisaki, J. Phys. Soc. Jpn. 81, 104710 (2012)
- 96. M. Nakajima et al., Proc. Natl. Acad. Sci. U.S.A. 108, 12238 (2011)
- 97. S. Ishida et al., Phys. Rev. B 84, 184514 (2011)
- M.H. Fang, H.D. Wang, C.H. Dong, Z.J. Li, C.M. Feng, J. Chen, H.Q. Yuan, EPL 94, 27009 (2011)
- H.D. Wang, C.H. Dong, Z.J. Li, S.S. Zhu, Q.H. Mao, C.M. Feng, H.Q. Yuan, M.H. Fang, EPL 93, 47004 (2011)
- 100. Z. Wang, Y.J. Song, H.L. Shi, Z.W. Wang, Z. Chen, H.F. Tian, G.F. Chen, J.G. Guo, H.X. Yang, J.Q. Li, Phys. Rev. B 83, 140505 (2011)
- 101. A.M. Zhang, T.L. Xia, K. Liu, W. Tong, Z.R. Yang, Q.M. Zhang, Sci. Rep. 3, 1216 (2013)
- 102. M. Yi et al., Phys. Rev. Lett. 110, 067003 (2013)
- 103. V.A. Gasparov et al., Phys. Rev. B 87, 094508 (2013)
- 104. J. Ge, J. Gutierrez, M. Li, J. Zhang, V.V. Moshchalkov, Appl. Phys. Lett. 103, 052602 (2013)
- 105. D. Chi-Heng, W. Hang-Dong, F. Ming-Hu, Chin. Phys. B 22, 087401 (2013)
- 106. H.H. Wen, Rep. Prog. Phys. 75, 112501 (2012)
- 107. E. Dagotto, Rev. Mod. Phys. 85, 849 (2013)

References 189

108. Y. Mizuguchi, H. Takeya, Y. Kawasaki, T. Ozaki, S. Tsuda, T. Yamaguchi, Y. Takano, Appl. Phys. Lett. 98, 042511 (2011)

- 109. Y.J. Yan, M. Zhang, A.F. Wang, J.J. Ying, Z.Y. Li, W. Qin, X.G. Luo, J.Q. Li, J. Hu, X.H. Chen, Sci. Rep. 2, 212 (2012)
- 110. F. Peng, W.P. Liu, C.T. Lin, J. Supercond. Nov. Magn. 26, 1205 (2013)
- M.T. Li, L. Chen, Z.W. Li, G.H. Ryu, C.T. Lin, J.C. Zhang, J. Phys.: Condens. Matter 25, 335701 (2013)
- 112. J.J. Ying et al., Phys. Rev. B 83, 212502 (2011)
- V. Tsurkan, J. Deisenhofer, A. Günther, H.A.K. von Nidda, S. Widmann, A. Loidl, Phys. Rev. B 84, 144520 (2011)
- 114. Y. Liu, Q. Xing, K.W. Dennis, R.W. McCallum, T.A. Lograsso, Phys. Rev. B 86, 144507 (2012)
- 115. D.M. Wang, J.B. He, T.L. Xia, G.F. Chen, Phys. Rev. B 83, 132502 (2011)
- 116. X.G. Luo et al., New J. Phys. 13, 053011 (2011)
- 117. F. Chen et al., Phys. Rev. X 1, 021020 (2011)
- 118. W. Li et al., Nat. Phys. 8, 126 (2011)
- 119. Y. Zhang et al., Nat. Mater. 10, 273 (2011)
- 120. A. Ricci et al., Phys. Rev. B 84, 060511 (2011)
- 121. A. Charnukha et al., Phys. Rev. Lett. 109, 017003 (2012)
- 122. S.C. Speller, T.B. Britton, G.M. Hughes, A. Krzton-Maziopa, E. Pomjakushina, K. Conder, A.T. Boothroyd, C.R.M. Grovenor, Supercond. Sci. Technol. 25, 084023 (2012)
- X. Ding, D. Fang, Z. Wang, H. Yang, J. Liu, Q. Deng, G. Ma, C. Meng, Y. Hu, H.H. Wen, Nat. Commun. 4, 1897 (2013)
- 124. T.M. McQueen, Q. Huang, V. Ksenofontov, C. Felser, Q. Xu, H. Zandbergen, Y.S. Hor, J. Allred, A.J. Williams, D. Qu, J. Checkelsky, N.P. Ong, R.J. Cava, Phys. Rev. B 79, 014522 (2009)
- 125. Y. Kuo-Wei, H. Tzu-Wen, H. Yi-lin, C. Ta-Kun, H. Fong-Chi, M.W. Phillip, L. Yong-Chi, C. Yan-Yi, C. Chi-Lian, L. Jiu-Yong, Y. Der-Chung, W. Maw-Kuen, EPL 84, 37002 (2008)
- 126. M.H. Fang, H.M. Pham, B. Qian, T.J. Liu, E.K. Vehstedt, Y. Liu, L. Spinu, Z.Q. Mao, Phys. Rev. B 78, 224503 (2008)
- K.W. Yeh, H.C. Hsu, T.W. Huang, P.M. Wu, Y.L. Huang, T.K. Chen, J.Y. Luo, M.K. Wu,
   J. Phys. Soc. Jpn. 77, 19 (2008)
- 128. S. Medvedev, T.M. McQueen, I.A. Troyan, T. Palasyuk, M.I. Eremets, R.J. Cava, S. Naghavi, F. Casper, V. Ksenofontov, G. Wortmann, C. Felser, Nat. Mater. 8, 630 (2009)
- 129. Q.Y. Wang, Z. Li, W.H. Zhang, Z.C. Zhang, J.S. Zhang, W. Li, H. Ding, Y.B. Ou, P. Deng, K. Chang, J. Wen, C.L. Song, K. He, J.F. Jia, S.H. Ji, Y.Y. Wang, L.L. Wang, X. Chen, X.C. Ma, Q.K. Xue, Chinese. Phys. Lett. 29, 037402 (2012)
- 130. D.F. Liu, W.H. Zhang, D.X. Mou, J.F. He, Y.B. Ou, Q.Y. Wang, Z. Li, L.L. Wang, L. Zhao, S.L. He, Y.Y. Peng, X. Liu, C.Y. Chen, L. Yu, G.D. Liu, X.L. Dong, J. Zhang, C.T. Chen, Z. Y. Xu, J.P. Hu, X. Chen, X.C. Ma, Q.K. Xue, X.J. Zhou, Nat. Commun. 3, 931 (2012)
- 131. S.Y. Tan, Y. Zhang, M. Xia, Z.R. Ye, F. Chen, X. Xie, R. Peng, D.F. Xu, Q. Fan, H.C. Xu, J. Jiang, T. Zhang, X.C. Lai, T. Xiang, J.P. Hu, B.P. Xie, D.L. Feng, Nat. Mater. 12, 634 (2013)
- 132. H. Okamoto, J. Phase Equilib. 12, 383 (1991)
- S.B. Zhang, Y.P. Sun, X.D. Zhu, X.B. Zhu, B.S. Wang, G. Li, H.C. Lei, X. Luo, Z.R. Yang,
   W.H. Song, J.M. Dai, Supercond. Sci. Technol. 22, 015020 (2009)
- 134. S.B. Zhang, X.D. Zhu, H.C. Lei, G. Li, B.S. Wang, L.J. Li, X.B. Zhu, Z.R. Yang, W.H. Song, J.M. Dai, Y.P. Sun, Supercond. Sci. Tech. 22, 075016 (2009)
- D. Chareev, E. Osadchii, T. Kuzmicheva, J.Y. Lin, S. Kuzmichev, O. Volkova, A. Vasiliev, CrystEngComm 15, 1989 (2013)
- B.H. Mok, S.M. Rao, M.C. Ling, K.J. Wang, C.T. Ke, P.M. Wu, C.L. Chen, F.C. Hsu, T.W. Huang, J.Y. Luo, D.C. Yan, K.W. Ye, T.B. Wu, A.M. Chang, M.K. Wu, Cryst. Growth Des. 9, 3260 (2009)

- 137. S.M. Rao, B.H. Mok, M.C. Ling, C.T. Ke, T.C. Chen, I.M. Tsai, Y.L. Lin, H.L. Liu, C.L. Chen, F.C. Hsu, T.W. Huang, T.B. Wu, M.K. Wu, J. Appl. Phys. **110**, 113919 (2011)
- J.I. Gorina, G.A. Kaluzhnaya, M.V. Golubkov, V.V. Rodin, N.N. Sentjurina, S.G. Chernook, Crystallogr. Rep. 57, 585 (2012)
- 139. M.W. Ma, D.N. Yuan, Y. Wu, X.L. Dong, F. Zhou, Phys. C 506, 154 (2014)
- 140. R.W. Hu, H.C. Lei, M. Abeykoon, E.S. Bozin, S.J.L. Billinge, J.B. Warren, T. Siegrist, C. Petrovic, Phys. Rev. B 83, 224502 (2011)
- 141. U. Patel, J. Hua, S.H. Yu, S. Avci, Z.L. Xiao, H. Claus, J. Schlueter, V.V. Vlasko-Vlasov, U. Welp, W.K. Kwok, Appl. Phys. Lett. 94, 082508 (2009)
- 142. C. Koz, M. Schmidt, H. Borrmann, U. Burkhardt, S. Rö?ler, W. Carrillo-Cabrera, W. Schnelle, U. Schwarz, Y. Grin, Z. Anorg, Allg. Chem. **640**, 1600 (2014)
- M. Ma, D. Yuan, Y. Wu, H. Zhou, X. Dong, F. Zhou, Supercond. Sci. Technol. 27, 122001 (2014)
- 144. Q. Wang, Y. Shen, B. Pan, Y. Hao, M. Ma, F. Zhou, P. Steens, K. Schmalzl, T.R. Forrest, M. Abdel-Hafiez, X. Chen, D.A. Chareev, A.N. Vasiliev, P. Bourges, Y. Sidis, H. Cao, J. Zhao, Nat. Mater. 15, 159 (2016)
- B.C. Sales, A.S. Sefat, M.A. McGuire, R.Y. Jin, D. Mandrus, Y. Mozharivskyj, Phys. Rev. B 79, 094521 (2009)
- 146. K.W. Yeh, C.T. Ke, T.W. Huang, T.K. Chen, Y.L. Huang, P.M. Wu, M.K. Wu, Cryst. Growth Des. 9, 4847 (2009)
- 147. Y. Liu, C.T. Lin, J. Supercond. Nov. Magn. 24, 183 (2011)
- 148. R. Khasanov et al., Phys. Rev. B 80, 140511(R) (2009)
- 149. T.J. Liu et al., Nat. Mater. 9, 718 (2010)
- 150. P.L. Paulose, C.S. Yadav, K.M. Subhedar, EPL 90, 27011 (2010)
- 151. K. Katayama et al., J. Phys. Soc. Jpn. 79, 113702 (2010)
- 152. M.J. Pitcher, D.R. Parker, P. Adamson, S.J.C. Herkelrath, A.T. Boothroyd, R.M. Ibberson, M. Brunelli, S.J. Clarke, Structure and superconductivity of LiFeAs. Chem. Commun. 45, 5918 (2008)
- 153. C.W. Chu, F. Chen, M. Gooch, A.M. Guloy, B. Lorenz, B. Lv, K. Sasmal, Z.J. Tang, J.H. Tapp, Y.Y. Xue, The synthesis and characterization of LiFeAs and NaFeAs. Phys. C 469, 326 (2009)
- 154. G.F. Chen, W.Z. Hu, J.L. Luo, N.L. Wang, Phys. Rev. Lett. 102, 227004 (2009)
- Y.J. Song, J.S. Ghim, B.H. Min, Y.S. Kwon, M.H. Jung, J.S. Rhyee, Appl. Phys. Lett. 96, 212508 (2010)
- 156. S.V. Borisenko et al., Phys. Rev. Lett. 105, 067002 (2010)
- 157. B. Lee et al., Single-crystal growth and superconducting properties of LiFeAs. EPL (Europhysics Letters) 91(6), 67002 (2010)
- 158. Y. Kamihara, H. Hiramatsu, M. Hirano, R. Kawamura, H. Yanagi, T. Kamiya, H. Hosono, J. Am. Chem. Soc. 128, 10012 (2006)
- 159. Z.A. Ren et al., Europhys. Lett. **83**, 17002 (2008)
- K. Miyazawa, K. Kihou, P.M. Shirage, C.H. Lee, H. Kito, H. Eisaki, A. Iyo, J. Phys. Soc. Japan 78, 034712 (2009)
- 161. H. Kito, H. Eisaki, A. Iyo, J. Phys. Soc. Japan 77, 063707 (2008)
- 162. J. Yang et al., Supercond. Sci. Technol. 21, 082001 (2008)
- 163. Z.A. Ren, Z.X. Zhao, Adv. Mater. 21(45), 4584 (2009)
- 164. N.D. Zhigadlo, S. Katrych, Z. Bukowski, S. Weyeneth, R. Puzniak, J. Karpinski, J. Phys.: Condens. Matter 20, 342202 (2008)
- 165. C. Martin et al., Phys. Rev. Lett. **102**(24), 247002 (2009)
- 166. A. Jesche, C. Krellner, M. de Souza, M. Lang, C. Geibel, New J. Phys. 11, 103050 (2009)
- 167. J.-Q. Yan et al., Appl. Phys. Lett. 95(22), 222504 (2009)
- 168. Y. Ma et al., arXiv preprint arXiv:1505.06014 (2015)
- 169. Z. Shermadini, A. Krzton-Maziopa, M. Bendele, R. Khasanov, H. Luetkens, K. Conder, E. Pomjakushina, S. Weyeneth, V. Pomjakushin, O. Bossen, A. Amato, Phys. Rev. Lett. 106, 117602 (2011)

References 191

170. D.A. Torchetti, M. Fu, D.C. Christensen, K.J. Nelson, T. Imai, H.C. Lei, C. Petrovic, Phys. Rev. B 83, 104508 (2011)

- 171. G. Friemel, J.T. Park, T.A. Maier, V. Tsurkan, Y. Li, J. Deisenhofer, H.A.K. von Nidda, A. Loidl, A. Ivanov, B. Keimer, D.S. Inosov, Phys. Rev. B 85, 140511(R) (2012)
- 172. N. Lazarević, M. Abeykoon, P.W. Stephens, H. Lei, E.S. Bozin, C. Petrovic, Z.V. Popović, Phys. Rev. B 86, 054503 (2012)
- 173. A.F. May, M.A. McGuire, H. Cao, I. Sergueev, C. Cantoni, B.C. Chakoumakos, D.S. Parker, B.C. Sales, Phys. Rev. Lett. 109, 077003 (2012)
- 174. J. Zhao, H. Cao, E. Bourret-Courchesne, D.H. Lee, R.J. Birgeneau, Phys. Rev. Lett. 109, 267003 (2012)
- 175. Z. Wang, Y. Cai, H.X. Yang, H.F. Tian, Z.W. Wang, C. Ma, Z. Chen, J.Q. Li, Chin. Phys. B 22, 087409 (2013)
- 176. S.C. Speller, P. Dudin, S. Fitzgerald, G.M. Hughes, K. Kruska, T.B. Britton, A. Krzton-Maziopa, E. Pomjakushina, K. Conder, A. Barinov, C.R.M. Grovenor, Phys. Rev. B 90, 024520 (2014)
- 177. J. Paglione, R.L. Greene, Nat. Phys. 6, 645 (2010)
- 178. A.S. Sefat, Rep. Prog. Phys. 74, 124502 (2011)
- C.A. McElroy, J.J. Hamlin, B.D. White, M.A. McGuire, B.C. Sales, M.B. Maple, Phys. Rev. B 88, 134513 (2013)
- U. Pachmayr, F. Nitsche, H. Luetkens, S. Kamusella, F. Brueckner, R. Sarkar, H.-H. Klauss,
   D. Johrendt, Angew. Chem. Int. Edit. 54, 293 (2015)
- 181. H. Sun, D.N. Woodruff, S.J. Cassidy, G.M. Allcroft, S.J. Sedlmaier, A.L. Thompson, P.A. Bingham, S.D. Forder, S. Cartenet, N. Mary, S. Ramos, F.R. Foronda, B.H. Williams, X. Li, S.J. Blundell, S.J. Clarke, Inorg. Chem. 54, 1958 (2015)
- 182. X. Dong, K. Jin, D. Yuan, H. Zhou, J. Yuan, Y. Huang, W. Hua, J. Sun, P. Zheng, W. Hu, Y. Mao, M. Ma, G. Zhang, F. Zhou, Z. Zhao, Phys. Rev. B 92, 064515 (2015)
- 183. G. Yu, G.Y. Zhang, G.H. Ryu, C.T. Lin, To appear in. J. Phys.: Condens. Matter (2015)
- 184. W. Bao, J. Phys-condens. Mat. 27, 023201 (2015)
- 185. N.R. Werthamer, E. Helfand, P.C. Hohenberg, Phys. Rev. 147, 295 (1966)
- 186. N. Doiron-Leyraud, P. Auban-Senzier, S. René de Cotret, C. Bourbonnais, D. Jérome, K. Bechgaard, L. Taillefer, Phys. Rev. B 80, 214531 (2009)
- 187. S. Ishida, M. Nakajima, Y. Tomioka, T. Ito, K. Miyazawa, H. Kito, C.H. Lee, M. Ishikado, S. Shamoto, A. Iyo, H. Eisaki, K.M. Kojima, S. Uchida, Phys. Rev. B **81**, 094515 (2010)
- 188. G.N. Tam, B.D. Faeth, J.S. Kim, G.R. Stewart, Phys. Rev. B 88, 134503 (2013)
- 189. Y. Ando, S. Komiya, K. Segawa, S. Ono, Y. Kurita, Phys. Rev. Lett. 93, 267001 (2004)
- 190. N.E. Hussey, J. Phys-condens. Mat. 20, 123201 (2008)
- 191. K. Jin, N.P. Butch, K. Kirshenbaum, J. Paglione, R.L. Greene, Nature 476, 473 (2011)
- 192. M.B. Maple, C.L. Seaman, D.A. Gajewski, Y. Dalichaouch, V.B. Barbetta, M.C. Deandrade, H.A. Mook, H.G. Lukefahr, O.O. Bernal, D.E. Maclaughlin, J. Low Temp. Phys. 95, 225 (1994)
- 193. Q. Si, F. Steglich, Science 329, 1161 (2010)
- 194. D. Jerome, J. Supercond. Nov. Magn. 25, 633 (2012)
- 195. L. Zhao, A. Liang, D. Yuan, Y. Hu, D. Liu, J. Huang, S. He, B. Shen, Y. Xu, X. Liu, L. Yu, G. Liu, H. Zhou, Y. Huang, X. Dong, F. Zhou, Z. Zhao, C. Chen, Z. Xu, X.J. Zhou. Nat. Commu. (2016) DOI: 10.1038/ncomms10608
- 196. X.H. Niu, R. Peng, H.C. Xu, Y.J. Yan, J. Jiang, D.F. Xu, T.L. Yu, Q. Song, Z.C. Huang, Y. X. Wang, B.P. Xie, X.F. Lu, N.Z. Wang, X.H. Chen, Z. Sun, D.L. Feng, Phys. Rev. B 92, 060504 (2015)
- Z. Du, X. Yang, H. Lin, D. Fang, G. Du, J. Xing, H. Yang, X. Zhu, H.-H. Wen, Nat. Commu. (2016) DOI: 10.1038/ncomms10565

A	C
$A_x Fe_{2-y} Se_2$ , 158	Ca, 42
AFM, 124, 151, 177	CaFeAsF, 176
AFM phase transition, 181	Centimeter-size, 153
$A_{1-x}K_xFe_2As_2$ , 148	Charge ordered RVB states, 17
Al-contamination, 75	Chemical homogeneity, 155
α-NaCoO <sub>2</sub> , 135	Chemical reaction, 121
Anisotropy, 182	Composite charge model, 16
Annealing, 92, 155	Composition, 63, 134
1/8 anomaly, 13, 19	Composition distribution, 28
$A_x M X_2$ , 115	Constitutional supercooling, 8
Applied oxygen pressure, 89	Contaminated, 80
	Convex growth, 122
В	Copper-based, 143
$Ba_2As_3$ -flux, 157	Crucible, 41
BaFe <sub>2</sub> As <sub>2</sub> , 149	Crucible-free Floating Zone, 54
$BaFe_2(As_{1-x}P_x)_2$ , 156	Crystal growth, 47
BaFe <sub>2-x</sub> Co <sub>x</sub> As <sub>2</sub> , 145, 155	Crystal habit, 56
$BaFe_{2-x}M_xAs_2$ , 148	Crystalline quality, 177
β-FeSe, 167	Crystal quality, 109
β-Na <sub>0.6</sub> CoO <sub>2</sub> , 131, 135	Crystals, 63, 64
Binary, 72	Crystal structure, 131, 136
(BiO) layer, 50	CuO <sub>2</sub> planes, 2
Bi-2201, 54	CuO-Cu <sub>2</sub> O phase diagram, 76
Bi-2223, 108	
Bi <sub>2</sub> O <sub>3</sub> -rich, 76	D
Bi <sub>2</sub> O <sub>3</sub> self-flux, 60	Decanting, 147
Bi <sub>2.1</sub> Sr <sub>1.5</sub> CaCu <sub>1.8</sub> O <sub>y</sub> solvent, 91	Decompose, 160
Bi <sub>2.4</sub> Sr <sub>1.5</sub> Ca <sub>1.0</sub> Cu <sub>1.8</sub> O <sub>y</sub> , 76	Defects, 35, 96
$Bi_2Sr_2CaCu_2O_{8+\delta}$ , 72	Degradation, 71
Bi <sub>2</sub> Sr <sub>2</sub> CuO <sub>y</sub> , 48	Dehydration process, 129
$Bi_2Sr_{2-x}La_xCuO_y$ , 60	$\Delta T_c$ , 92
Bridgman, 78, 80, 169	Diffusion limited, 109
Bridgeman method, 172	Disproportionation reaction, 94
Bronze-type, 115	Dominant, 106

Doping, 153	I
Double-mirror type, 82	Improved, 109
Double nodeless superconducting gaps,, 185	Incongruently, 51, 121
Drawbacks, 77	Inhomogeneous, 137
DTA-TG, 120	INS measurements, 154
	Intercalation, 117
E	Intergrowth problem, 96
EDX, 124	Intrinsic superconducting phases, 14
EDX analysis, 102	Ion/cluster exchange, 179
Effective distribution coefficients, 4	Iron-based, 143
Electrochemical method, 125	Iron content, 160
Electron-dominant charge transport, 182	Iron-vacancy-ordered states, 161
Electronic, 149	Isostatically pressed, 84
Electronic phase diagram, 178	
Electronic properties, 177	K
Electron-like bands, 184	KCl–AlCl <sub>3</sub> flux, 166
Electron pockets, 185	KCl solution, 166
Equilibrium, 51	$K_{0.80}Fe_{1.81}Se_2$ , 161
Etch pattern, 36	$K_{0.80}$ Fe <sub>1.88</sub> Se <sub>2</sub> , 162
Etch pit, 37	$K_{0.8}Fe_{1.6}Se_2$ , 179
Eutectic, 72	K <sub>2</sub> NiF <sub>4</sub> -type structure, 1
Evacuated container, 125	KOH, 40
F	L
FeAs-flux, 157	La-doped, 61
Feed rod composition, 103	$LaFeAsO_{1-x}F_x$ , 174
Fermi surface, 185	La <sub>2</sub> O <sub>3</sub> –CuO system, 4
Ferroelastic, 33	Laser-heating, 12
FeSe <sub>0.94</sub> , 166	Lattice parameter, 64
FeX <sub>4</sub> tetrahedral, 144	Layer-by-layer growth mechanism., 149
Floating-zone, 62, 159	Layer-intercalation mechanism, 107
Floating zone method, 119	LiCl-CsCl flux, 166
Flux, 27	LiFeAs, 171
Flux-grown, 53, 80	$(Li_{1-x}Fe_x)OHFe_{1-y}Se, 177$
Flux method, 118	(Li <sub>0.84</sub> Fe <sub>0.16</sub> )OHFe <sub>0.98</sub> Se, 180, 183
	Low growth rate, 99
G	Low-oxygen limit, 103
$\gamma$ -Na <sub>0.7</sub> CoO <sub>2</sub> , 119	Low-temperature orthorhombic (LTO), 3
Growth, 52	
Growth mechanisms, 37	M
Growth parameters, 159	Magic hole concentrations, 14
	Magnetic, 149
H	Magnetic properties, 170
Halogen lamps, 99	Magnetic susceptibility, 31, 67, 137
Heterovalent substitution, 59	Mass consumption, 7
High-quality, 74	Melting behavior, 41, 52, 120
Hillocks, 37	Micrometer-scale, 163
Hole-like bands, 184	Microstructure analysis, 163
Homogeneity, 102	Mirror tilted up, 12
Homogeneous, 63, 162	Misorientation, 75
Homogeneous crystal, 167	Modulation structures, 68
Hopper-like morphology, 38	Molten, 7
HTT-LTO transition, 11	Molten zone, 55
Hydration, 126	Molten zone refinement, 78

Morphology, 125	Primary crystallization field, 73
Mosaicity, 64	Pseudo-binary, 4
Mott insulator, 3	P-T (pressure–temperature) diagram, 25 The pure (Ca-free) Bi-2201, 51
N	•
NaAs flux, 175	Q
Na <sub>x</sub> CoO <sub>2</sub> , 118	Quasi-two-dimensional structure, 179
Na <sub>0.35</sub> CoO <sub>2</sub> •1.3H <sub>2</sub> O, 116	Quaternary, 50
Na-extracted, 125	•
NaFeAs, 174	R
Na <sub>2</sub> O, 122	Raveau phase, 49
Narrow crystallization field, 105	RE-Ba-Cu-O, 23
Naturally cleaved, 169	RE-123, 31
Negative coupling constant, 16	Resistivity, 149, 171
Nelson-Riley (N-R) function, 134	$RFeAsO_{0.9}F_{0.1}$ , 175
Neutron, 69	Rocking curves, 57, 69, 161
NMR, 152	
Non-superconducting, 139	S
Nucleation-controlled method, 30	Saturation, 86
Nucleation pole, 147	Screw dislocation, 37
0	SDW, 177
Ontimal superconducting phase 129	SDW state, 150
Optimal superconducting phase, 128	SDW transition, 150
Optimum hydrate, 129	Secondary phase, 58
Orthorhombic, 93	Seed crystals, 9
Over-doped, 93 Overdoped Bi-2212 crystals, 89	Segregation coefficient, 30, 155 Self-adjusted, 98
Over doped regime, 67	Self-flux method, 39, 169, 176
Over-hydrated, 129	Self-stabilizing, 8
Oxygen atmosphere, 122	Single-phase crystals, 105
Oxygen partial pressure, 34	Slow growth rate, 101
Oxygen partial pressure, 54 Oxygen pressure, 58	Sluggish, 109
Oxygen treatment, 93	Sm-123, 31
Oxygen treatment, 93	Sn flux, 146, 150, 175
P	Sn-flux method, 173
P2, 122	Soaking, 84
P6 <sub>3</sub> /mmc, 118	Sol-gel approaches, 9
Paramagnetically, 49	Solid-liquid interface, 62, 86
Partial oxygen pressure, 83	Solution, 39
Pb-doped crystals, 103	Solvent, 9
PbFCl structure type, 171	Spin fluctuations, 168, 182
PbO-type, 164	Square pits, 36
Pb-substitution, 69	SrFe <sub>2</sub> As <sub>2</sub> , 148
Peritectically, 95	Stabilization energy, 17
Peritectic reaction, 52	Structural modulation, 60
Phase diagrams, 24, 139, 171	Structure, 131
Phase separation, 163	Structure of cleaved crystals, 64
Physical properties, 131	Substitution, 41
Planar crystallization front, 87	Superconducting transition, 71, 106
Polycrystalline, 133	Superconductivity, 47, 58, 182
Post-annealing, 157	Superconductor, 136, 143
Pre-melting, 55, 120	Susceptibility, 108
Pressure, 81	Susceptibility measurements, 137
11000010, 01	Susceptionity measurements, 157

T	Undoped, 49
Temperature-composition (T-C) diagram, 25	Uniaxial pressure, 34
Temperature oscillation method, 28	Unstable, 129
Tetragonal (HTT), 3	
Tetragonal structure, 64	$\mathbf{V}$
Thermoelectronic, 116	Vacuum, 92
Thermomechanical detwinning, 33	
Three-layer, 131	X
TM doped, 154	XRD, 122, 129
Transition, 77	
Transport, 170	Y
Traveling-solvent floating-zone, 167	Y-123, 27
TSFZ process, 6	Y-124, 41
TSSG method, 28	$YBa_2Cu_3O_{7-\delta}$ , 23
Twin, 33	$YBa_2Cu_4O_8$ , 23
Two-layer, 118	
11 type, 164	Z
1111 type, 174	Zn, 42
122 type, 145, 158	$ZrO_2$ , 41
U	

Underdoped, 108